TID-4500, UC-34
Physics

LAWRENCE LIVERMORE LABORATORY
University of California/Livermore, California/94550

UCRL-51232

NEUTRON SPECTRA EMITTED BY ^{239}Pu, ^{238}U, ^{235}U, Pb, Nb, Ni, Al, AND C IRRADIATED BY 14 MeV NEUTRONS

John Luther Kammerdiener
(Ph.D. Thesis)

MS. date: July 5, 1972

NOTICE

This report was prepared as an account of work sponsored by the United States Government. Neither the United States nor the United States Atomic Energy Commission, nor any of their employees, nor any of their contractors, subcontractors, or their employees, makes any warranty, express or implied, or assumes any legal liability or responsibility for the accuracy, completeness or usefulness of any information, apparatus, product or process disclosed, or represents that its use would not infringe privately owned rights.

DISTRIBUTION OF THIS DOCUMENT IS UNLIMITED

GG

Table of Contents

Neutron Spectra Emitted by ^{239}Pu, ^{238}U, ^{235}U
Pb, Nb, Ni, Fe, Al, and C Irradiated by 14 MeV Neutrons

John L. Kammerdiener

(Ph.D. Thesis)

ABSTRACT

The ICT time-of-flight facility at Lawrence Livermore Laboratory was used to measure the elastic and inelastic differential scattering cross sections of nominally 14 MeV neutrons from targets of ^{239}Pu, ^{238}U, ^{235}U, Pb, Nb, Ni, Fe, Al, and C. Ring geometry and time-of-flight were used to measure scattered neutrons over four decades of energy between 10 keV and 14 MeV at an energy resolution of $E^{3/2}/200$ (MeV). Measurements were made in 5 degree increments between 20 and 160 degrees (lab) with an angular resolution of 2 degrees. An Ne 213 scintillation detector was used to detect scattered neutrons with energy greater than one MeV. Pulse shape discrimination circuitry allowed simultaneous recording of both neutron and gamma (pulse height spectrum) data with low background. A ^{6}Li-glass detector was used for measurements below 1 MeV. Statistical uncertainties are less than 10%. Scattering from the 1 cm x 2 cm x 22 cm ring targets was corrected for multiple scattering, flux attenuation, isotopic abundance by Monte Carlo calculations. The 2^{+} levels of Fe and Ni were clearly resolved but 3^{-} levels expected at similar excitation energies in ^{239}Pu, ^{238}U, ^{235}U were not seen.

I. INTRODUCTION

The applied science of controlled thermonuclear reactor design has made it imperative that neutron transport calculations be accurate for neutron energies up to 14 MeV. Recent testing of such calculations against simple integral experiments has drawn attention to the lack of good cross section data for neutron scattering in the region near 14 MeV.[1, 2, 3, 4, 5] These measurements were undertaken to partially correct that deficiency and define the necessary neutron transport code inputs.

The ICT facility at Lawrence Livermore Laboratory was used to measure the neutron emission spectra from ring geometry targets of ^{239}Pu, ^{238}U, ^{235}U, Pb, Nb, Ni, Fe, Al, and C. The targets were bombarded by nominally 14 MeV neutrons produced by the $T(d,n)^4He$ reaction. Measurements were made with higher energy resolution and over a greater energy range than had been previously possible in this type experiment. The differential cross sections derived from these data were corrected for flux attenuation and multiple scattering.

Time resolution was less than 1.5 nanoseconds FWHM (full-width-half-maximum) at 831 centimeters flight path. The neutron emission spectra were measured over four decades of energy, from 14 MeV to a few keV.

Ring geometry and time-of-flight techniques were employed. Measurements were made in three overlapping energy ranges. A NE 213 scintillation detector was used in two steps to measure the energy range 14 MeV - 1 MeV. A Li-glass scintillation detector was used to extend the range to 10 keV. Pulse shape discrimination was used above 1 MeV to suppress gamma background

Neutron cross section measurements are difficult due to the basic nature of neutron interactions with matter. The primary physical phenomena used in observing the results of nuclear interactions is the Coulomb force field. The neutron interacts only weakly with a Coulomb field through its magnetic dipole. The experimentalist is thus constrained to observing the effects of charged particles first scattered by neutrons via the nucleon-nucleon interaction due primarily to the strong nuclear force. Neutrons interact only once in reasonably sized detectors and deposit only a fraction of their energy. For this reason, the direct determination of neutron energy is exceedingly difficult. The time-of-flight technique is the best known method for measuring neutron energy and was used here.

The time-of-flight of each observed neutron is accurately determined by bombarding the scatterer with short pulses of neutrons and using electronics with sub-nanosecond resolution to measure the elapsed time between neutron generation and detection. In the present experiment, the source-scatterer distance was made small compared to the scatterer-detector distance such that the elapsed time measured was the flight time of the scattered neutrons. With the flight time known, a relativistic calculation, quickly made by the computer, yields the energy of the scattered neutron.

Thus constrained to a time-of-flight experiment, ring geometry was chosen as the best of several alternative methods. Ring geometry is described and compared to cylindrical geometry and flat plate geometry in appendix A. It was chosen because it came closest to fulfilling

the needs of a good neutron cross section measurement in the present case.

The needs of a good neutron cross section measurement are:

1. Good energy resolution.
2. Good spatial definition.
3. Coverage of energy range of interest.
4. Adequate statistics.
5. Reasonable running time.

Each of these needs will be discussed briefly and the results obtained in these measurements will be noted.

Good energy resolution is obtained in time-of-flight by using an isoergic source in short time pulses coupled with a long flight path. Short time pulses result in a low duty cycle which then causes a low source flux of neutrons. Long flight paths reduce the neutron flux at the detector. These factors must be balanced in order that adequate statistics can be obtained in reasonable running times. The energy resolution of these experiments was $E^{3/2}/200$ where E is the observed neutron energy in MeV.

Good spatial definition is required for three general reasons. First, the scattering angle is defined only to the accuracy of the angle intercepted by the scatterer. Correction for this effect is extremely difficult if not impossible. Second, multiple scattering in the scatterer is proportional to the distance the scattered neutron must travel through the scatterer after first scatter has occured. This distance must be limited to less than 1/4 mean-free-path if reasonable multiple scattering corrections

are to be made using some type of multiple scattering calculation. The above two requirements can be met, and good spatial resolution obtained, only when the scatterer is very small. The scattered flux of neutrons is directly proportional to the scatterer's mass. High mass scatterers and good spatial resolution are possible in ring geometry. The rings used in these experiments had an average radius of 11 centimeters, were 1 centimeter thick axially and 2 centimeters thick radially. The scatterers intercepted an angle of 3 to 5 degrees, depending on angle, thus giving fair angular resolution and the scattered neutron traversed less than 1/4 mean-free-path of the scattering material, yielding data which could be corrected for multiple scattering using Monte Carlo calculational techniques. The third requirement of good spatial definition is that scattering be observed at a sufficient number of angles to determine angular distributions of the scattered neutrons. This is especially important for source neutron energies as high as 14 MeV, which was the case here. Neutron scattering was observed in 5 degree intervals between 25 and 85 degrees and in 10 degree intervals to 155 degrees. Since scattering was observed at as many as 20 detector positions, running time at each angle had to be minimized.

Since the scatterer mass in grams was 138 times its density, the flux of scattered neutrons was kept high and adequate statistics were obtained quickly. The energy range of an experiment is determined by the type of data needed. It is desirable in this case to determine the total number of scattered neutrons. To accomplish this, the flux of scattered neutrons was measured at energies from a few keV to source energy, an energy range of four decades. Since neutron flight times scale as

$\frac{\text{Flight Path}}{\sqrt{\text{Energy}}}$, low energies are observable at long flight path only when the pulse rate, and therefore the duty cycle and source flux, are very low. The measurements over the complete energy range of interest were thus expedited by making three separate measurements, each tailored to a portion of the energy range.

Using ring geometry and subdividing the energy range of observation into three parts, adequate statistics were obtained for each isotope in about one hour running time per angle. Counting statistics were kept at less than 10% over the entire energy range of interest.

II. Experimental Method

The neutron emission spectra from most of the targets reported were measured in three steps, covering three overlapping energy ranges. Since each of the three steps concentrated on detecting neutrons in a different energy range, experimental technique varied greatly with each I shall note these differences while describing the experimental methods all three had in common. The three steps will be referred to as hign, medium, and low energy.

High energy covers the energy range of the maximum energy scattered neutron (14 MeV) down to 4 MeV. In this range, time and energy resolution of the incident neutron pulse were kept at the minimum value attainable experimentally. Scattering was observed at many angles. This region covers the bulk of the experimental data. These data have finer energy resolution, and measured energy distributions cover more scattering angles, than achieved hereto.

The low energy measurements employed a ^{6}Li-glass scintillator to measure neutrons in the energy range 2 MeV-10 keV. This was the first time emission spectra from targets bombarded by 14-MeV neutrons were measured to such low energy. Only the 95° (LAB) spectra were observed, since scattering to this energy range can be assumed isotropic[6] to within the accuracy the absolute detector efficiency is known.

The medium energy measurements employed a doubly biased NE 213 detector to measure neutrons in the energy range from 600 keV to 14 MeV. Emphasis was placed on the region between 1 MeV and 5 MeV. This measurement thus overlapped the high and low measurements and completed the range of emission energies. The spectra were measured at 45°, 95°, and 135° in this mode.

IIA. Neutron Source

Source neutrons were generated by the Lawrence Livermore Laboratory Insulated Core Transformer facility. The high neutron fluxes generated by this accelerator allowed rapid data acquisition. The machine was operated in three different modes in order to take the high, medium, and low energy data. Fig. 1 is a schematic of the ICT facility showing the three modes of operation used. Route I, denoted by the single line, was used for high energy data; route II was used for medium energy data; and route III was used for low energy data.

NEUTRON SOURCE

Fig. 1

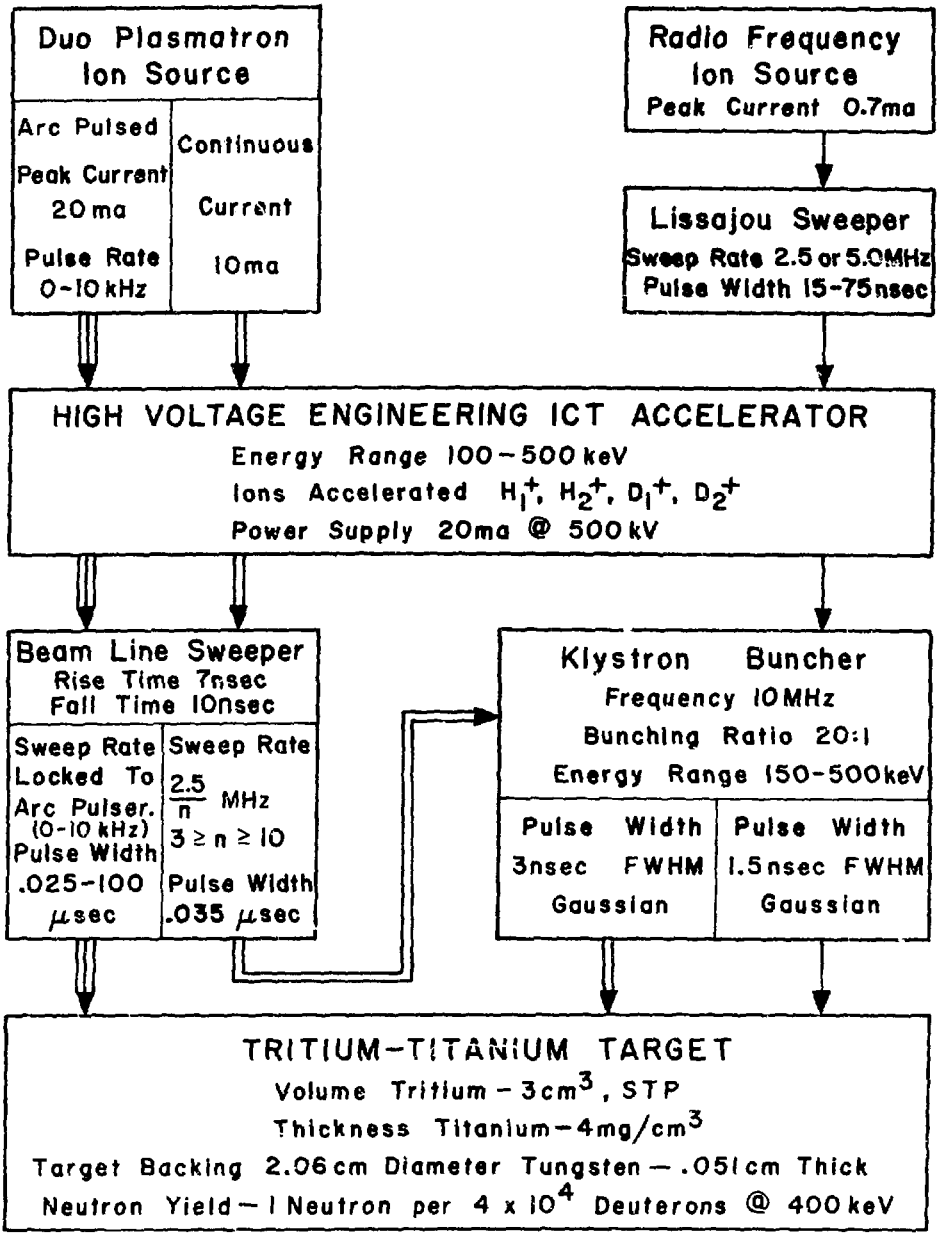

IIA.1 Insulated Core Transformer (Positive Ion Accelerator)

The High Voltage Engineering ICT - Model 500N accelerator* was used to accelerate the D^+ ions. Low and medium energy runs were made using 400 keV D^+ ions. High energy runs were made using 190 keV D^+ ions to improve the isotropy of the neutron source and to improve the energy resolution caused by the spread in reaction energy of the D^+ ions (see Sect. IIA.8) The machine automatically maintained terminal voltage to within a few kV. Manual override by the operator kept the accelerating potential constant to within a kV, so that the buncher stayed in phase with the pulsed beam.

*Reference to a company or product name does not imply approval or recommendation of the product by the University of California or the U. S. Atomic Energy Commission to the exclusion of others that may be suitable.

IIA.2. D^+ Ion Source

The ICT has two ion sources available, each capable of supplying D^+, D_2^+, H^+, and H_2^+ ions. The ion sources are located in the machine terminal where they see the terminal voltage as ground.

The Duo-Plasmatron source is capable of microsecond pulsing and D.C. operation. The RF source is coupled to a terminal mounted sweeper which allows nanosecond pulsing of the beam.

IIA.2.a. RF Ion Source and Sweeper

The RF ion source operates at peak currents of 1 ma. D^+ ions are extracted through a voltage of several 10's of keV and focused on an aperture by a three element Einzel lens. The beam is swept at 2.5 MHz (crystal controlled) in both the horizontal and vertical directions, thus crossing the aperature once each cycle, resulting in a pulse of ions every 400 nsec. This pulse can be varied in length from 15-75 nsec. The pulse is then accelerated by the ICT to ground.

The RF ion source was used for the high energy runs. The sweeper was modified by grounding the horizontal sweeper plates, thus causing double passage over the aperture each cycle, resulting in a pulse each 200 nsec. Slightly unequal (in time) sweeping resulted but this was overcome by modifying the electronics.(See Sec.II.D.1) Pulse length was 35 nsec. The pulse was bunched (See Sec. IIA.3) after acceleration.

IIA.2.b. Duo-Plasmatron Ion Source and Sweeper

The Duo-Plasmatron ion source operates in a D.C. mode at 10 mA or in microsecond pulse mode with 20 mA peak current. Both of these modes were used, but in each case a beam sweeper was inserted into the beam line after the accelerator. The sweeper operates either at the Duo-Plasmatron pulsing frequency or at a frequency of 2.5 MHz/n, where $3 \geq n \geq 10$.

The Duo-Plasmatron source was employed in the D.C. mode for the medium energy runs. The sweeper was operated at 733.3 kHz and the pulse length was 35 nsec with a peak current of 7 ma. Rise time for the pulse was 7 nsec. Fall time was 10 nsec. The pulse was then bunched (See Sec. IIA.3).

The Duo-Plasmatron was arc-pulsed for the low energy runs. The sweeper was phase locked to the arc pulser and used to reduce the pulse length to either 100 nsec or 500 nsec. The buncher was not used when low energy data were taken.

IIA.3. Buncher

A gridded klystron buncher, operating at 10 MHz, was employed for both high and medium energy runs. The buncher was redesigned to allow optimum operation at beam energies of 200 keV and 400 keV. Four 95% pass grids were employed at 200 keV to reduce buncher focusing effects.

The buncher is phase-locked to the 2.5 MHz RF sweeper frequency. A frequency multiplier generates the 10 MHz operating frequency. Buncher voltage and phase are variable. Since only half of the 100 nsec period of the sweeper can be used, a 50 nsec pulse length maximum is established. The buncher will form satellite peaks 100 nsec before or after the main peaks if the pulse tail extends beyond 100 nsec. The buncher voltage is sinusoidal, and since the bunching occurs only if the bunching voltage is nearly linear, the entire half-period of the buncher cannot be used. For these reasons, a maximum pulse length of 35 nsec was used, thus obtaining maximum current and optimum time resolution. Overall system resolution was determined by observing the prompt gamma rays. In the high energy mode of operation, system resolution as measured in this manner was consistently kept below 1.5 nsec FWHM.

When the swept Duo-Plasmatron beam was bunched for the medium energy runs, the observed prompt gamma peak was about 3 nsec FWHM. Slow rise and fall times of the Duo-Plasmatron beam sweeper caused the pulse to tail into the non-linear region of the buncher, resulting in the broader bunched pulse. The peak current in this mode was about six times the peak current in the high energy mode. This resulted in a higher space charge and caused the beam to blow up slightly, contributing to the observed poorer resolution.

IIA.4. Beam Transport System

The D^+ ion beam is focused in the ICT terminal by a magnetic lens before being allowed to accelerate to ground through the accelerator tube gradient resistors such that there is a crossover point at the beam line sweeper located in the machine room. The beam then passes through vertical and horizontal steering magnets and a focusing quadrapole magnet before passing through a 1.5 meter thick concrete wall and into the target pit, where it enters a bending magnet at another beam crossover point. The bending magnet deflects the beam 26 degrees to the center of the target pit. The bending magnet also analyzes the beam, thereby discarding any unwanted species such as D_2^+ which would not be in phase with the buncher. A horizontal steering magnet then corrects any horizontal displacement introduced by the bending magnet before the beam enters the klystron buncher. The defocusing properties are partially overcome by gridding the buncher. After passing the buncher, the ion beam passes two more focusing quadrapole magnets before striking the tritium target.

II.A.5. Titanium-Tritium Target

The accelerated D^+ ions strike a composite target of tritium-titanium-tungsten. The target is made by evaporating a 4 gm/cm^2 layer of titanium onto a disk of tungsten 0.051 cm thick. The Ti-W disk is then heated to 400°C and cooled in a tritium environment. About 4 cc of T is absorbed by the Ti layer giving a T/Ti ratio of 1 to 1.5.

Target cooling was required due to the high D^+ ion flux. Some medium energy runs were made with 40 microamperes of 400 keV D^+ ions. Water spray cooling of the target was required to dissipate the 16 watts of energy deposited in the target by the beam. Cooling was necessary to prevent flaking of the titanium from the tungsten backing and to impede evolution of the gas from the target into the machine vacuum system. High energy runs were made with 40 microamperes of D^+ ion current at 190 keV beam energy. Air cooling was used to dissipate the 7.6 watts of energy deposited in the target.

IIA.6. Source Anisotropy

The $T(d,n)^4He$ reaction is isotropic in the center-of-mass frame of reference if the energy of the D^+ ion is less than 400 keV.[6] All measurements were made under these conditions. Source anisotropies exist however, due to the CM-Lab transformation, although these effects are small because the reaction Q-value of 17.58 MeV is much larger than the energy of the center of mass system.

The D^+ ion is stopped in the T-Ti layer. For an incident ion energy of 190 keV, about 1 D^+ ion in every 10^5 creates a neutron. The other D^+ ions are neutralized and trapped in the target, resulting in deuterium contamination of the target. Targets were replaced when contamination resulted in a background of $D(d,n)^3He$ neutrons whose flux strength was 0.1% that of the $T(d,n)^4He$ neutrons. Since the energy and direction of the D^+ ion at the time of the nuclear reaction are uncertain due to Rutherford scattering before the reaction,[7] the energy and flux distribution of the neutron source cannot be calculated directly, even though the reaction is known to be isotropic. The energy and shape of the elastically scattered peak at each angle allows calculation, using the known kinematic relations, of the source energy distribution at that angle. The energy distribution thus measured is then duplicated by calculating, trial and error fashion, the energy distribution for various D^+ ion reaction energies. In this manner the average of the D^+ ion reaction energies is determined. The average reaction energy for 400 keV and 190 keV incident D^+ ions was determined to be 200 keV and 140 keV respectively. These energies are needed to calculate the flux distribution of the source.

The flux distribution thus determined differs from previous measurements by Hansen et al.[5] where the detector efficiency was assumed constant at all angles. Their measurements, corrected for efficiency variation with angle (and therefore energy), agree with the flux calculated in the manner described above. The probability of the reaction occurring at D^+ ion energy E is:

$$\text{Reaction probability (E)} = \frac{\frac{\sigma(E)}{dE/dx}}{\int_0^{E_{max}} \frac{\sigma(E)dx}{dE/dx}}$$

dE/dx, the ion energy loss smoothly varying below 400 keV. The reaction probability therefore peaks near the resonance in the $T(d,n)^4He$ reaction at 100 keV. The average reaction energy is much higher, however, as stated in the preceeding paragraph.

Source neutron energy varied from 14.9 MeV at 20 degrees to 13.4 MeV at 155 degrees for the high energy measurements where a 190 keV D^+ ion beam was used. The flux varied by 10.1% in the same range. When 400 keV D^+ ions were used for the low and medium energy runs, the energy and flux varied by 9.9% and 10.1% from 45° to 135°.

Tables I and II show calculated values of energy and neutron flux versus Lab angle for the $T(d,n)^4He$ source for 190 keV and 400 keV deuteron energy, respectively.

Table I Calculated energy and flux variation of source neutrons at 190 keV D^+ beam energy

LAB Angle (deg)	Energy (MeV)	Relative Intensity
0	14.92	1.000
5.0	14.92	1.000
10.0	14.91	0.999
15.0	14.89	0.998
20.0	14.87	0.997
25.0	14.84	0.995
30.0	14.81	0.993
35.0	14.77	0.990
40.0	14.72	0.987
45.0	14.68	0.984
50.0	14.62	0.980
55.0	14.57	0.976
60.0	14.50	0.972
65.0	14.44	0.968
70.0	14.38	0.964
75.0	14.31	0.959
80.0	14.24	0.955
85.0	14.17	0.950
90.0	14.10	0.945
95.0	14.03	0.941
100.0	13.96	0.936
105.0	13.90	0.932
110.0	13.83	0.927
115.0	13.77	0.923
120.0	13.71	0.919
125.0	13.65	0.915
130.0	13.60	0.911
135.0	13.55	0.908
140.0	13.50	0.905
145.0	13.46	0.902
150.0	13.43	0.900
155.0	13.40	0.898
160.0	13.37	0.896
165.0	13.35	0.895
170.0	13.34	0.894
175.0	13.33	0.893
180.0	13.32	0.893

Table II Calculated energy and flux variation of source neutrons at 400 keV D^+ beam energy.

LAB Angle (deg)	Energy (MeV)	Relative Intensity
0	15.11	1.000
5.0	15.11	1.000
10.0	15.10	0.999
15.0	15.08	0.998
20.0	15.05	0.996
25.0	15.02	0.994
30.0	14.98	0.991
35.0	14.93	0.988
40.0	14.87	0.985
45.0	14.82	0.981
50.0	14.75	0.976
55.0	14.68	0.972
60.0	14.61	0.967
65.0	14.53	0.962
70.0	14.45	0.957
75.0	14.37	0.952
80.0	14.29	0.946
85.0	14.21	0.941
90.0	14.12	0.935
95.0	14.04	0.930
100.0	13.96	0.924
105.0	13.88	0.918
110.0	13.80	0.914
115.0	13.73	0.909
120.0	13.65	0.904
125.0	13.59	0.900
130.0	13.52	0.895
135.0	13.46	0.891
140.0	13.41	0.888
145.0	13.36	0.885
150.0	13.32	0.882
155.0	13.28	0.879
160.0	13.26	0.877
165.0	13.23	0.876
170.0	13.21	0.875
175.0	13.20	0.874
180.0	13.20	0.874

IIA.7. Line Shape

The time and energy spreads of the neutron source itself were thoroughly investigated. The following sources of energy and time spreads have been considered:

1. Time dependence of the D^+ ion beam.
2. Energy spread induced by D^+ ion energy loss in the Ti-T target.
3. Neutron scattering in materials near the neutron source.
4. Neutron scattering in air.
5. Neutron scattering in materials near the detector.
6. Time spread due to electronics and detector size.
7. Multiple scattering in the ring.

The time dependence of the neutron source resulting from 1, above, is the major effect. It is approximately gaussian in shape and results in an apparent energy spread since energy is determined by time-of-flight. The current on the Ti-T target was monitored with a fast sampling oscilloscope to insure that the accelerator and buncher remained tuned to the optimum time resolution of 1.5 nsecs.

Item 1 is measured by inspecting the gamma rays from a ring positioned at 95° where it encounters the minimum energy spread of the source. Item 2 is a minimum at ~90° and a maximum at 0° and 180° since the energy spread of the D^+ ion energies at reaction time results in an energy spread of C-M energies which transform as the cosine.[8] The time spread in Item 6 is caused mainly by transit time of neutrons through the 5.08 centimeter long scintillator and amounts to 1 nsec for 14 MeV neutrons and 3 nsec for 1.5 MeV neutrons. This is one reason why 3 nsec time resolution was used for the medium energy runs. Most of the mass near the neutron

source is represented by the idealized low mass target assembly shown in Fig. 2a.

Line shape was analyzed by calculating the experimentally observed line shape. Calculations using Monte Carlo Neutron Transport Code TART,[9] based on the assembly in Fig. 2a, surrounded by air, were made and are compared with an experiment run without shadow shield in Fig. 2b. The solid lines are generated by connecting calculated points two nsec apart. Error bars are plotted on every tenth point. Also shown in Fig. 2b is a calculation which shows that air scattering only attenuates the direct flux and has negligible effect on the line shape. The contribution in the "tail" is $\leq 10^{-4}$ of the direct peak. Since source normalization is accomplished by measuring the associated alpha counts (α_o) per detected neutron (I_o), the same attenuation is present in neutrons detected during a run (I); hence I/I_o at 14 MeV is unaffected by air scattering. Since the nitrogen and oxygen total and non-elastic cross sections are not rapidly varying between 2 and 14 MeV, I/I_o is also essentially unaffected by air scattering at other energies.

The effects of the collimator on the resolution function were investigated using the collimator set shown schematically in Fig. 2c. This represents most of the mass near the detector. The calculated time spread of an isoergic 15-MeV source distributed uniformly across the collimator entrance and coaxially with the collimator is shown in Fig. 2d. Time spreads due to collimator and target assembly are folded together and shown in Fig. 2e. Good agreement with the experimentally observed spectrum with the shadow shield removed provides evidence the observed line shape is well understood.

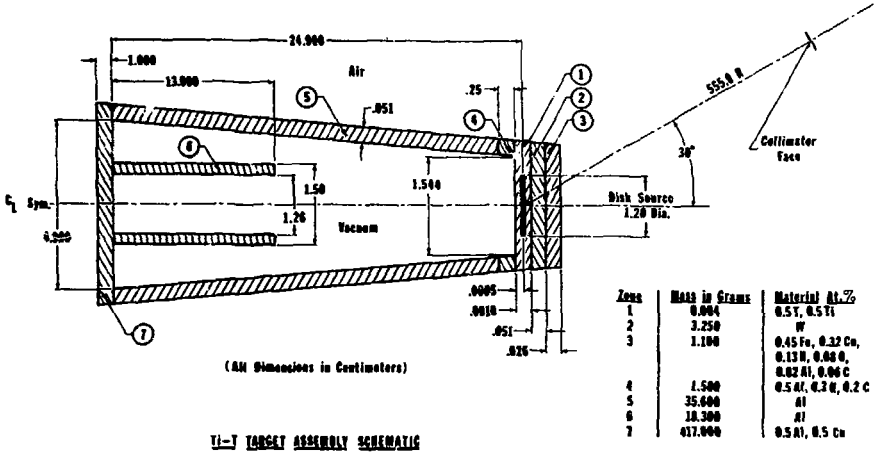

Zone	Mass in Grams	Material At.%
1	0.004	0.5 T, 0.5 Ti
2	3.250	W
3	1.100	0.45 Fe, 0.32 Cu, 0.13 H, 0.08 O, 0.02 Al, 0.06 C
4	1.500	0.5 Al, 0.3 O, 0.2 C
5	35.600	Al
6	18.300	Al
7	417.000	0.5 Al, 0.5 Cu

Idealized target assembly used to calculate line shape effects.

Fig. 2a

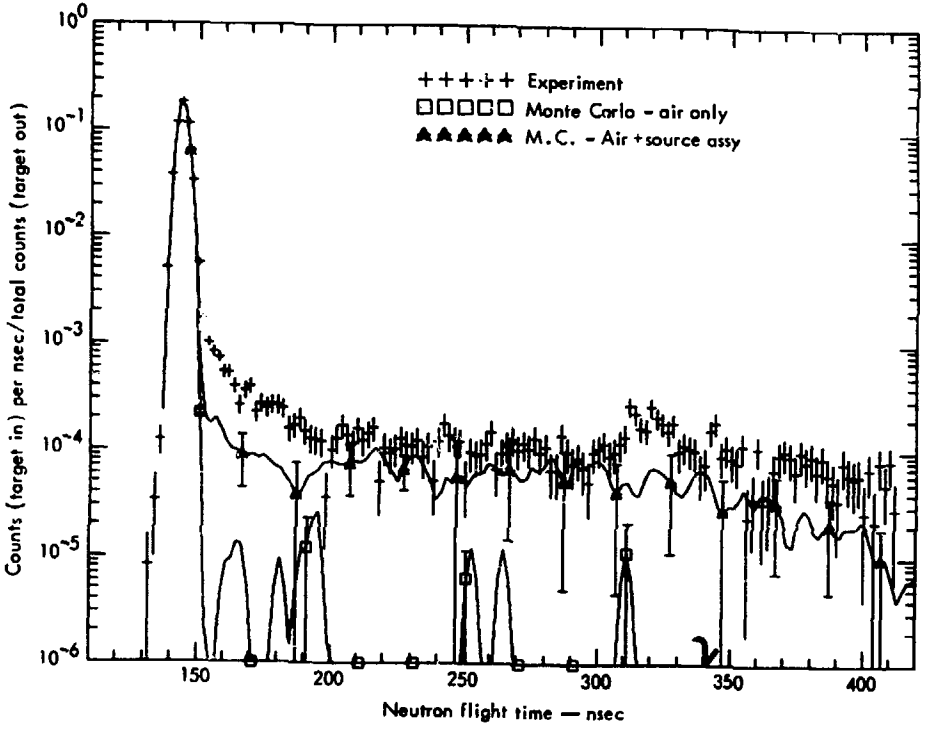

Monte Carlo calculation of air and target assembly scattering.

Fig. 2b

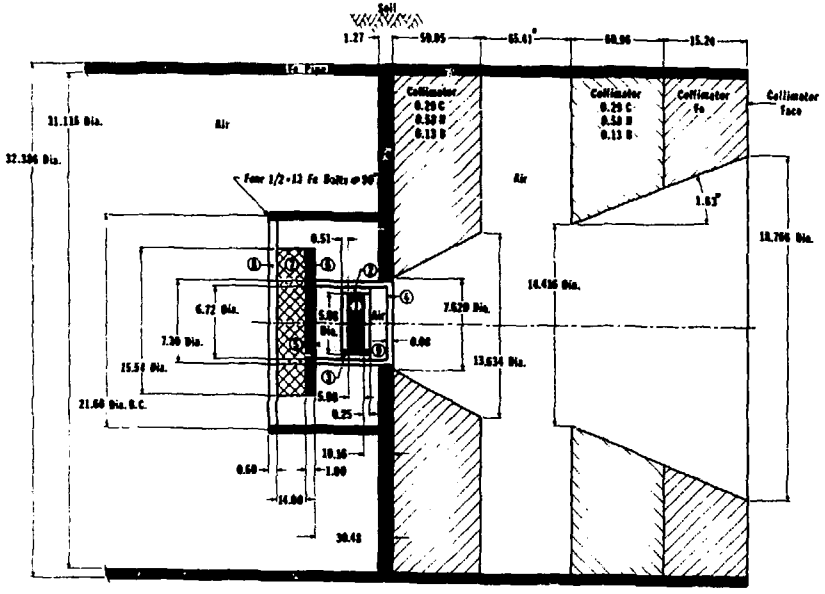

COLLIMATOR AND DETECTOR ASSEMBLY SCHEMATIC

No Scale
(All Dimensions in Centimeters)

Zone	Mass in Grams	Material Wt. %
1	91	0.45 C, 0.55 B
2	62	Al
3	44	Glass
4	533	Al
5	174	PM Tube and Base
6	1414	Fe
7	1166	Pre amp
8	877	Al
9	24	Al

Fig. 2c

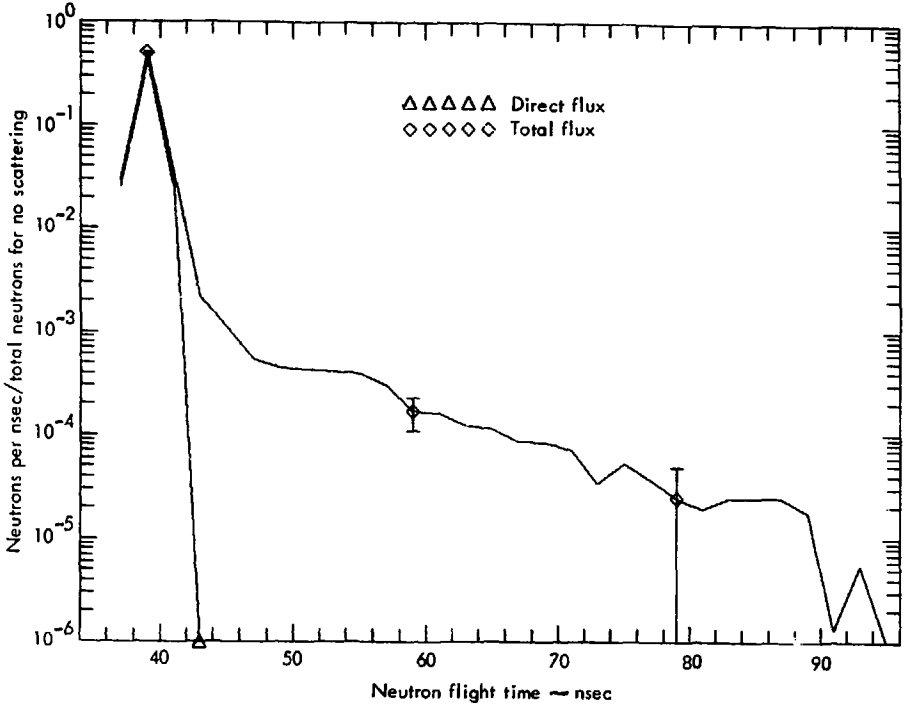

Monte Carlo calculation of collimator streaming effects.

Fig. 2d

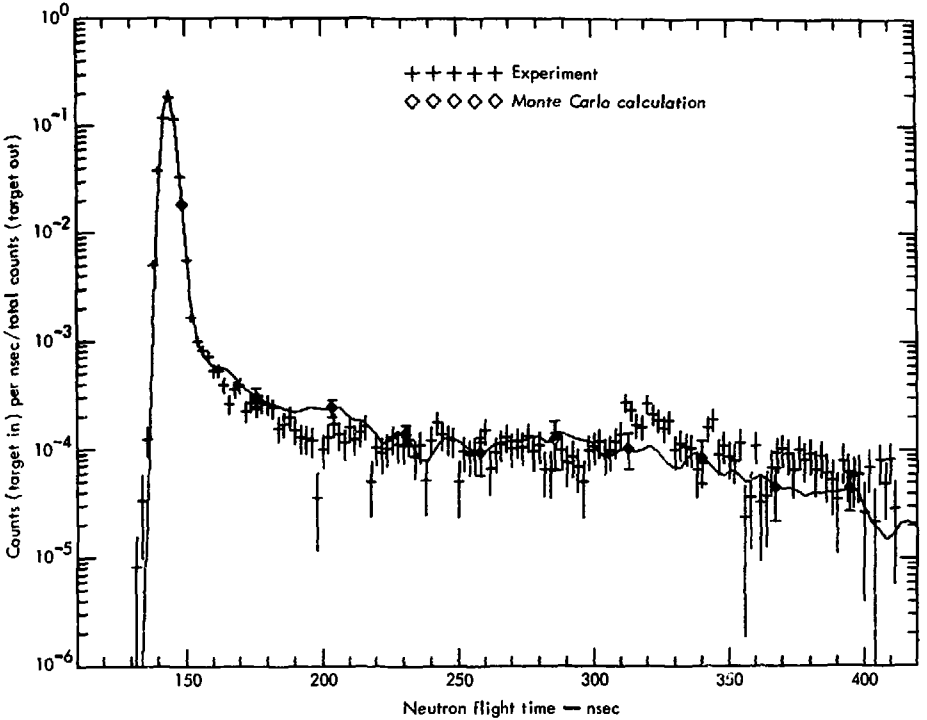

Comparison of measurement with calculation of target assembly and collimator scattering. d+d buildup neutrons are evident at a flight time of approximately 315 nsec.

Fig. 2e

The data and calculations in Figs. 2b and 2c were taken with the detector located in an alternate collimator hole 30° off beam line at a distance of 767 cm, but the effects on line shape due to these changes is negligible.

II.B. Ring Geometry Experiment

Ring geometry experimental techniques are well documented.[10,11,12,13] See appendix A for a detailed discussion of ring geometry techniques. The present application is the first on a facility which combines both high flux and good time resolution. Data of good statistical accuracy were taken at a rate of about one angle per hour. Machine and electronics fluctuations which degrade the resolution of data were minimized by the rapid data acquisition.

The ring transport apparatus allowed precise angular changes and blank runs without entering the target pit area. Target position was continuously monitored by closed circuit television. Collimation and shielding were optimized for each data set. Special safety measures were used since some of the targets involved kilogram quantities of fissile material.

Fig. 3 is a schematic of the experimental layout. The light aluminum support structure was supported from the ceiling. The detector was located in a line of sight tube drilled into the concrete wall. Fig. 2c is a better representation of detector and collimator geometry. There were several feet of air space behind the detector to reduce the probability of neutrons being back scattered into the detector.

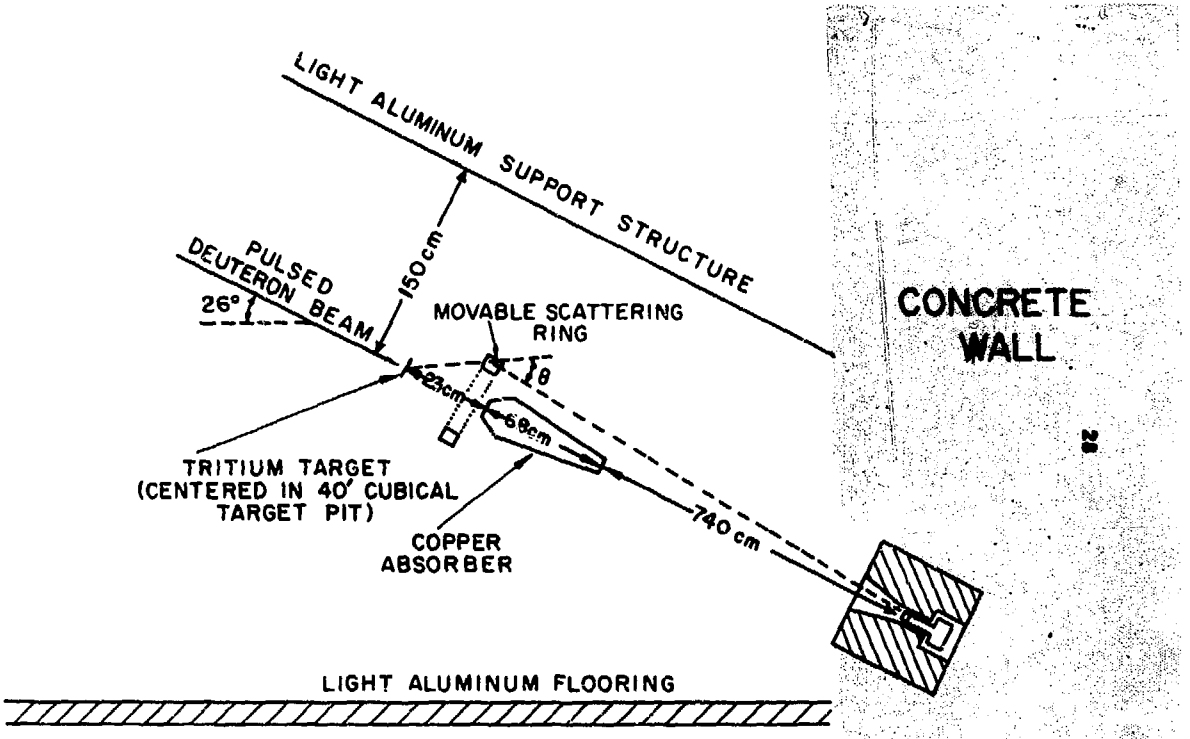
LIGHT ALUMINUM SUPPORT STRUCTURE
CONCRETE WALL
PULSED DEUTERON BEAM
26°
150 cm
MOVABLE SCATTERING RING
θ
23cm
69cm
740 cm
TRITIUM TARGET (CENTERED IN 40' CUBICAL TARGET PIT)
COPPER ABSORBER
LIGHT ALUMINUM FLOORING
BASEMENT

FIG. 3

II.B.1 Ring Transport

The ring transport rack referred to as a light aluminum support structure in Fig. 3 was used to position the ring targets and copper shadow shield. The rack was not viewed by the detector. A remotely controlled ring suspension carriage and ring removal mechanism allowed angular changes and blank runs without interrupting machine operation. Ring position was checked by closed circuit television. This system proved to be precise to within a millimeter. The ring position was checked with instruments to insure that the ring axis of symmetry moved along the beam axis. The ring was positioned so that it was orthogonal to the beam axis. Reproducibility of ring location was excellent.

II.B.2. Shielding and Collimation

The copper shadow shield (see Fig. 3) effectively stopped the source neutrons from entering the detector directly. A low mass target assembly, light string ring suspension lines, and ability to keep all heavy materials at least one meter from the source resulted in a "clean" experiment.

The detector was collimated as shown in Fig. 2c. Only neutrons from the narrow 3.26 degree cone defined by the collimator are seen by the detector. The air and shadow shield in this cone scatter neutrons in a consistent fashion, resulting in an "air peak" in the background. The high energy blank run data shown in Fig. 4 is dominated by the air peak near channel 450. A high energy data run is shown in Fig. 5. The air peak is located near channel 450 as it is in the blank run. The twin peaks near channel 425 are caused by neutrons elastically scattered from the plutonium and elastically scattered from the iron can which encases the plutonium ring. The peak near channel 415 is the result of neutron scattering from the 845 keV level in iron.

The collimator system shown in Fig. 2c was used for both high and medium energy runs. When using the system for low energy runs a large outscatter-inscatter effect was observed. This effect was due to the neutrons in the elastic and air peak scattering from the detector into the nearby walls, thermalizing,and returning to the detector resulting in abnormally high count rates in the region corresponding to a few hundred keV. The experimental arrangement was changed for low energy runs. A 30 cm hole through a concrete wall 1.5 meters thick to the room housing a Van de Graaff accelerator provided a flight path to a detector suspended

at a distance 1 meter from all structures. The outscatter-inscatter effect was reduced and cancelled completely when the time dependent blank was subtracted.

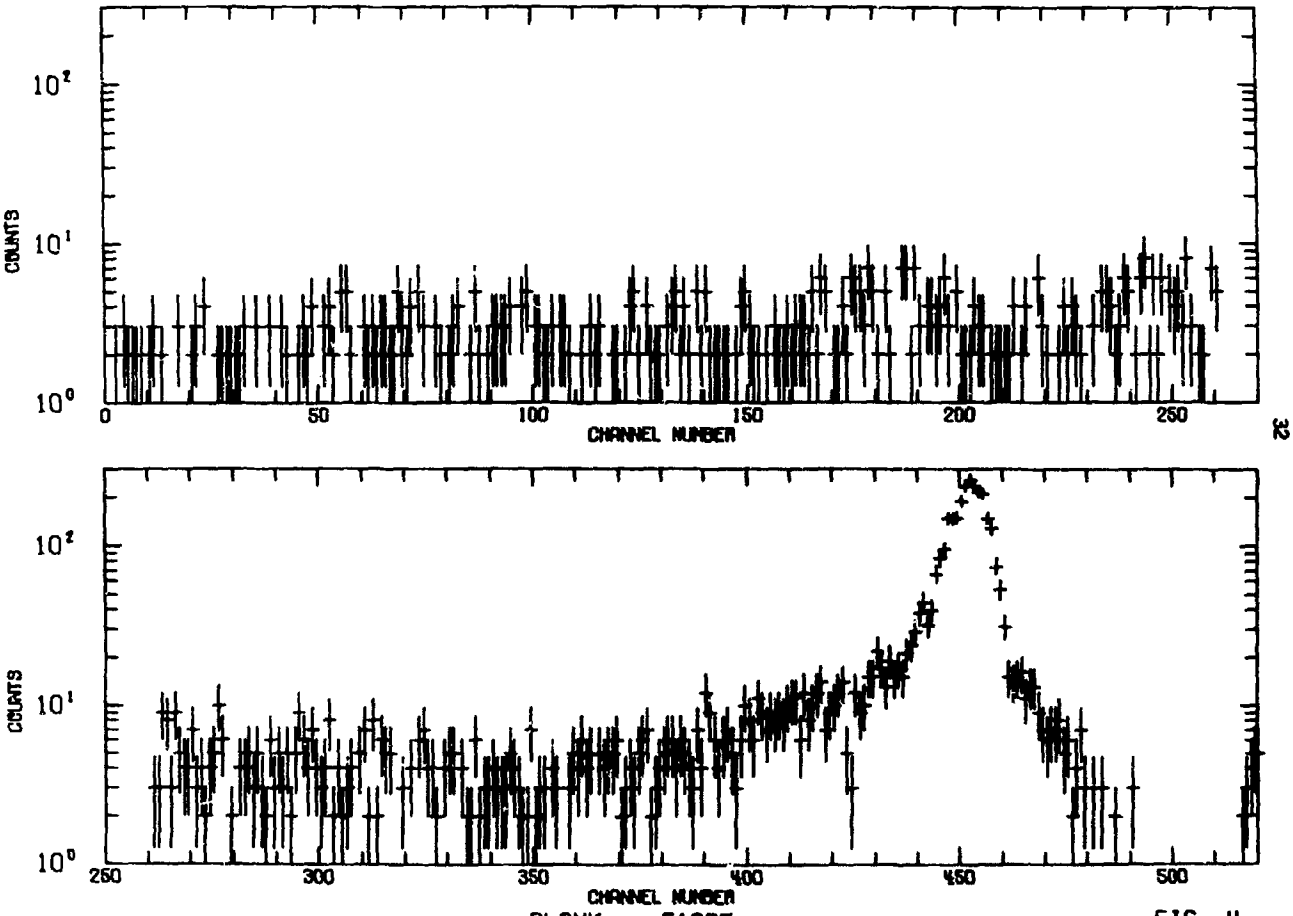

•• BLANK -- 51325 ••

FIG. 4

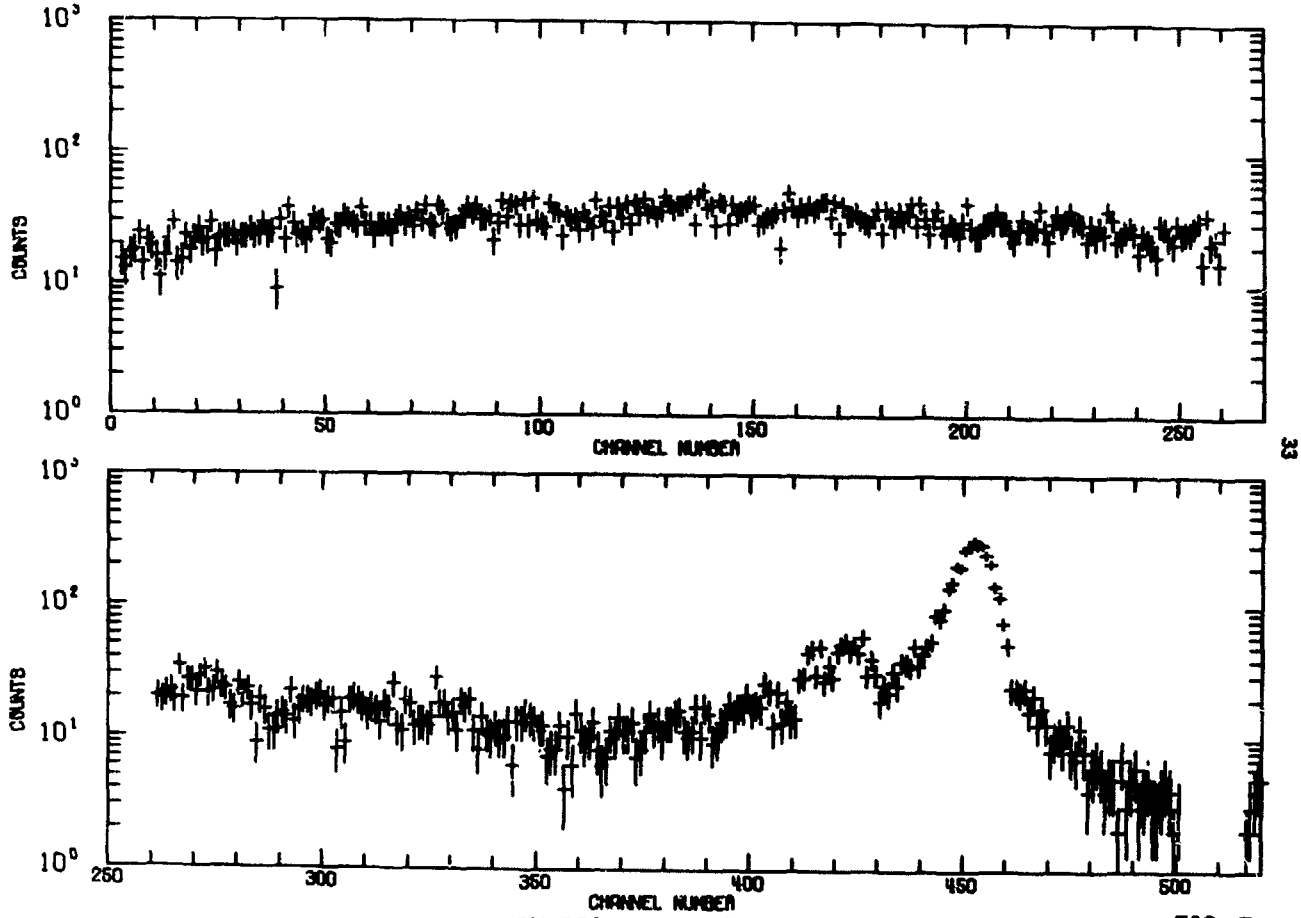

•• PU-239 -- 125 DEG ••

FIG. 5

II.B.3. Ring Targets

Optimum ring target design is a compromise of many factors including angular resolution, count rate requirements, source flux attenuation, and multiple scattering. The high source flux available allowed use of relatively thin scattering rings. Most rings had an average radius of 11 cm, were 1 cm thick azimuthally, and 2 cm thick radially. The heavy rings were less than 1/4 mean free path thick to scattered neutrons. This thickness produced a large flux of scattered neutrons without excessive multiple scattering.

Since three of the target materials were alpha emitters (^{238}U, ^{235}U, and ^{239}Pu) and quite massive (2-3 kg), special safety measures were required in handling them. For example, the ^{239}Pu ring was encased in a stainless steel container to prevent handling equipment from becoming contaminated by the alpha-particle emitter. The ring was thermally hot to the touch because of the alpha activity. The fissionable targets were kept isolated in separate cages to negate the chance of assembling a critical mass. Only one ring was out of its cage at a time. Neutron activation of the rings was a minor problem. Personnel exposure to a recently run ring was minimized to reduce the exposure to gamma activity induced by the experiment.

II.C. Detectors

Two scintillation detectors were used sequentially in separate experiments to cover the entire range of energies from source energy to a few keV. The fast timing characteristics of this type detector are ideally suited to a time-of-flight experiment. Time resolution was affected only by the detector size in the case of the NE 213 detector. High and medium energy runs (15 MeV-1 MeV) were made with a NE 213 detector using gamma discrimination. Measurements below 1 MeV were made using a ^{6}Li-glass detector. Each of these detectors is described in detail in the following sections.

II.C.1. NE 213 Detector

High and medium energy runs were made using a NE 213 liquid scintillation detector 5.08 cm long and 5.08 in diameter. The detector was light coupled to a RCA 8575 photomultiplier tube. The detector may be identified in Fig. 2c as zone 1. Zones 1 through 7 make up the detector, PM tube, and Pre-amp package and show its location relative to the collimator.

The detector was biased at the 1.28 MeV gamma line of a ^{22}Na source. The observed Compton edge of the 1.28 MeV line corresponds to the maximum recoil electron energy of 1.07 MeV. This corresponds to a proton recoil energy of 3.5 MeV.[14,15] Bias on the slow signal (see Sect. II.D.1) was set at the half-height of the observed 1.28 gamma Compton edge. Precision checks indicated that this method insured that the setting was the same for all runs. The bias was set or checked at least once daily.

Medium energy runs were made with a bias "window" to insure that the pulse height remained within the range that the pulse shape discrimination electronics could handle, thus insuring good gamma discrimination for both high and medium energy runs. The low side of the "window" was set at one-fourth the pulse height of the Compton edge of the 511 keV line of ^{22}Na, corresponding to 600 keV neutron energy. The bias of the low window was scaled using a precision pulser. The high side of the medium energy detector "window" is set at the Compton edge of the 1.28 MeV ^{22}Na line (3.5 MeV). Neutrons above 3.5 MeV are observed, however, since the neutron-proton reaction in the detector produces protons of all energies up to the incident neutron energy, some

of which are in the medium energy detector "window."

Detector efficiencies were calculated.[16] Multiple scattering from carbon in the detector was allowed, but the calculation was terminated after the first n-p collision. Multiple n-p scattering affects the efficiency of the detector most near bias cutoff. The calculated efficiency of the detector may be as much as 15% low near bias cut off. Multiple scattering in the detector is thus the largest source of systematic error, resulting in final data that may be 15% too high near bias cutoff. For this reason, data was taken in three overlapping energy regions and data near the bias cut-off was discarded.

II.C.2. ^{6}Li-Glass Scintillation Detector

Neutrons emitted from the rings with energies below two MeV were detected in a ^{6}Li-glass scintillation detector. Experimental geometry was altered so as to use a flight path through a 30 cm hole 1.5 meters long in the concrete wall separating the target pit from an adjacent room housing another accelerator. This change in technique allowed suspension of the detector far from any massive object in order that the time dependent background due to prompt neutrons outscattering from the detector and subsequently inscattering to the detector was minimized.

The detector used was a Nuclear Enterprises model 912, composed of three 0.635 cm thick discs 5.08 cm in diameter. The discs were coupled with optical grease to a 0.635 cm thick quartz light pipe and mounted atop a 8575 RCA photomultiplier. The quartz light pipe optimized pulse height resolution of the detector so that a narrow window could be set on the detector signal thereby minimizing the background due to time independent gamma rays.

An LLL chemist determined the detector composition to be:

	weight %
Si	35.1
Li (95% ^{6}Li)	7.6
O	53.1
Ce	1.2
Al & Mg	3.0

The detection mechanism is provided by the exoergic ^{6}Li(n,α)T reaction (Q-value = +4.8 MeV) and subsequent light scintillation from the cerium. Although this detector provides high efficiency detection

of low energy neutrons, it suffers from calibration difficulties due to multiple scattering of neutrons above the 250 keV resonance, inability to separate the detected gamma rays, and resonances in silicon and oxygen.

A similar detector was constructed of ^{7}Li and used to monitor the gamma background. Fig. 6 shows the pulse height spectra of the two detectors, with a thermal neutron flux incident. The peak near channel 60 is due to thermal neutrons. This peak was made sharper than the peak observed in earlier efforts by inserting a quartz light pipe between the ^{6}Li-glass and the photomultiplier tube. Gamma background was suppressed somewhat by setting a window on the neutron peak in the pulse height spectrum, thereby eliminating gamma pulses below the level corresponding to channel 50.

The multiple scattering effect was calculated using SORS Monte Carlo computational techniques.[17] The ^{6}Li-glass detector was experimentally calibrated against a low efficiency ^{235}U fission chamber. Results of the calibration are shown in Fig. 7.

The ^{6}Li-glass detector package is shown in Fig. 8. The boron pad is included to shield against unwanted epi-thermal background neutrons. This allowed a pulse rate of 10 kHz since the energy overlap from the previous cycle contained only neutrons with energies less than 36 eV. Most of these neutrons were stopped by the boron pad or formed a time-independent background.

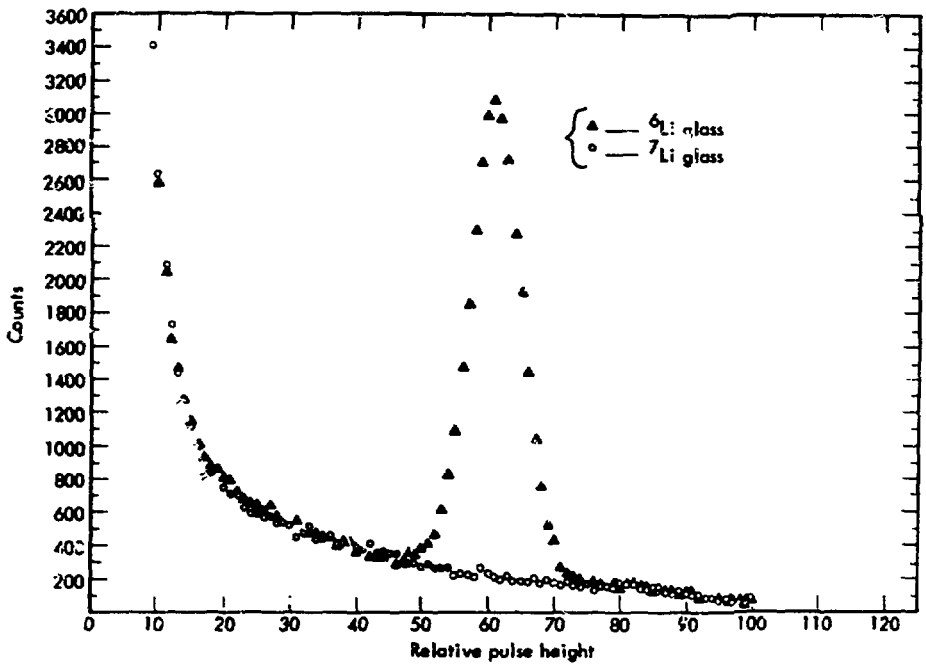

Fig. 6

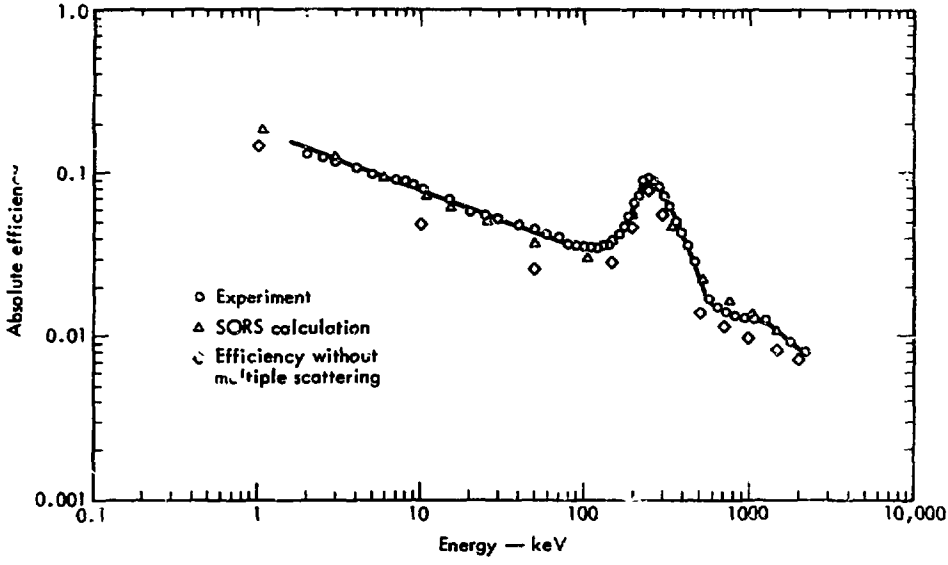
1.0
0.1
0.01
0.001
Absolute efficiency
0.1
1
10
100
1000
10,000
Energy — keV
Experiment
SORS calculation
Efficiency without multiple scattering

Fig. 7

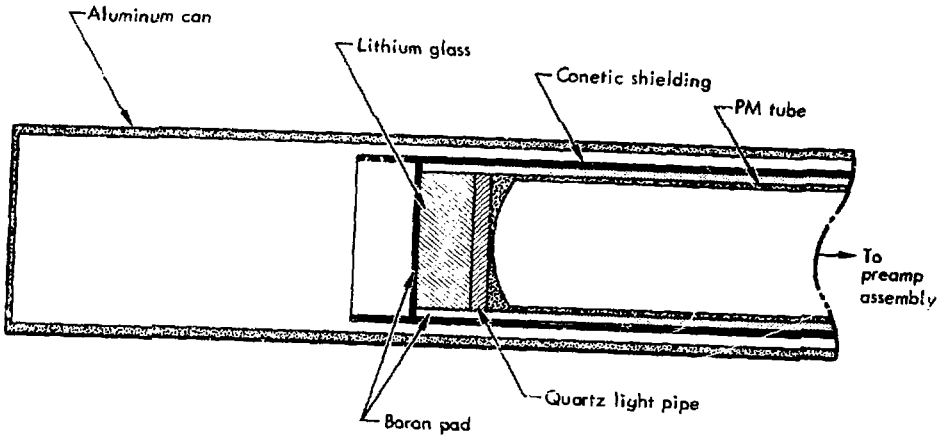
Aluminum can
Lithium glass
Conetic shielding
PM tube
To preamp assembly
Quartz light pipe
Boron pad

Fig. 8

IID.1. High and Medium Energy Electronics

The LLL time-of-flight group electronics ensemble was used. Several modifications were made which improved the time resolution and increased the variety of data recorded during each experimental run. Fig. 9 is a schematic of the electronics system used for high energy data runs.

A fast preamplifier, attached to the annode of the photo-multiplier tube is triggered by a tunnel diode to provide the fast rise time pulse used in the timing circuit. The pulse from the preamp is transmitted to the control room and through a time pickoff control (TPC) box which generates the start pulse. The start pulse starts the ramp in the time to pulse height converter (TAC). A stop pulse is generated for each beam pulse by amplifying the beam current pulse in a fast amplifier and feeding it to a TPC which generates the stop pulse. If uneven sweeping occurs, as it did for the high energy data runs, it is important that the stop pulse generated by the detected pulse be used to eliminate double neutron peaks. This procedure will generate a double prompt gamma peak because the gamma peak falls on the previous ramp. If a start pulse has started the ramp in the TAC, the stop pulse terminates current buildup (the ramp is a capacitor being charged at a constant rate). The TAC then generates a pulse whose height is proportional to the charge on the capacitor. The TAC pulse is amplified, delayed to wait for the slower pulse shape discrimination circuit, and fed to the analog-to-digital converter (ADC). The ADC counts cycles of a 50 mHz oscillator in proportion to the time needed to charge a capacitor to the same level as the pulse height from the TAC. The digital information (channel

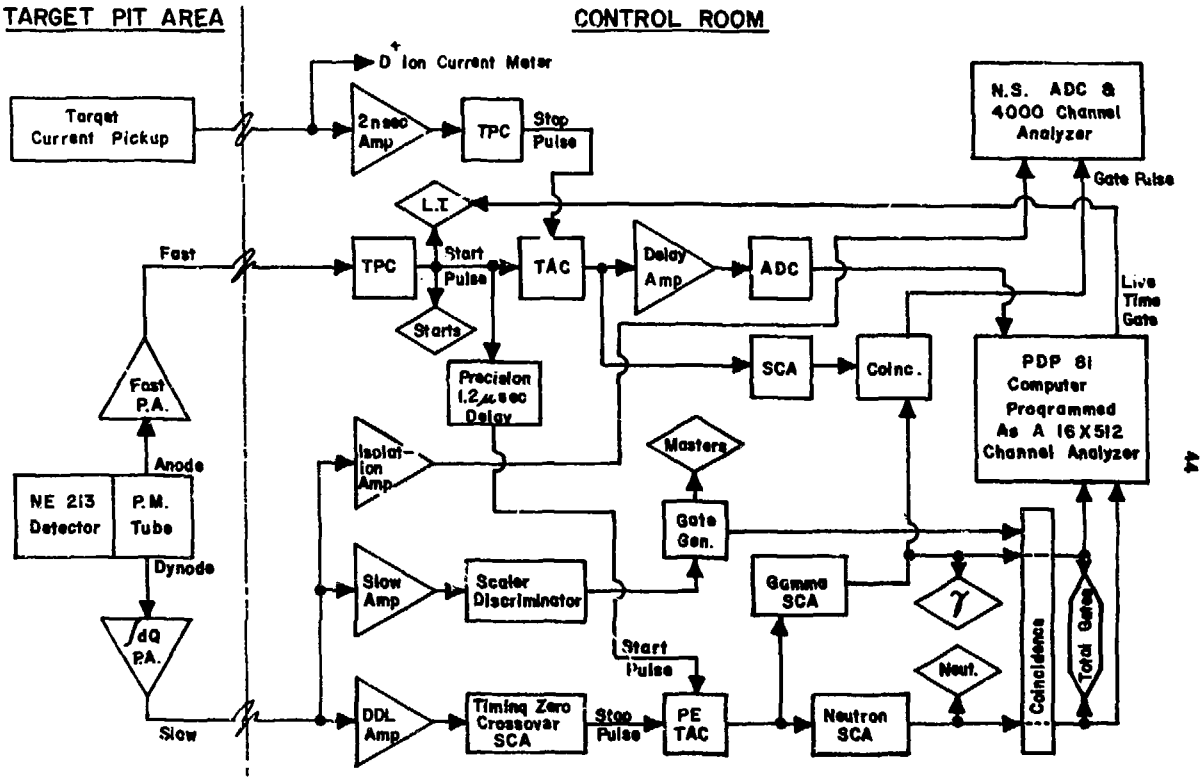

HIGH AND MEDIUM ENERGY ELECTRONICS SCHEMATIC

Fig. 9

number) created in this manner is then sent to the PDP-8i which stores it in the proper channel of the proper group in external memory if a routing pulse is received from the pulse shape discrimination network.

A charge sensitive pre-amplifier (integrator) amplifies the current pulse from the 9th dynode of the photomultiplier tube. This signal is transmitted to the control room and split three ways. One branch goes through a slow amplifier to the master scaler discriminator, which is used to set the detector bias for high energy data runs (see Sect. IIC.1). Detector pulses above the bias then trigger a gate generator which feeds the coincidence box. Pulses from this branch which are in coincidence with pulses from the pulse shape discriminator circuit become routing pulses to the PDP-8i.

A second branch of the signal from the charge sensitive preamp is fed through a double delay line amplifier. Pulses from proton recoil (neutron induced) have a slower decay time constant than pulses from electron recoil (gamma induced). This results in a later zero cross-over of the doubly delayed pulse. The DDL pulse is fed to a timing zero cross over single channel analyzer which creates a stop pulse at zero cross-over for pulses in the single channel analyzer window. This window is left "open" for high energy runs and the scaler discriminator is used to set the detector bias. For medium energy runs, the window is set and the scaler discriminator bias is lowered below the lower level of the timing zero cross over SCA. In this manner gamma suppression was enhanced by decreasing the range of acceptable pulse heights from the detector. The start pulse from the fast timing circuit is delayed

and used to start the ramp in the proton-electron discriminator time to pulse height converter (PETAC). PETAC output is fed to two SCA's; one of which is set on the gamma peak, the other on the neutron peak. A small overlap is accepted to ensure that all neutrons are counted. As a result, a few gammas leak through and are counted as neutrons. Except for a small prompt gamma peak, these gammas form a time independent background of less than one count per channel (~1%).

If pulses from the PETAC which pass the neutron SCA are in coincidence with pulses from the scaler discriminator, a routing pulse is generated by the coincidence box and sent to the PDP-8i computer. This causes a count to be stored in the neutron group of computer external memory and in the channel of that group corresponding to the binary number created by the ADC. A similar procedure takes place for pulses passing the gamma SCA. A sample of this type gamma spectrum is shown in Fig. 10.

The third branch of the slow preamp signal was sent to an isolation amplifier (so as not to perturb the rise time of the P-E signal). The amplified signal was gated by the gamma SCA to a Northern Scientific ADC and 4000 channel analyzer where the gamma pulse height spectrum was recorded. A sample of such a spectrum from iron is shown in Fig. 11. A rough energy calibration can be made by noting the channel locations of the prominent Compton edges from the 846 keV and 1.3 MeV gamma rays in channels 25 and 55. Several scalers are also noted in Fig. 9 as diamonds. The ratio of start scaler count to live time scaler (L.T.) count provides a dead time correction. The sum of gamma scaler counts (γ) and neutron scaler counts should roughly equal the number of total gates

scaler counts. This is a check on gamma SCA and neutron SCA window overlap. The master scaler count is a check of overall system performance and should scale as the associated particle count or as the integral of charge on the target.

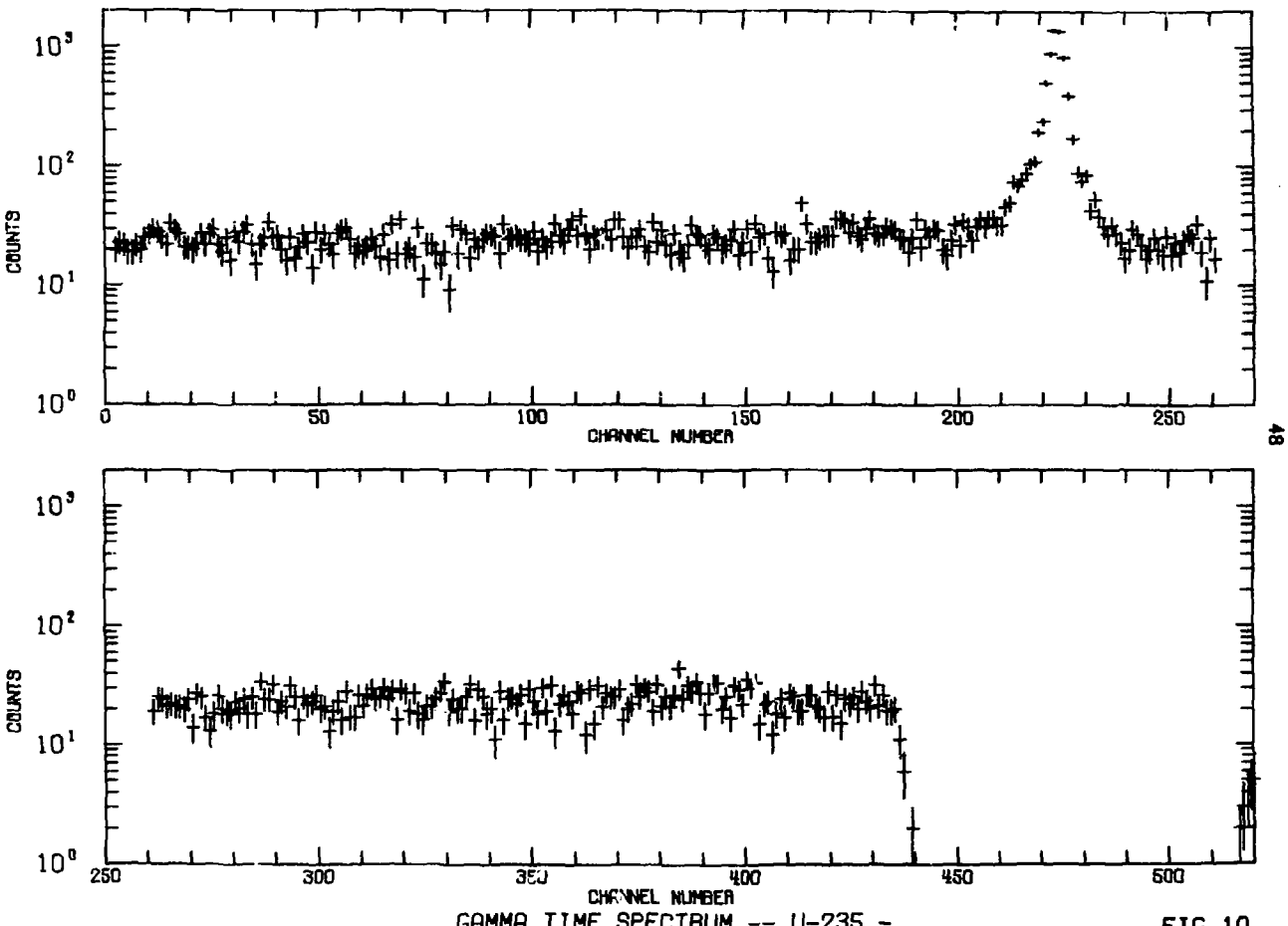

GAMMA TIME SPECTRUM -- U-235 -

FIG.10

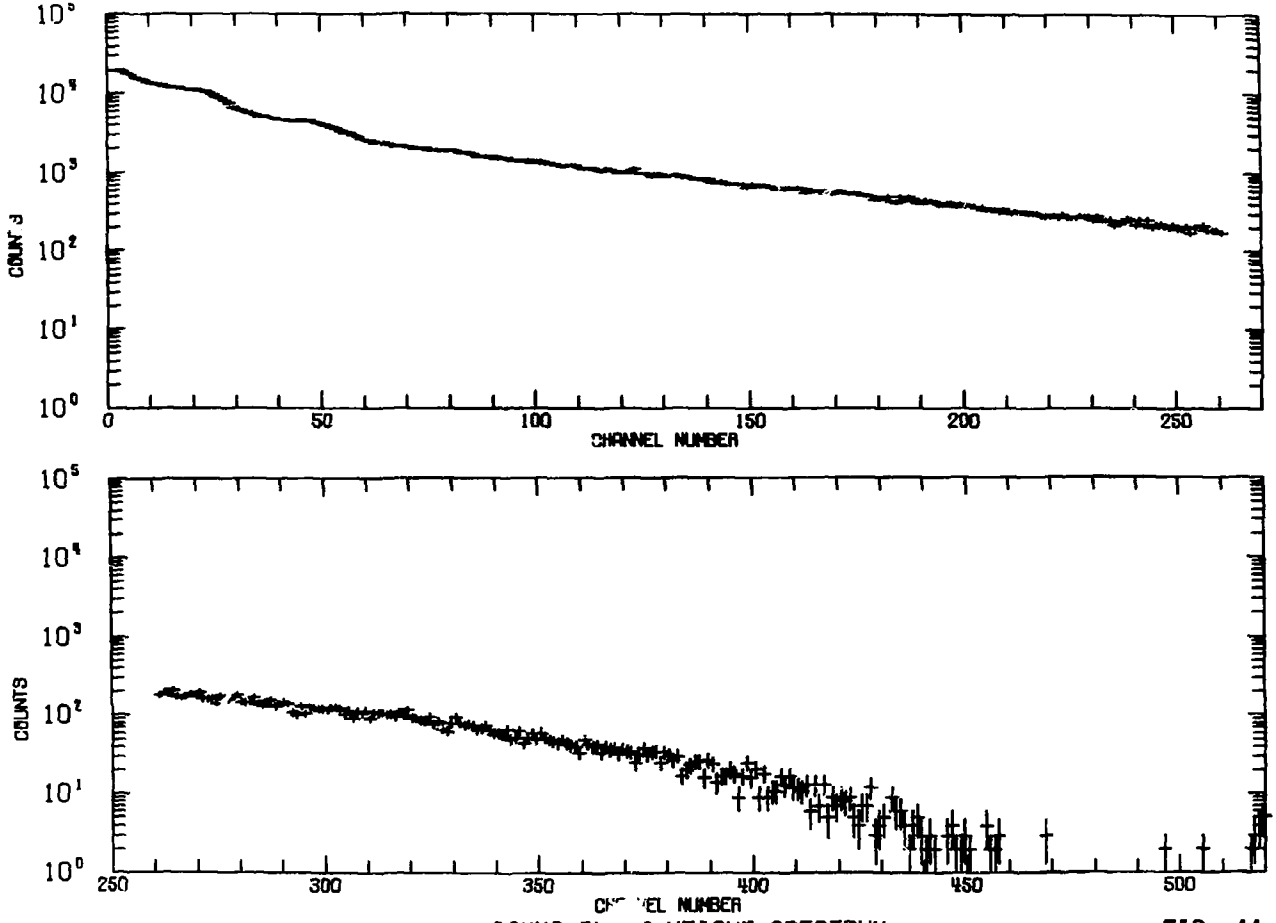

GAMMA PULSE HEIGHT SPECTRUM

FIG. 11

IID.2. Low Energy Electronics

Fig. 12 is a schematic of the low energy electronics. Since resolution is not a problem in this energy region, only the slow signals from the ^{6}Li-glass and ^{7}Li-glass detectors are used. Stop pulses are generated by a capacitive beam pickoff unit located in the beam pipe about one meter from the target. The slow signals are fed through DDL amplifiers to zero cross-over timing single channel analyzers. It is this SCA window which is set on the neutron peak (see Sect. IIC.2.) These SCA's generate start pulses which are fed to the TAC. Due to the long ramp times necessary to cover this energy range, an anti-coincidence "busy signal" box is set to prevent a change in routing pulse while the TAC is charging the ramp. The TAC sets the busy signal. TAC output is then amplified and sent to the ADC and PDP-8i multichannel analyzer.

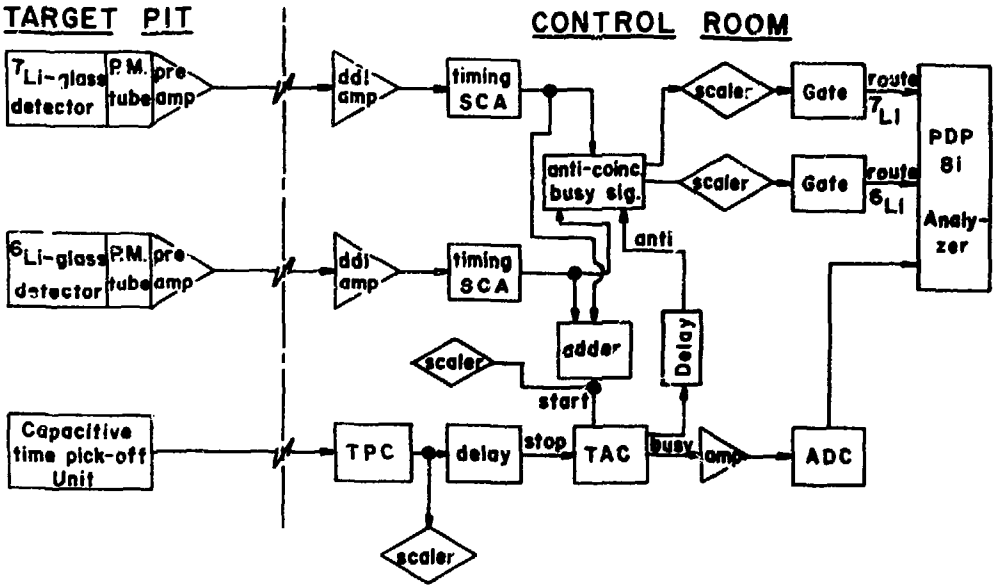

LOW ENERGY ELECTRONICS SCHEMATIC

Fig. 12

II.D.3. Associated Particle Detector Electronics

A relative neutron source strength determination is made by counting neutrons from the bare source (no shadow bar collimator or ring). An alpha counter mounted at 174° to the D^+ beam line counts the associated alpha particles in a fixed ratio to the number of neutrons produced. Neutrons detected in this manner are at the source energy. Therefore only errors in the relative shape of the detector efficiency curve introduce errors in the high energy data. The same is almost true for the medium energy data but in theory absolute errors in the detector efficiency affect low energy data. In fact, even the low energy data have correct relative normalization since the ^{6}Li-glass detector was calibrated against a fission chamber detector which was normalized to the high energy detector. Relative source normalization is accomplished for runs of all energies by observing the source with a NE 213 detector at high bias.

Pulses from a solid state lithium drifted silicon detector are amplified, delayed, and input to an ADC. An SCA sets a window on the alpha peak (deuterons are also observed). Pulses in the window cause the SCA to generate a gate to the ADC. These gates are scaled as alpha counts. Gated ADC information is stored in a multi-channel analyzer to insure that no drift or other anomaly has occurred, resulting in a non-valid alpha count which could lead to improper source normalization. The master scaler (see Fig. 9) serves as a rough validity check on the alpha count. A schematic of the associated particle counter electronics appears in Fig 13.

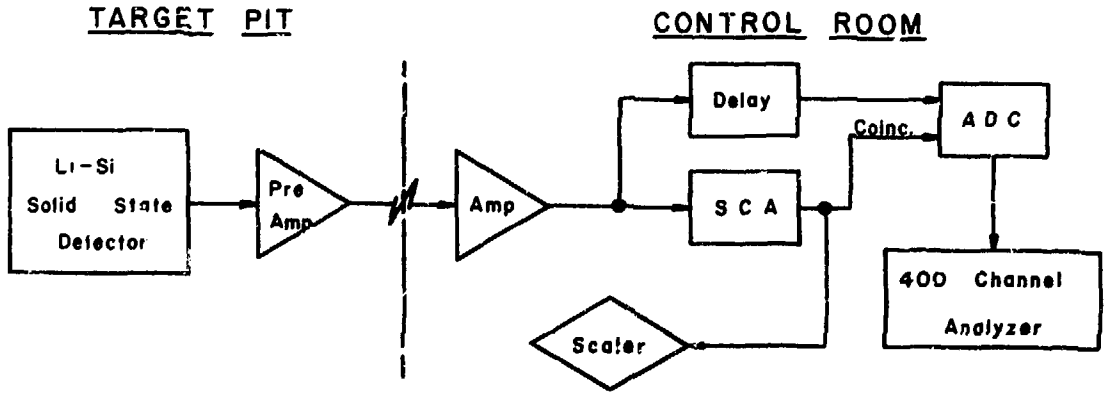

ASSOCIATED PARTICLE COUNTER

Fig. 13

II.E. Data Accumulation

Data were accumulated for each target in three steps, each corresponding to the energy region of interest. These three steps are described in the following paragraphs as high, medium, and low energy data accumulation techniques. Raw data were plotted using a computer code named RAW enabling rapid and detailed validity checks. Experiments could be repeated before the experimental parameters were changed.

II.E.1. High Energy Data Accumulation Technique

Both gamma suppressed and neutron suppressed time-of-arrival spectra were recorded. Fig. 14 is the RAW output plot of a typical neutron time of arrival spectrum. The spectrum is from the lead ring positioned at 95°. The air peak is in channel 455; the elastic peak is in channel 437; and the effect of the 2.6 MeV 3^- level is seen in channel 388. RAW code breaks the 512 channels into quarters to expand detail. Fig. 15 is the fourth quarter of Fig. 14, for example.

The neutron suppressed gamma time-of-arrival spectrum is recorded concurrently. The gamma spectrum is used to time scale and time initialize the neutron spectrum. Fig. 16 is the raw output of the gamma time-of-arrival spectrum corresponding to Fig. 14. The twin gamma peaks in channels 267 and 273 are a result of unequal sweeping and the fact that the gamma start pulse is stopped by the current pick up from the previous deuteron pulse (see Sec. II.D.1.) Neutrons in the air peak (channel 455) of high energy runs have flight times equivalent to the direct flight of 14.7 MeV neutrons, or 155 nanoseconds. Prompt gammas arrive in 30 nanoseconds. Since the gamma peak is from the next pulse,

RAW CODE OUTPUT

LEAD - 95 DEG.

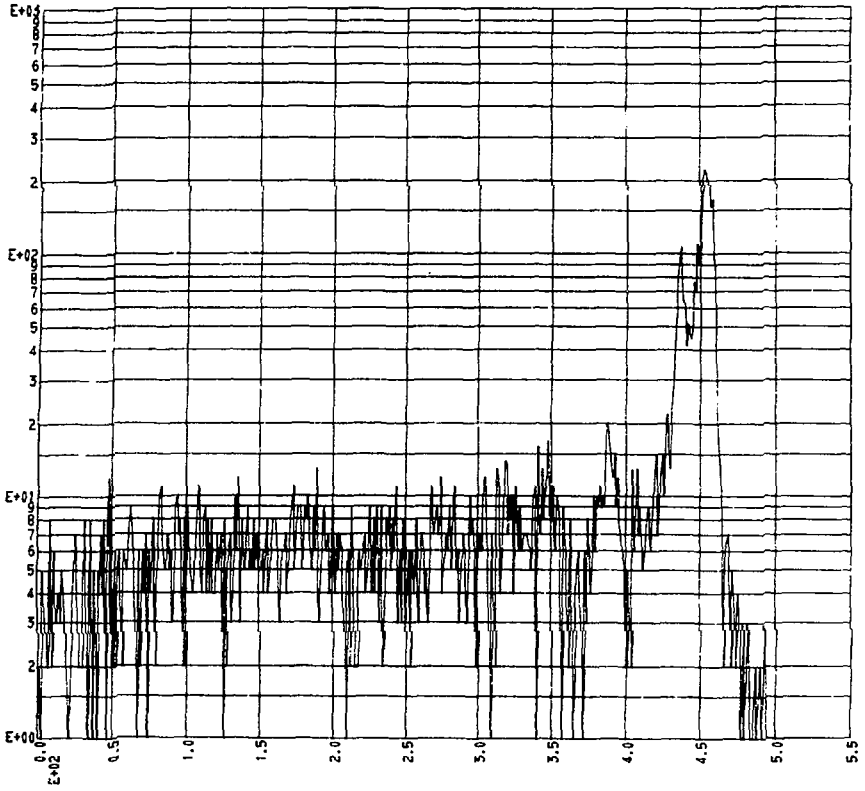

TIME-OF-FLIGHT SPECTRUM

FIG. 14

RAW CODE OUTPUT

LEAD - 95 DEG.

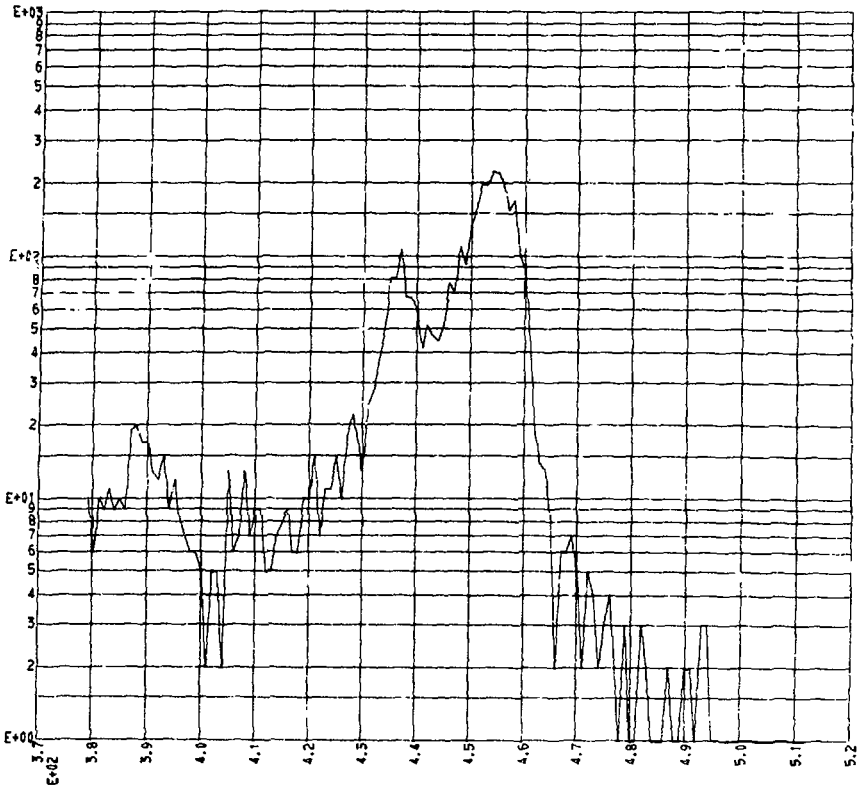

TOF SPECTRUM(EXPANDED SCALE)

FIG. 15

RAW CODE OUTPUT

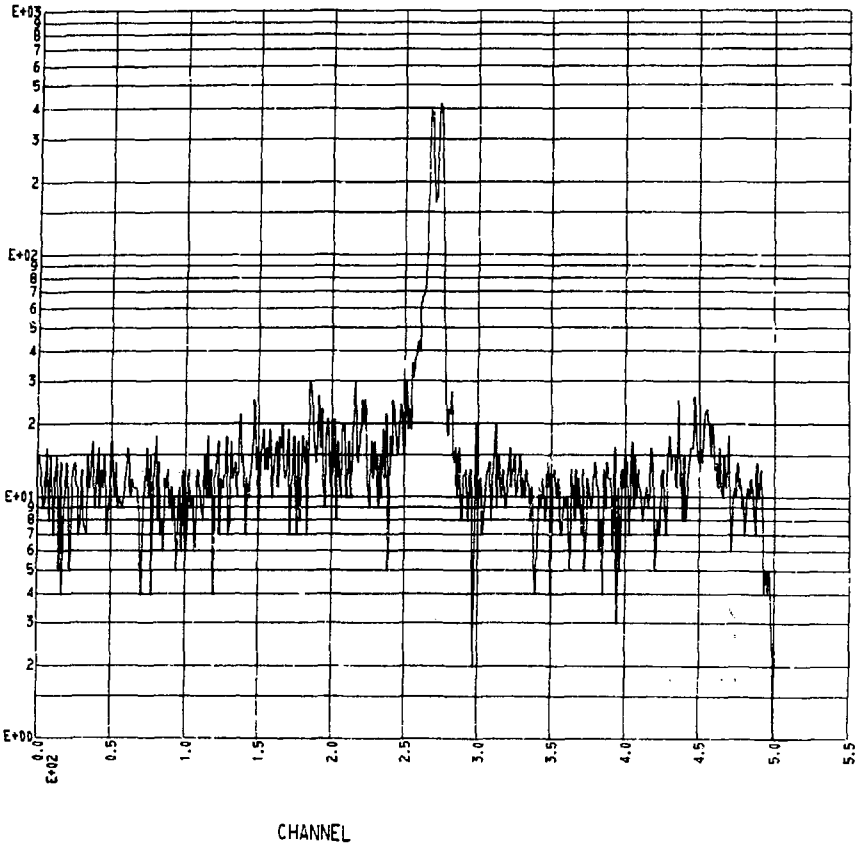

GAMMA TIME-OF-ARRIVAL SPECTRUM (PB-95 DEG.)

FIG. 16

its arrival time is 230 nanoseconds. The "true" gamma peak location is channel 270. A quick time scaling in Fig. 14, assuming linear and flat electronics, (not assumed in actual data reduction) is 0.4 nanoseconds per channel. Since the gamma peak is less than four channels FWHM, the time resolution is about 1.5 nanoseconds.

Periodic blank spectra are recorded by remotely removing the ring target. The blank spectrum is later subtracted from the data spectrum. Fig. 17 is a RAW plot of a typical blank spectrum. It is dominated by the air peak in channel 455. Fig. 18 is the gamma time-of-arrival spectrum corresponding to Fig. 17. The weak peaks in channels 160, 180, and 220 can be ascribed to (n,γ) reactions from massive parts of the beam line and its support structure. The peak in channel 450 is due to (n,γ) reactions in the detector and collimator. Periodic source strength calibration runs are made by recording the direct flux of neutrons versus the number of alpha counts with the shadow shield (see Fig. 2) removed. Fig. 19 is a RAW plot of such a spectrum. Fig. 20 is the concomitant neutron suppressed gamma time-of-arrival spectrum. The gamma peak in channel 455 is caused by neutrons producing gamma rays in the detector and its assembly by non-elastically scattering from carbon and aluminum.

The linearity and slope of the system time response are periodically checked by generating start pulses with a gamma source and detector located outside the target pit. The stop pulses continue to be generated by the deuteron current pickup. A linear system should generate a horizontal line. Fig. 21 is the response typically observed. This "random" spectrum is later used in computerized data reduction as an accurate means of time scaling (see Sect. III.A.2).

RAW CODE OUTPUT

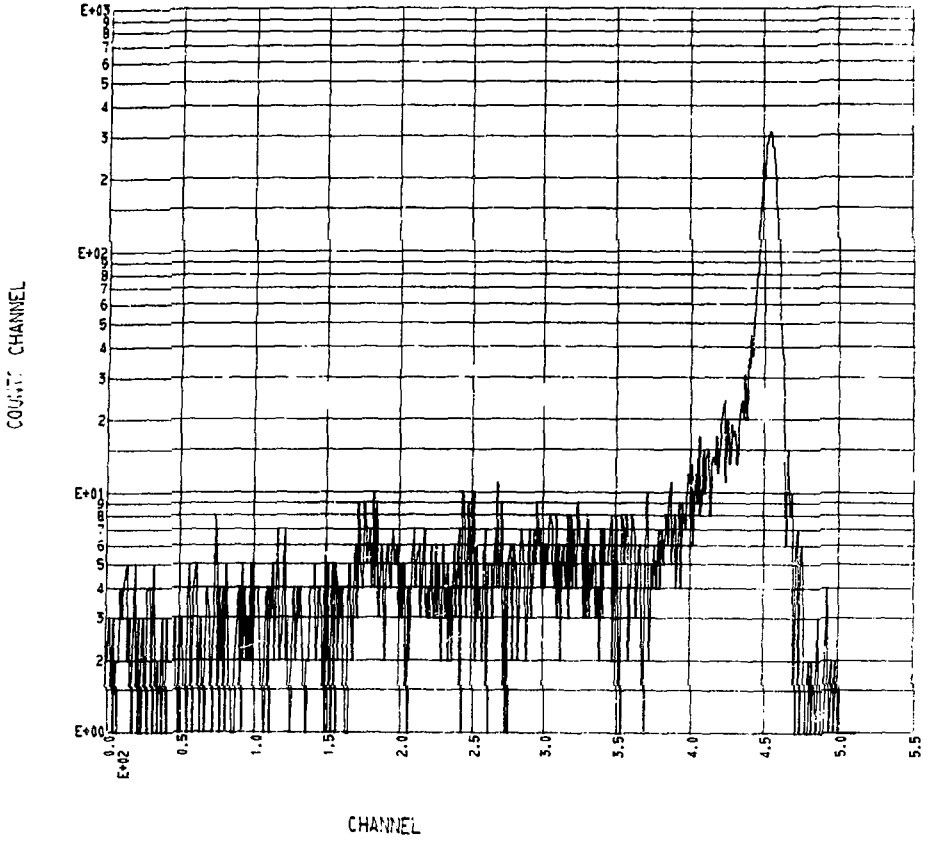

BLANK SPECTRUM

FIG. 17

RAW CODE OUTPUT

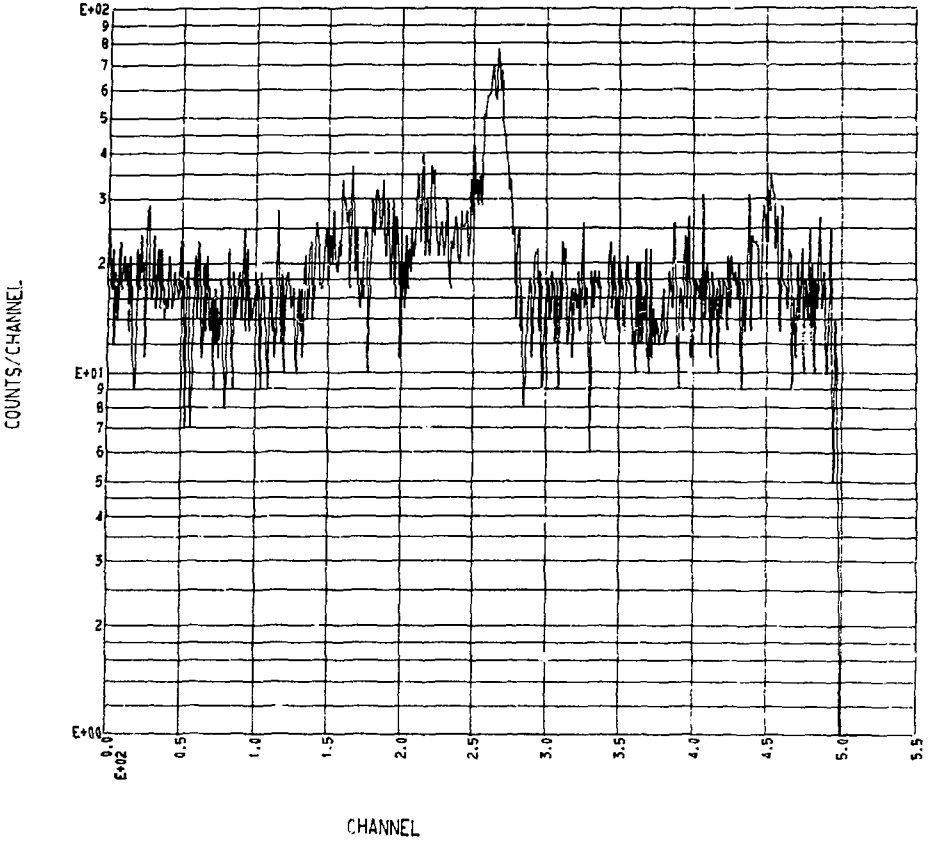

GAMMA TIME-OF-ARRIVAL SPECTRUM (BLANK)

FIG. 18

SOURCE NEUTRON CALIBRATION SPECTRUM

(SHADOW SHIELD REMOVED)

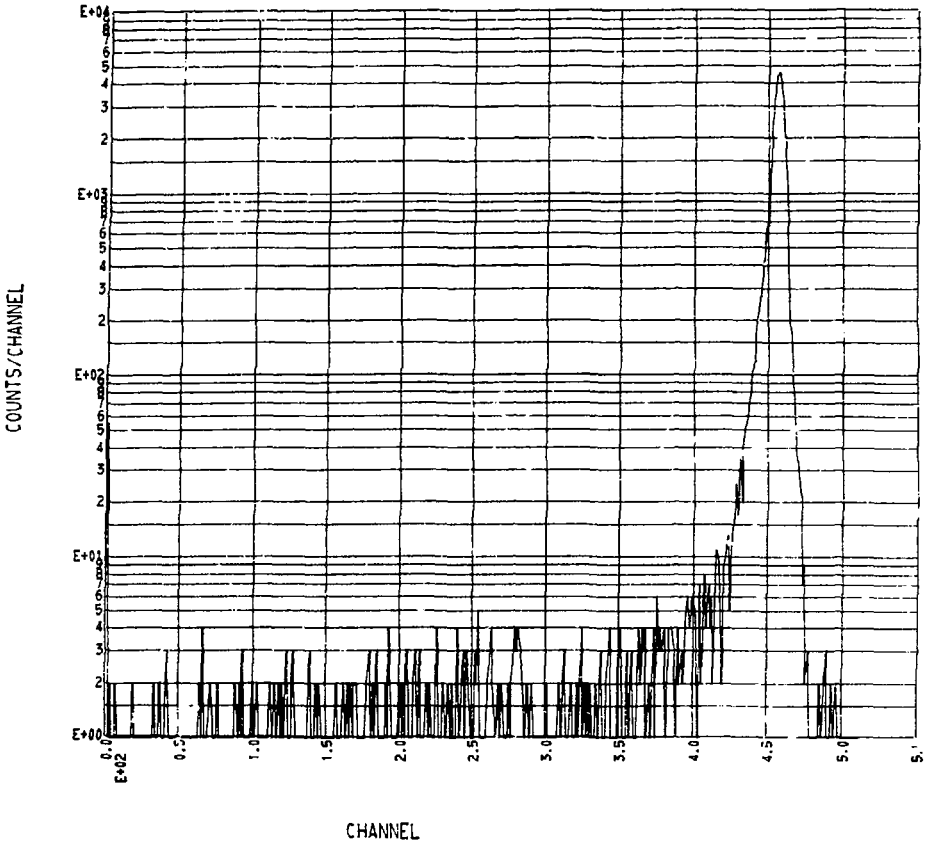

RAW CODE OUTPUT

FIG. 19

GAMMA TIME-OF-ARRIVAL SPECTRUM

(SHADOW SHIELD REMOVED)

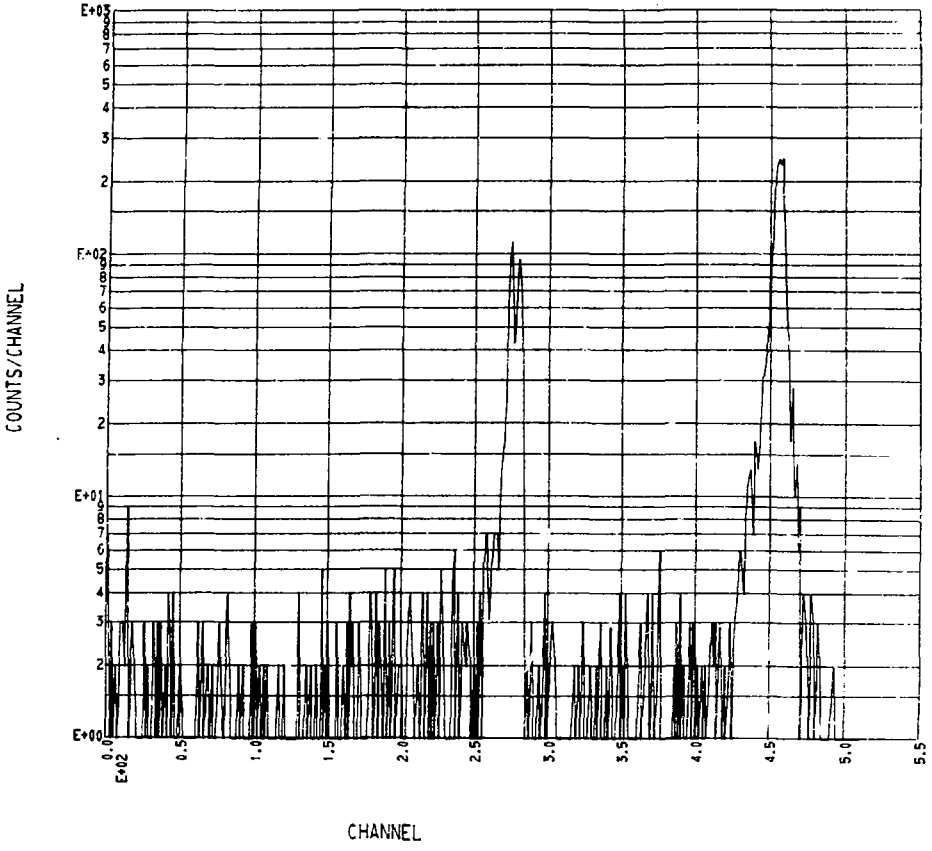

RAW CODE OUTPUT

FIG. 20

RANDOM SPECTRUM

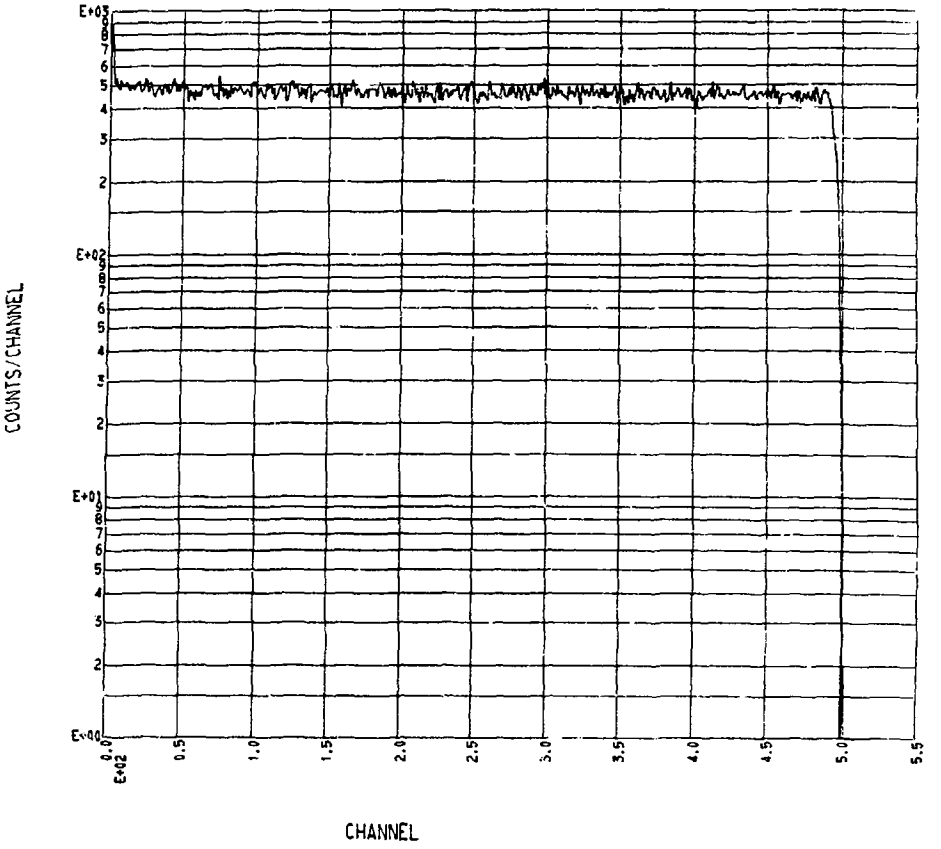

RAW CODE OUTPUT

FIG. 21

II.E.2. Medium Energy Data Accumulation

Data in the energy range between source energy and 600 keV are accumulated in similar fashion to the high energy data. Fig. 22 is a plot of medium energy data. The neutron pulse rate is reduced to 833.3 kHz so that the bias cutoff at 600 keV (766 nanoseconds) can be observed. Since only one pulse is produced each 1200 nanoseconds, the bias is high enough to prevent the observation of overlap neutrons. Time resolution is 3 nanoseconds. Since only the data below 5 MeV are used, energy resolution is better than 2.2 percent.

Approximately 4% of the gammas are permitted to leak through the gamma suppression electronics to insure that all the neutrons are counted. The peak in channel 394 of Fig. 22 is the prompt gamma peak; the air peak is in channel 323. A rough time scaling of the spectrum in Fig. 22 is 1.75 nanoseconds per channel. The elastic peak of scattered neutrons is in channel 312, neutrons scattered from the 4.43 MeV level of carbon appear in channel 289, and neutrons from the 9.6 MeV level are near channel 211. Neutrons scattered from the continuum are clearly in evidence between channels 50 and 240. Spectra similar to that in Fig. 22 were taken for each ring positioned at 45, 95, and 135 degrees.

Gamma time-of-arrival spectra, blank spectra, and random spectra were also taken. Source calibration for these spectra was accomplished with the detector biased at the Compton edge of the 511 keV line of ^{22}Na (1.6 MeV).

The medium energy data overlap the energy range of high energy data (above 3.5 MeV) and low energy data (below 2 MeV). This overlap

permits the used of the most accurate data available, considering systematic errors which may be present (see Sect. III.C). The technique also serves as a rough consistency check on the *normalization* of all three data taking modes.

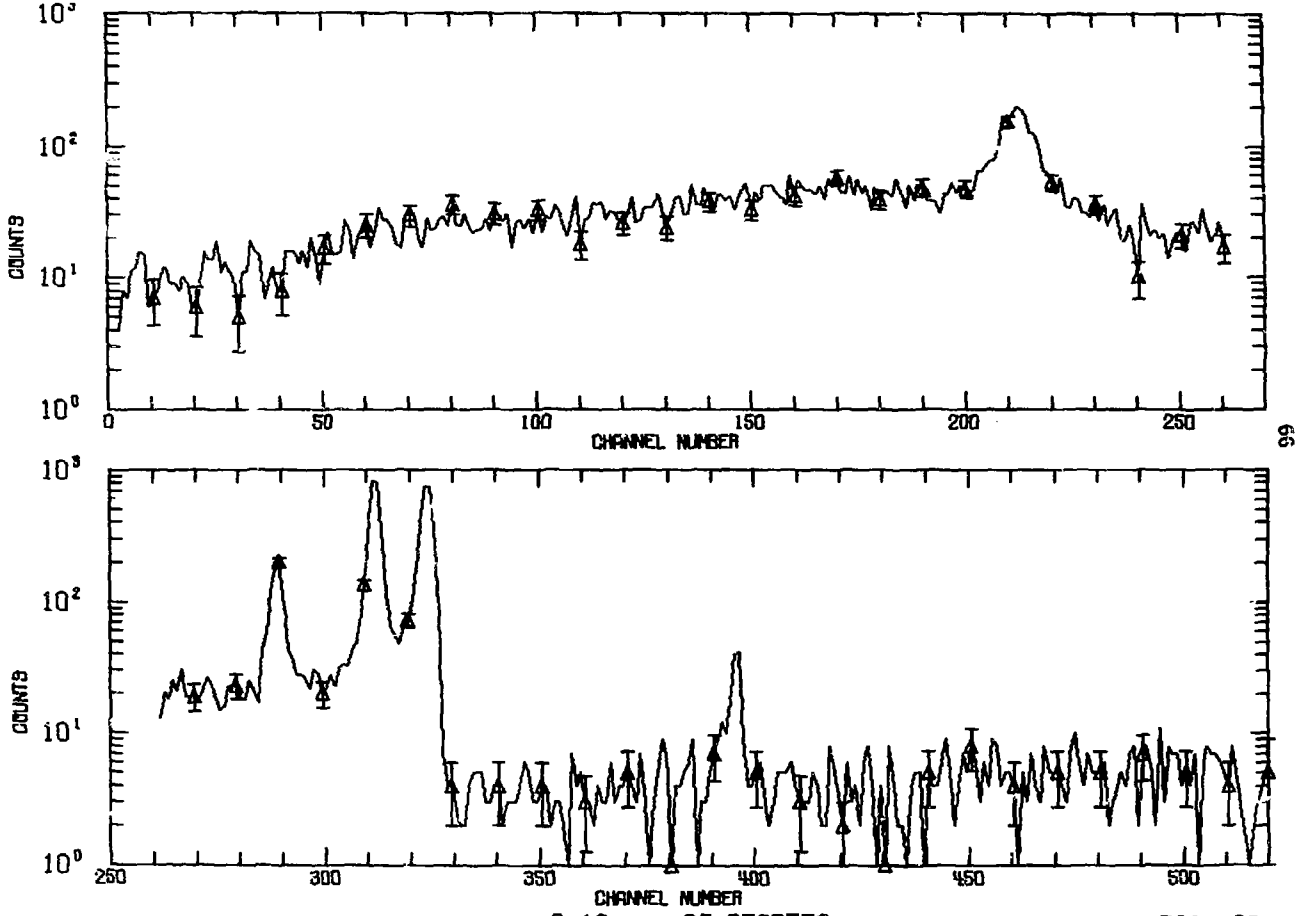

66

-- C-12 -- 95 DEGREES --

FIG. 22

II.E.3. Low Energy Data Accumulation

The low energy data taking technique differed greatly from that of high and medium energy. The accelerator was operated in such a manner as to produce 10 kHz pulses of neutrons (see Sec. II.A.). Only 95° scattering was observed. Both 100 and 500 nanosecond pulses were used, corresponding to 16.6% and 83.1% energy resolution at 250 keV.

A typical low energy spectrum is shown in Fig. 23. The prompt gamma peak and elastic neutron peak appear near channel 340. The broad peak starting near channel 310 is the effect of the Li-glass detector resonance (see Fig. 7).

Pulse shape discrimination of gammas is not possible with the detector used, so that a considerable gamma background is present in the spectrum. A blank run is a close check on the magnitude and shape of the background. The blank run spectrum is subtracted from the foreground spectrum.

Since the prompt gamma peak and the elastic neutron peak are so closely spaced, a precision time delay unit is used to displace the spectrum known units of time, allowing time calibration of the data.

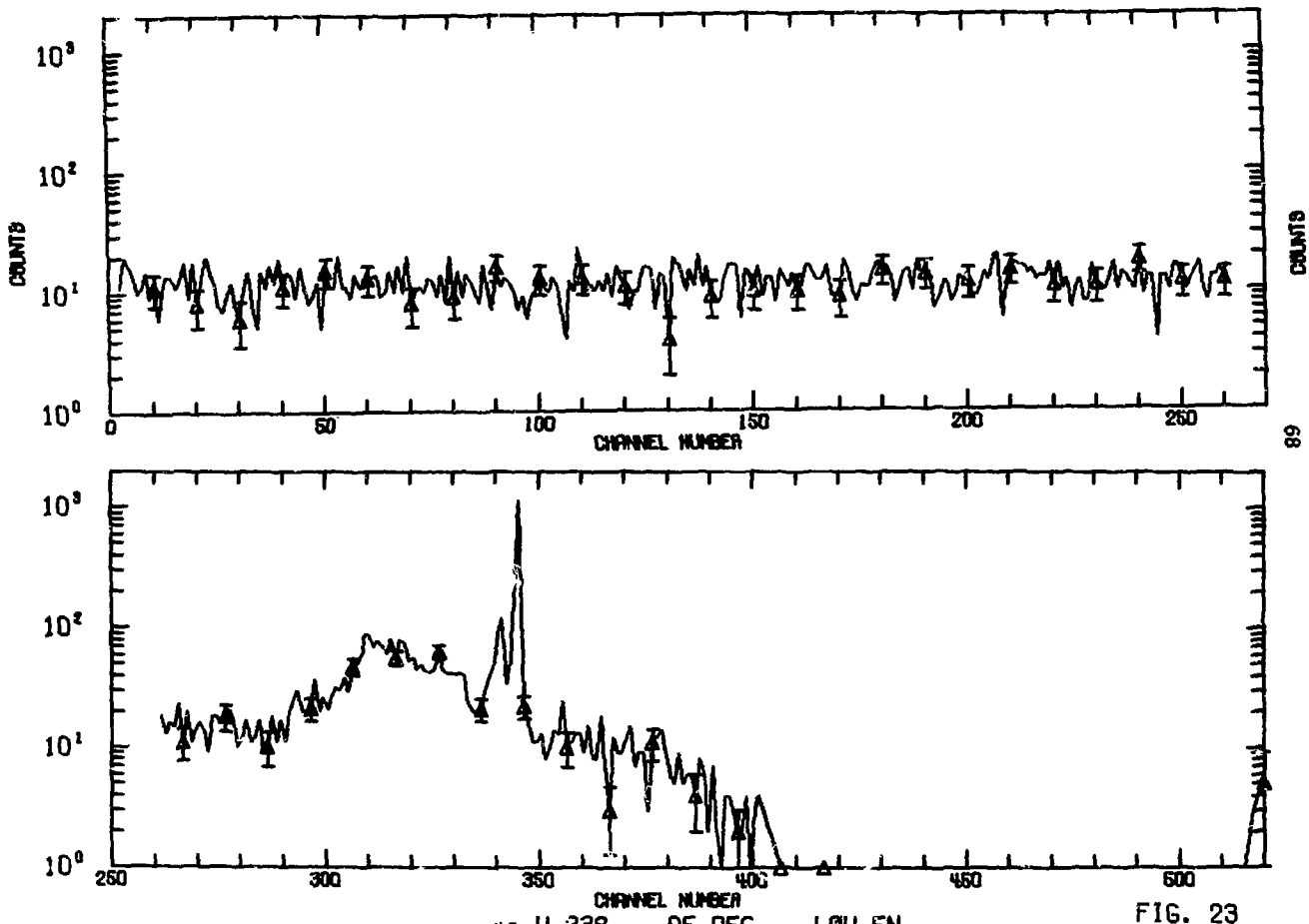

** U-238 -- 95 DEG -- LOW EN

FIG. 23

II.E.4. Typical Raw Data

Additional plots of raw data are presented as Figs. 24 thru 29 as examples of data quality as the scattering angle and scattering material are changed. The two peaks near channels 290 and 300 in Fig. 24 are leak thru gammas. Gamma suppression was almost perfect in the spectra presented as Figs. 25 thru 29. Each of the spectra is dominated by the air peak on the high channel side of the spectrum. At forward angles, the elastic peak merges with the air peak. Various detail characteristics of the isotope are observed at lower channel numbers (lower energy, later times).

The solid line in Figures 24 and 29 is generated by connecting a data point for each channel. Representative error bars are plotted each ten channels. Individual data points are plotted in Figures 25 thru 28. The horizontal tic mark represents the magnitude, and the length of the vertical line represents the error (standard deviation).

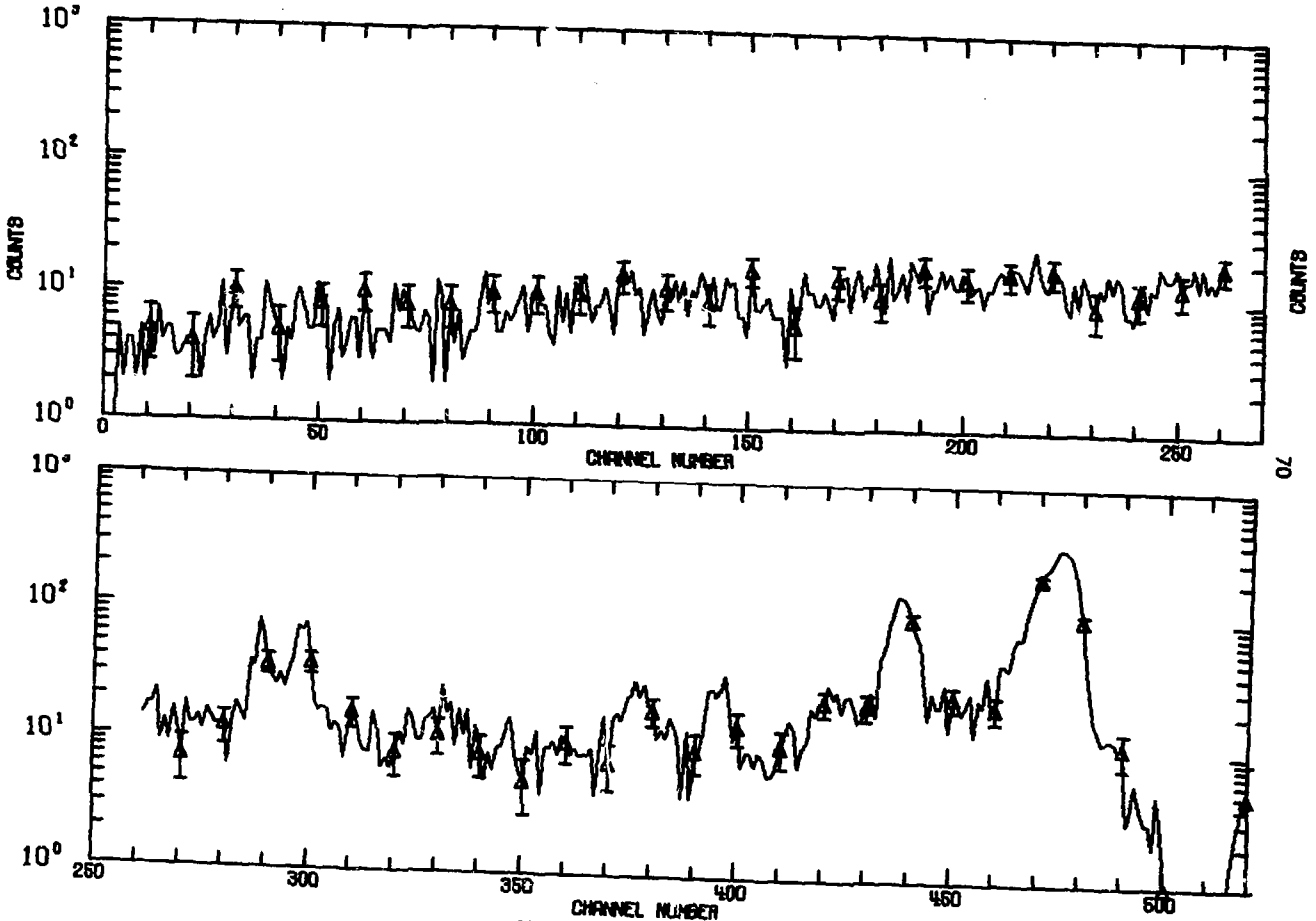

** ALUMINUM -- 100 DEG **

FIG. 24

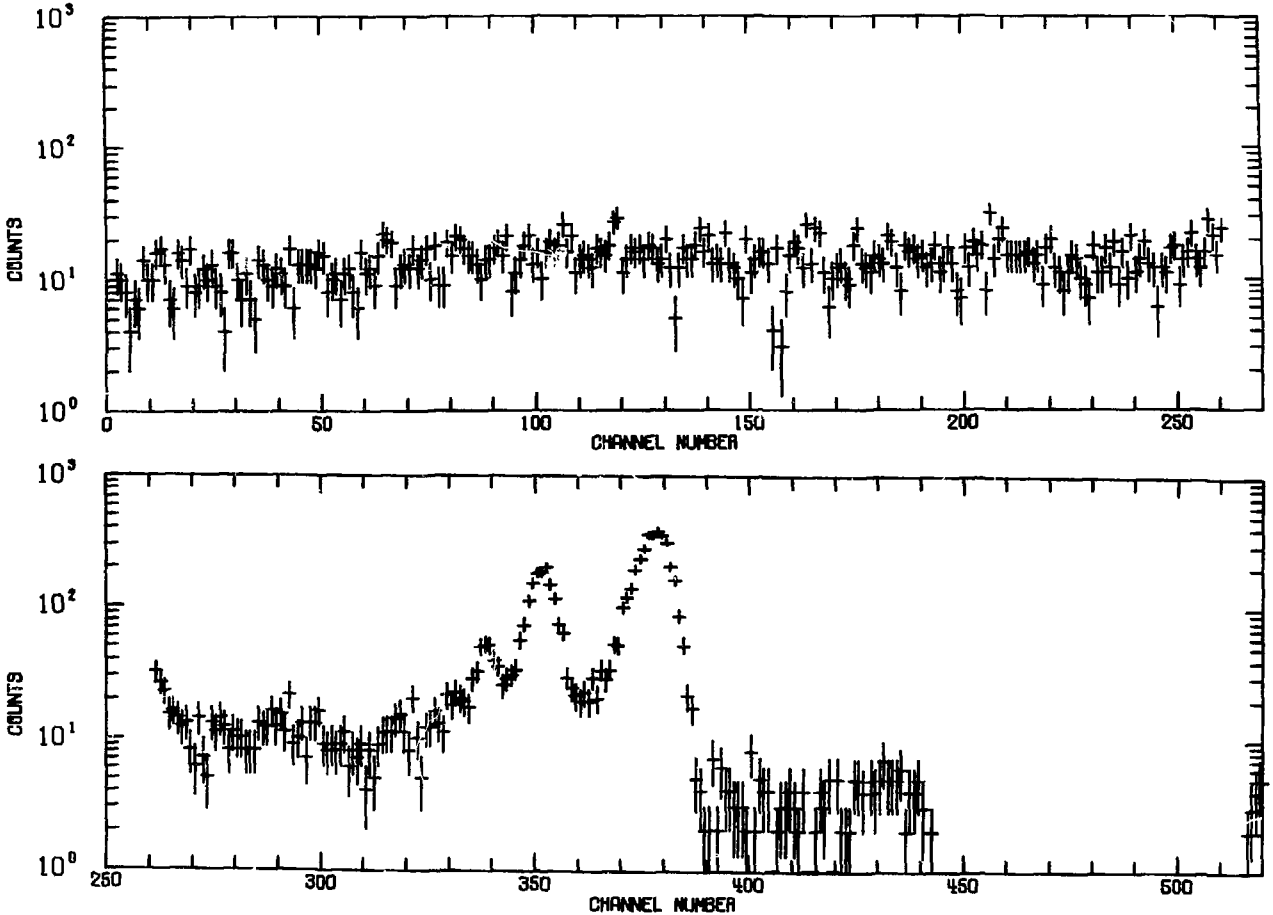

71

** IRON -- 100 DEG **

FIG. 25

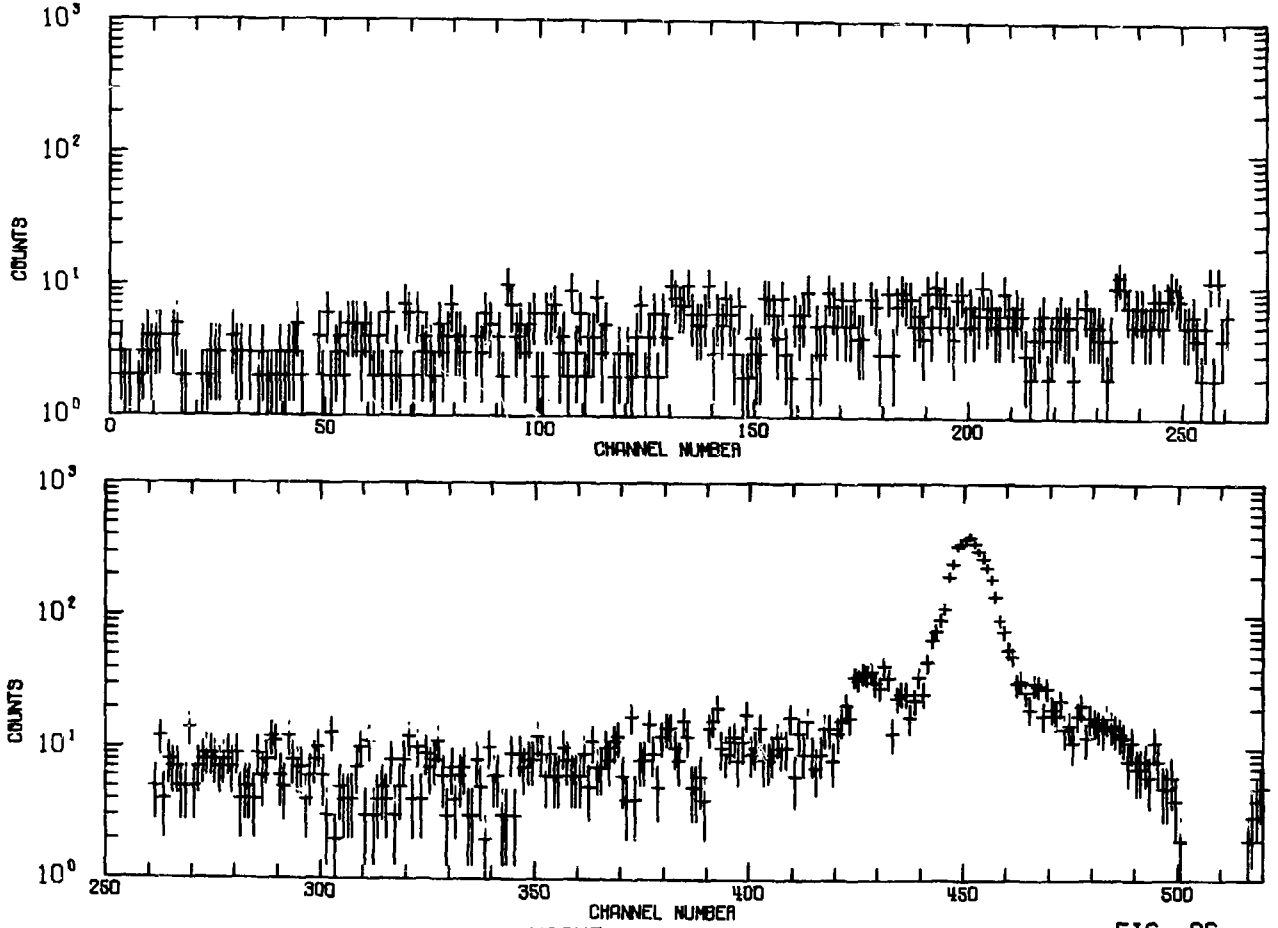

72

•• NICKEL -- 35 DEGREES ••

FIG. 26

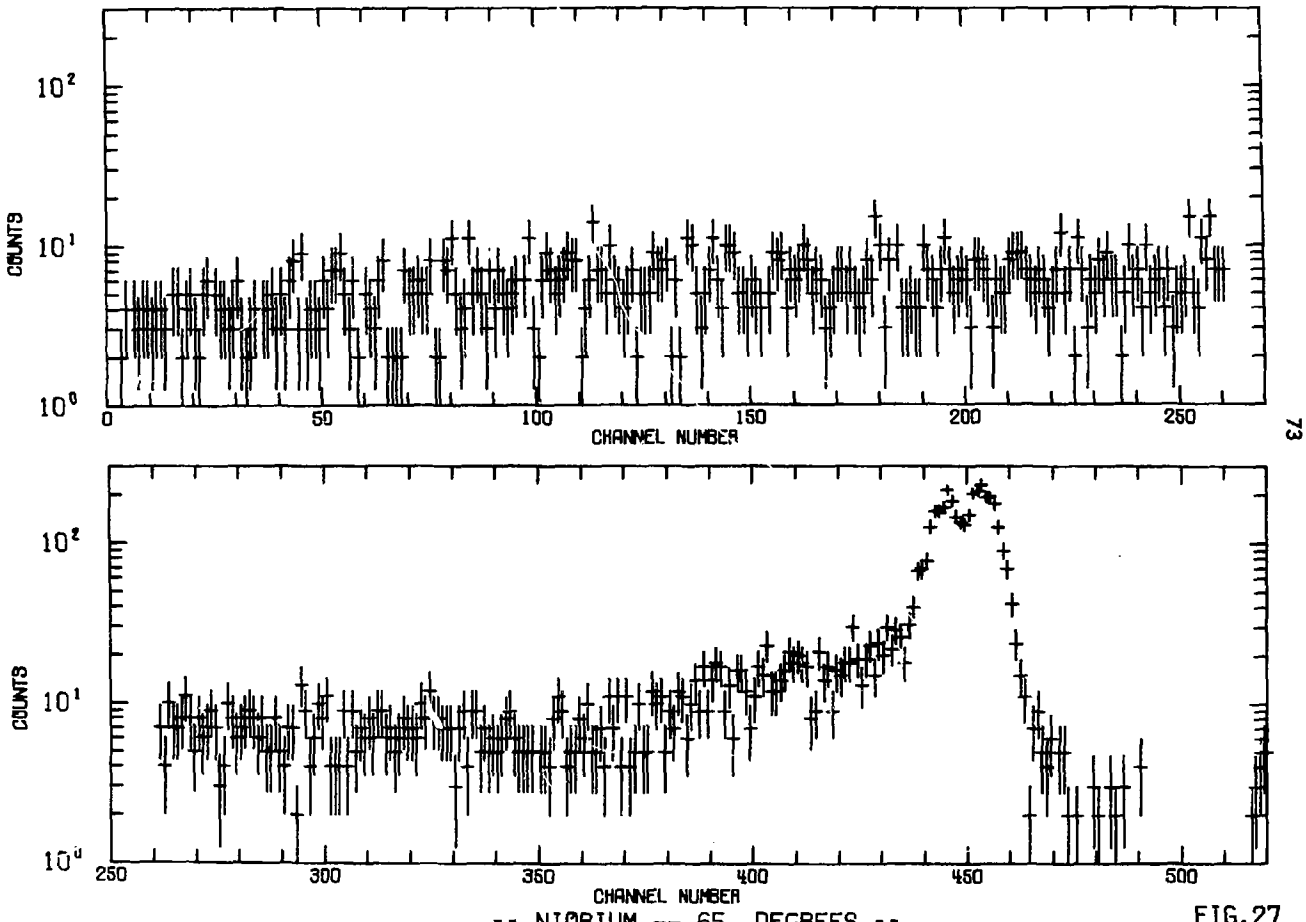

73

•• NIOBIUM -- 65 DEGREES ••

FIG.27

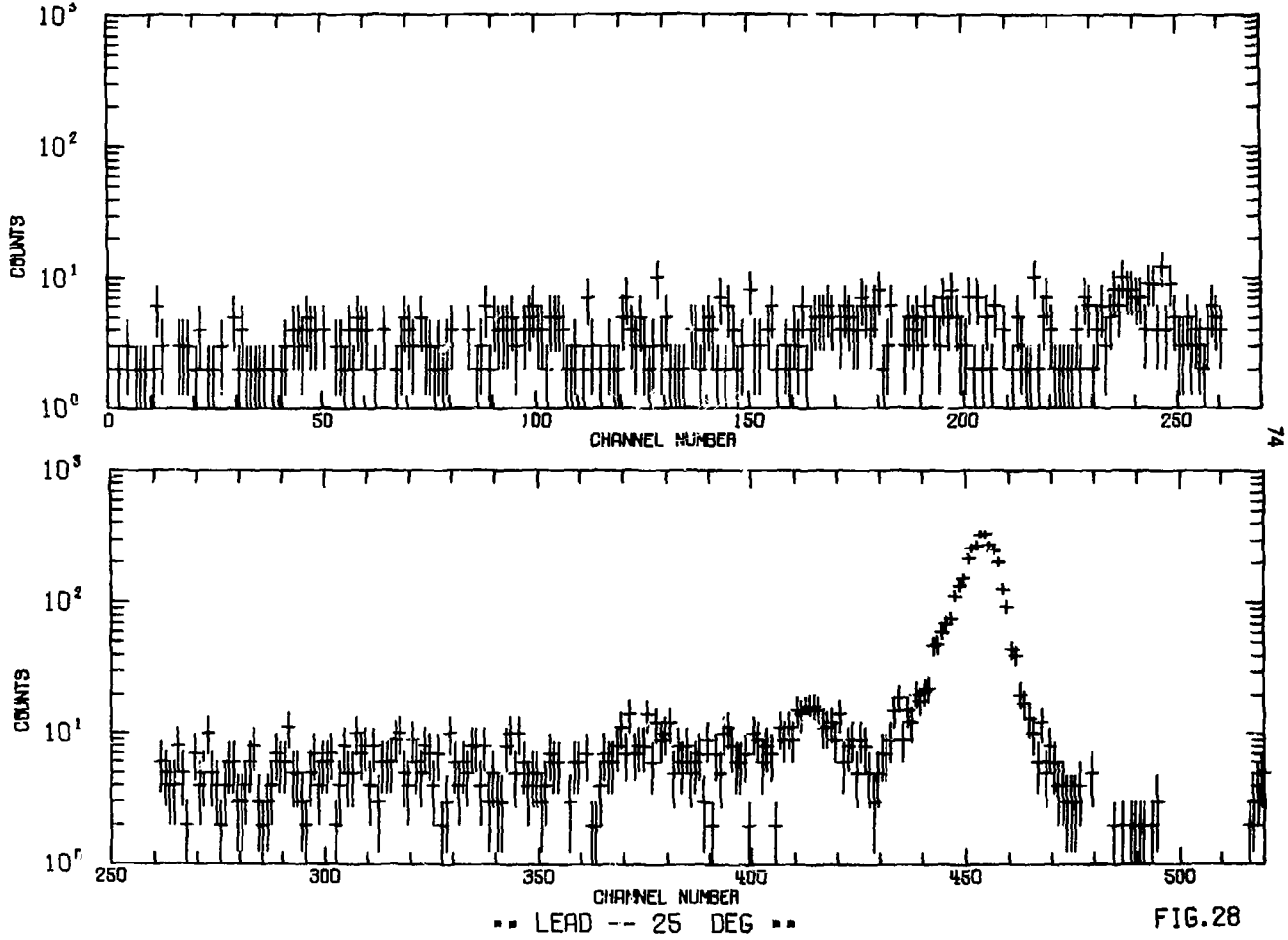

FIG.28

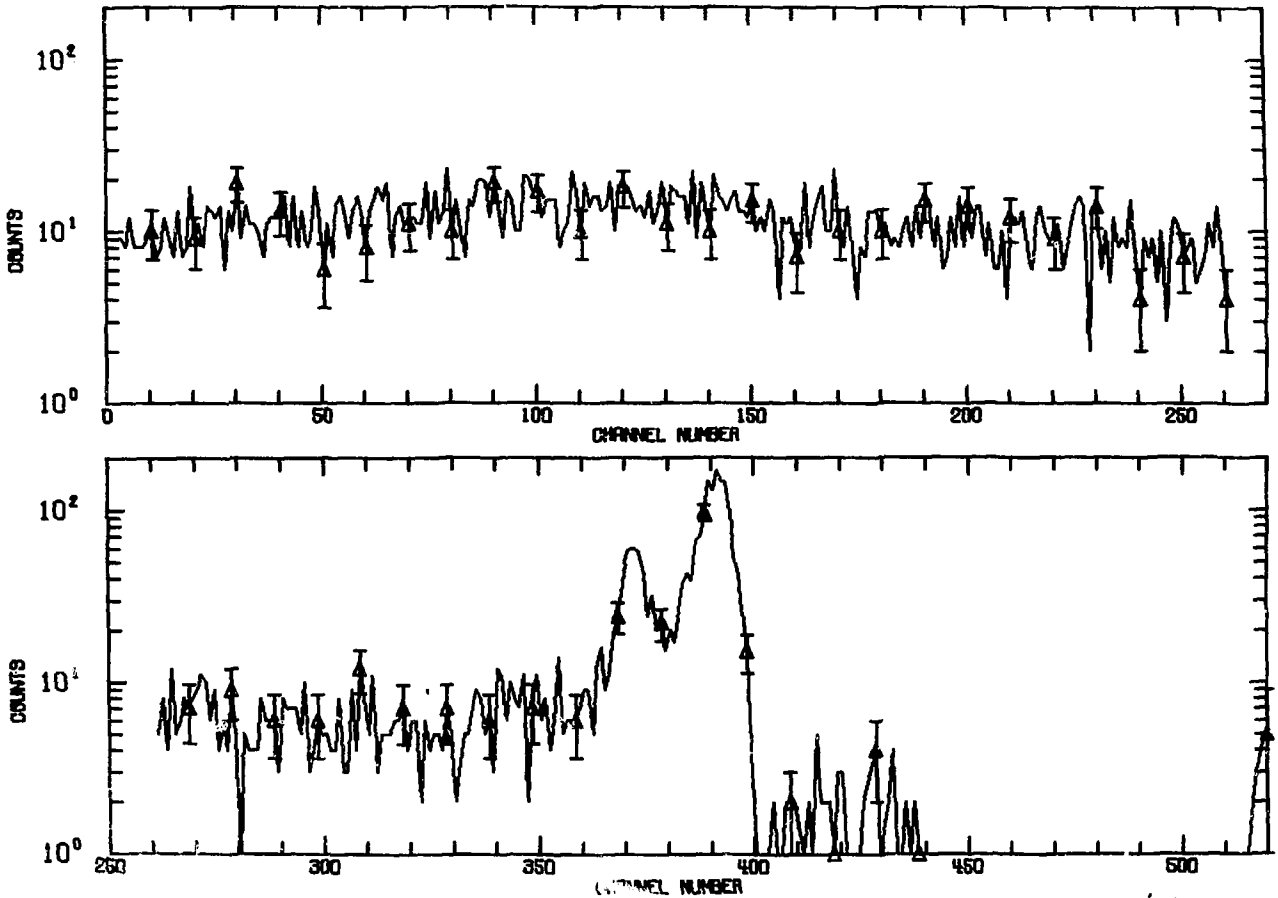

75

** U-235 -- [illegible] DEG **

FIG. 29

III. Data Reduction

The entire data reduction process is computerized. Three purposes are served. Time consumed in handling volumes of data is not linear. The utility of a proven experimental technique is thereby expanded, facilitating an increase in the amount of data taken and analyzed. Coding the data reduction process on a computer also serves as a clear, concise, and complete record of what was done to the data. This record serves any future re-examination of the dat , even if done by others in the absence of the original experimenter. The third purpose served is that data are reduced without any conscious or subconscious bias by the experimenter.

Extensive use was made of computer generated graphic displays. This technique made possible a complete picture of results at each step of the data process. Systematic trends and isolated errors were quickly spotted and corrected. Ideas were quickly coded, displayed and discarded or kept, depending on their actual value and validity.

In this manner the computer becomes a familiar tool, easily shaped and molded to fit the needs of the experimenter. Since the coded data reduction process deserves a lengthy treatise in its own right, only the functions of the process are described here. The codes make full use of the LRLTRAN language and are not easily converted to use on computers outside LLL.

Four codes were written by the author to facilitate preparation of this thesis. FAW code is used in preliminary data reduction. RING code extracts cross sections from the data. CCRING code corrects the data for multiple scattering based on input from a Monte Carlo code and prepares the final data plots on an off-line plotter. CC3D code plots the data in three dimensional representation.

IIIA.1. Preliminary Data Reduction

The data accumulated in memory of the multi-channel analyzer was output to magnetic tape via the PDP-8i computer. Backup data was output via a Franklin printer to printed fanfold paper tape. The magnetic tape was read into a CDC 6600 computer which transferred the data to cards used as input to further data analysis and reduction. The utility code RAW was used for this step. RAW also plotted the data. The plots were generated on 35 mm film using a cathode ray tube and printed via a Xerox process. See Fig. 14 for a sample of RAW output. A hard copy data listing including a running sum was also generated by RAW.

IIIA.2. Data Reduction Using RING Code

The RAW output facilitated generation of input to the one step data reduction code RING, written especially for ring geometry time-of-flight data reduction. The RING code is quite general in many aspects, and the powerful features of the code have been put to use in reducing other types of data.

RING code processes the data, each set (each angle) to completion, in serial fashion, thereby using only a small part of the CDC 6600 core memory, facilitating RING code use in a time sharing environment such as that at LLL. A data set consists of the neutron time-of-flight spectrum, a suitable blank spectrum, and a random spectrum (see Figs. 14, 17, and 21). If the blank spectrum has features in common with the data spectrum, such as the air peak which appears in all ring geometry data and blank data, RING code shifts the blank spectrum relative to the data in such a manner as to find the null point of the common feature. This is done by inputting the channel limits of the common feature, and summing the squares of the difference, channel by channel between those limits for each of three background shifts. The three by three matrix is solved for the null point. If no minimum is found or if the calculated null point is outside prescribed limits, a search is started to find three sets of values which have the prescribed minimum. When the set is found, successively finer shifts are made about the apparent null point to zero in on the correct background shift for the data run being analyzed. The shift is used when subtracting the properly normalized background from the data. In this manner, experimentally determined time dependent backgrounds are properly subtracted without undue labor by the

experimenter, in unbiased computer fashion. Fig. 30 shows a detailed view of the region (between the x's) used to find the null in the background shift. Fig. 31 is the entire raw data spectrum after the time dependent background was subtracted. Note the value of X1, the background shift.

Further data reduction involves transforming data from counts per channel to counts, neutrons, or cross section per unit time, energy, or other basis. In every case, the basis step is calculated as a time step which is derived from the data by incrementing through the random spectra. (See Sect. IIE.4. for an explanation of the random spectrum.) The random spectra provide a means of removing any non-linearities from the data, since they are generated in such a way as to contain the same non-linearities. Two points of known time or energy are chosen in the data spectrum or its concomitant gamma spectrum. For the high and medium energy data these points are the prompt gamma peak channel and the air peak channel. The RAW output provides an easy means for making these selections. For the low energy data the prompt gamma peak is used and a second point determined by observing spectral shifts obtained by increasing the precision delay of the stop pulse by known amounts. RING calculates the time between these points and sums the random spectrum over the same region. This provides a random increment per time increment. The relationship between a known starting time and its channel location is established by calculating the time difference between the starting time and the gamma peak location. The calculated number of random increments corresponding to the number of time increments are summed

RING CODE OUTPUT

TYPICAL TIME DEPENDENT BACKGROUND SUBSTRACTION

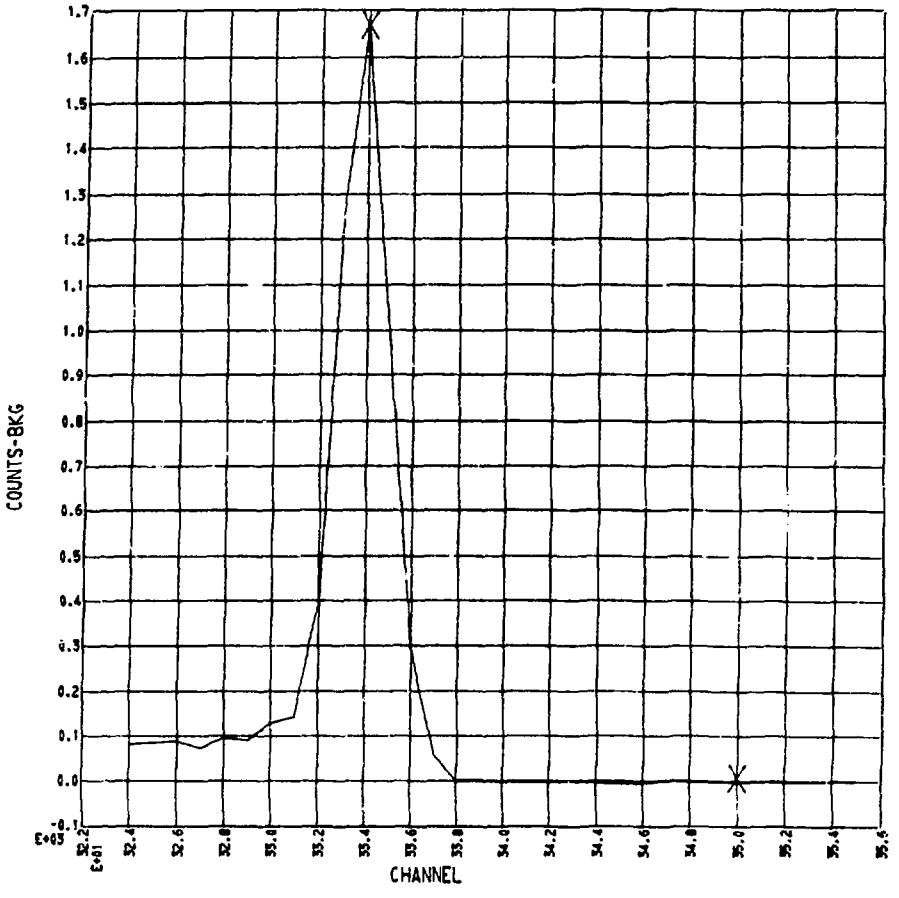

** U-238 -- 45 DEGREES -- 40804 ** X1= -0.23

Fig. 30

RING CODE OUTPUT

TYPICAL FOREGROUND MINUS BACKGROUND

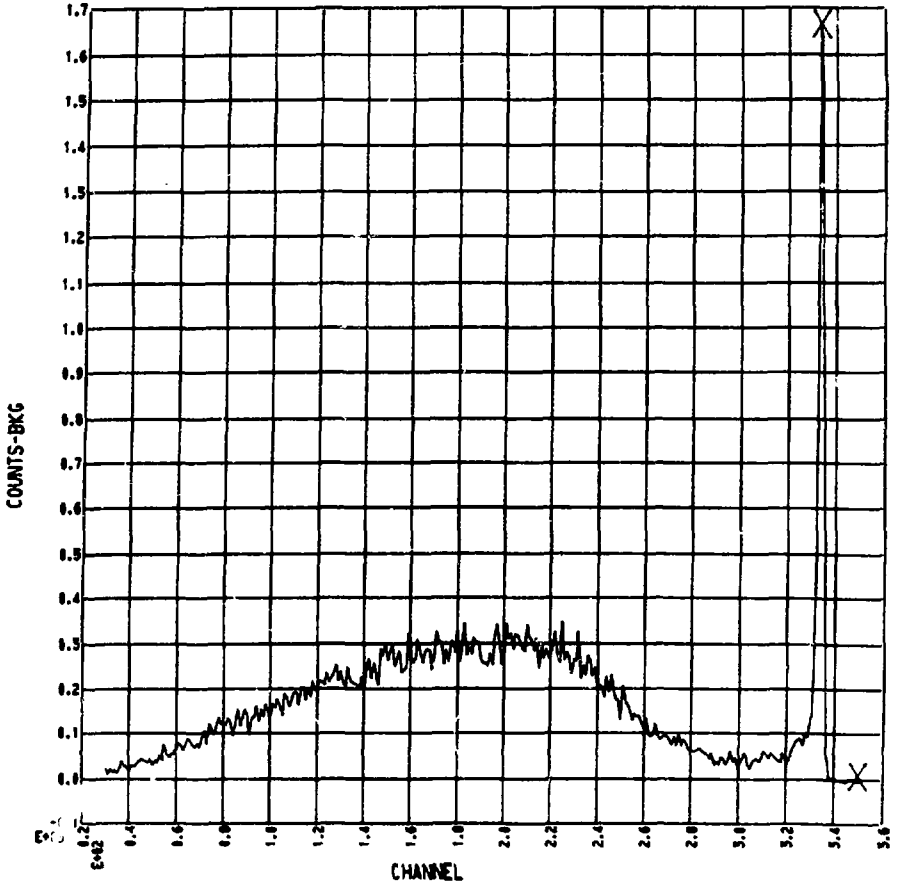

** U-238 -- 45 DEGREES -- 40804 ** X1= -0.23

Fig. 31

in the random spectra until the channel location is found. Further incrementation is done from this point forward in time. Counts are summed in each increment and an error computed. The code determines the degree to which errors in the interval are correlated and correctly sums errors either in quadrature or in ratio. Each channel was assigned an error when the subtraction of the background was made. The formulation of this error calculation provides a hint of the flexibility built into the ring code.

$$ERR_i = (C_i \times CNORM + (Y+BBACK) \times BNORM + (2 \times CBACK \times CNORM)^2)^{\frac{1}{2}}$$

where C_i is the number of counts in raw data channel i and Y is the number of counts in the corresponding combination of channel fractions in the shifted background. Both the data and the background can be normalized to offset the different source neutron fluxes and dead time corrections. Each of the spectra can have a time independent component subtracted in the first stage of data reduction (BBACK and CBACK). When these factors are considered, the errors computed are based only on counting statistics. The first spectrum reduced is the time spectrum, as shown in Fig. 32. The curve is generated by connecting points generated two nanosecond steps. The diamonds plotted correspond to boundaries, between which the cross section is later summed. Many options on inputting these boundaries exist. The ones shown correspond to one MeV steps in residual nucleus excitation except for the one at 450 nanoseconds, which represents a 0.5 MeV step from the previous point of 12.5 MeV excitation plotted near 390 nanoseconds. At this point the data are corrected for detector efficiency, flux asymmetry, and solid angle. Since the $T(d,n)^4He$ reaction is isotropic in the center of mass below 400 keV incident deuteron energy,[7] the average reaction energy was determined by examination of the data and this value used to calculate

RING CODE OUTPUT

TYPICAL TIME-OF-FLIGHT SPECTRUM

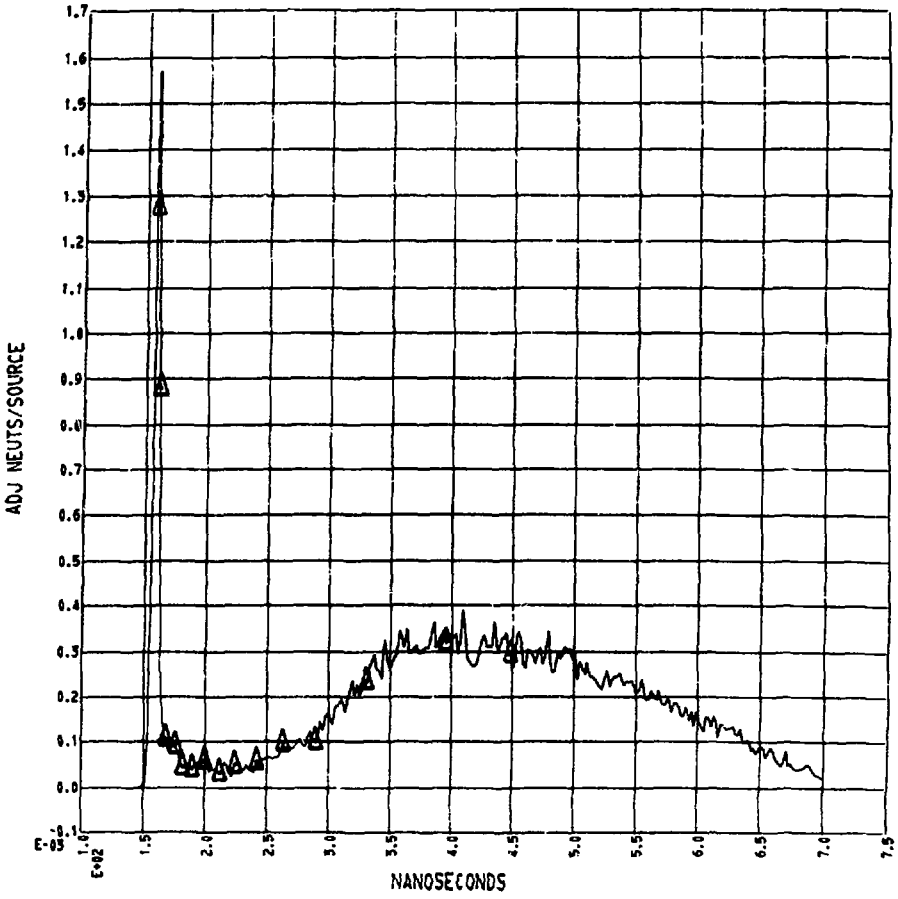

** U-238 -- 45 DEGREES -- 40804 **

Fig. 32

the flux asymmetry. The solid angle correction makes the appropriate changes in data magnitude to account for the fact source-ring and ring-detector distances vary with angle. Each data set was normalized to a ninety degree ring position, using the factor

$$\Omega = \frac{R_g^2 R_n^2}{R_r^2(R_r^2 + R_o^2)}$$

where R_n is the source-ring distance, R_g is the ring-detector distance, R_r is the ring radius and R_o is the source-detector distance. The time-of-arrival of each energy was calculated from the source-ring flight time plus the ring-detector flight time. The source energy also varied with angle as did the flux. Using an observed average reaction energy of 140 keV for 190 keV incident deuteron energy, the following kinematic relations were used to determine the source energy and flux at each angle.

$$E(\psi) = (E_1+Q)\, B[\cos(\psi) + (D/B - \sin^2\psi)^{1/2}]^2$$

$$F(\psi) = E(\psi)/(E_1+Q)/(AC)^{1/2}\,(D/B - \sin^2\psi)^{1/2}$$

where $E(\psi)$ and $F(\psi)$ are the neutron energy and flux ratio $Q = 17.58$, the Q value of the neutron source reaction, E_1 is the incident deuteron energy, and

$$A = \frac{8}{25}\, E_1/(E_1+Q)$$

$$B = \frac{A}{4}$$

$$C = \frac{3}{25}\left(1 + \frac{2}{3}\frac{Q}{E_1}\right)$$

$$D = 4C$$

Figure 33 is a plot generated by RING code displaying low energy data versus scattering energy. The solid curve is generated by connecting points in 10 keV steps. The diamonds indicate the input energy steps for which the cross section was calculated. Fig. 34 is a similar spectrum displaying medium energy data versus scattering energy. The curve is generated by connecting points each 100 keV, the diamonds were a code input based on residual nucleus excitation energy. The cross section was summed between diamonds. Fig. 35 is a composite plot, generated by RING code, in which synthesis of low, medium, and high energy data is accomplished. The data below one MeV are that from Fig. 33; the data between 1 and 5 MeV are that from Fig. 34; and the data above 5 MeV are from a high energy data run. A figure such as Fig. 35 was generated for each angle and each material for which high, medium, and low energy data were taken. The curve is generated by connecting points each 100 keV.

The data in Fig. 36 are medium energy data plotted versus Q value, where Q-value is the negative of the apparent residual nuclear excitation. Such a definition loses meaning for observed fission neutrons, but the plot remains a valuable tool for quick theoretical analysis. The data in Fig. 36 are the same as that in Fig. 34. Fig. 37 is the same data on a semi-log plot after division by the center of mass energy of the outgoing neutron. Such a plot is an aid in interpreting compound phenomena,[18,19] since it represents the level density of the residual nucleus. RING code also calculates cross sections and plots the angular distribution versus angle or cosine in both lab and center-of-mass for quick comparison with existing data. The angular distributions in Figs. 38 and 40 are two

examples of RING generated cross section data. The data in Fig. 38 are the cross sections observed between calculated Q-values of plus and minus 0.5 MeV. This is essentially the observed elastic scattering. Fig. 39 is a table of the cross sections plotted in Fig. 38 and similar plots vs angle in both lab and CM. Fig. 40 is a plot of the cross section observed at a higher residual nuclear excitation. The angular errors quoted represent the total angle subtended by the target and take into account the finite size of the neutron source and the detector. They are therefore the upper limits of reasonable angular error.

RING CODE OUTPUT

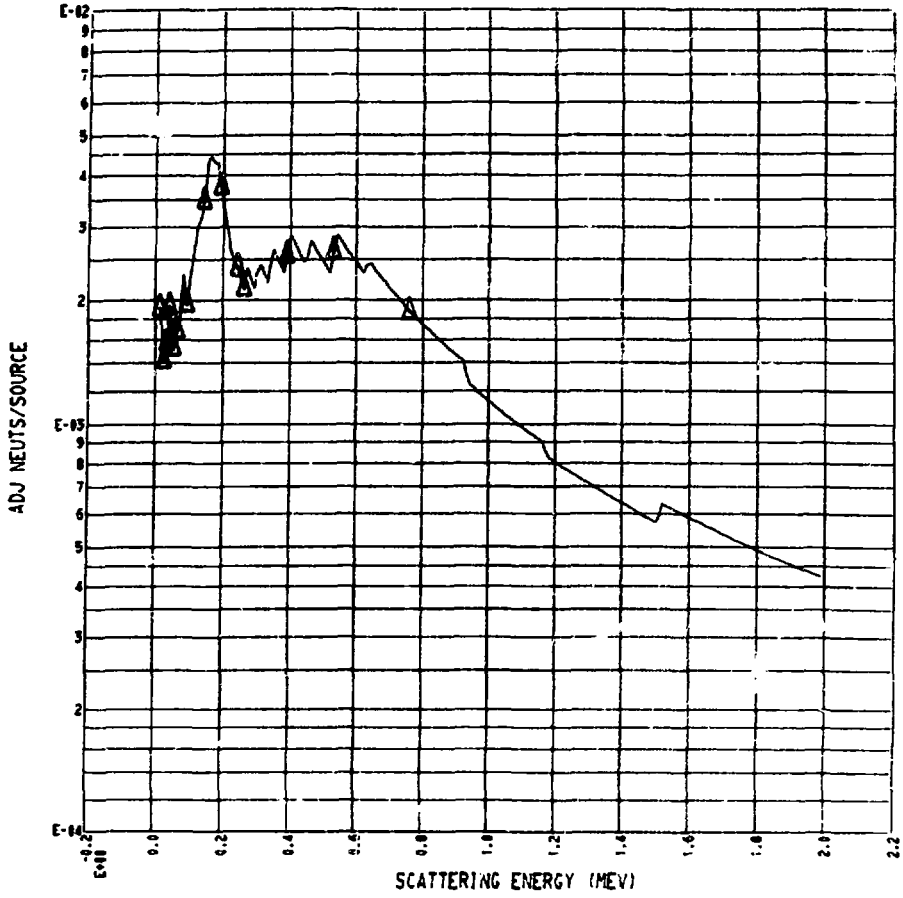

** LOW EN U-238 -- 40604 **

FIG. 33

RING CODE OUTPUT

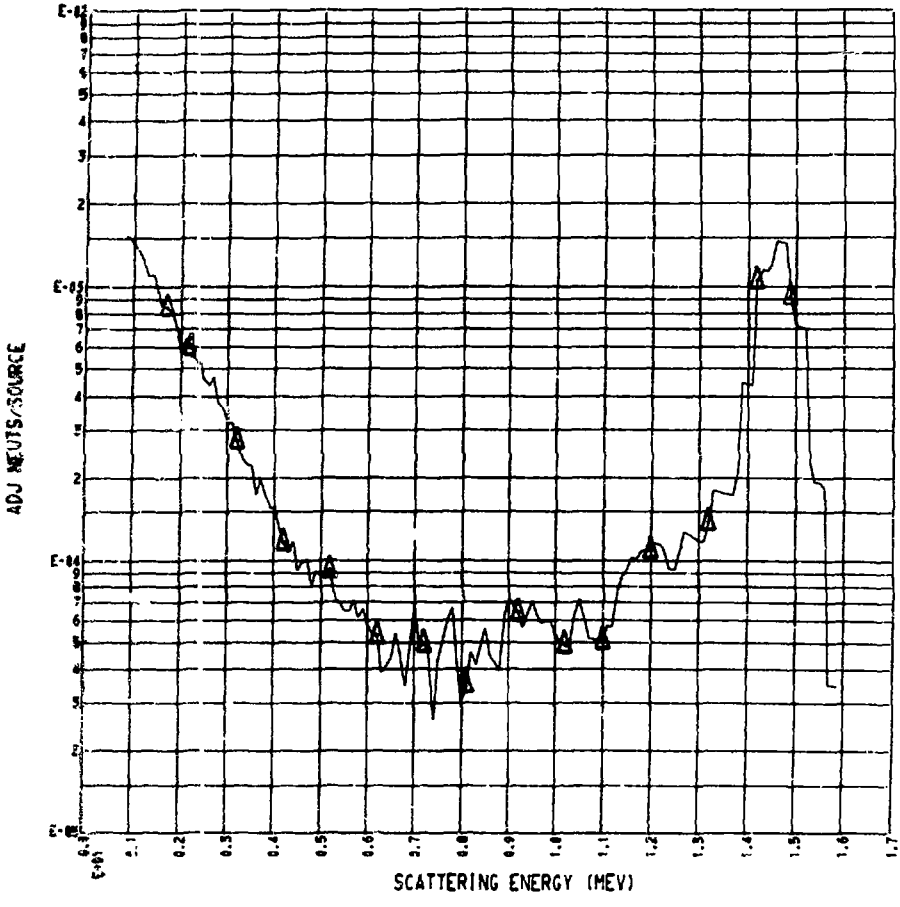

** U-238 -- 45 DEGREES -- 40804 **

FIG. 34

RING CODE OUTPUT

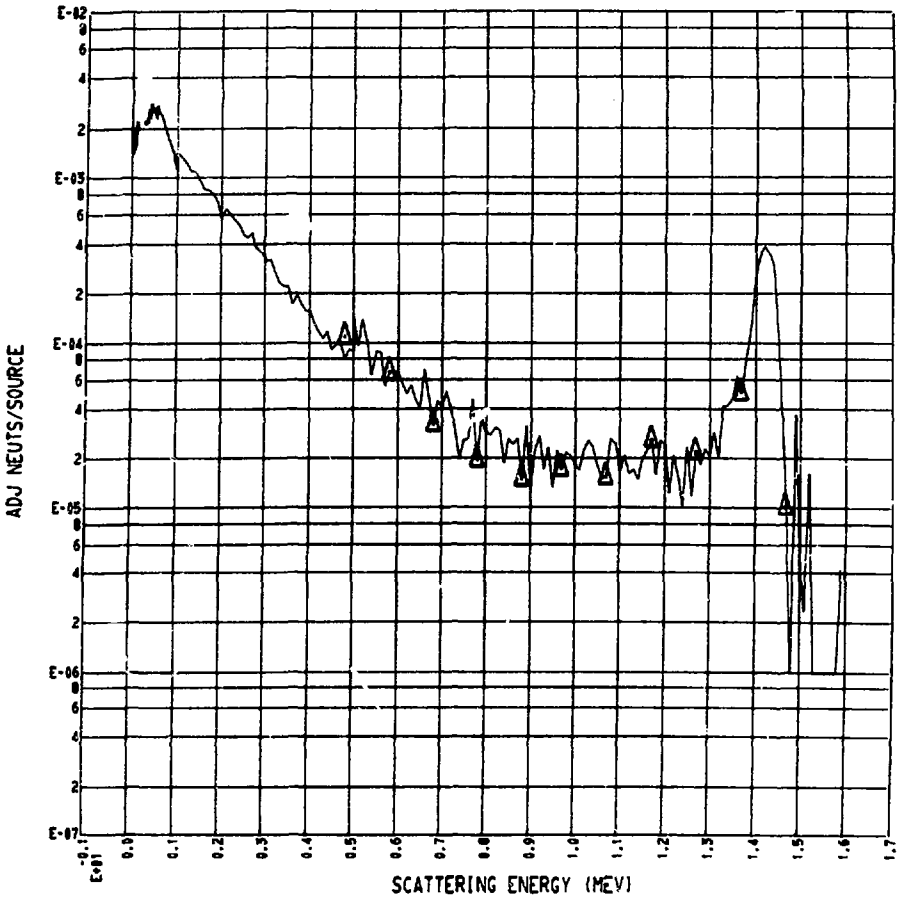

** U-238 -- 70 DEGREES **

FIG.35

RING CODE OUTPUT

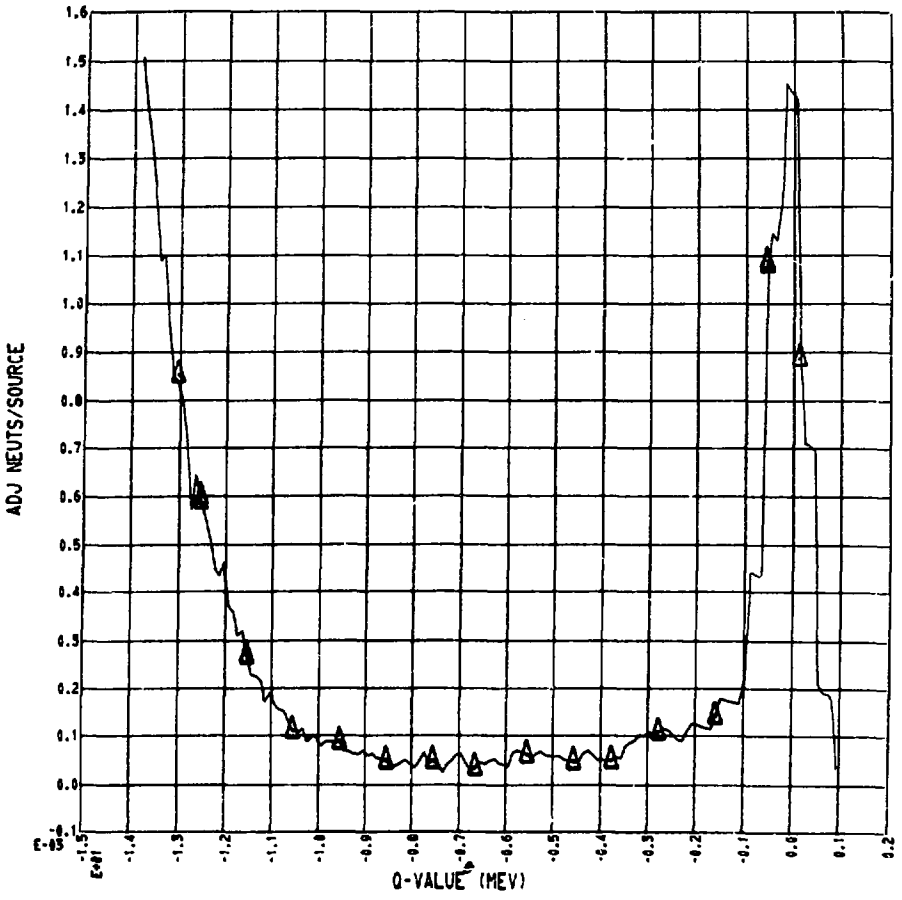

** U-238 -- 45 DEGREES -- 40804 **

MEDIUM ENERGY DATA

FIG. 36

RING CODE OUTPUT

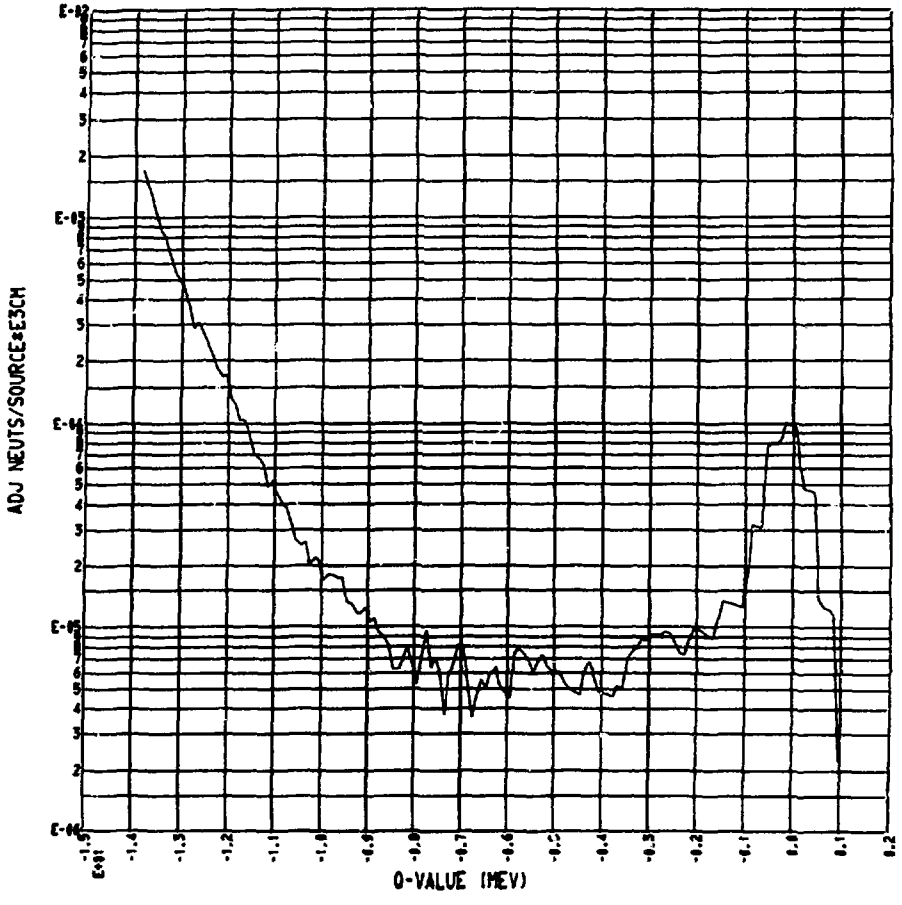

** U-238 -- 45 DEGREES -- 40804 **

MEDIUM ENERGY DATA

FIG. 37

RING CODE GENERATED OUTPUT

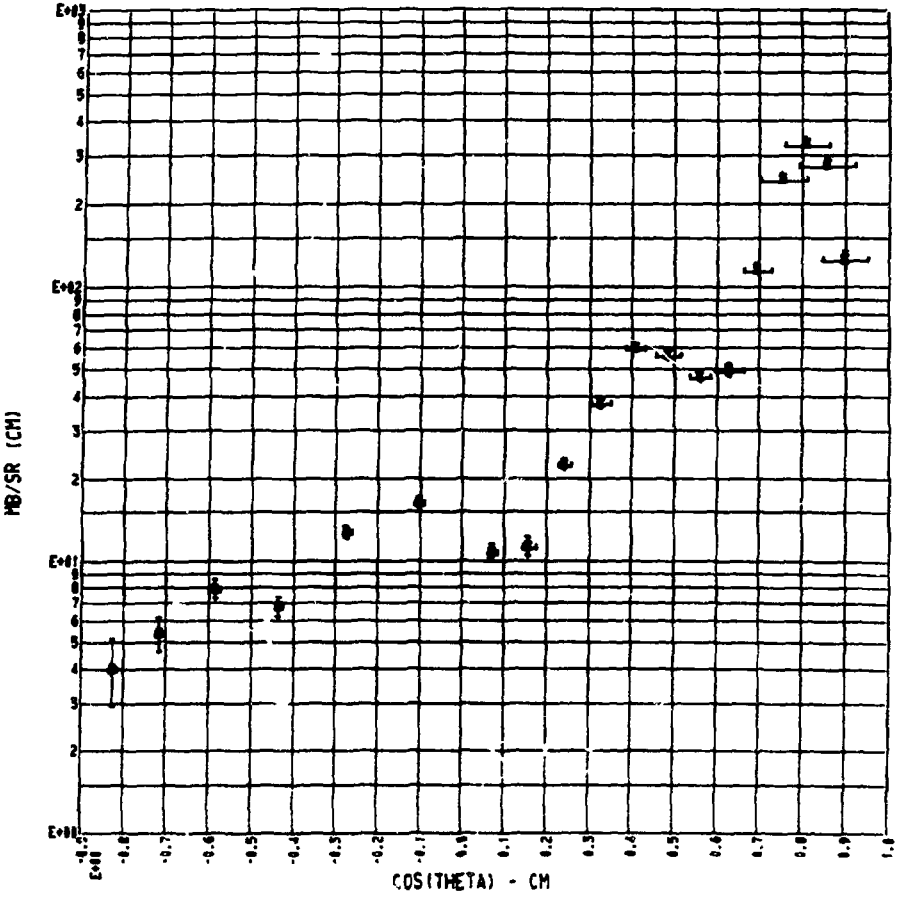

URANIUM-238 REACTIO Q-VALUE SUM BETWEEN 0.50 AND -0.50 MEV
(ELASTIC)

FIG. 38

RING CODE GENERATED OUTPUT

REACTION Q-VALUE SUM BETWEEN .5 AND -.5 MEV

ANGLE(LAB)	ANGLE(CM)	ERR	CROSS SECTION	ERROR
2.578E+01	2.588E+01	2.712E+00	1.251E+02	1.261E+02 6.300E+00
3.078E+01	3.090E+01	3.162E+00	2.755E+02	2.775E+02 6.596E+00
3.577E+01	3.591E+01	3.577E+00	3.256E+02	3.278E+02 4.736E+00
4.077E+01	4.092E+01	3.939E+00	2.449E+02	2.464E+02 4.512E+00
4.577E+01	4.594E+01	4.238E+00	1.138E+02	1.145E+02 2.591E+00
5.077E+01	5.095E+01	4.463E+00	4.889E+01	4.915E+01 2.442E+00
5.576E+01	5.596E+01	4.605E+00	4.639E+01	4.661E+01 1.664E+00
6.076E+01	6.097E+01	4.660E+00	5.586E+01	5.609E+01 1.877E+00
6.576E+01	6.598E+01	4.622E+00	5.950E+01	5.970E+01 1.368E+00
7.076E+01	7.098E+01	4.498E+00	3.731E+01	3.741E+01 1.377E+00
7.576E+01	7.599E+01	4.266E+00	2.219E+01	2.224E+01 8.319E-01
8.076E+01	8.099E+01	3.954E+00	1.110E+01	1.112E+01 9.078E-01
8.576E+01	8.599E+01	3.564E+00	1.063E+01	1.065E+01 6.182E-01
9.576E+01	9.599E+01	3.076E+00	1.596E+01	1.595E+01 6.102E-01
1.058E+02	1.060E+02	3.778E+00	1.252E+01	1.249E+01 5.546E-01
1.158E+02	1.160E+02	4.134E+00	6.644E+00	6.620E+00 5.502E-01
1.257E+02	1.259E+02	4.118E+00	7.771E+00	7.735E+00 6.372E-01
1.357E+02	1.359E+02	3.750E+00	5.298E+00	5.266E+00 7.577E-01
1.457E+02	1.459E+02	3.089E+00	3.952E+00	3.925E+00 1.072E+00

FIG. 39

RING CODE GENERATED OUTPUT

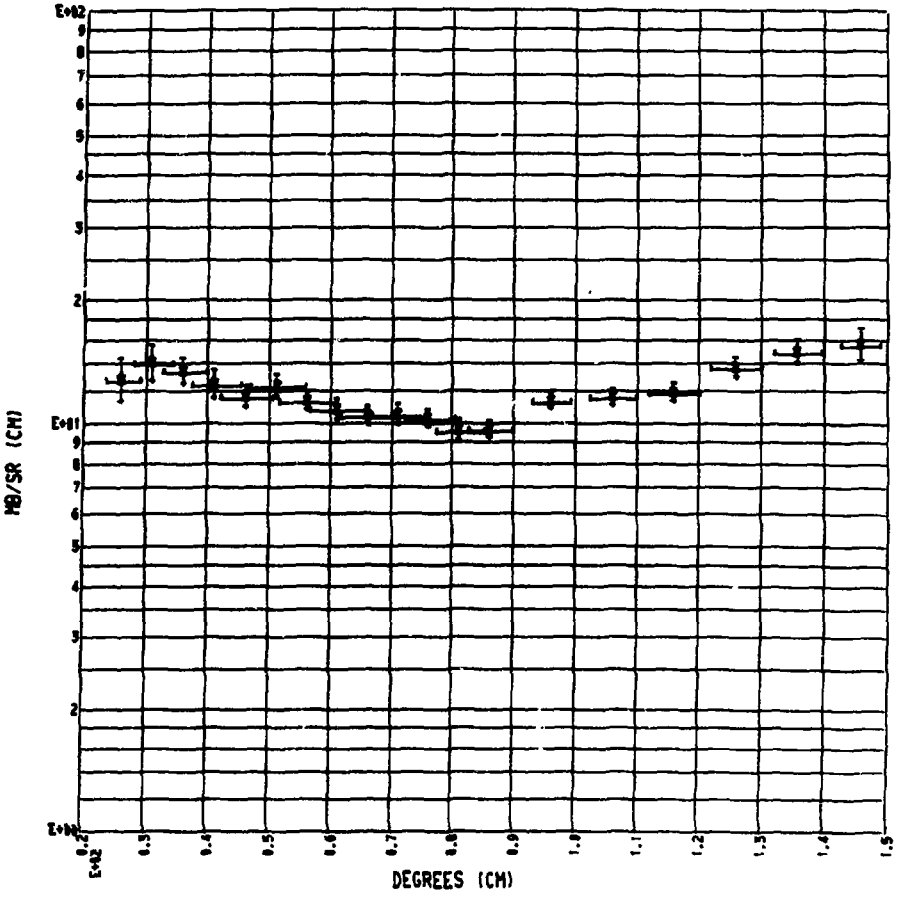

URANIUM-238 REACTIO Q-VALUE SUM BETWEEN -7.50 AND -8.50 MEV

FIG. 40

III.B. Data Adjustment

The data were corrected for effects due to impurities, multiple scattering and absorption; the corrections were made in one step using SORS-MSC, a Monte Carlo neutron transport code.[20] The SORS code[17] was extensively modified by David Cummings[20] for the purpose of making multiple scattering corrections. His modifications enabled the code to force collisions and calculate the scattering probability to ten detector positions at once. The multiple scattering theory employed was that of Parker[21,22] and Amster.[23]

This was the first application of the SORS-MSC code. The code was further modified, enabling it to calculate unattenuated first scatter probability from each isotope to each energy and angular group. This quantity, when divided by the total scatter to that energy and angle from all collisions from all isotopes, was used as a multiplication correction to each data point. Since each isotope has approximately 300 data points at each of 20 angles, the process was programmed on the computer.

$$\phi(E_i,\theta_n,I)_{\text{corrected}} = \frac{\phi_1(E_i,\theta_k,I)}{\phi_t(E_i,\theta_k)} \; \phi(E_i,\theta_k)_{\text{measured}} \qquad \begin{matrix} i = 1,300 \\ k = 1,20 \end{matrix} \qquad \text{III(1)}$$

where $\phi(E,\theta,I)_{\text{corrected}}$ is the corrected data point, $\phi_1(E,\theta,I)$ is the calculated unattenuated first scatter probability, (in essence the input cross section), ϕ_t is the calculated total scattering probability, and ϕ_{measured}

is the measured value. Binary disc files were generated by RING and SORS-MSC. The operation indicated in III(1) above was performed by a small code written especially for that purpose. The corrected data were displayed on CRT plots. The measured data and the calculated first scatter probabilities are also displayed. The corrected data are then input as the new cross sections; when the corrected data points and the first scatter probabilities converge, the correction is complete.

The following is a non-rigorous analysis of the multiple scattering correction. It allows a qualitative argument as to the important experimental considerations. The argument is confined to the isotropic scattering region of heavy nuclei. The analysis is further simplified by considering only elastic, inelastic, and total cross sections. $\bar{\nu}_{ne}$ and $\bar{\nu}_t$ are used to label the neutron multiplication factors, i.e.

$$\bar{\nu}_{ne} = \frac{\sigma_{n,n'} + 2\sigma_{n,2n} + 3\sigma_{n,3n} + \bar{\nu}\,\sigma_f}{\sigma_{ne}}$$

$$\bar{\nu}_t = \frac{\bar{\nu}\sigma_{ne} + \sigma_{el}}{\sigma_t}$$

The number of neutrons of energy E_i, if only first and second scatters are considered, is then:

$$N_d(E_i) = N_o(E_o)(1-\exp^{-\mu_o t_o})\left[\frac{\bar{\nu}\sigma_{ne}(E_o,E_i)}{\bar{\nu}_t\sigma_t(E_o)}\right.$$

$$\left(1-(1-\exp^{\mu_i t'})\frac{(\sigma_{el}(E_i)+\sigma_{ne}(E_i))}{\sigma_t(E_i)}\right)\exp^{-\mu' t''}$$

$$+\frac{\sigma_{el}(E_o)}{\bar{\nu}_t\sigma_t(E_o)}\left(1-\exp^{-\mu_o t'}\right)\frac{\bar{\nu}\sigma_{ne}(E_o-\delta,E_i)}{\bar{\nu}_t\sigma_t(E-)}\,e^{-\mu_i t''}$$

$$+\frac{\bar{\nu}\sigma_{ne}(E_o,E_i+\delta)}{\bar{\nu}_t\sigma_t(E_o)}\left(1-\exp^{-\mu_i t''}\right)\frac{\sigma_{el}(E_i+\delta)}{\bar{\nu}_t\sigma_t(E_i+\delta)}\exp^{-\mu_i t''}$$

$$+\frac{\bar{\nu}\sigma_{ne}(E_o,E')}{\bar{\nu}_t\sigma_t(E_o)}\left(1-\exp^{-\mu' t''}\right)\frac{\bar{\nu}\sigma_{ne}(E',E_i)}{\bar{\nu}_t\sigma_t}\exp^{-\mu_i t''}\Big]$$

where $N_o(E_o)(1-\exp^{-\mu_o t_o})$ is the expectation value for the number of first collisions. The first term in the brackets is the probability that the neutron scatters to energy E_i in the first collision, with the possibility of removal by a second scatter shown explicitly. The second term is the probability that the neutron loses energy δ in an elastic first collision and then scatters to E_i. The third term is probability of inelastic scatter to $E_i + \delta$, then elastic scatter to E_i. The fourth term is the probability of two inelastic scatter events resulting in a detected neutron of energy E_i.

Assume $t' \approx t''$, i.e. that the collision - detector path lengths are similar after both the first and second scatter events.

Assume $\mu_o = \mu_1 = \mu'$, i.e. that the total cross section is constant.

Assume $\sigma(E_o - \delta, E_i) \approx (E_o, E_i)$, i.e. that so little energy is lost in the elastic scatter event that the cross section for inelastic scatter to E_i is unchanged. The ratio of detected events to first scatter events is then

$$\frac{N_d(E_i)}{N_o(E_o)(1-\exp^{-\mu_o t_o}) \frac{\bar{\nu}\sigma_{in}(E_o,E_i)}{\bar{\nu}_t\sigma_t(E_o)}} =$$

$$1 + (1-\exp^{-\mu' t'}) \left[- \frac{\sigma_{el}(E_i)}{\sigma_t(E_i)} - \frac{\sigma_{in}(E_i)}{\sigma_t(E_i)} + \frac{\sigma_{el}(E_o)}{\bar{\nu}'\sigma(E_o)} \frac{\sigma_{el}(E_i)}{\bar{\nu}'\sigma_t(E_i)} \right.$$

$$\left. + \frac{\bar{\nu}\sigma_{ne}(E_o,E')}{\bar{\nu}\sigma_{ne}(E_o,E_i)} \frac{\bar{\nu}\sigma_{ne}(E',E_i)}{\bar{\nu}'\sigma_t(E')} \right] \exp^{-\mu_i t''}$$

The elastic and nonelastic cross sections are divided evenly at most energies, therefore the right hand portion of the equation becomes

$$= 1 + (1-\exp^{-\mu' t'}) \exp^{-\mu_i t''} \left[-\tfrac{1}{2} - \tfrac{1}{2} + \frac{1}{2\bar{\nu}'} + \frac{\bar{\nu}}{2\bar{\nu}'} + \frac{\bar{\nu}}{2\bar{\nu}} \int \frac{\sigma_{ne}(E_o,E')}{\sigma_{ne}(E_o,E_i)} \right]$$

$$= 1 + (1-\exp^{-\mu' t'}) \exp^{-\mu_i t''} \left[\frac{1-\bar{\nu}'}{\bar{\nu}'} + \frac{\bar{\nu}}{2\bar{\nu}} \frac{\sigma_{ne}(E_o,E')}{\sigma_{ne}(E_o,E_i)} \right]$$

Cross sections are to be obtained by dividing data by the expression on the right. It is evident that if $\mu' t' \ll 1$, no correction is necessary. This is achieved by making the target thin. Unfortunately a similiar expression governs the probability of first scatter events. Targets must be moderately thick, therefore,or the counting statistics are poor. The expression in brackets should be examined more closely. $\bar{\nu}'$ is 2.4 for ^{235}U and the first term is negative. It is observed that the correction is small so long as $\int_{E'} \sigma_{ne}(E_o,E')/\sigma_{ne}(E_o,E_i)$ is small. The integration is explicitly noted for the first time. Observe that the expression is ≈ 1 if only fission is considered. If the other non-elastic processes are considered alone, the expression is $\ll 1$. If $E_i \ll E_o$, the expression becomes large.

Target thickness was 1/4 mean-free-paths or less. Since this is the μt in the above equations, it is eacy to see that the upper limit of multiple scattering effects can be set at about 20% based on this analysis. The more exact Monte Carlo calculations showed that the effect was much less than 20% over most of the energy range. In some cases, notably for elastic scattering and for neutrons scattered from the fissionable isotopes with energy below 100 keV, the correction exceeded 20%. But in those special cases, μt was greater than 1/4.

III.C. Experimental Uncertainties

The data are presented in Sect. V with the statistical error plotted for selected points. Data which has been corrected for multiple scattering and flux attenuation have been plotted with the combined errors of experimental counting statistics and the computed standard deviation of the Monte Carlo methods used in computing corrections. The experimental statistical error is taken as the square root of the number of counts in the interval indicated. The standard deviation of the Monte Carlo calculation is computed by making five sample calculations. The error is then taken as:

$$\text{Error} = \sqrt{\frac{\sum_{i=1}^{n} (x_i - \bar{x})^2}{n - 1}}$$

where x_i is the i^{th} sample value of the calculated correction, $\bar{x}$ is the average value of the five samples and n is the number of samples.

Statistical errors have been kept small in most cases, since counting statistics are good. In almost all cases, counting statistics are less than 10%. This error can be readily improved by making bin sizes larger. Most of the data in Sect. V are displayed in 100 keV steps.

Systematic uncertainties dominate. The primary systematic error is the uncertainty in the detector efficiency. These uncertainties are discussed in the sections describing the detectors.

There is a known systematic uncertainty(see Sect. II.A.8) resulting from finite experimental time and energy resolution; the resulting uncertainty in quoted energy of the emitted neutron causes resolvable energy levels to have an unnatural width which is characteristic of the energy resolution at that energy.

There is a systematic error in the source neutron energy caused by

the known energy anisotropy of the neutron source (see Tables I and II in Section II.A.6). Because of energy anisotropy, source energy is slightly different at each angle of a measured angular distribution. This error is believed to be small since the source energy varies only about one MeV over the range of the measurements and the source energy is higher than any expected resonance structure in the cross section. Therefore, the differential cross section is expected to be slowly varying. Errors from this uncertainty are small, probably less than 10%.

Data uncertainties also exist due to the limited number of measurements below 5 MeV. Scattered neutrons with energy between one and five MeV were measured only at 45°, 95°, and 135° angles. Scattered neutrons below one MeV were measured only at 95°. These data were composited with the finer angular resolution data measurements above 5 MeV. Errors result due to possibly non-isotropic scattering and the variations in the incident neutron energy. Discontinuities may be noted in the data at one and five MeV. The magnitudes of these discontinuities reflect both the uncertainties mentioned in this paragraph and uncertainties in detector efficiency.

IV. Data Presentation

The data are presented without comparison to other experimental data. With the exception of differential elastic scattering data, few direct comparisons are possible due to the lack of other data, or the superior energy resolution and extended energy range of observation attained in the present work. Only the work of Anufrienko et al.[24] approaches the present work in scope, but his time resolution was 7 nsec compared with 1.5 nsec in this work; his flight path was 2 meters compared with 8.3 meters; he did not suppress gamma background; his scattering samples were larger; and he did not correct for multiple scattering. There are measurements made in point scatterer geometry with resolution almost equal that in this work, but the energy range of the observed neutrons is limited and experimental running times of 100 hours per point[25] limit the scope of such work.

All elastic angular distributions were extracted from the data and compared with the optical model calculations of Agee et al.[26] Many of the elastic distributions were compared to data of Coon et al.[10] and Anderson et al.[27] In all cases, agreement was acceptable.

Mention is made of checks against other data, where sufficiently detailed information is available, in the discussion of each isotope.

There are gamma pulse height data available for most of the isotopes. A sample spectrum for this type of data is shown as Fig. 11. See Sect. II.C.1 for details. The gamma pulse height data were only partially analyzed, and the bulk of the data are not included here. Paul Robinson[28] is analyzing the niobium gamma pulse height data in conjunction with work he is doing for his doctoral thesis. The plotted data are available as output from RAW code (see Sect. III.A.1) and on IBM cards.

IV.A. Carbon

Carbon data were taken as a first step experiment. The purpose of the carbon data was to prove the experimental technique and to provide a data set to use in debugging the RING code, which was later used to reduce all data taken. Fig. 41 presents the carbon data in a three dimensional oblique projection. Although spectra were taken at only six angles, it is relatively easy to surmise the success of the experiment in measuring the angular distribution of both the elastic peak and 4.43 MeV level. The absence of serious background problems is made evident by the regions of zero measured cross section between the expected peaks. The carbon data were taken at 3 nanoseconds full-width-half-maximum time resolution. Later data were taken at 1.5 nanoseconds resolution.

The measured elastic angular distribution of carbon was in excellent agreement with the measurements of Nakada et al.[29] and Bouchez et al.[30] The measured angular distribution of the 4.43 MeV level in carbon was in excellent agreement with the measurements of Anderson et al.[31] and Bouchez et al.[30]

The excellent agreement of the carbon data with good data in existence provided a measure of confidence in both the experimental method and in the RING data reduction code.

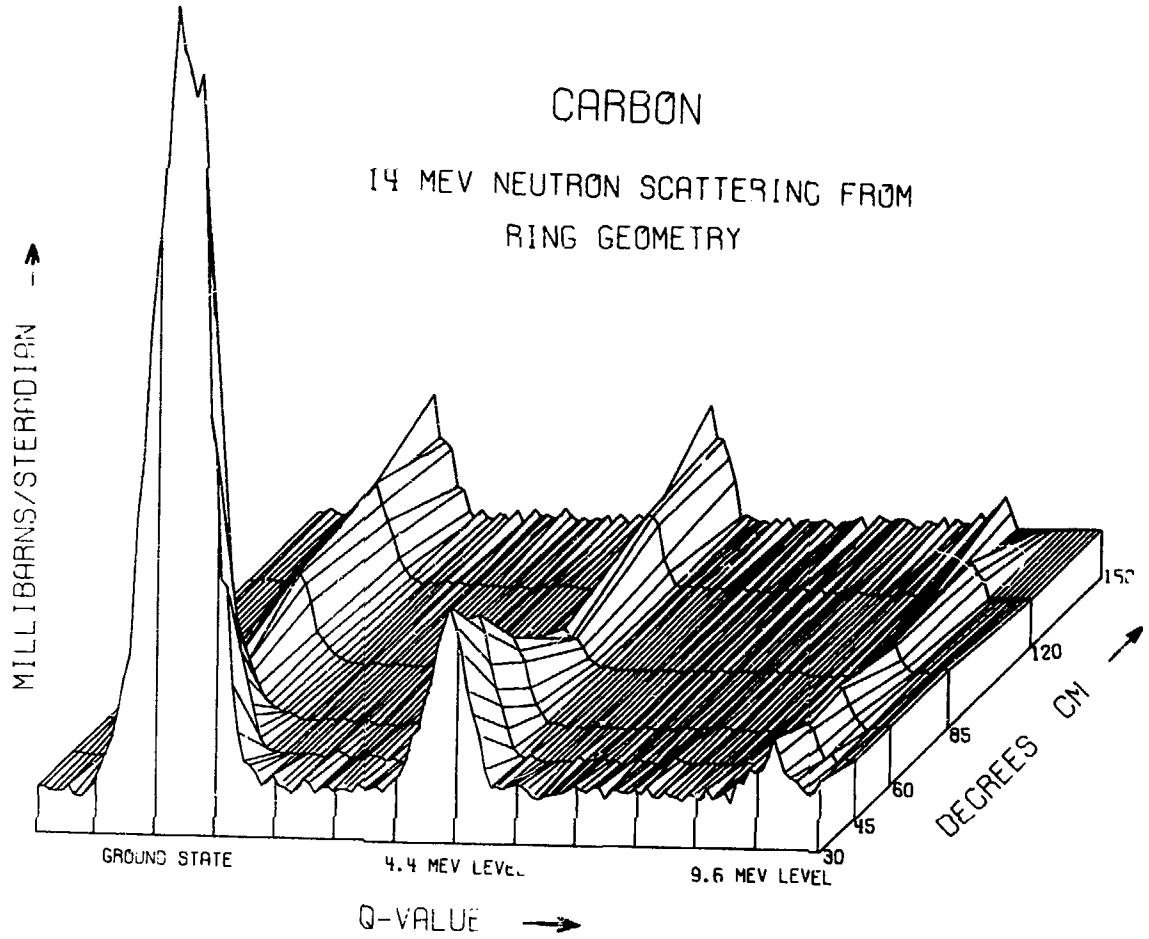
CARBON
14 MEV NEUTRON SCATTERING FROM
RING GEOMETRY
MILLIBARNS/STERADIAN
GROUND STATE
4.4 MEV LEVEL
9.6 MEV LEVEL
Q-VALUE
DEGREES CM
150
120
85
60
45
30

FIG. 41

IV.B. Aluminum

Aluminum data were taken primarily as a demonstration of experimental resolution. The data are the best of their type available however, so that the entire data set is presented.

The elastic cross section was extracted from the data set and is presented as Fig. 42. The multiple scattering correction was made and both raw data and corrected data are presented.

Figs. 43 thru 46 contain the entire data set. The solid curve connects points generated each 100 keV. Since the multiple scattering correction proved insignificant for inelastically scattered neutrons, only the raw data are presented. Each curve is a combination of high and medium energy data. The measured elastic angular distribution was favorably compared to the measurement of Coon et al.[10] A crude comparison of the inelastic spectra was made with the work of Voignier et al.[32]

Figs. 47, 48, and 49 are plots of the experimental angular distributions for low lying levels and groups of levels in aluminum below 3.50 MeV excitation. Vertical error bars are statistical and horizontal error bars depict the upper limit of angular uncertainty.

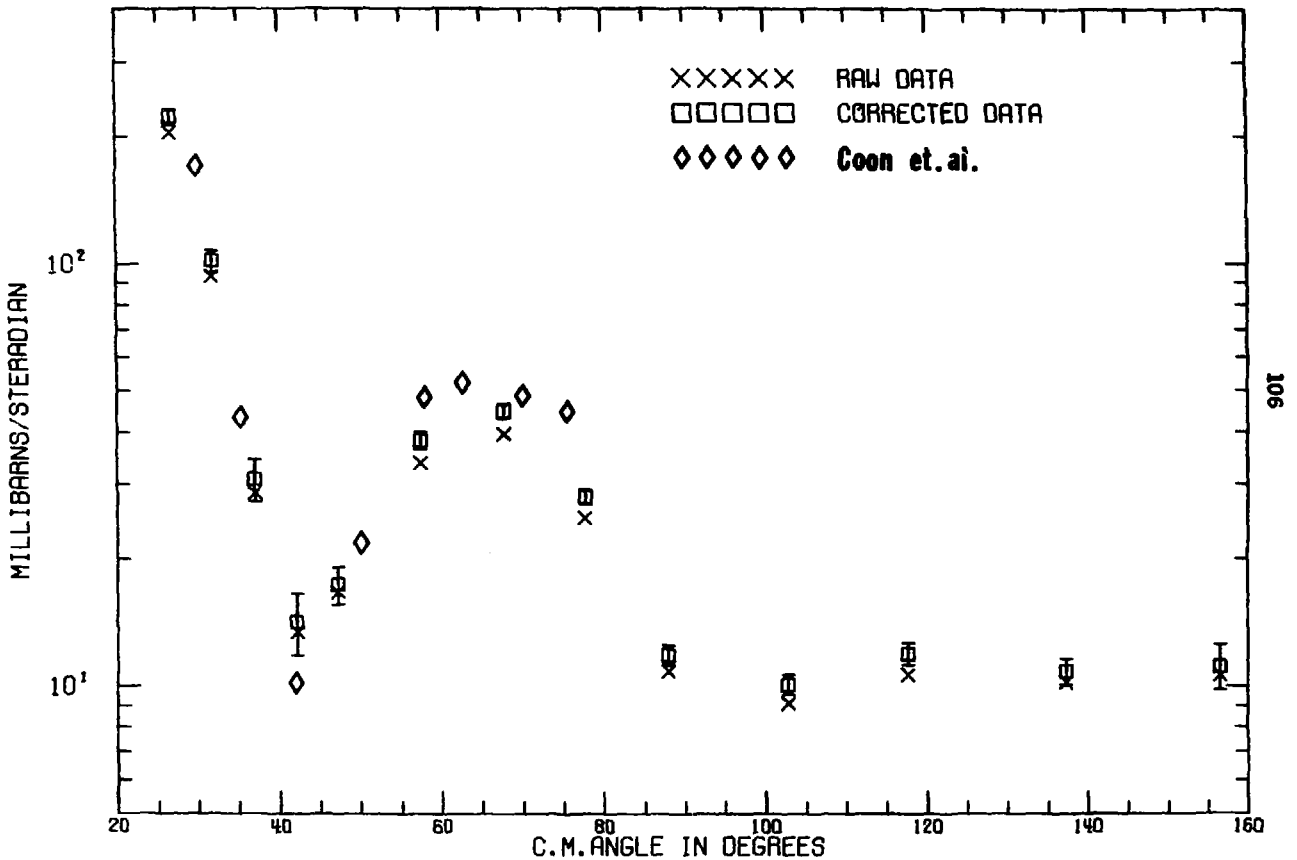

ALUMINUM ELASTIC SCATTERING

FIG. 42

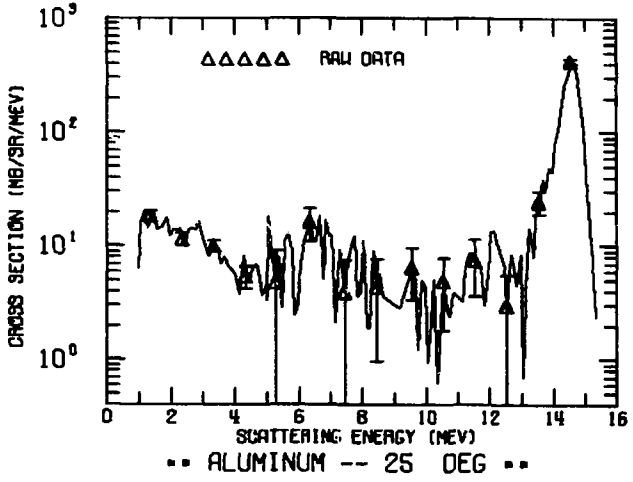

•• ALUMINUM -- 25 DEG ••

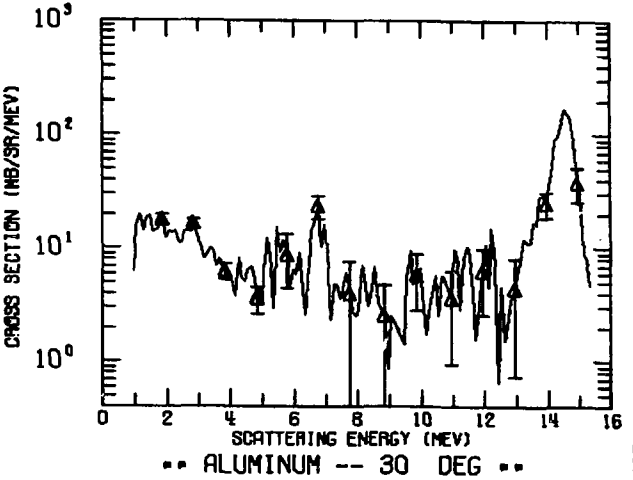

•• ALUMINUM -- 30 DEG ••

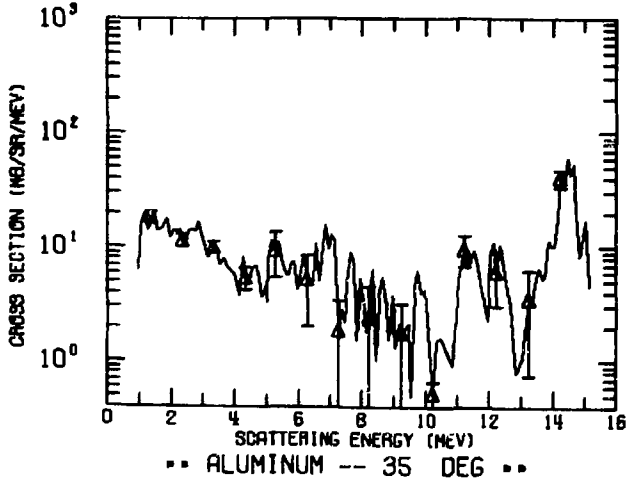

•• ALUMINUM -- 35 DEG ••

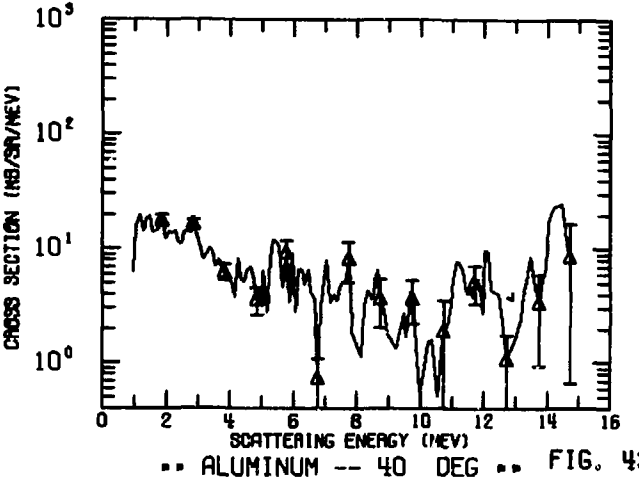

•• ALUMINUM -- 40 DEG ••

FIG. 43

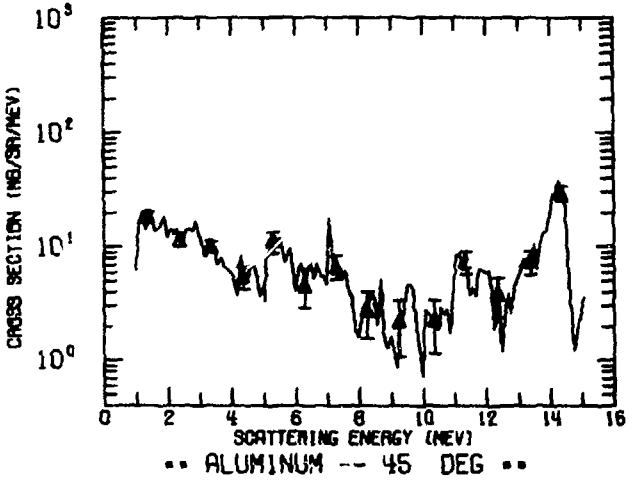
CROSS SECTION (MB/SR/MEV)
SCATTERING ENERGY (MEV)
** ALUMINUM -- 45 DEG **

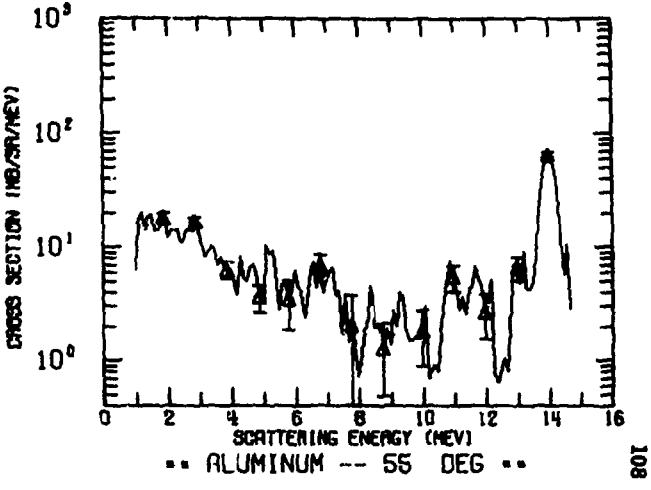
CROSS SECTION (MB/SR/MEV)
SCATTERING ENERGY (MEV)
** ALUMINUM -- 55 DEG **

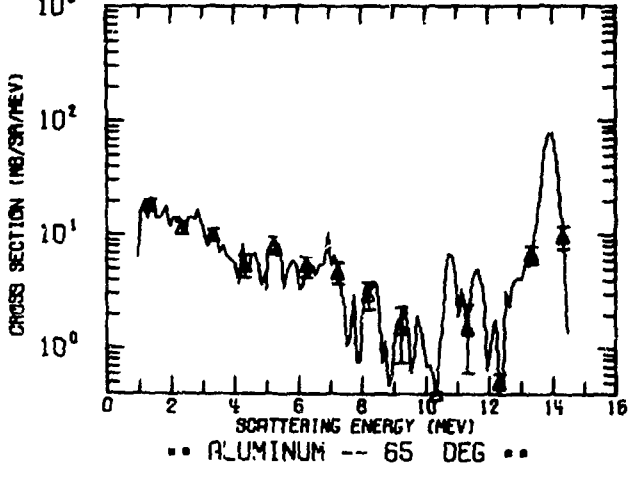
CROSS SECTION (MB/SR/MEV)
SCATTERING ENERGY (MEV)
** ALUMINUM -- 65 DEG **

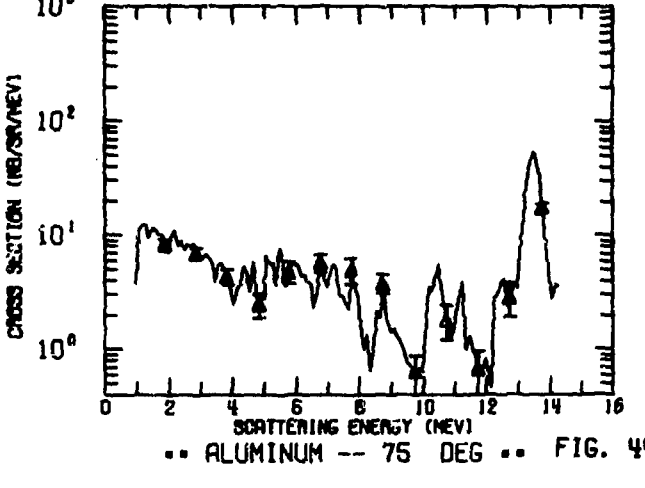
CROSS SECTION (MB/SR/MEV)
SCATTERING ENERGY (MEV)
** ALUMINUM -- 75 DEG **

FIG. 44

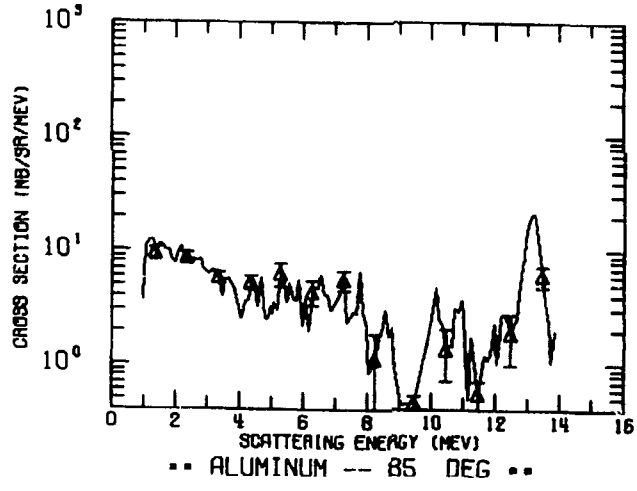
CROSS SECTION (MB/SR/MEV)
SCATTERING ENERGY (MEV)
** ALUMINUM -- 85 DEG **

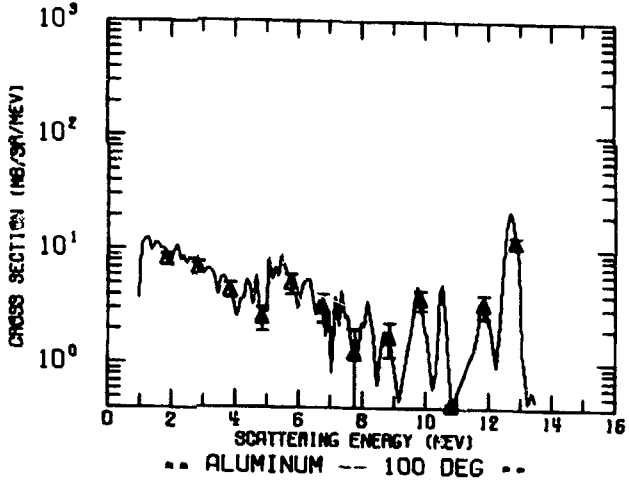
CROSS SECTION (MB/SR/MEV)
SCATTERING ENERGY (MEV)
** ALUMINUM -- 100 DEG **

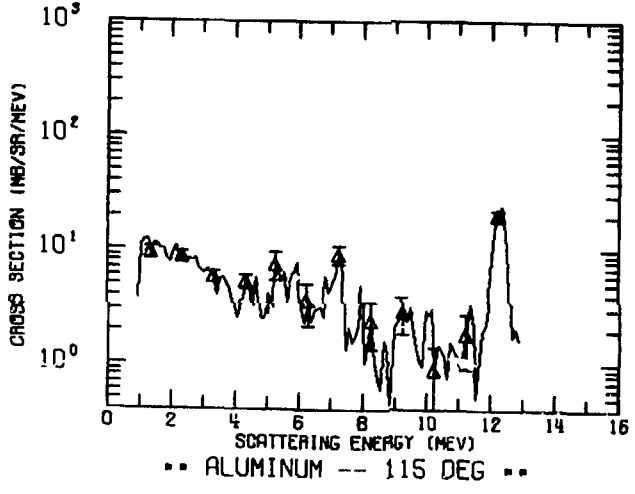
CROSS SECTION (MB/SR/MEV)
SCATTERING ENERGY (MEV)
** ALUMINUM -- 115 DEG **

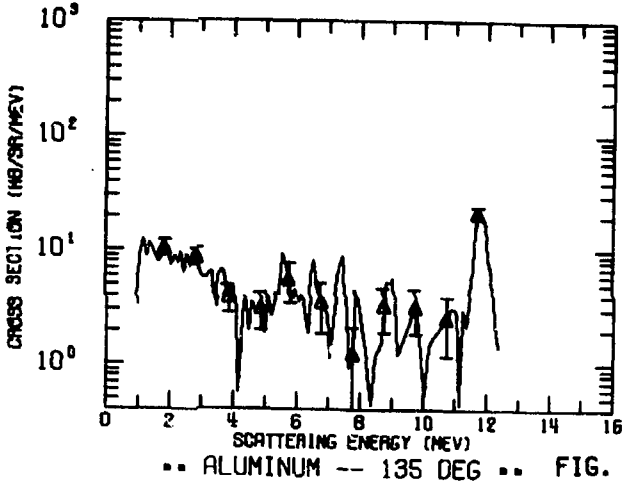
CROSS SECTION (MB/SR/MEV)
SCATTERING ENERGY (MEV)
** ALUMINUM -- 135 DEG **

FIG. 45

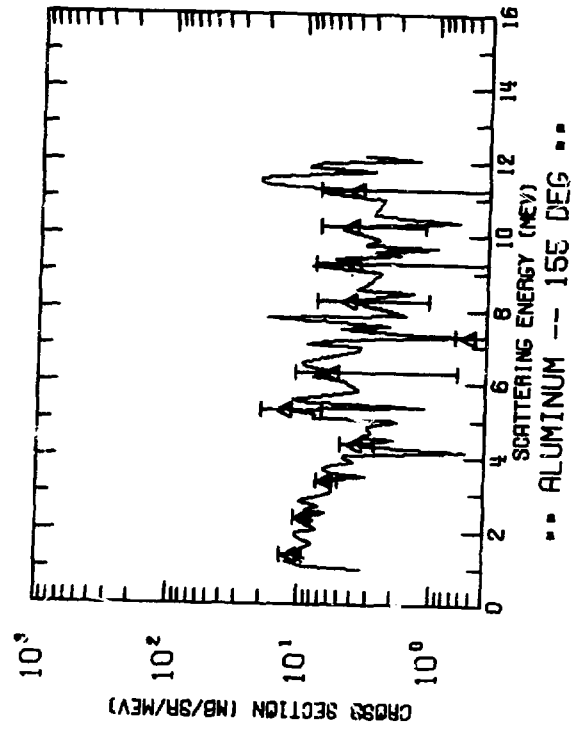
CROSS SECTION (MB/SR/MEV)
10^3
10^2
10^1
10^0
0
2
4
6
8
10
12
14
16
SCATTERING ENERGY (MEV)
** ALUMINUM -- 155 DEG **

FIG. 46

EXPERIMENTAL ANGULAR DISTRIBUTION SUMMED FOR THE 0.842

AND 1.013 MEV LEVELS OF ALUMINUM

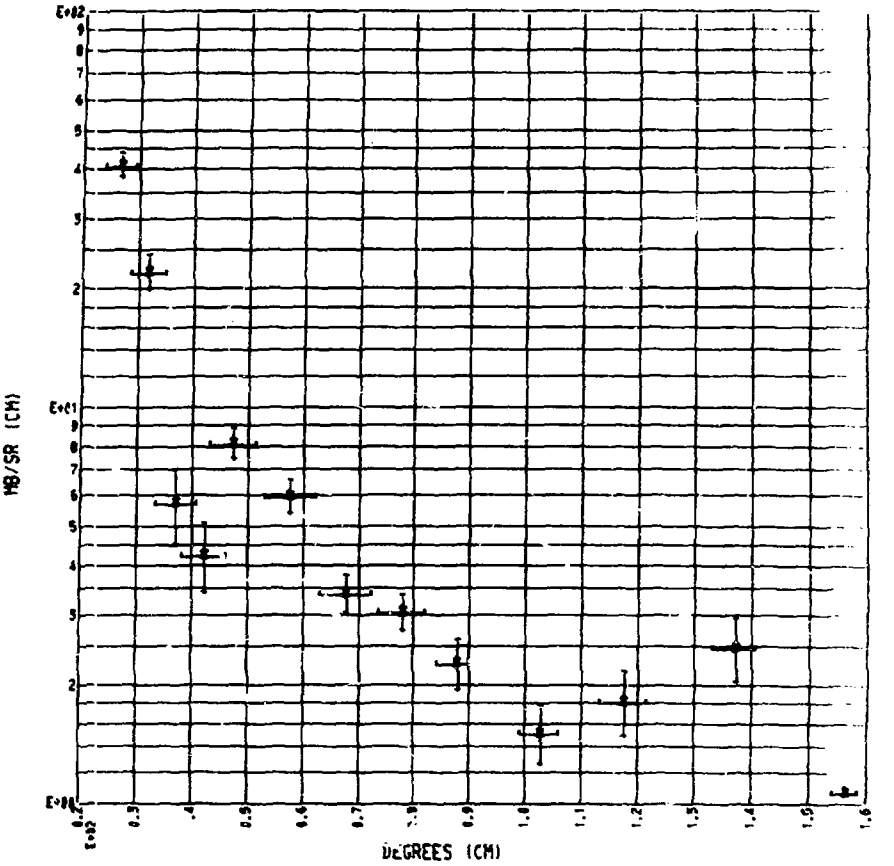

** ALUMINUM Q-VALUE SUM BETWEEN -0.50 AND -1.50 MEV -

FIG. 47

EXPERIMENTAL ANGULAR DISTRIBUTION FOR THE 2.21 MEV

LEVEL OF ALUMINUM

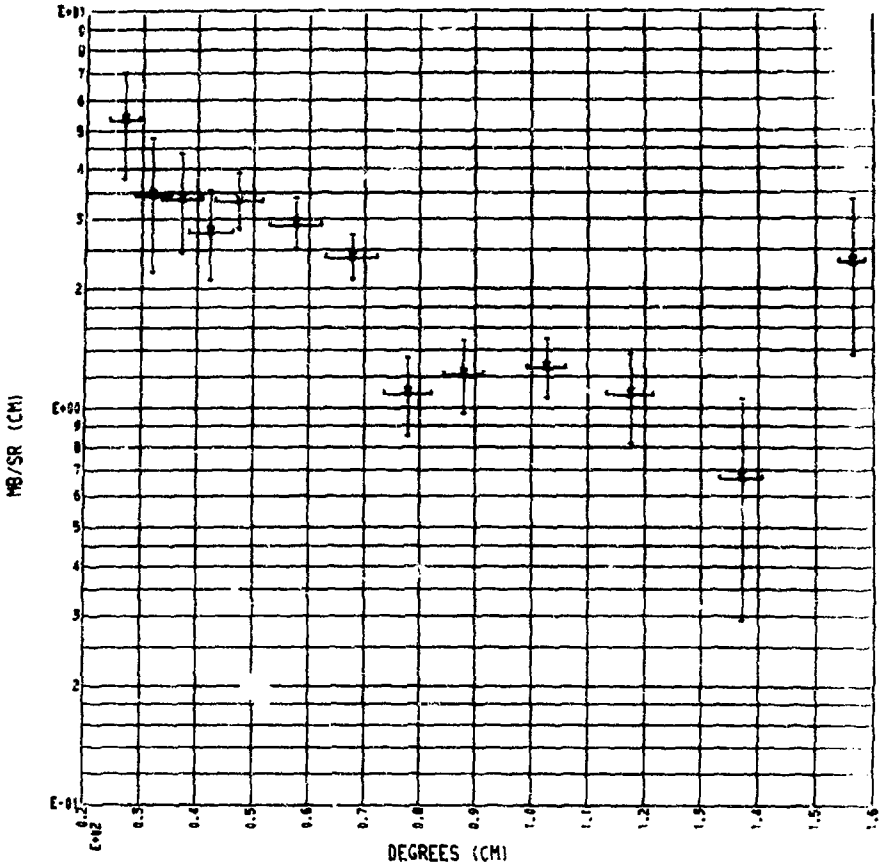

** ALUMINUM Q-VALUE SUM BETWEEN -1.50 AND -2.50 MEV

FIG. 48

EXPERIMENTAL ANGULAR DISTRIBUTION SUMMED FOR THE 2.73, 2.98 AND 3.00 MEV LEVELS IN ALUMINUM

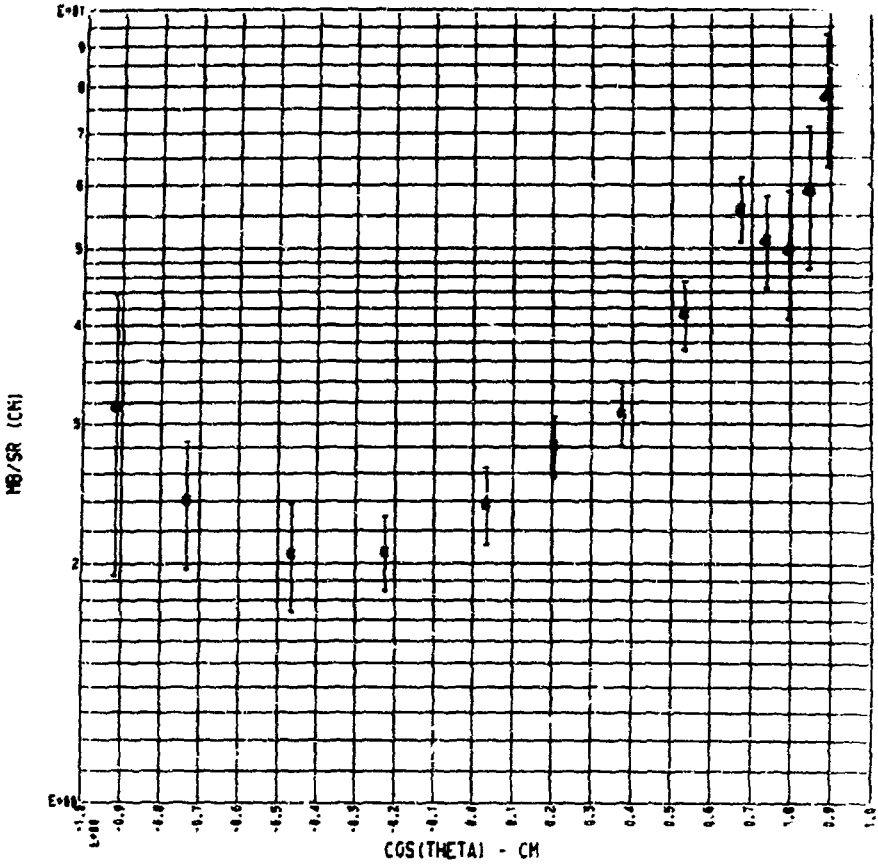

** ALUMINUM Q-VALUE SUM BETWEEN -2.50 AND -3.50 MEV

FIG. 49

IV.C. Iron

The natural iron data presented in Figs. 50 through 54 are inhomogeneous in that machine resolution changed somewhat between angles due to the fact that the data were taken over a period of weeks and experimental technique improved somewhat in the interim. A comparison of 125° data (Fig. 54) with the 75° data (Fig. 53) shows an improvement in time resolution from 3 nsec FWHM to 1.5 nsec FWHM. The separation of the 846 keV level from the ground state was excellent at 1.5 nsec FWHM.

Fig. 50 shows the iron elastic distribution. Figs. 51-54 show the completed data set for iron. Each curve is a composite of high, medium, and low energy data, and is generated by connecting points each 100 keV.

The iron elastic angular distribution was favorably compared with the data of Coon et al.[10] Partial comparison of the inelastic data can be made with the measurements of Sal'nikov et al.[33] and Graves et al.[34]

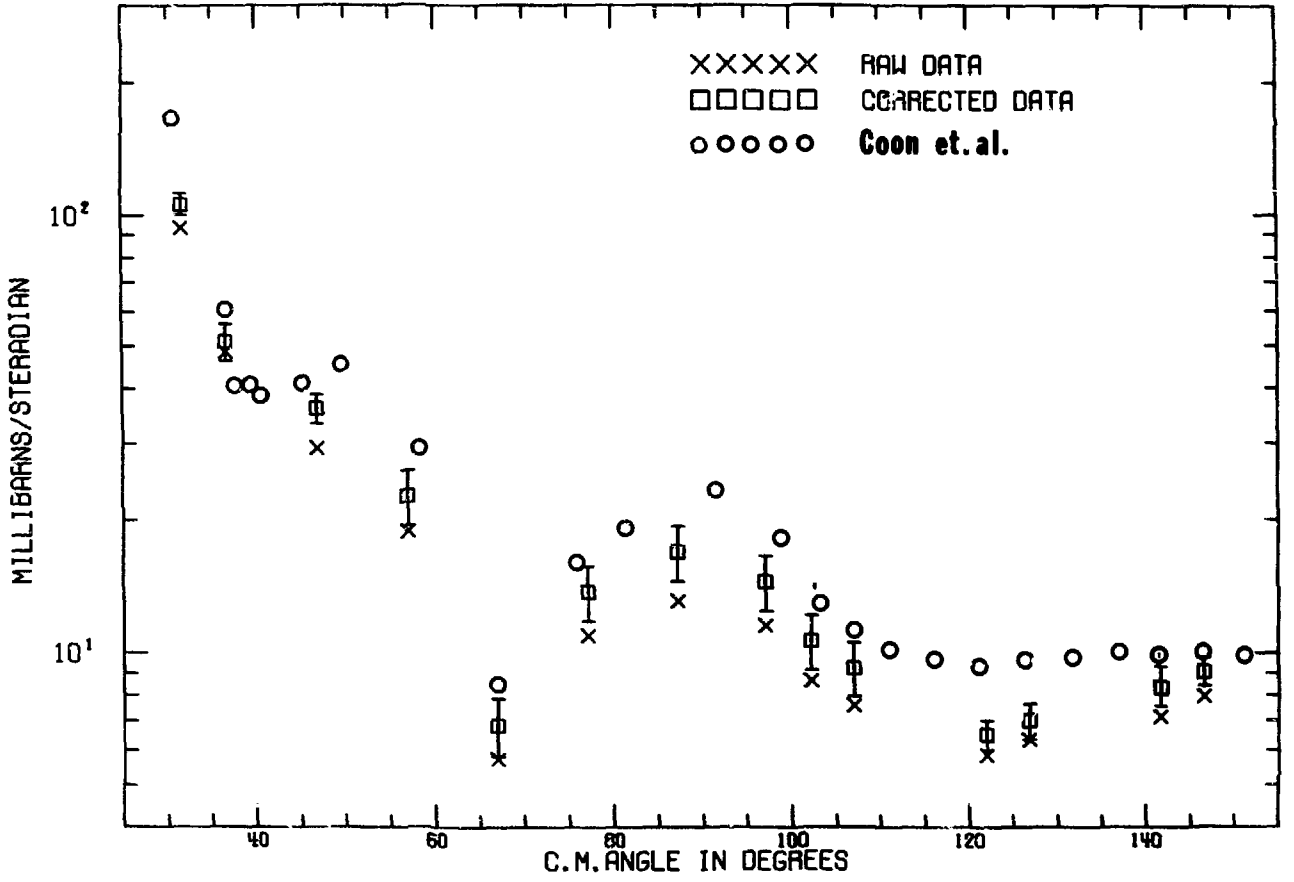

IRON ELASTIC SCATTERING

FIG. 50

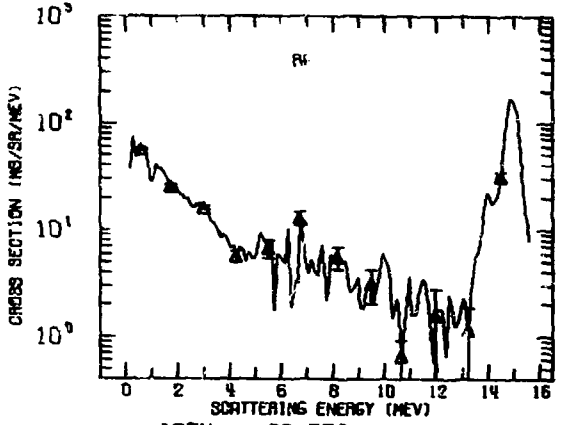

IRON - 30 DEG -

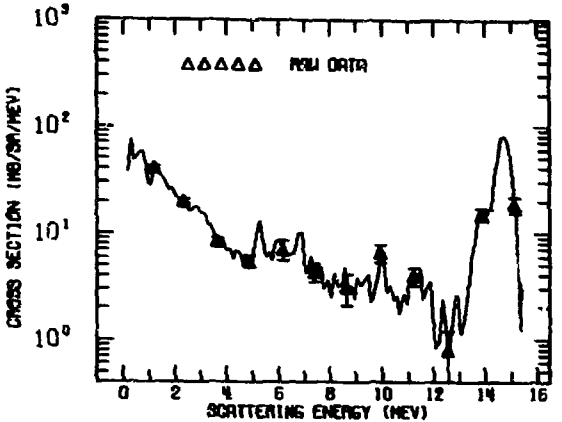

IRON - 35 DEG -

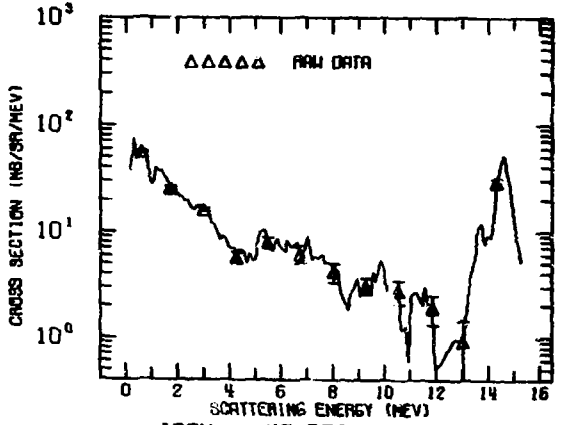

IRON - 45 DEG -

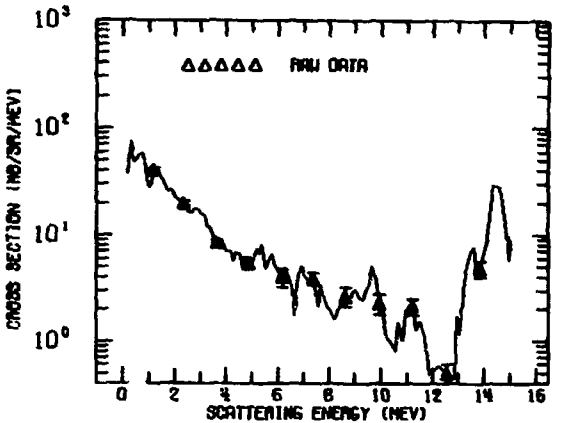

IRON - 55 DEG -

FIG. 51

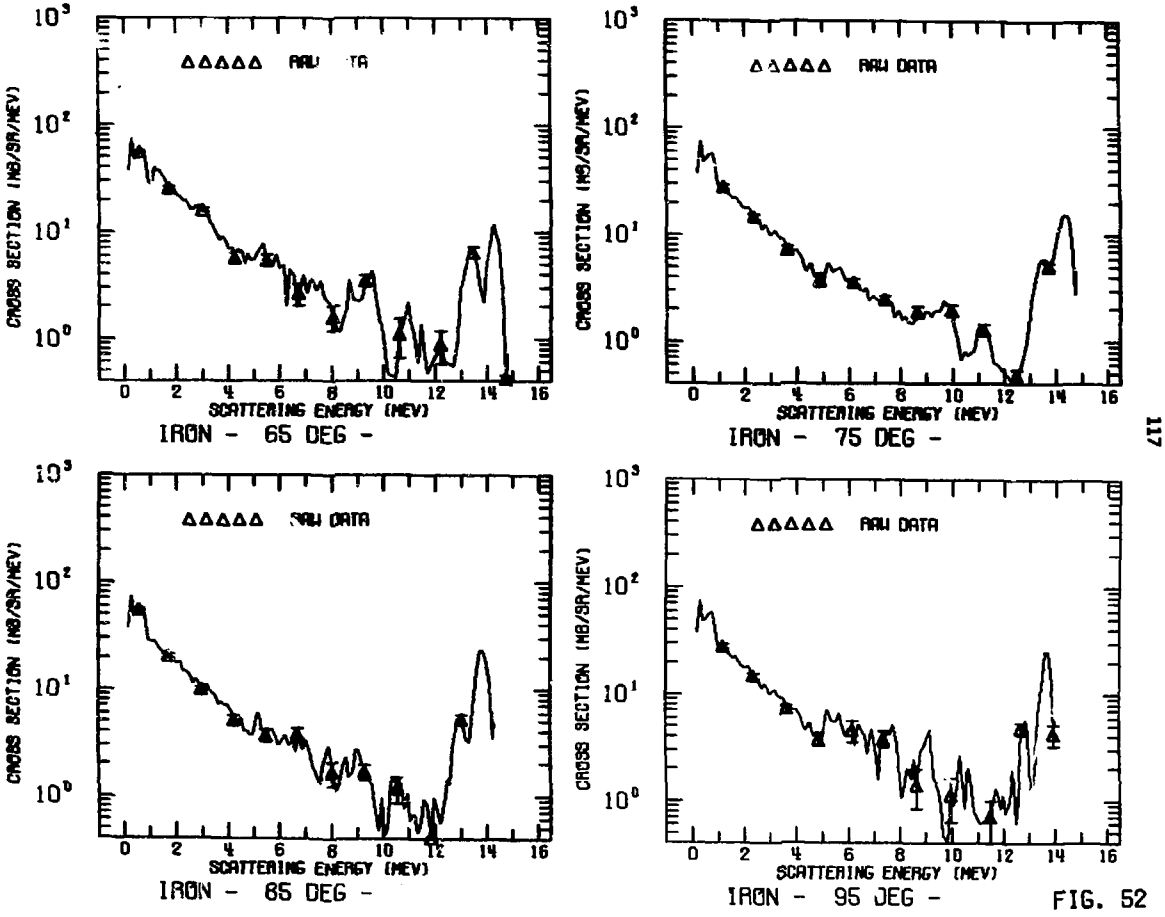
ΔΔΔΔΔ RAW DATA
CROSS SECTION (MB/SR/MEV)
SCATTERING ENERGY (MEV)
IRON - 65 DEG -
ΔΔΔΔΔ RAW DATA
CROSS SECTION (MB/SR/MEV)
SCATTERING ENERGY (MEV)
IRON - 75 DEG -
ΔΔΔΔΔ RAW DATA
CROSS SECTION (MB/SR/MEV)
SCATTERING ENERGY (MEV)
IRON - 85 DEG -
ΔΔΔΔΔ RAW DATA
CROSS SECTION (MB/SR/MEV)
SCATTERING ENERGY (MEV)
IRON - 95 DEG -

FIG. 52

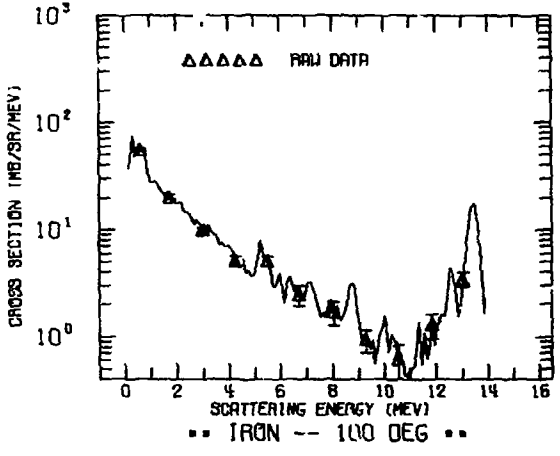

•• IRON -- 100 DEG ••

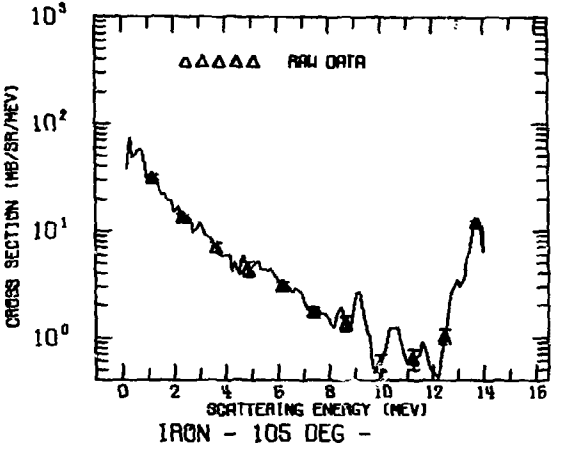

IRON - 105 DEG -

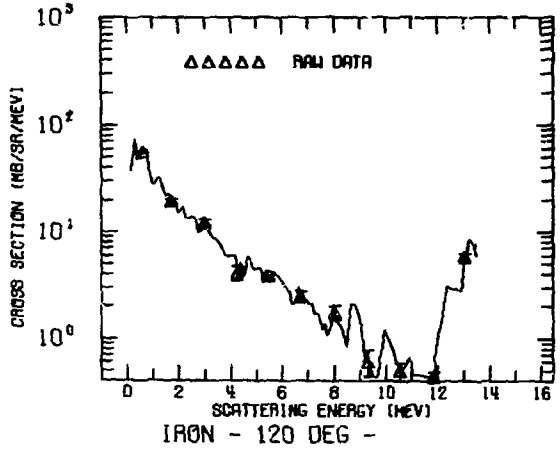

IRON - 120 DEG -

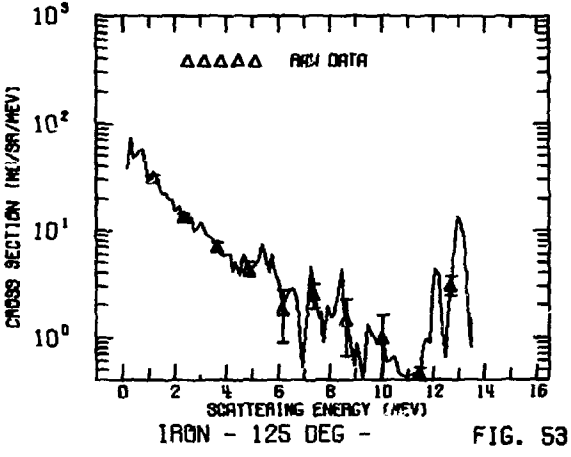

IRON - 125 DEG -

FIG. 53

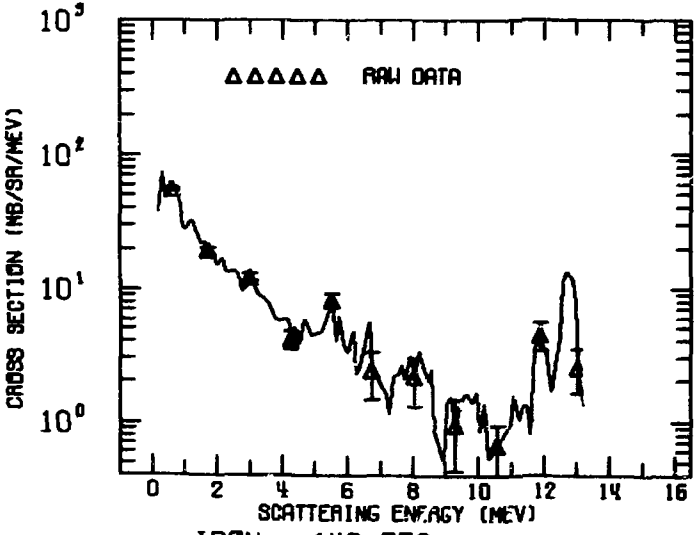

IRON - 140 DEG -

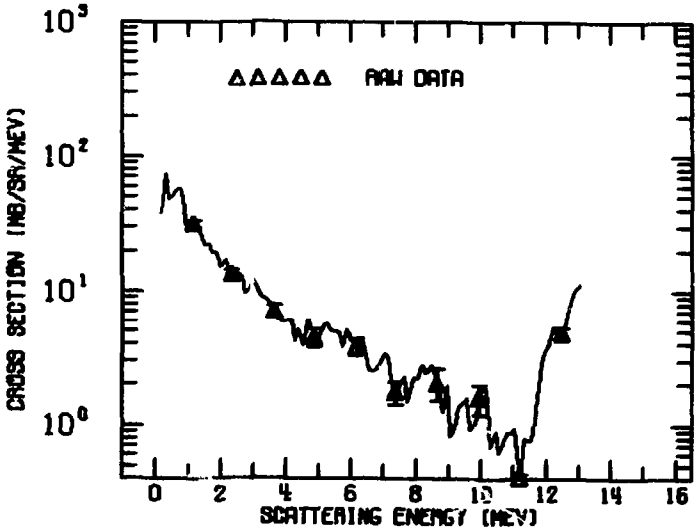

IRON - 145 DEG -

FIG. 54

IV.D. Nickel

The emission spectrum from natural nickel with 14-MeV neutrons incident was measured to check the behavior of the 2^+ level. The elastic angular distribution is shown in Fig. 55, and the entire set of measured emission spectra is shown in Figs. 56 through 58. Multiple scattering corrections, although insignificant, are shown. The data are also shown in a three dimensional oblique projection as Fig. 59. The curves in Figs. 56-59 connect points each 100 keV. The 2^+ level, which is a combination of scattering from the 1.45 MeV level in ^{58}Ni (67.9%) and the 1.33 MeV level in ^{60}Ni(26.2%), is clearly resolved.

Only high energy spectra were taken. The data are displayed again in Figs. 60 through 62 without the multiple scattering correction and with a 0.25 MeV bin size to improve statistics. The smoother curves of Figures 60 through 62 are generated by connecting points each 0.25 MeV. The experimental angular distribution of inelastic scattering from the first 2^+ levels in nickel is shown as Fig. 63. The measured elastic angular distribution compares favorably with the measurement of Bauer et al.[35] and Clarke et al.[36]

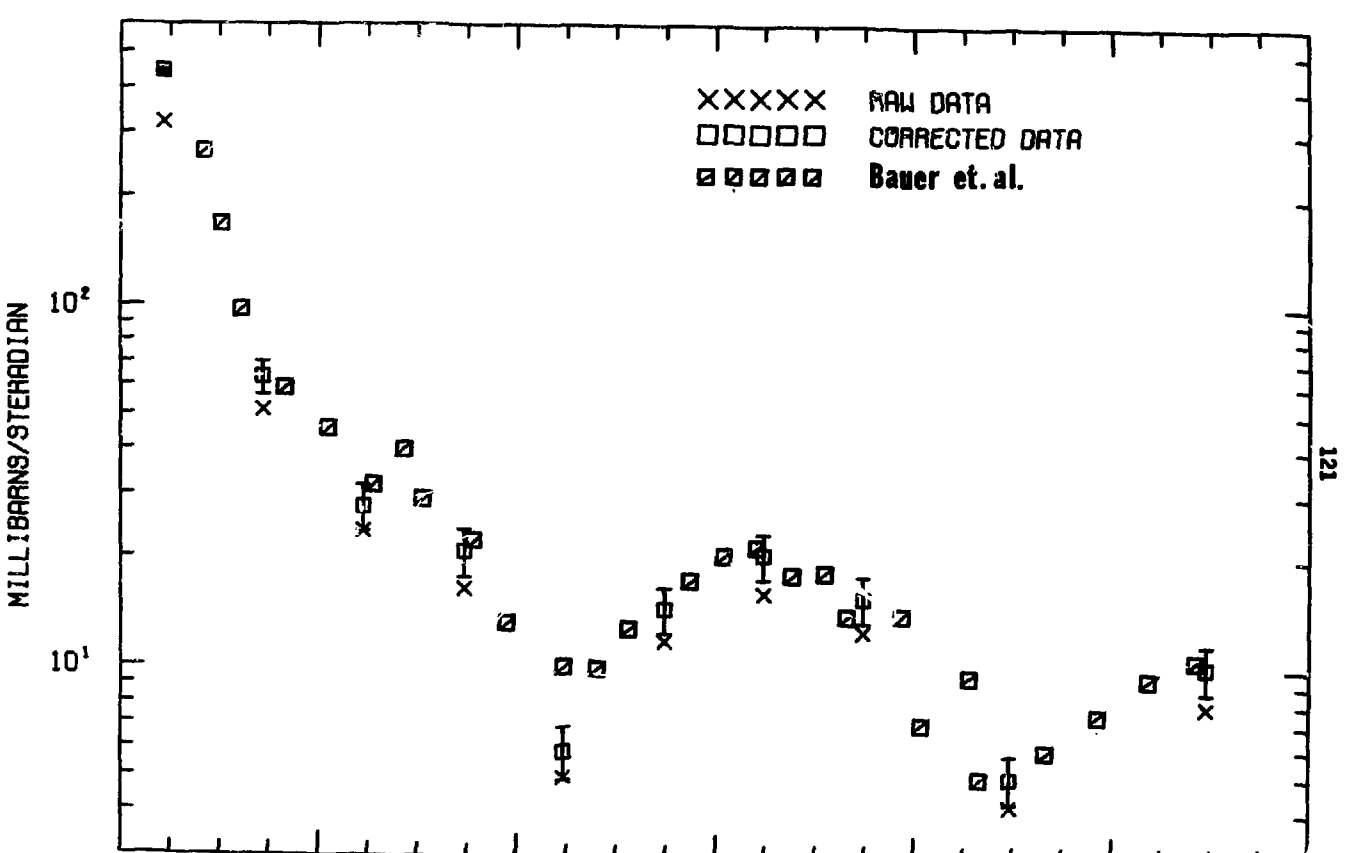

NICKEL ELASTIC SCATTERING

FIG. 55

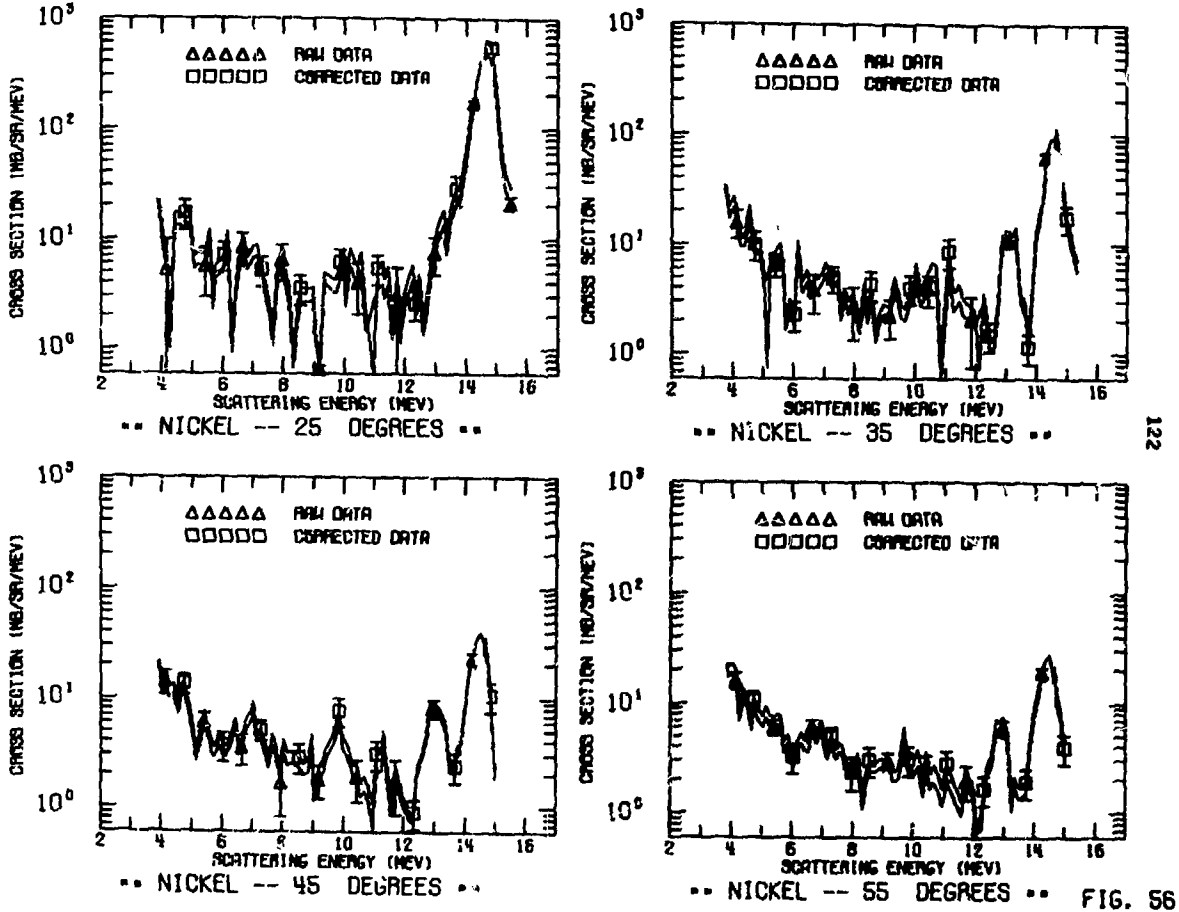
ΔΔΔΔΔ RAW DATA
□□□□□ CORRECTED DATA
CROSS SECTION (MB/SR/MEV)
SCATTERING ENERGY (MEV)
•• NICKEL -- 25 DEGREES ••
•• NICKEL -- 35 DEGREES ••
•• NICKEL -- 45 DEGREES ••
•• NICKEL -- 55 DEGREES ••

FIG. 56

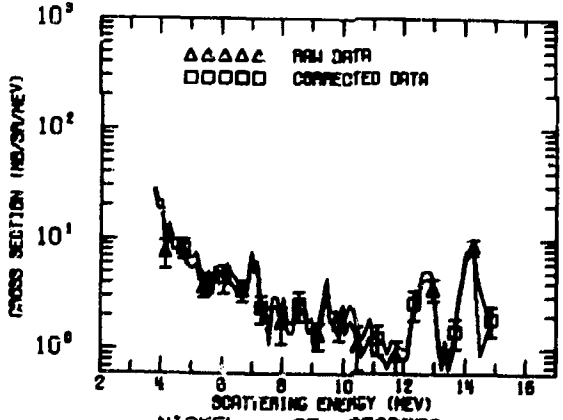

•• NICKEL -- 65 DEGREES ••

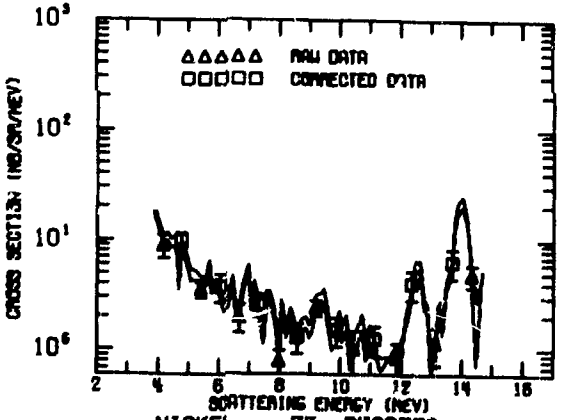

•• NICKEL -- 75 DEGREES ••

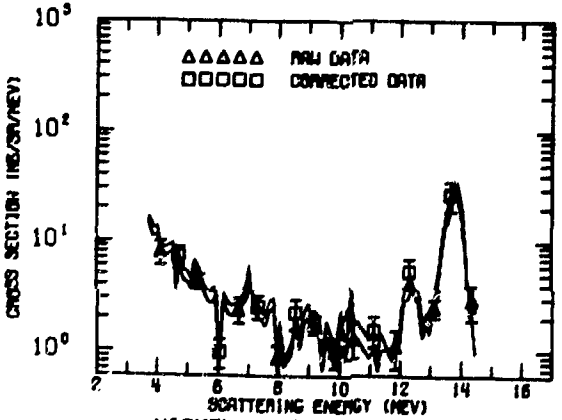

•• NICKEL -- 85 DEGREES ••

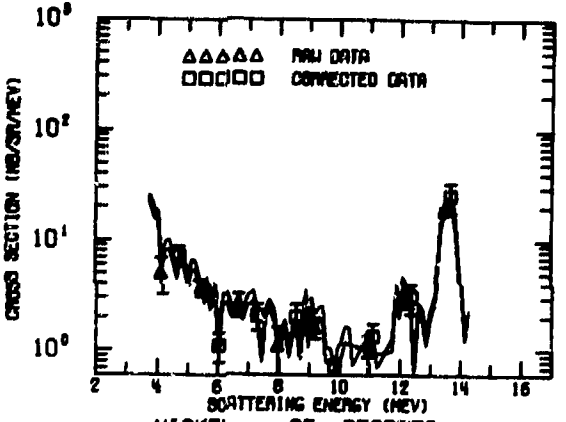

•• NICKEL -- 95 DEGREES ••

FIG. 57

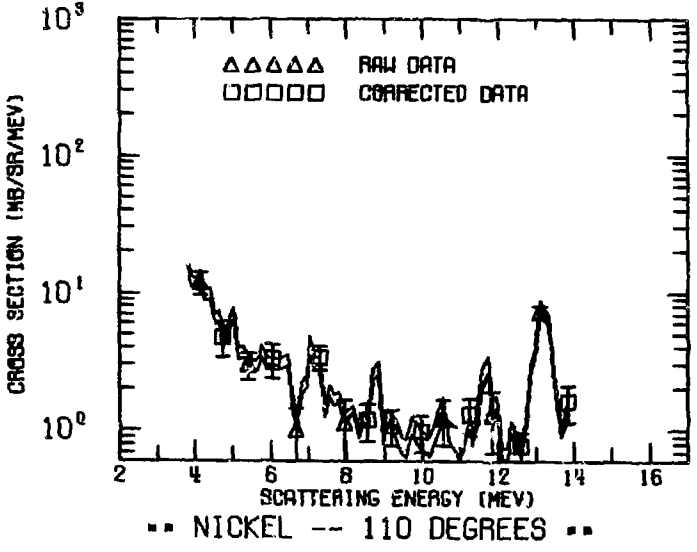
ΔΔΔΔΔ RAW DATA
□□□□□ CORRECTED DATA
CROSS SECTION (MB/SR/MEV)
SCATTERING ENERGY (MEV)
•• NICKEL -- 110 DEGREES ••

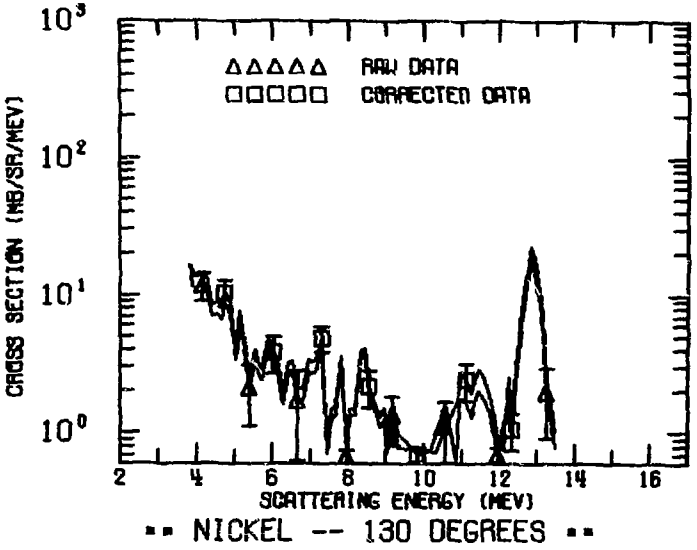
ΔΔΔΔΔ RAW DATA
□□□□□ CORRECTED DATA
CROSS SECTION (MB/SR/MEV)
SCATTERING ENERGY (MEV)
•• NICKEL -- 130 DEGREES ••

FIG. 58

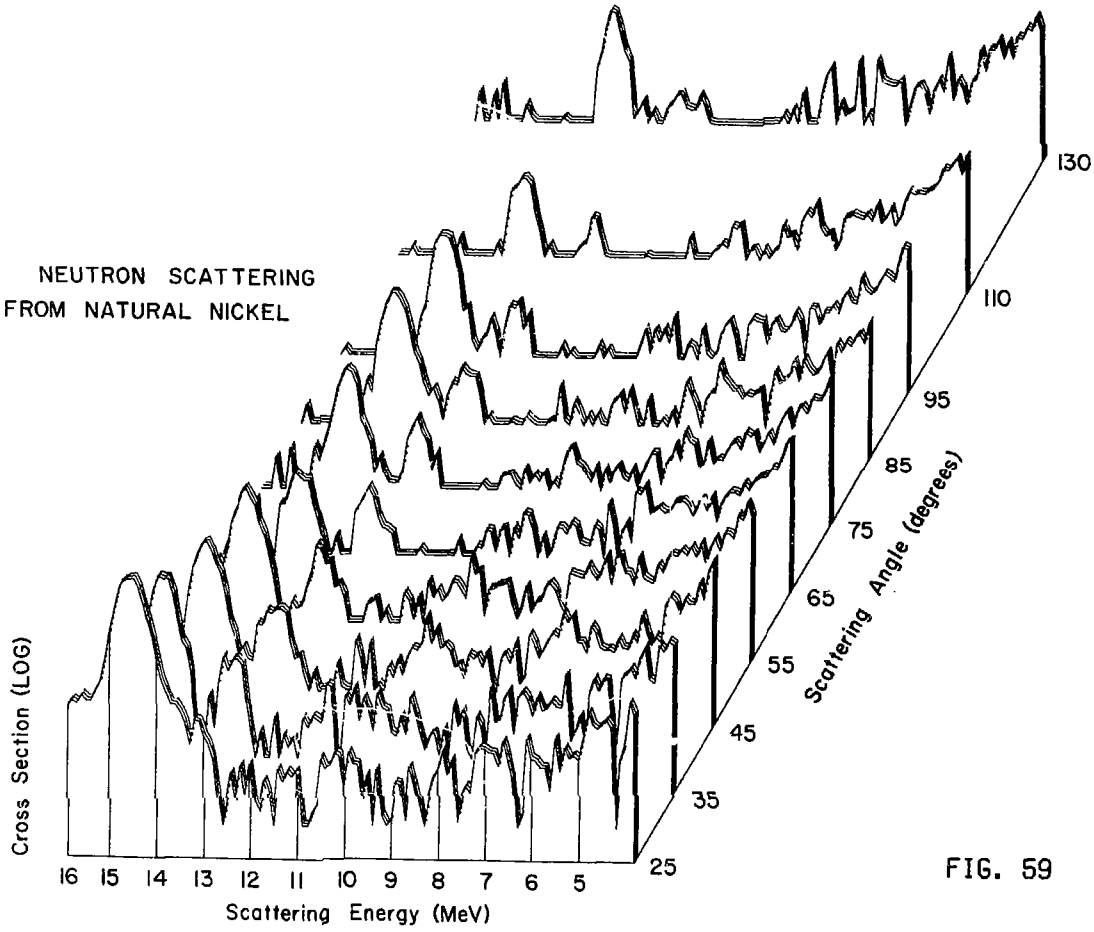
NEUTRON SCATTERING
FROM NATURAL NICKEL
Cross Section (LOG)
16 15 14 13 12 11 10 9 8 7 6 5
Scattering Energy (MeV)
25 35 45 55 65 75 85 95 110 130
Scattering Angle (degrees)

FIG. 59

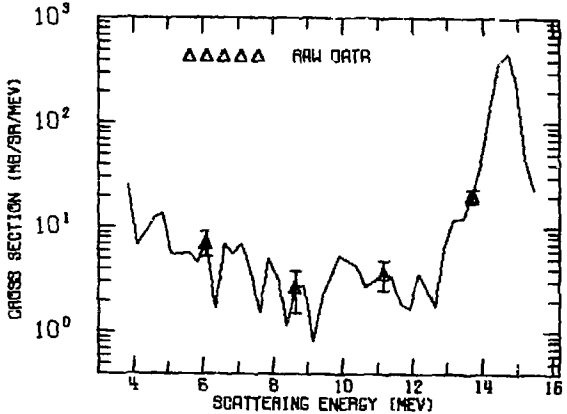

** NICKEL -- 25 DEGREE

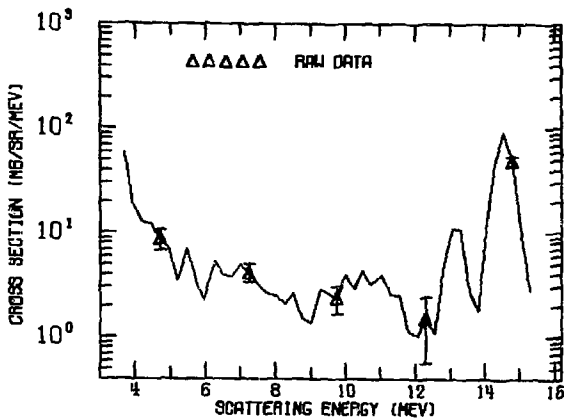

** NICKEL -- 35 DEGREE

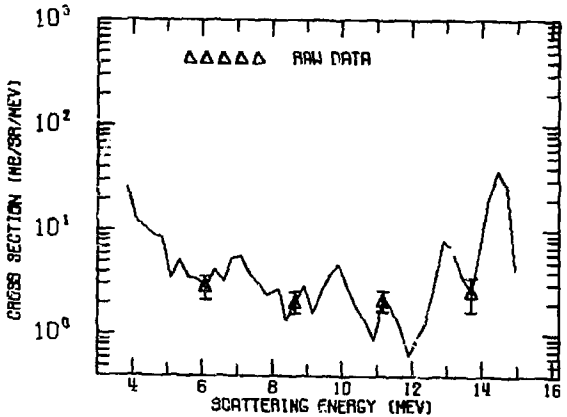

** NICKEL -- 45 DEGREE

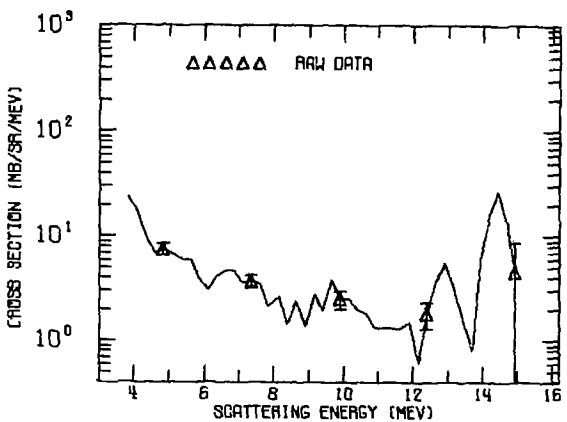

** NICKEL -- 55 DEGREE FIG. 60

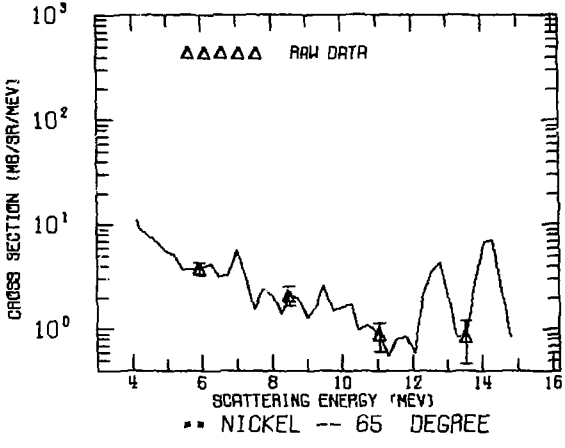

** NICKEL -- 65 DEGREE

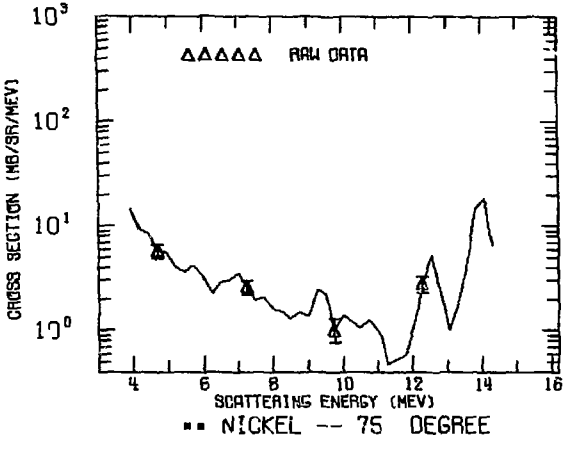

** NICKEL -- 75 DEGREE

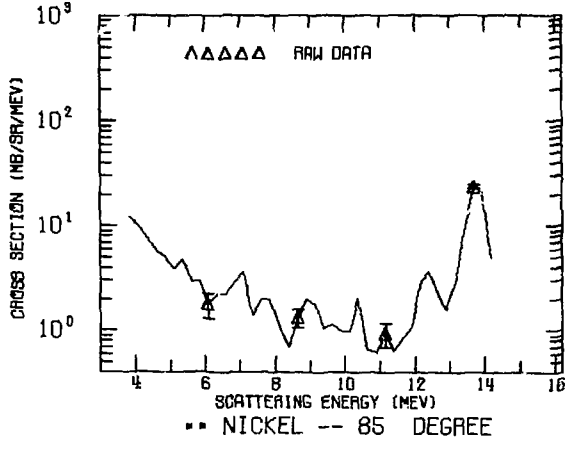

** NICKEL -- 85 DEGREE

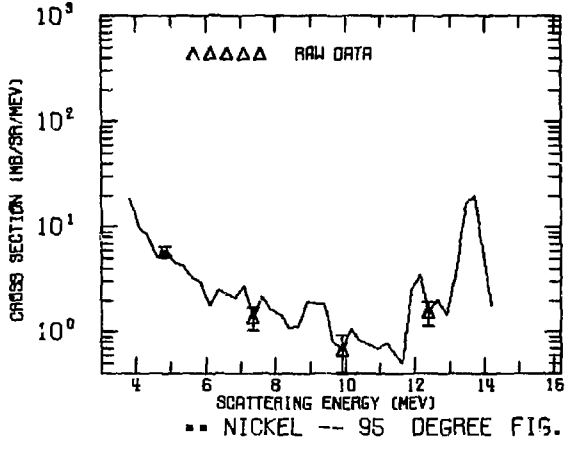

** NICKEL -- 95 DEGREE FIG. 61

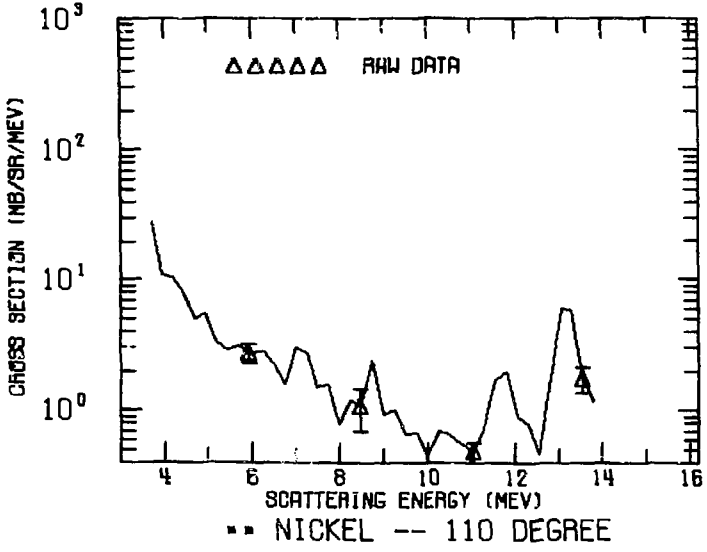
10^3
10^2
10^1
10^0
CROSS SECTION (MB/SR/MEV)
ΔΔΔΔΔ RAW DATA
4
6
8
10
12
14
16
SCATTERING ENERGY (MEV)
** NICKEL -- 110 DEGREE

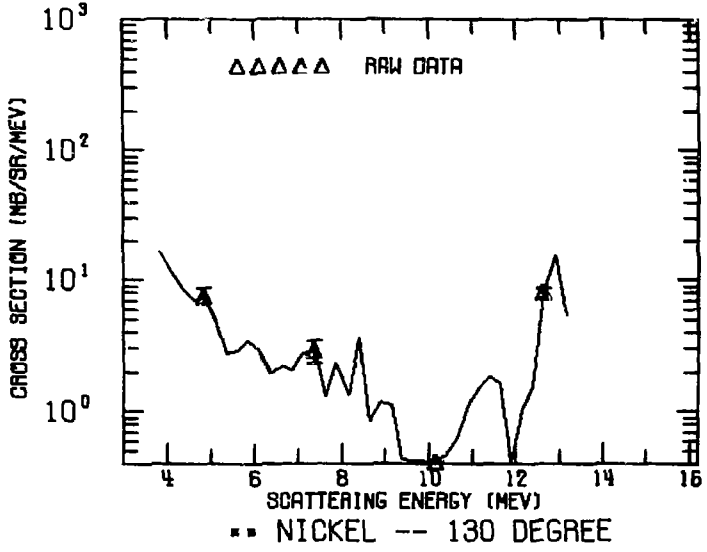
10^3
10^2
10^1
10^0
CROSS SECTION (MB/SR/MEV)
ΔΔΔΔΔ RAW DATA
4
6
8
10
12
14
16
SCATTERING ENERGY (MEV)
** NICKEL -- 130 DEGREE

FIG. 62

EXPERIMENTAL ANGULAR DISTRIBUTION SUMMED FOR THE 1.45 MEV LEVEL IN NI-58 AND THE 1.33 MEV LEVEL IN NI-60

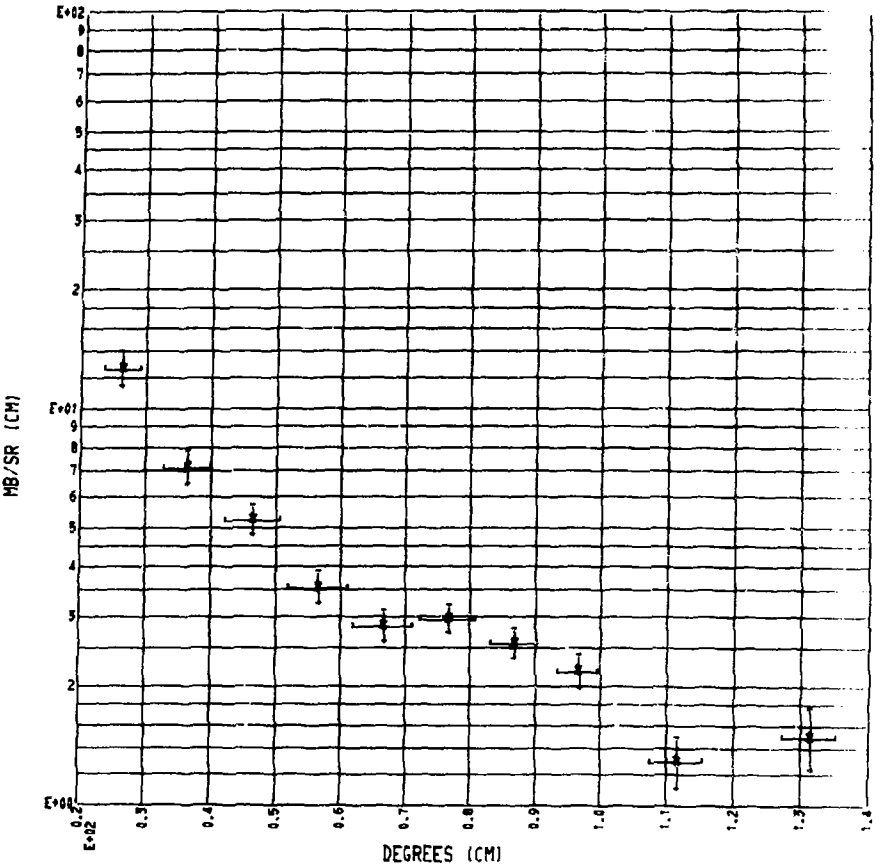

* NICKEL * Q-VALUE SUM BETWEEN -1.00 AND -2.00 MEV

FIG. 63

IV.E. Niobium

The probable use of niobium as the containment vessel for controlled thermonuclear reactors[37,38] has generated the need for measurements of 14 MeV neutrons scattering by natural niobium. The data presented in Figs. 64 through 70 fill that need.

A three dimensional oblique projection of the observed energy distributions at all angles for which data were taken is presented as Fig. 64. Data were summed and plotted in 100 keV bins. There are no clearly resolved levels because $^{93}_{41}Nb$ is an odd-even nucleus, but a considerable direct scattering cross section is observed.

The elastic angular distribution is extracted, corrected for flux attenuation and multiple scattering, and presented as Fig. 65, and the entire data set is presented as Figs. 66 through 70, where the cross section was summed into 0.5 MeV bins. No measurement was made of the emission spectra below 4 MeV.

The angular distributions from groups of levels between 1.50 and 9.00 MeV excitation are shown in Figs. 71 thru 75. Each plot covers a 1.5 MeV range in excitation energy.

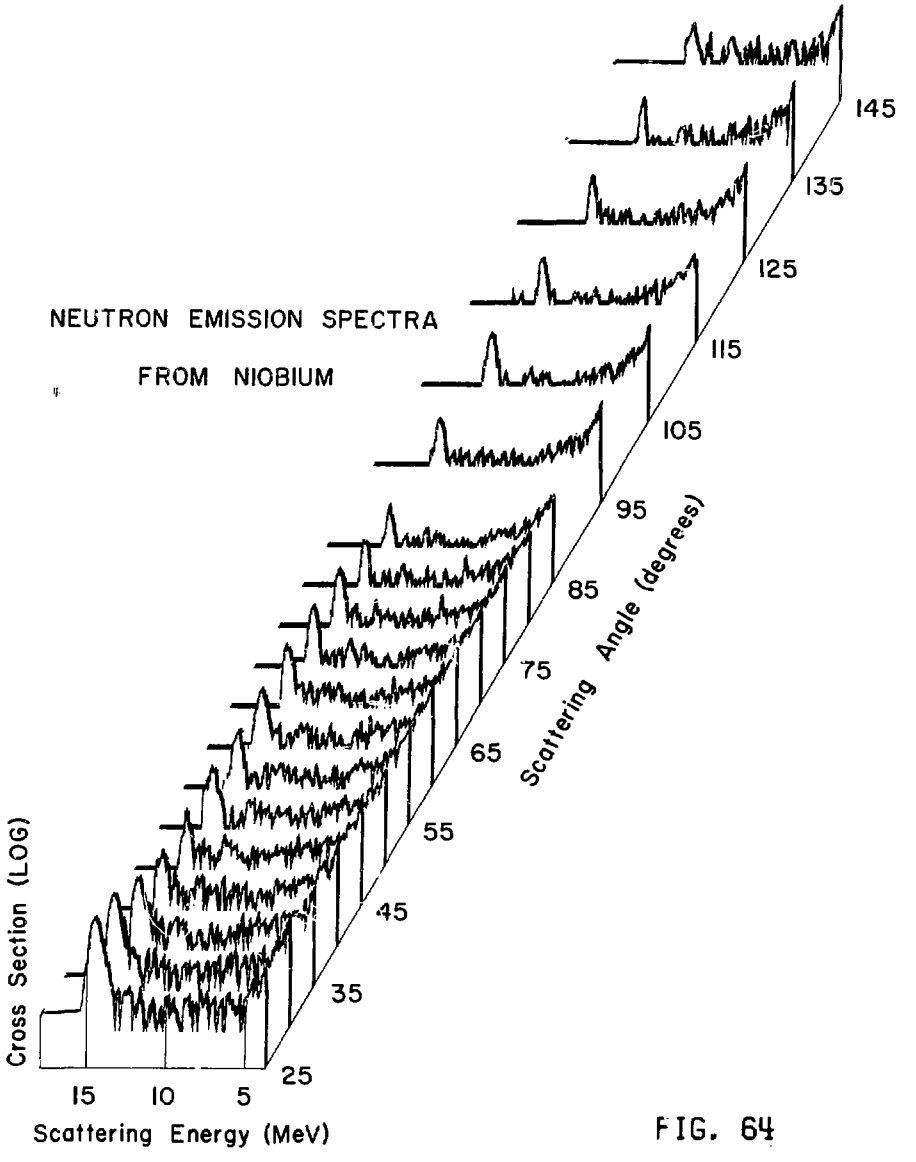
NEUTRON EMISSION SPECTRA
FROM NIOBIUM
Cross Section (LOG)
Scattering Energy (MeV)
15
10
5
Scattering Angle (degrees)
25
35
45
55
65
75
85
95
105
115
125
135
145

FIG. 64

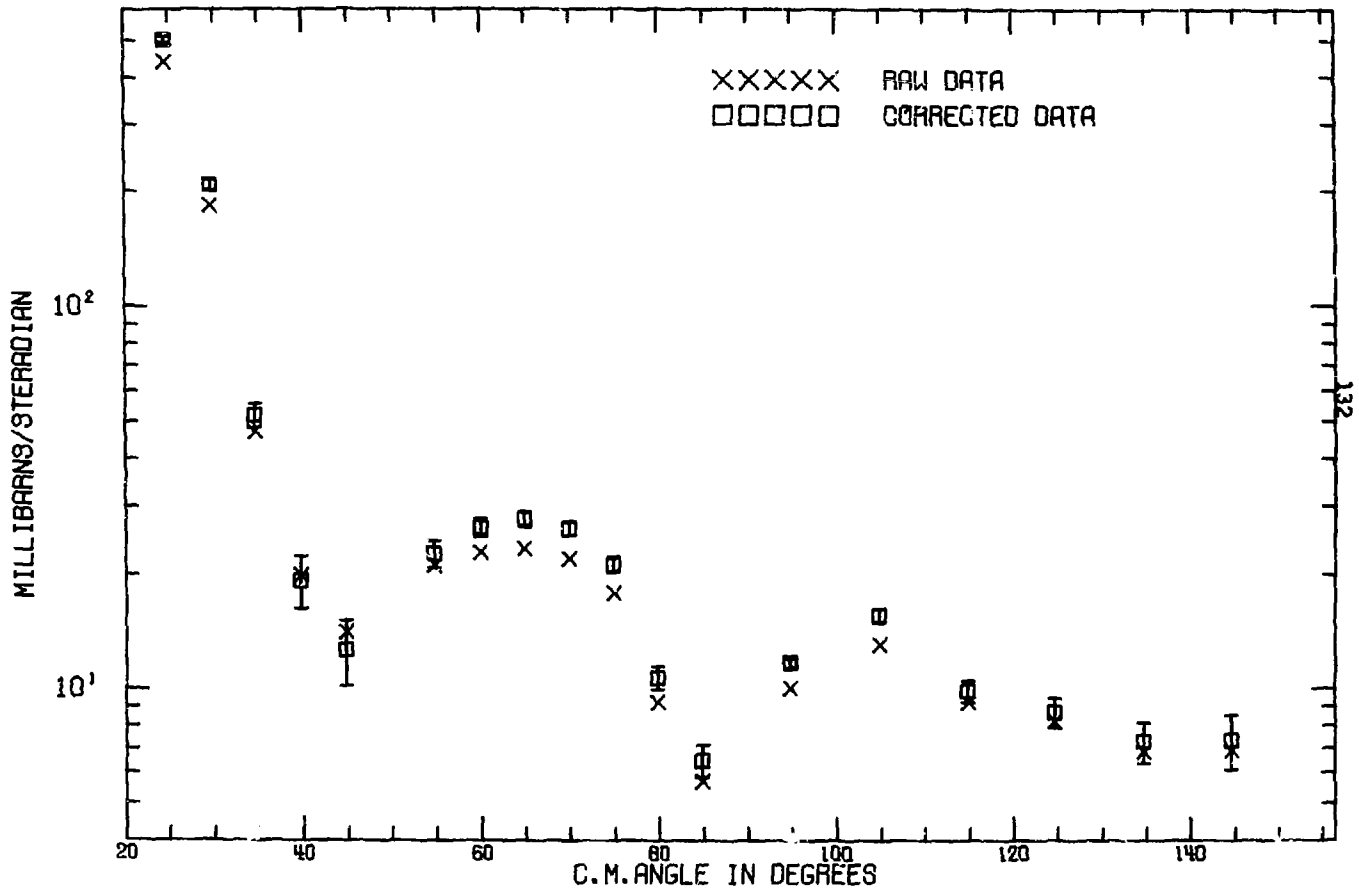

NIØBIUM ELASTIC SCATTERING

FIG. 65

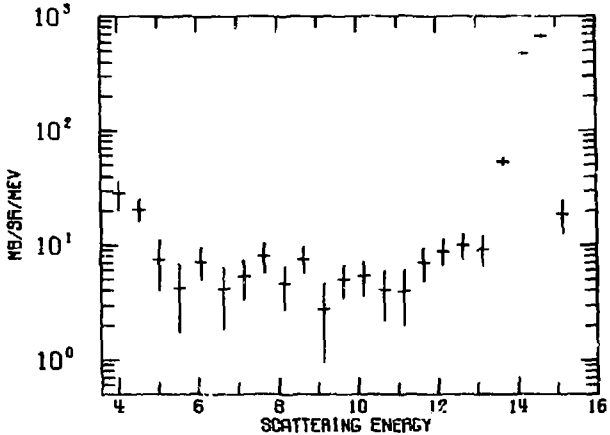
MB/SR/MEV
SCATTERING ENERGY
•• NIOBIUM -- 25 DEGREES ••

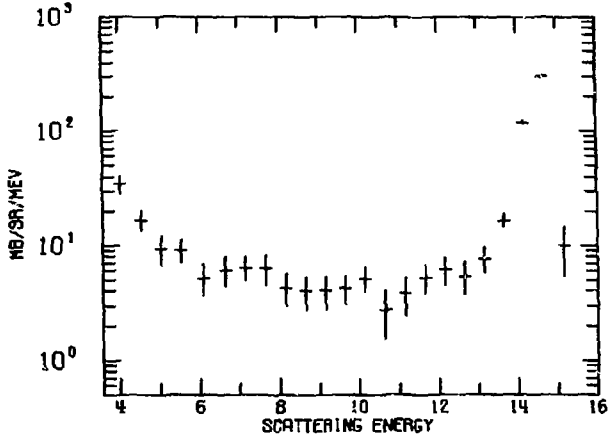
MB/SR/MEV
SCATTERING ENERGY
•• NIOBIUM -- 30 DEGREES ••

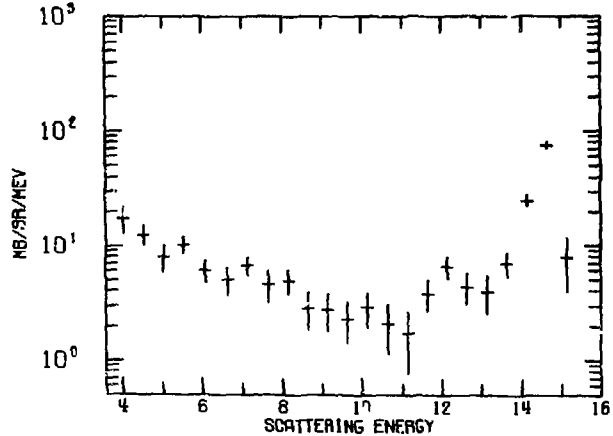
MB/SR/MEV
SCATTERING ENERGY
•• NIOBIUM -- 35 DEGREES ••

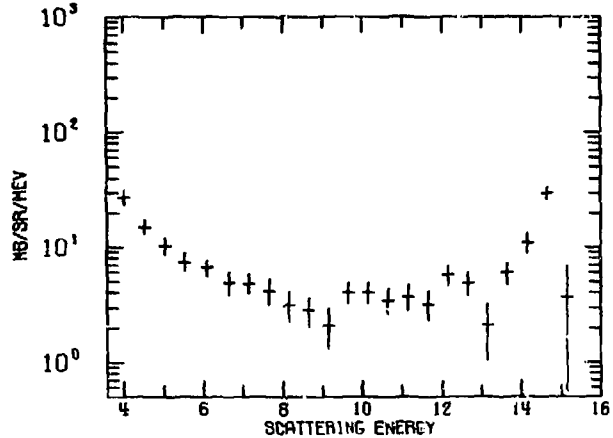
MB/SR/MEV
SCATTERING ENERGY
•• NIOBIUM -- 40 DEGREES ••

FIG. 66

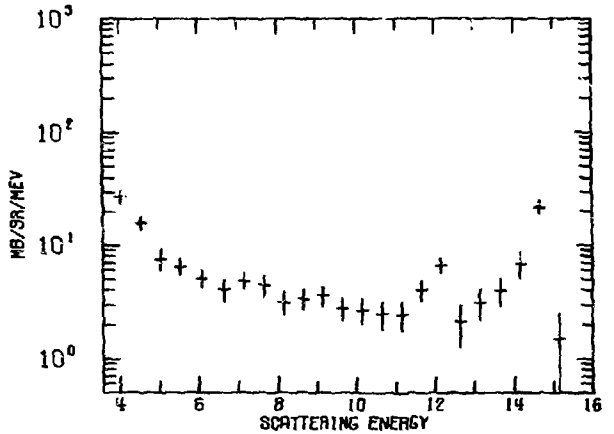

** NIOBIUM -- 45 DEGREES **

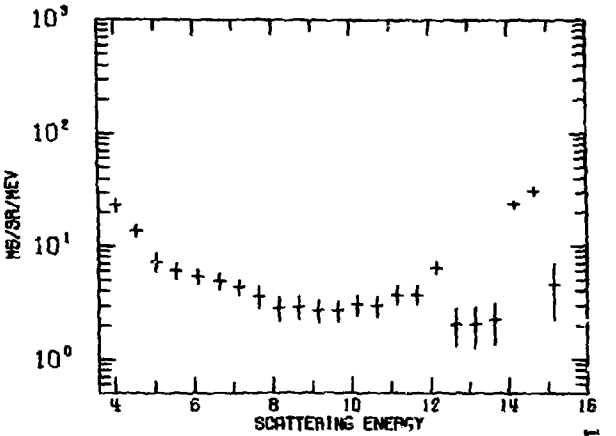

** NIOBIUM -- 50 DEGREES **

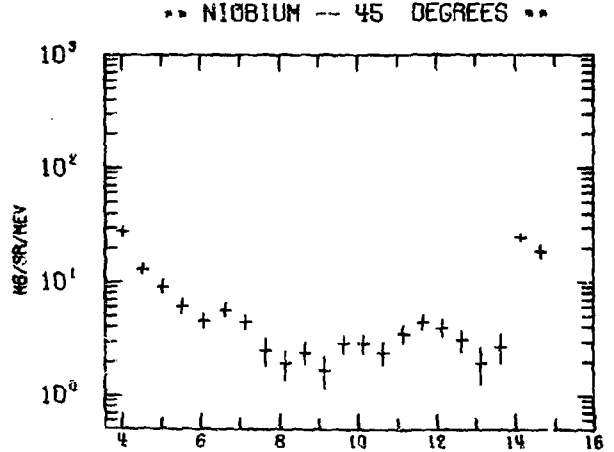

** NIOBIUM -- 55 DEGREES **

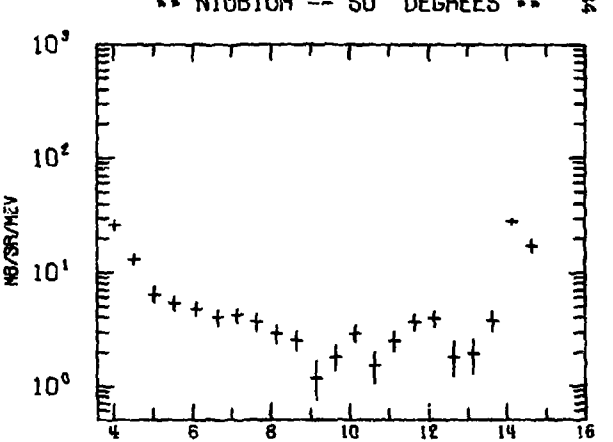

** NIOBIUM -- 60 DEGREES FIG. 67

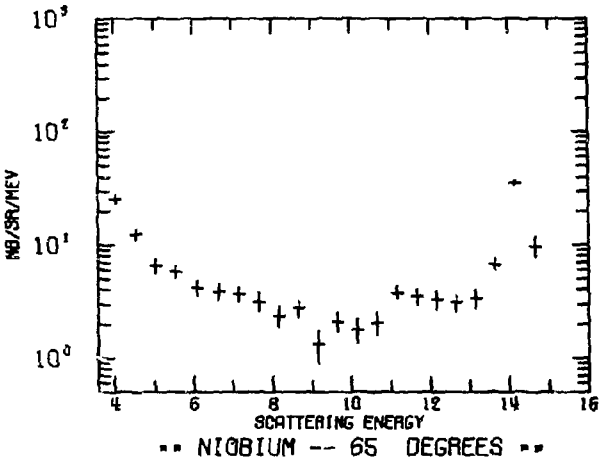

** NIOBIUM -- 65 DEGREES **

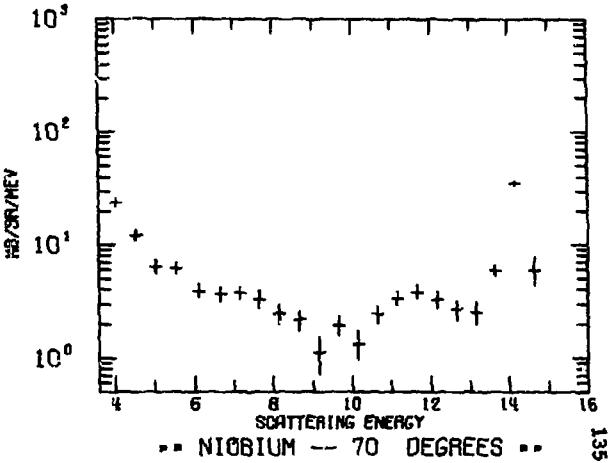

** NIOBIUM -- 70 DEGREES **

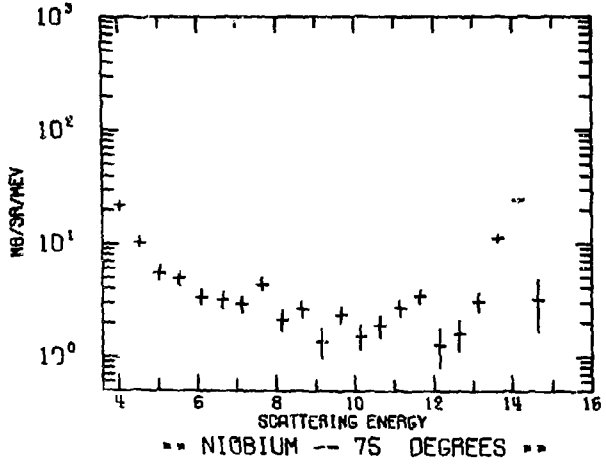

** NIOBIUM -- 75 DEGREES **

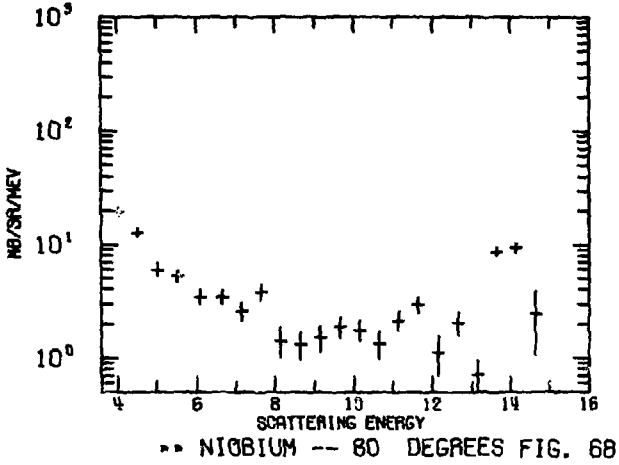

** NIOBIUM -- 80 DEGREES FIG. 68

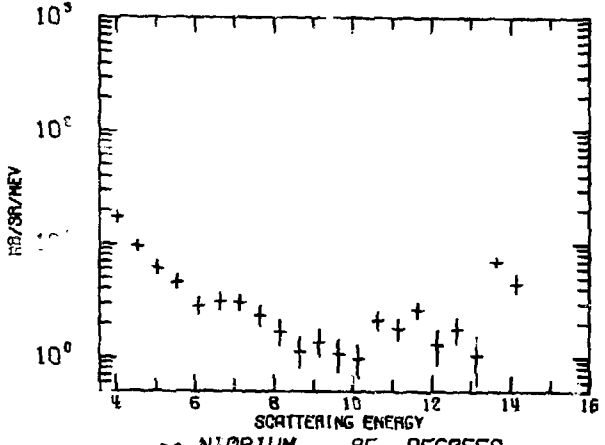

** NIOBIUM -- 85 DEGREES **

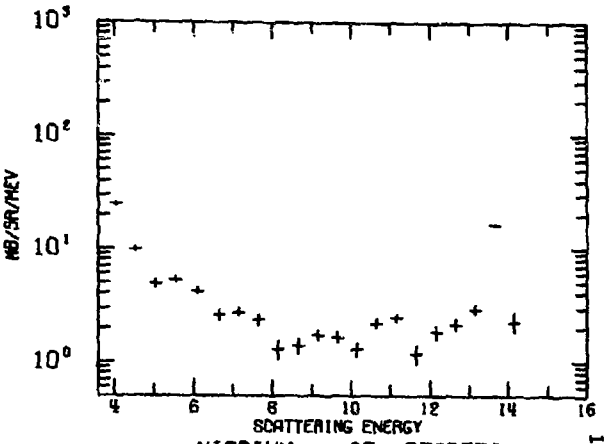

** NIOBIUM -- 95 DEGREES **

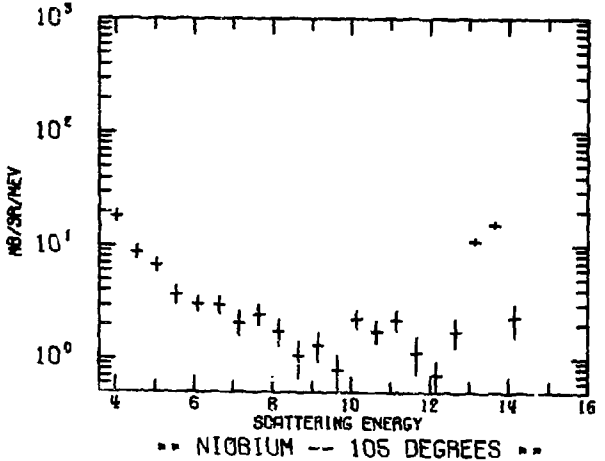

** NIOBIUM -- 105 DEGREES **

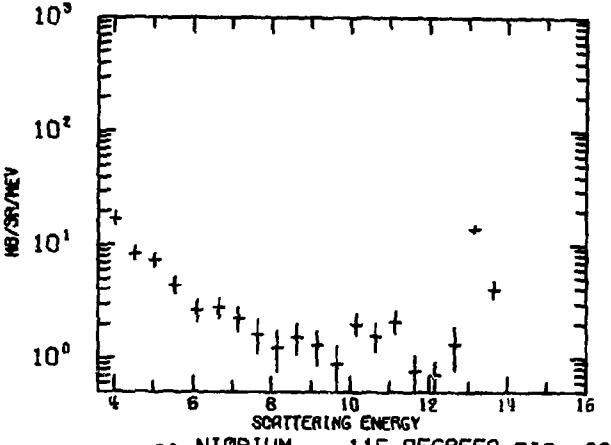

** NIOBIUM -- 115 DEGREES FIG. 69

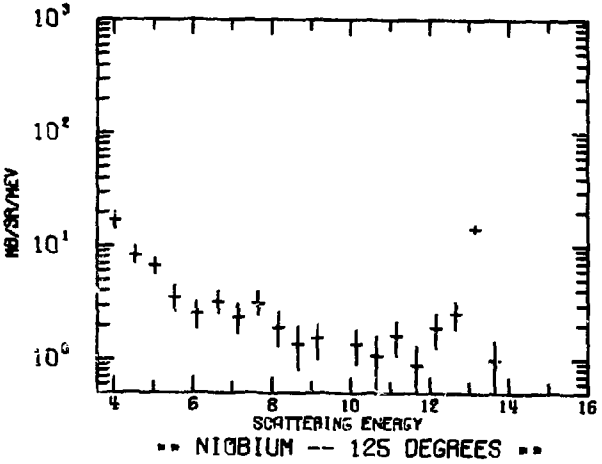
MB/SR/MEV
SCATTERING ENERGY
** NIOBIUM -- 125 DEGREES **

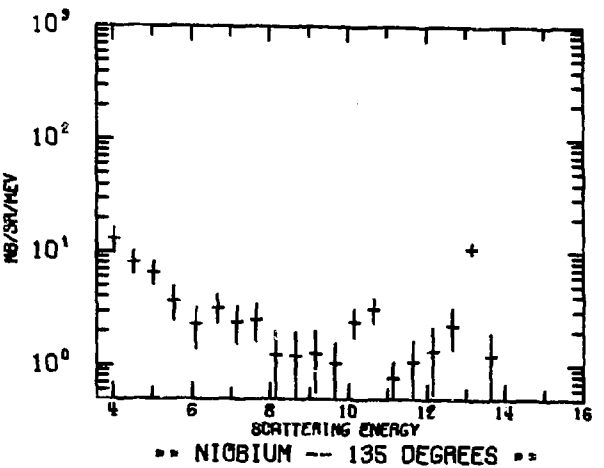
MB/SR/MEV
SCATTERING ENERGY
** NIOBIUM -- 135 DEGREES **

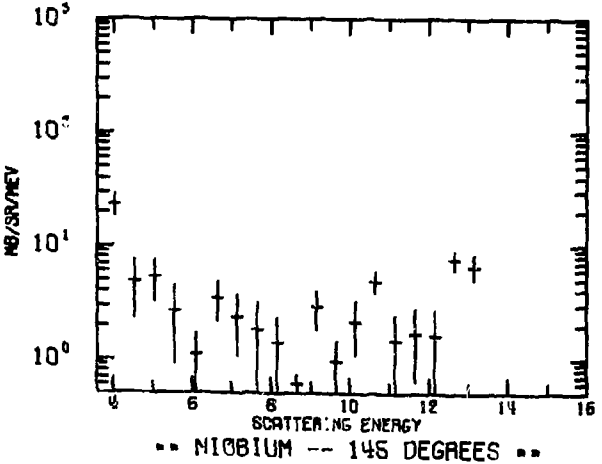
MB/SR/MEV
SCATTERING ENERGY
** NIOBIUM -- 145 DEGREES **

FIG. 70

EXPERIMENTAL ANGULAR DISTRIBUTION

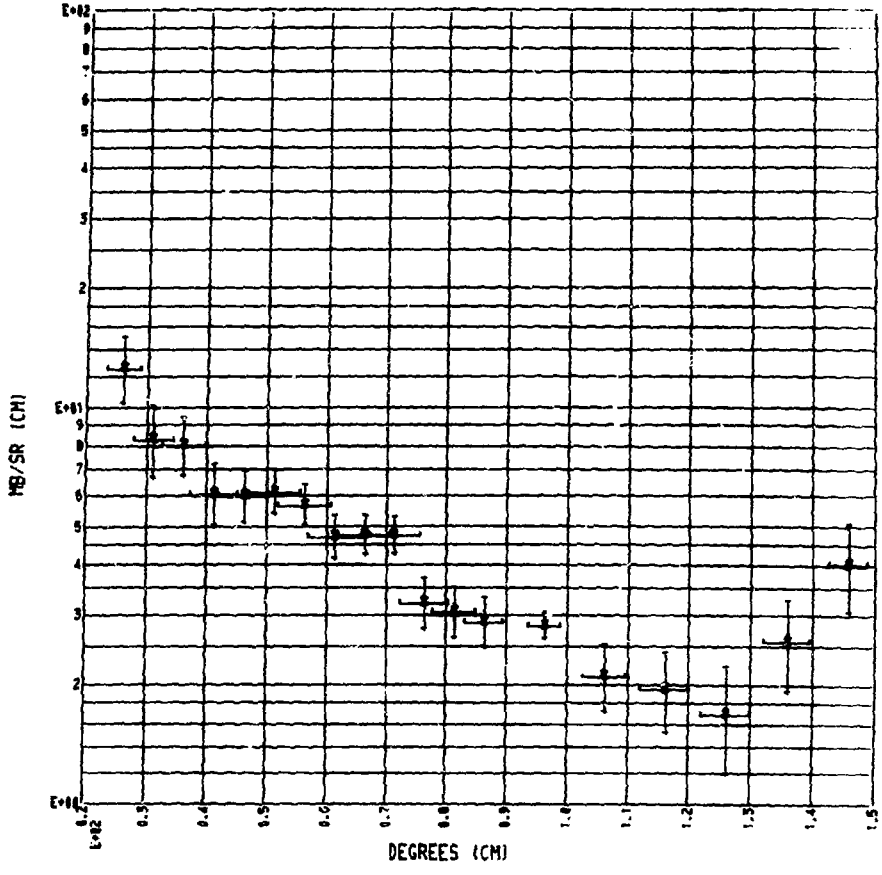

** NIOBIUM * Q-VALUE SUM BETWEEN -1.50 AND -3.00 MEV

FIG. 71

EXPERIMENTAL ANGULAR DISTRIBUTION

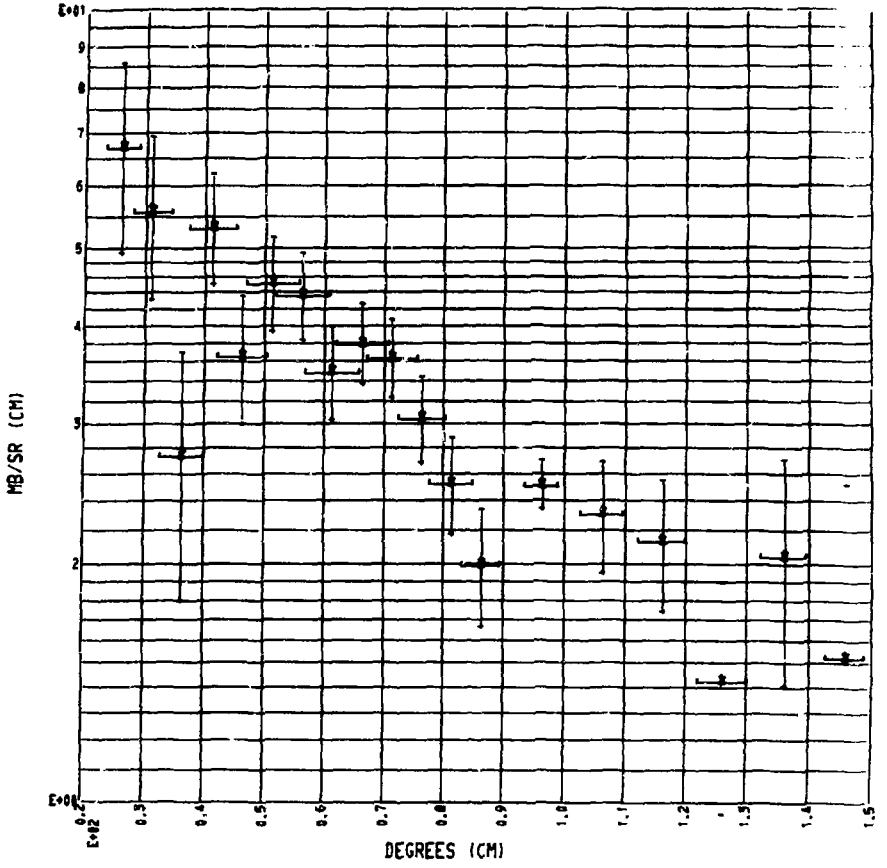

** NIOBIUM * Q-VALUE SUM BETWEEN -3.00 AND -4.50 MEV -

FIG. 72

EXPERIMENTAL ANGULAR DISTRIBUTION

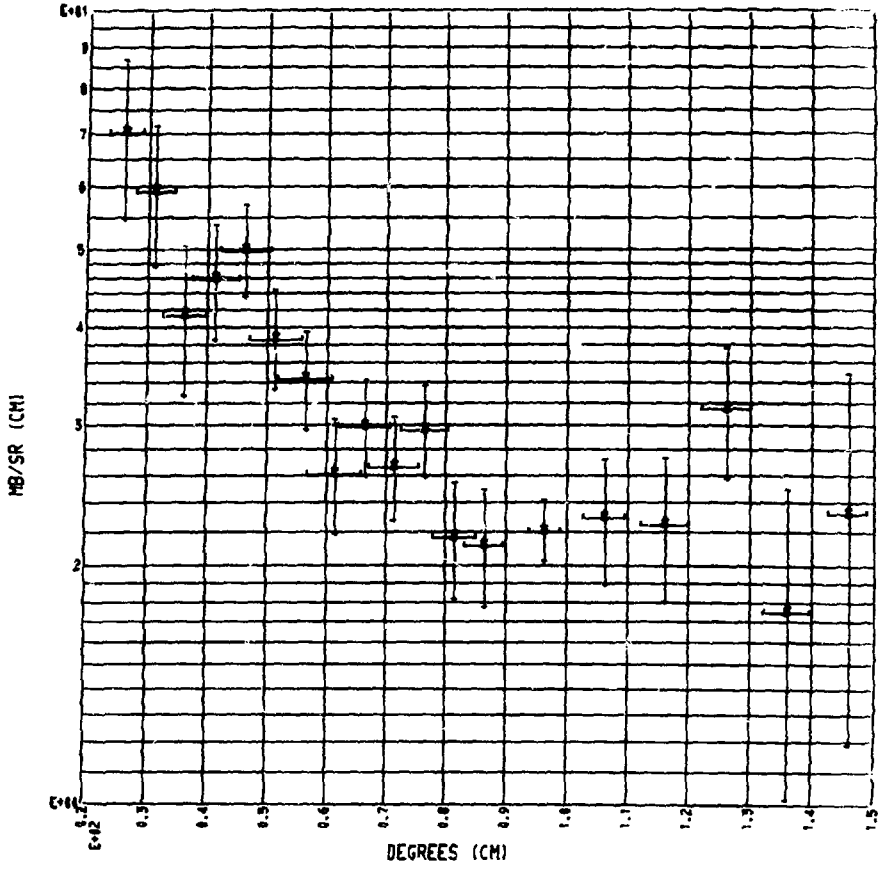

** NIOBIUM * Q-VALUE SUM BETWEEN -4.50 AND -6.00 MEV

FIG. 73

EXPERIMENTAL ANGULAR DISTRIBUTION

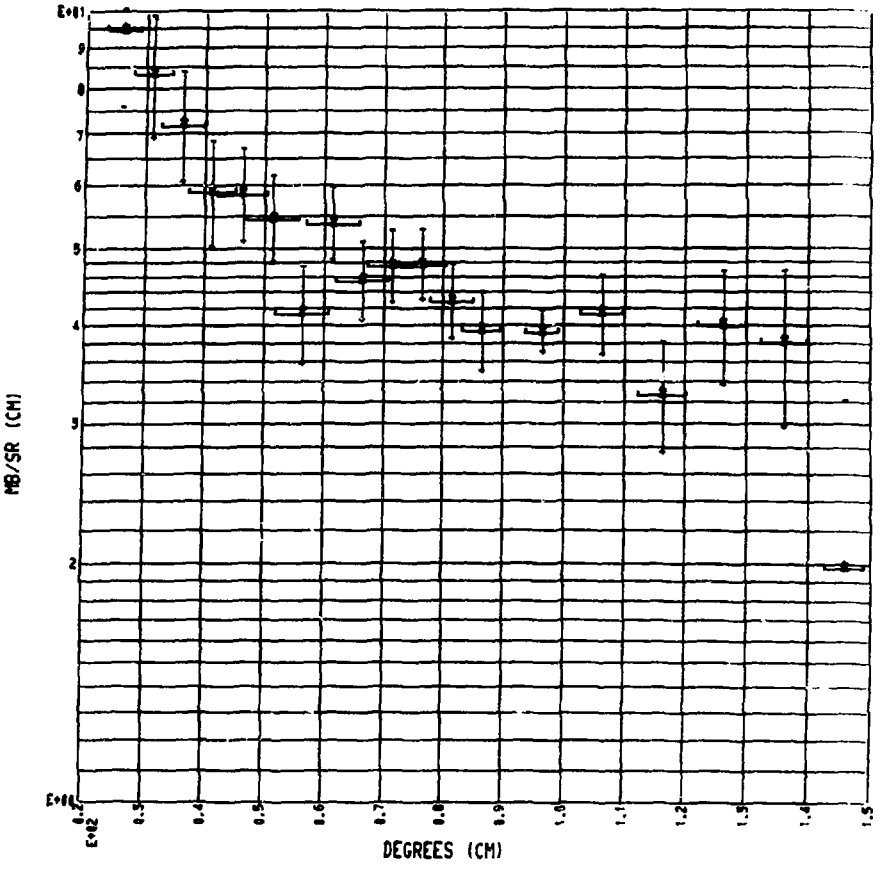

** NIOBIUM * Q-VALUE SUM BETWEEN -6.00 AND -7.50 MEV -

FIG. 74

EXPERIMENTAL ANGULAR DISTRIBUTION

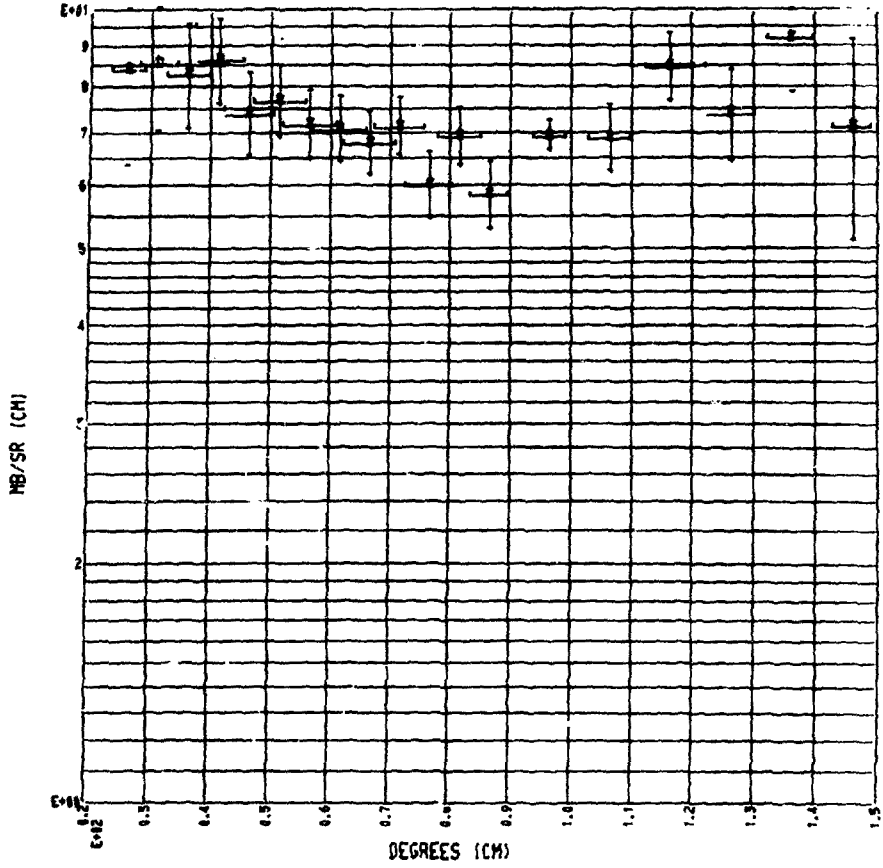

** NIOBIUM * Q-VALUE SUM BETWEEN -7.50 AND -9.00 MEV

FIG. 75

IV.F. Lead

Lead data were taken as a natural prelude to the fissionable isotopes. Although the scattering phenomena of this isotope are well known[10,32,39] the data are presented here because of the excellent resolution.

Fig. 76 is the extracted elastic angular distribution and Figs. 77 through 80 contain the complete data set. Each curve is a combination of high and medium energy data. Several levels and groups of levels are resolved. The 2.6 MeV level is especially noticeable.

Fig. 81 is an oblique projection of data taken in the early stages of experimentation when the resolution was 3 nsec FWHM. It is presented as a graphical display technique which was later modified to the type display shown in Fig. 64.

The angular distribution from the levels between 1.80 and 3.30 MeV excitation in natural lead are shown in Fig. 82. The 3^- levels at 2.60 MeV in ^{208}Pb and ^{206}Pb dominate in this range of excitation energies. Fig. 83 shows the angular distribution of a group of levels observed near 4.50 MeV. Figs. 84 and 85 depict the angular distribution of groups of levels at higher excitation energy.

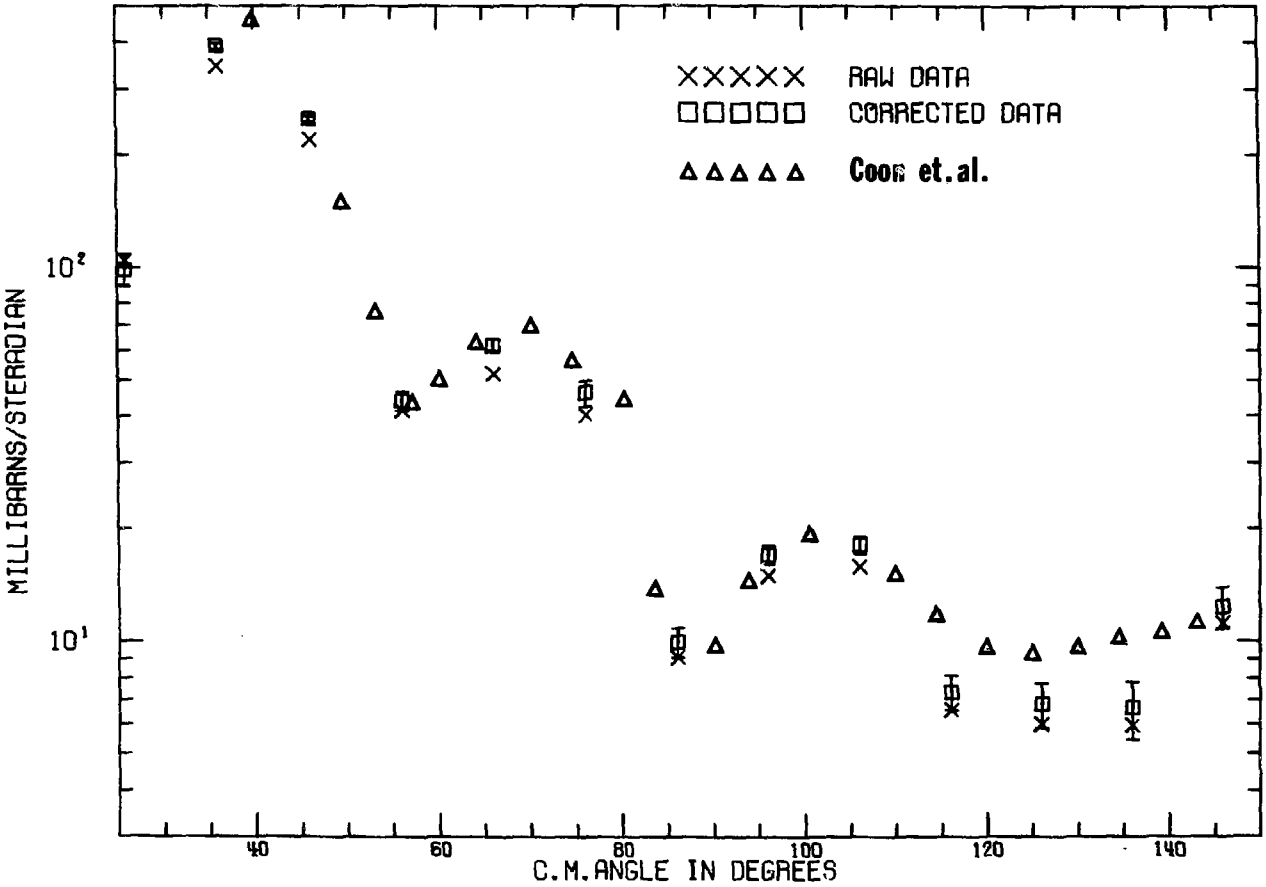

NATURAL LEAD ELASTIC SCATTERIN

FIG. 76

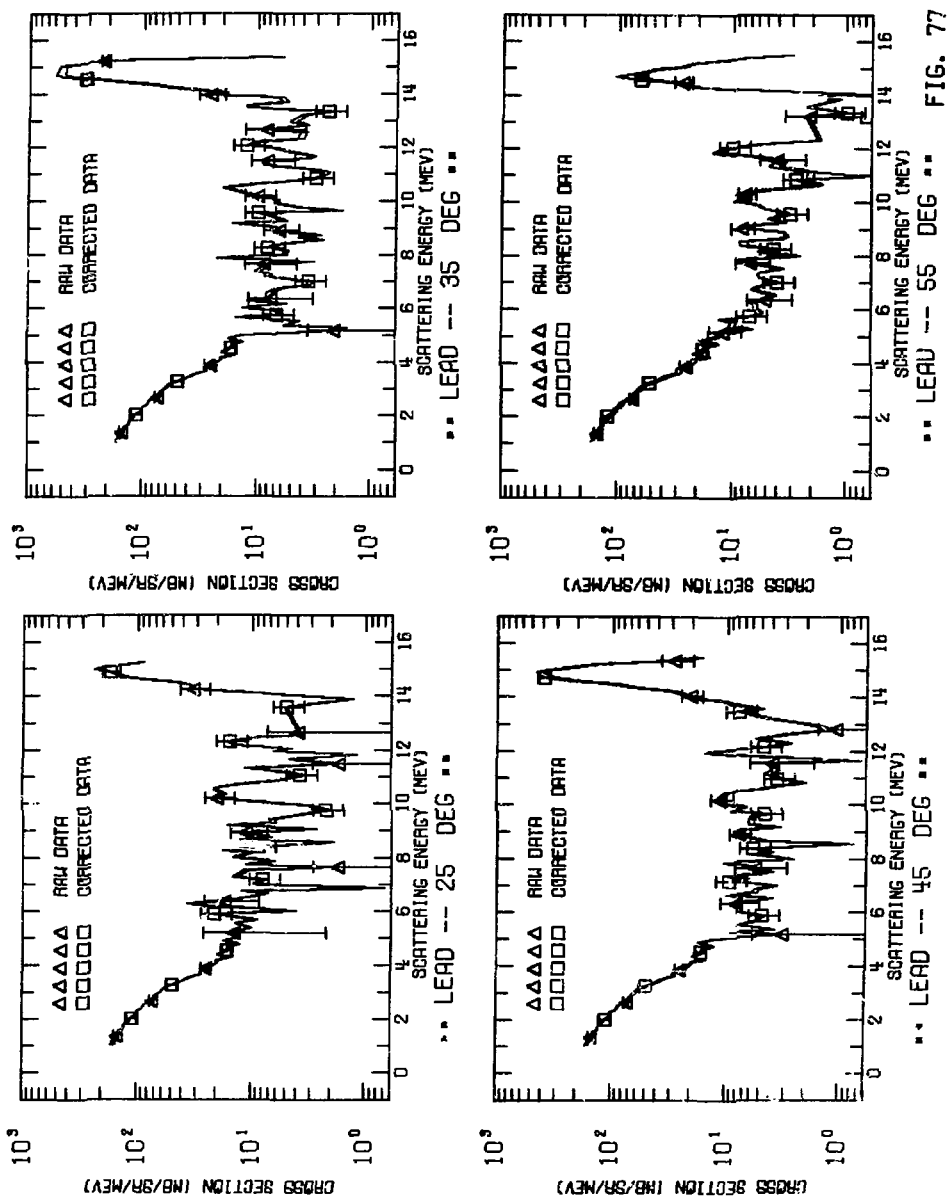
ΔΔΔΔΔ RAW DATA
□□□□□ CORRECTED DATA
CROSS SECTION (MB/SR/MEV)
SCATTERING ENERGY (MEV)
** LEAD -- 25 DEG **
** LEAD -- 35 DEG **
** LEAD -- 45 DEG **
** LEAD -- 55 DEG **

FIG. 77

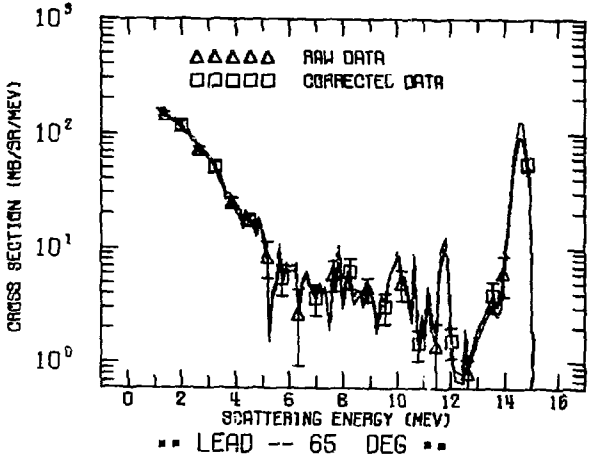
ΔΔΔΔΔ RAW DATA
□□□□□ CORRECTED DATA
CROSS SECTION (MB/SR/MEV)
SCATTERING ENERGY (MEV)
** LEAD -- 65 DEG **

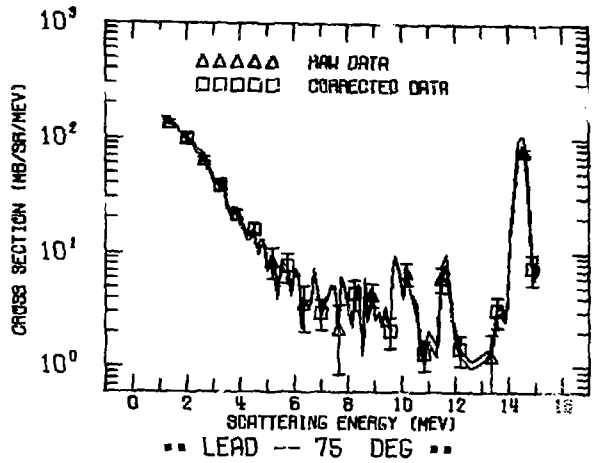
ΔΔΔΔΔ RAW DATA
□□□□□ CORRECTED DATA
CROSS SECTION (MB/SR/MEV)
SCATTERING ENERGY (MEV)
** LEAD -- 75 DEG **

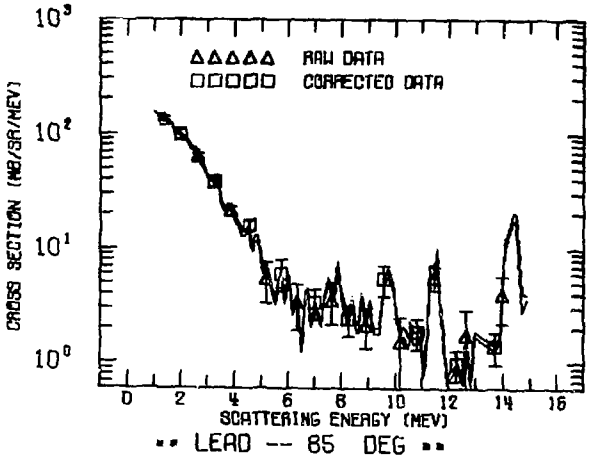
ΔΔΔΔΔ RAW DATA
□□□□□ CORRECTED DATA
CROSS SECTION (MB/SR/MEV)
SCATTERING ENERGY (MEV)
** LEAD -- 85 DEG **

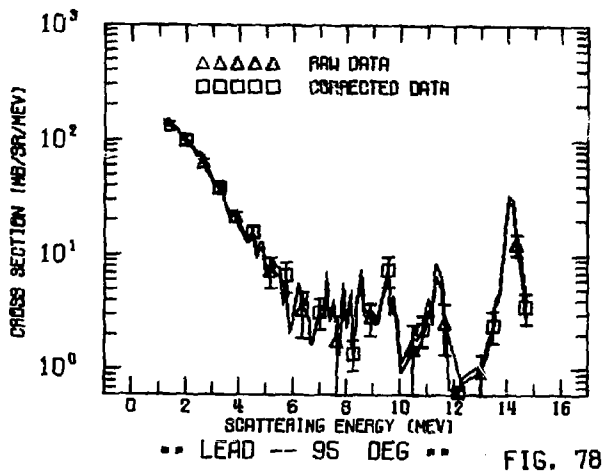
ΔΔΔΔΔ RAW DATA
□□□□□ CORRECTED DATA
CROSS SECTION (MB/SR/MEV)
SCATTERING ENERGY (MEV)
** LEAD -- 95 DEG **

FIG. 78

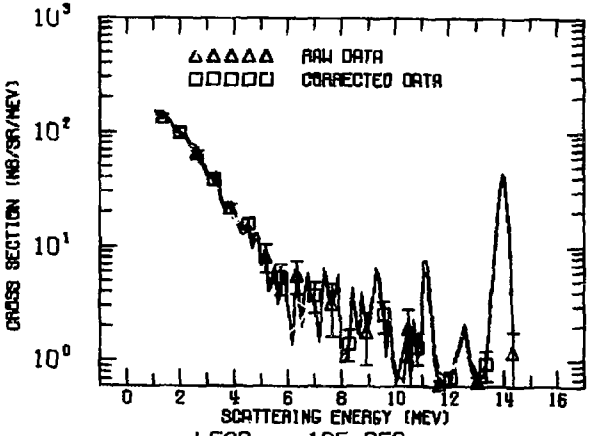
ΔΔΔΔΔ RAW DATA
□□□□□ CORRECTED DATA
CROSS SECTION (MB/SR/MEV)
SCATTERING ENERGY (MEV)
** LEAD -- 105 DEG **

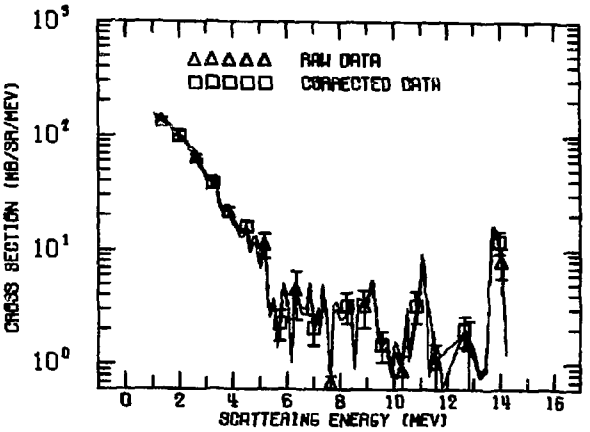
ΔΔΔΔΔ RAW DATA
□□□□□ CORRECTED DATA
CROSS SECTION (MB/SR/MEV)
SCATTERING ENERGY (MEV)
** LEAD -- 115 DEG **

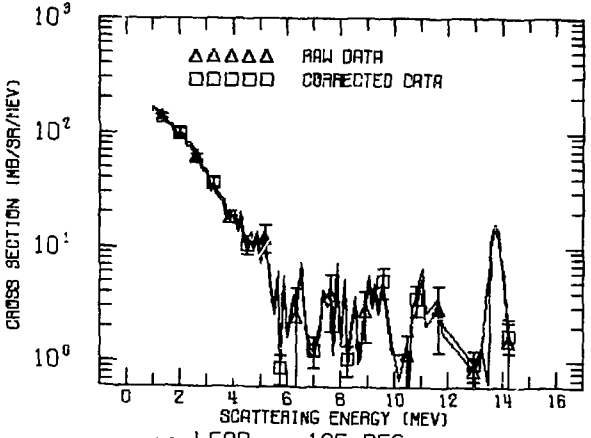
ΔΔΔΔΔ RAW DATA
□□□□□ CORRECTED DATA
CROSS SECTION (MB/SR/MEV)
SCATTERING ENERGY (MEV)
** LEAD -- 125 DEG **

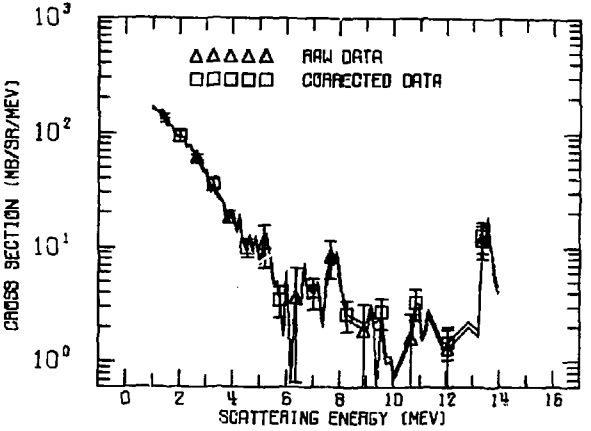
ΔΔΔΔΔ RAW DATA
□□□□□ CORRECTED DATA
CROSS SECTION (MB/SR/MEV)
SCATTERING ENERGY (MEV)
** LEAD -- 135 DEG **

FIG. 79

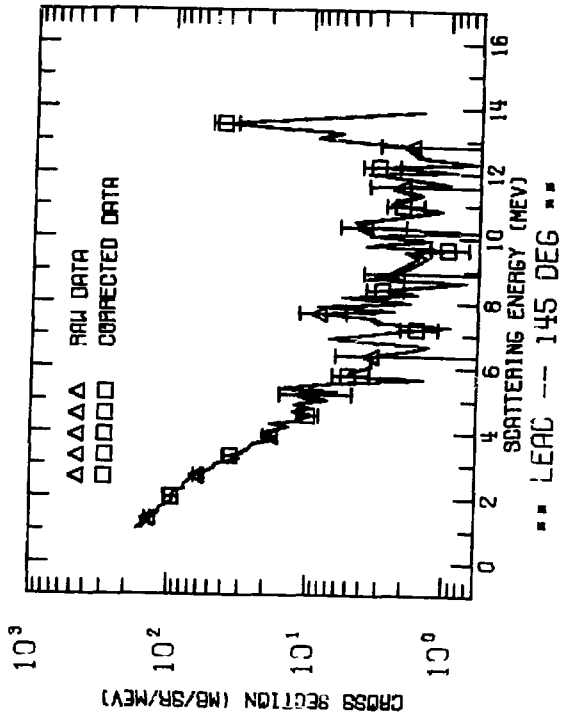
ΔΔΔΔΔ RAW DATA
□□□□□ CORRECTED DATA
** LEAD -- 145 DEG **
SCATTERING ENERGY (MEV)
CROSS SECTION (MB/SR/MEV)
10^3
10^2
10^1
10^0
0
2
4
6
8
10
12
14
16

FIG. 80

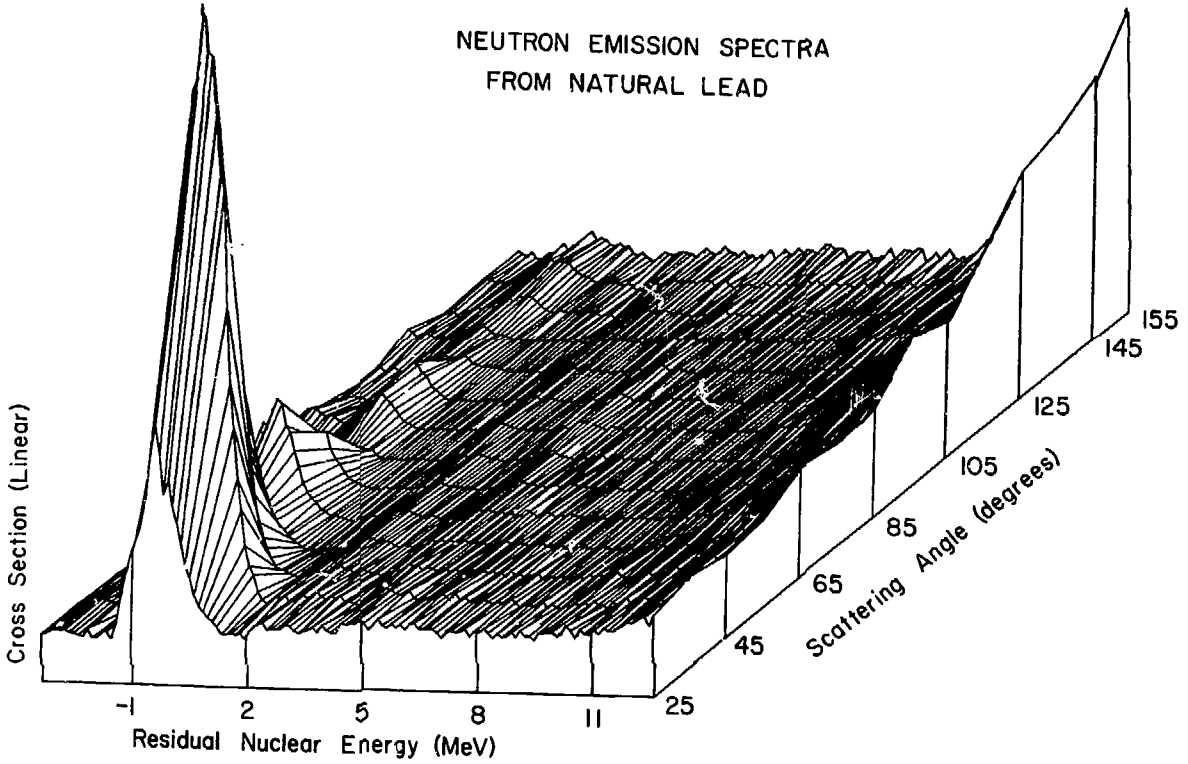
NEUTRON EMISSION SPECTRA
FROM NATURAL LEAD
Cross Section (Linear)
-1
2
5
8
11
Residual Nuclear Energy (MeV)
25
45
65
85
105
125
145
155
Scattering Angle (degrees)

FIG. 81

EXPERIMENTAL ANGULAR DISTRIBUTION FROM THE 2.6 MEV LEVEL IN NATURAL LEAD

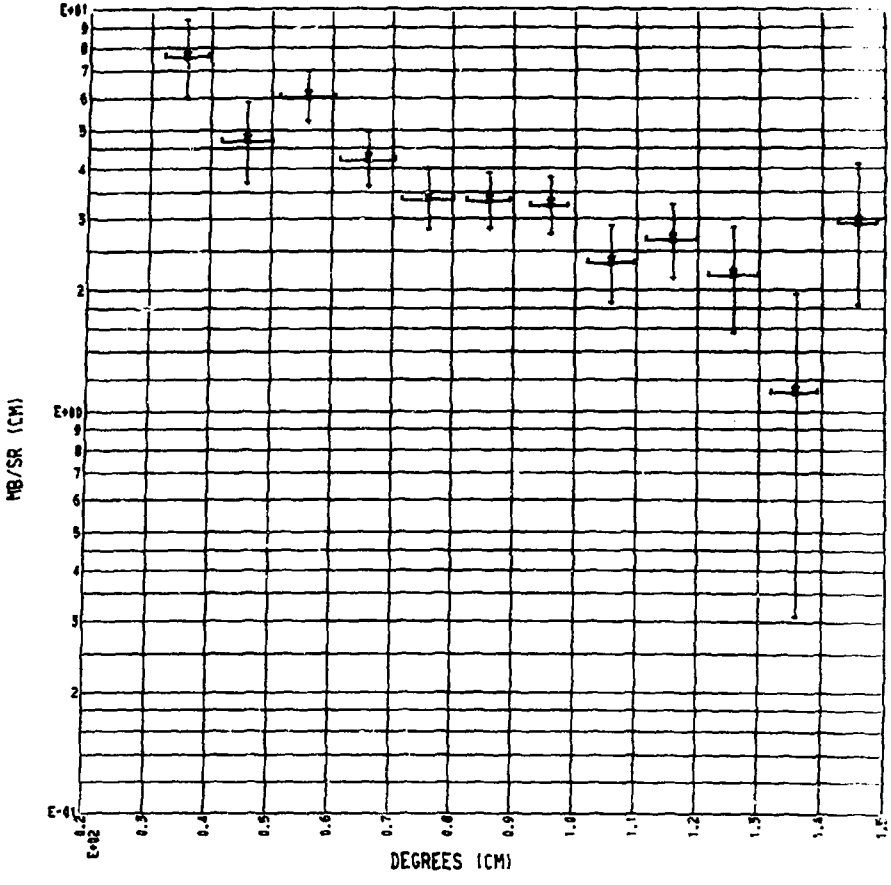

** LEAD **- Q-VALUE SUM BETWEEN -1.80 AND -3.30 MEV

FIG. 82

EXPERIMENTAL ANGULAR DISTRIBUTION

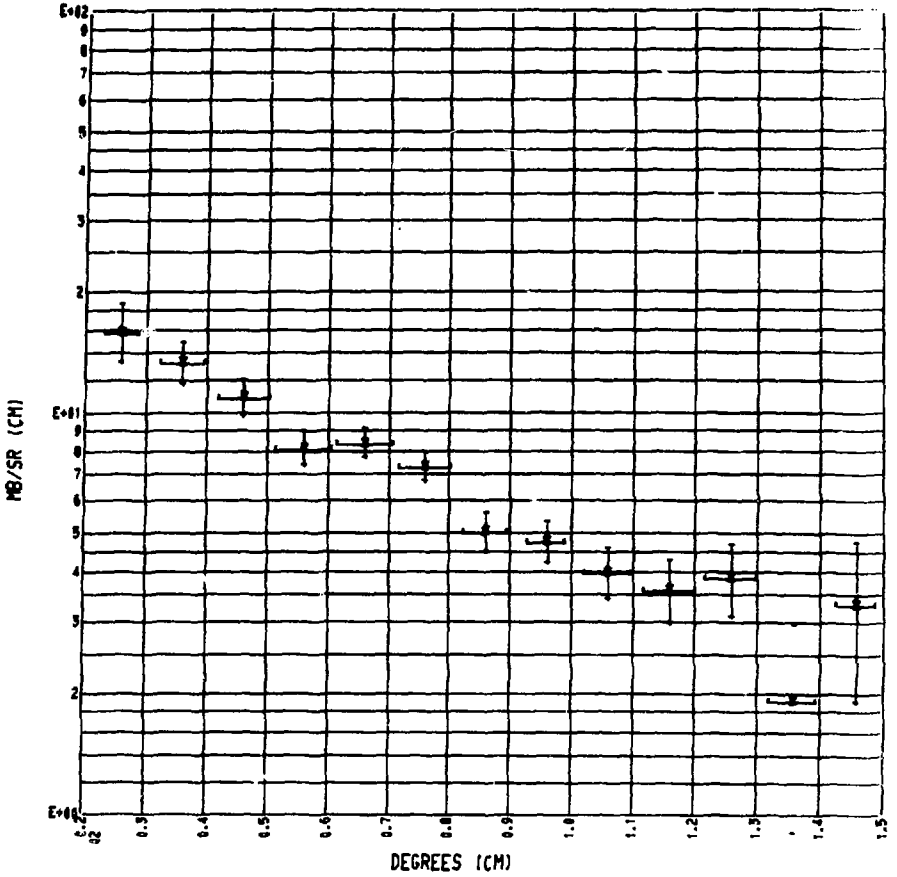

** LEAD **

Q-VALUE SUM BETWEEN -3.30 AND -5.30 MEV

FIG. 83

EXPERIMENTAL ANGULAR DISTRIBUTION

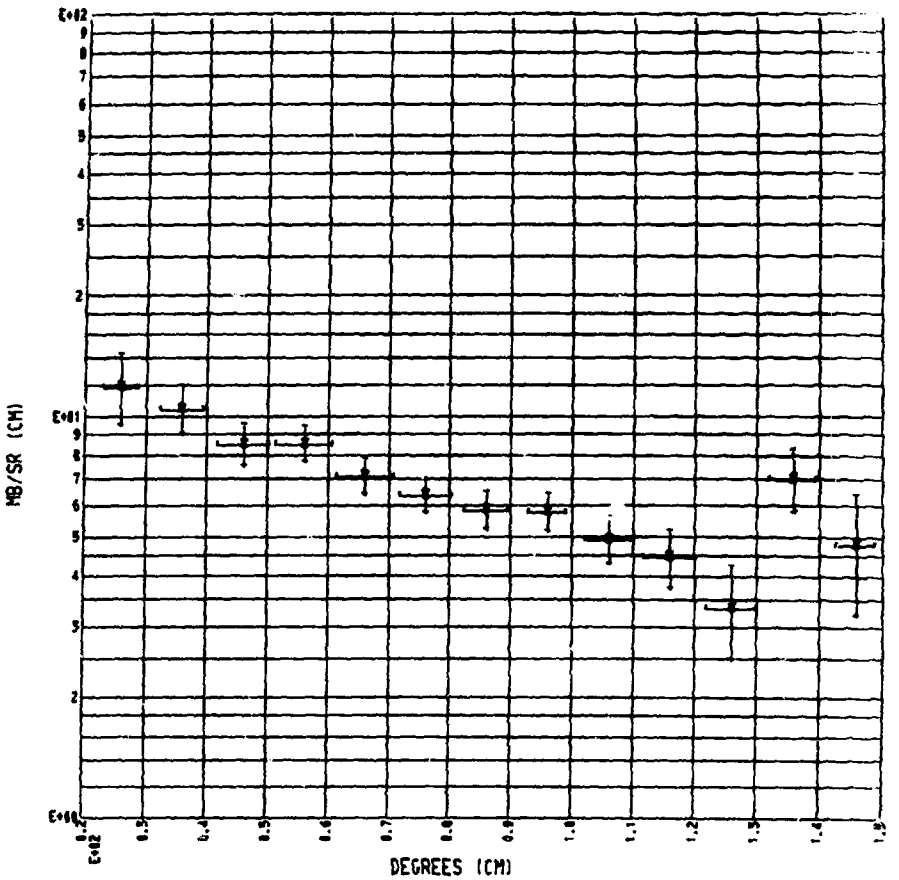

** LEAD ** Q-VALUE SUM BETWEEN -5.30 AND -7.00 MEV

FIG. 84

EXPERIMENTAL ANGULAR DISTRIBUTION

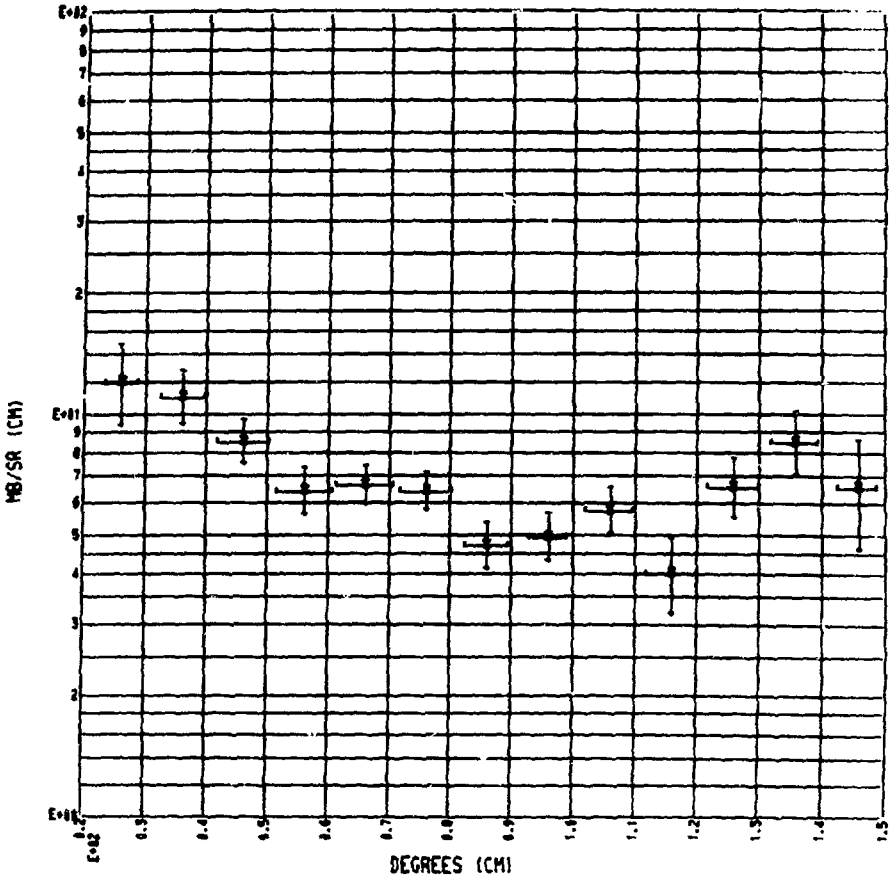

** LEAD **

Q-VALUE SUM BETWEEN -7.00 AND -8.50 MEV

FIG. 85

IV.G. Uranium-235

The emission spectra from a target containing 93.5% ^{235}U and 6.5% ^{238}U were observed at 20 angles. The elastic angular distribution was extracted from these measurements and is shown as Fig. 86. The spectrum at each angle is shown in Figs. 87 through 91. Each of these spectra is a composite of high, medium and low energy data. The solid line is generated by connecting points each 100 keV. The data have been corrected for isotopic abundance, flux attenuation and multiple scattering. Figs. 92 and 93 are linear and semi-log oblique projections of the raw data.

Figs. 94 through 97 show the angular distributions of groups of levels in ^{235}U. The vertical error bars are statistical. The horizontal error bars are the upper limits of the angle subtended by the target.

Based on the success in separating the 2^+ level in iron at 845 keV excitation, it was expected that the 3^- excitation level at about that energy in the fissionable isotopes would be seen and measured. It was not clearly resolved, an indication that its strength is less than two millibarns.

Previously published ^{235}U data[40,41] lack in accuracy.

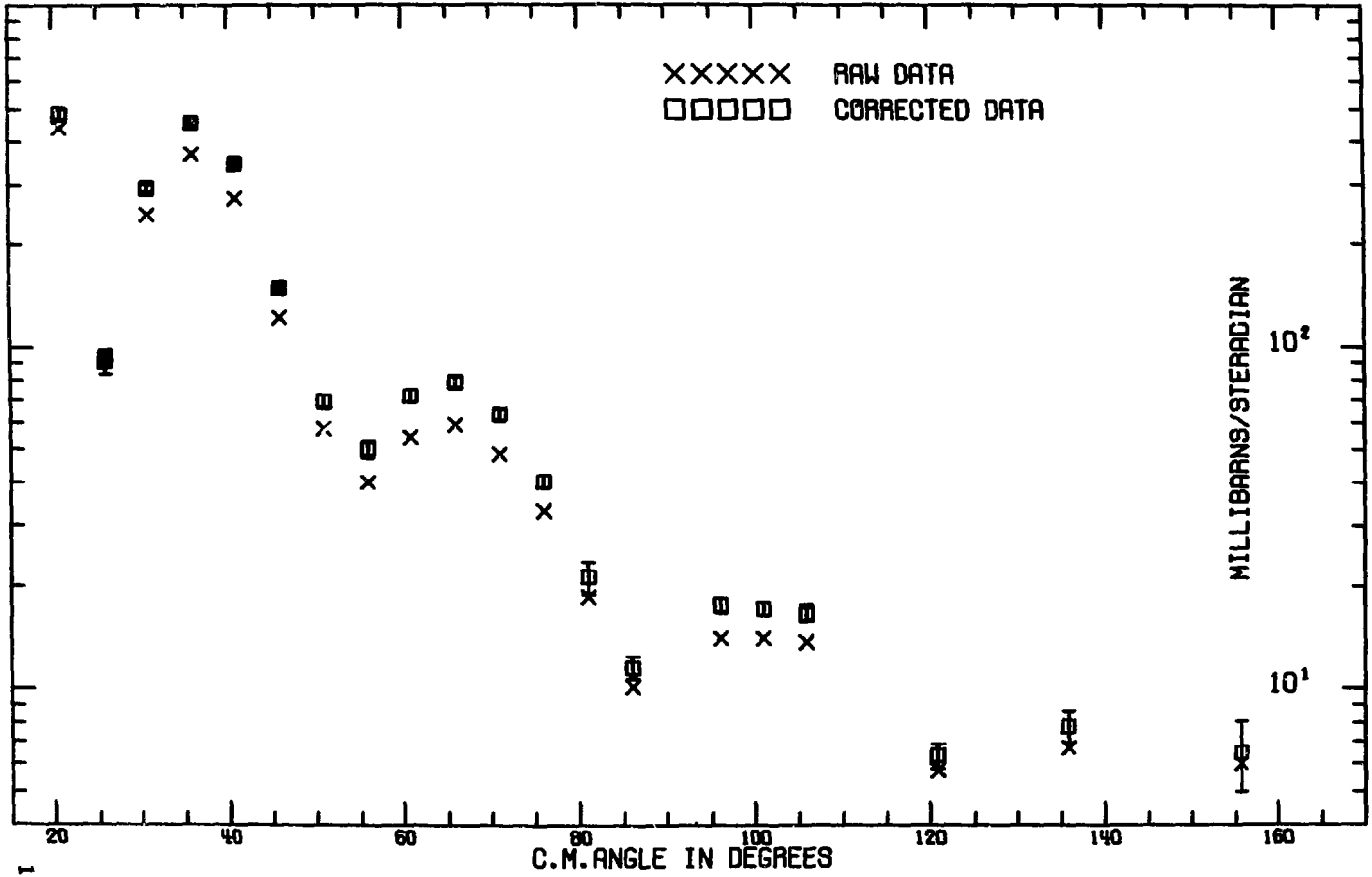

URANIUM-235 ELASTIC SCATTERING

FIG. 86

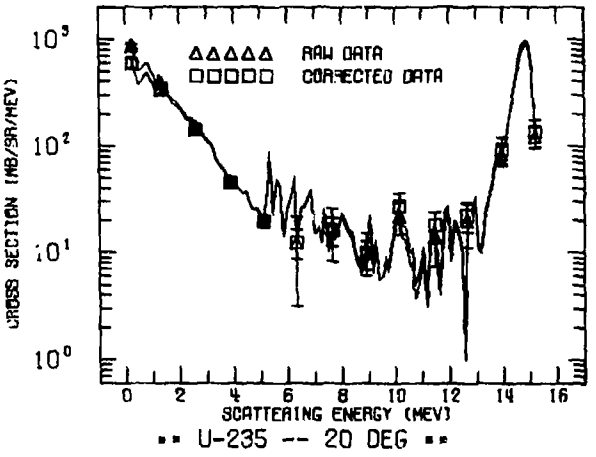
ΔΔΔΔΔ RAW DATA
□□□□□ CORRECTED DATA
CROSS SECTION (MB/SR/MEV)
SCATTERING ENERGY (MEV)
** U-235 -- 20 DEG **

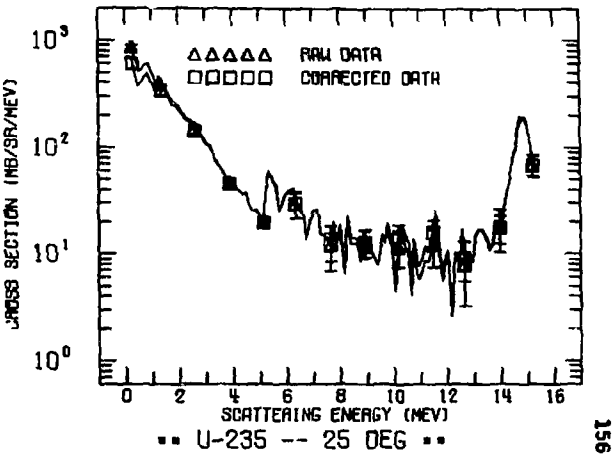
ΔΔΔΔΔ RAW DATA
□□□□□ CORRECTED DATA
CROSS SECTION (MB/SR/MEV)
SCATTERING ENERGY (MEV)
** U-235 -- 25 DEG **

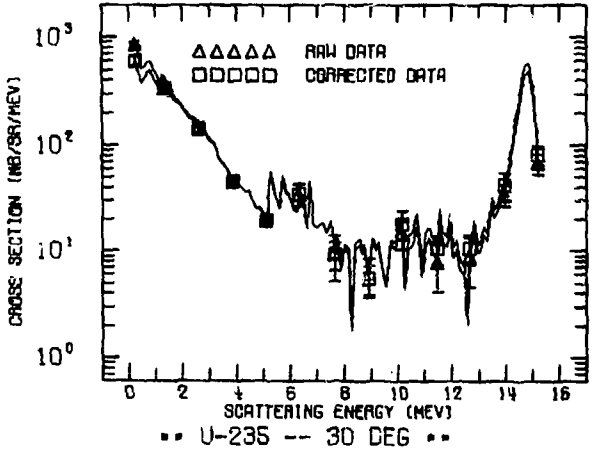
ΔΔΔΔΔ RAW DATA
□□□□□ CORRECTED DATA
CROSS SECTION (MB/SR/MEV)
SCATTERING ENERGY (MEV)
** U-235 -- 30 DEG **

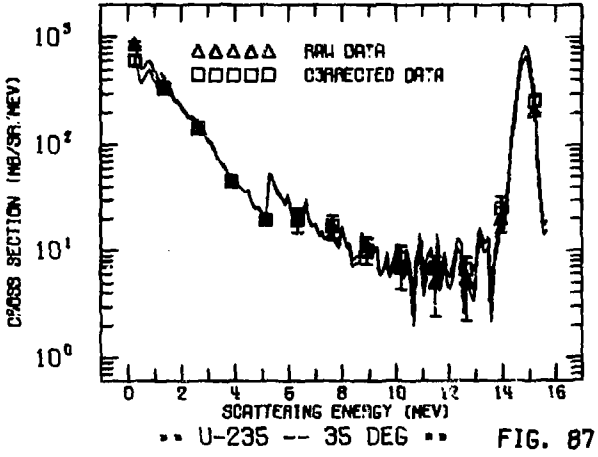
ΔΔΔΔΔ RAW DATA
□□□□□ CORRECTED DATA
CROSS SECTION (MB/SR/MEV)
SCATTERING ENERGY (MEV)
** U-235 -- 35 DEG **

FIG. 87

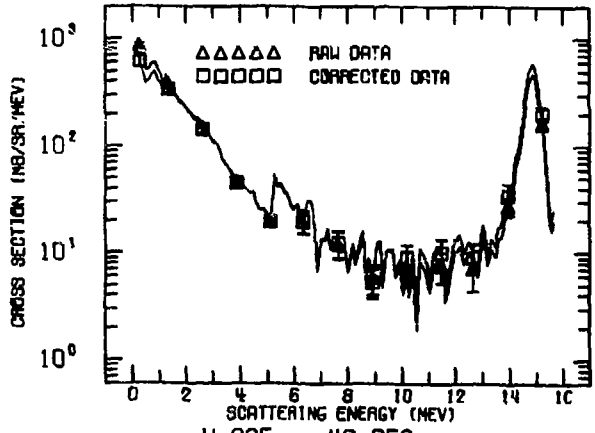

•• U-235 -- 40 DEG ••

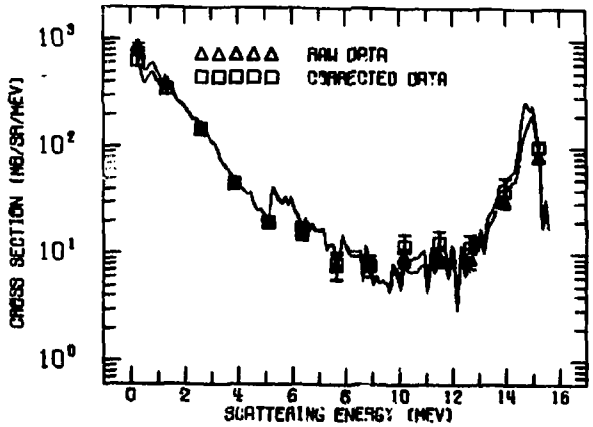

•• U-235 -- 45 DEG ••

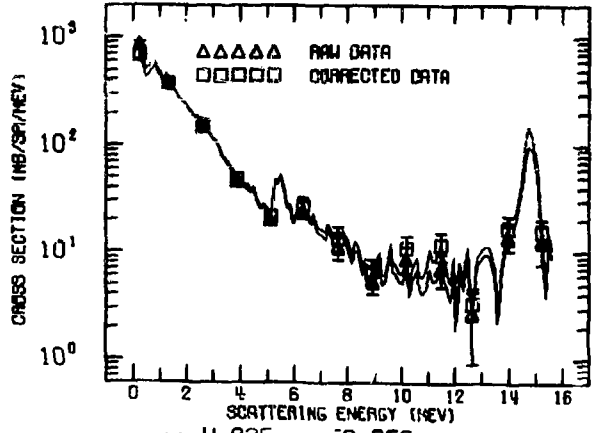

•• U-235 -- 50 DEG ••

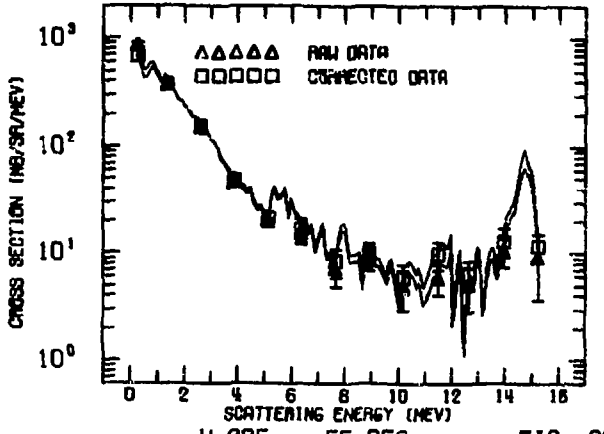

•• U-235 -- 55 DEG ••

FIG. 88

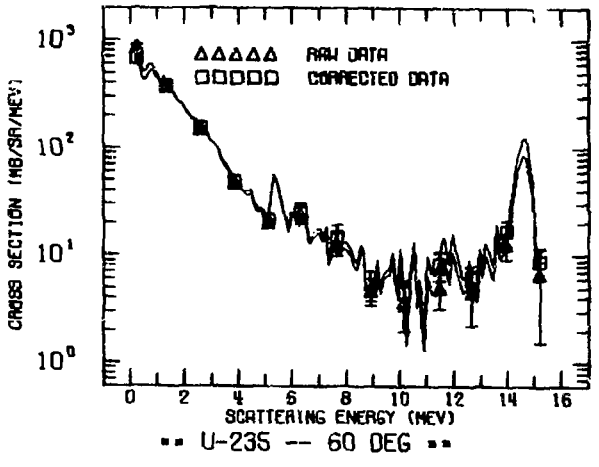
ΔΔΔΔΔ RAW DATA
□□□□□ CORRECTED DATA
CROSS SECTION (MB/SR/MEV)
SCATTERING ENERGY (MEV)
** U-235 -- 60 DEG **

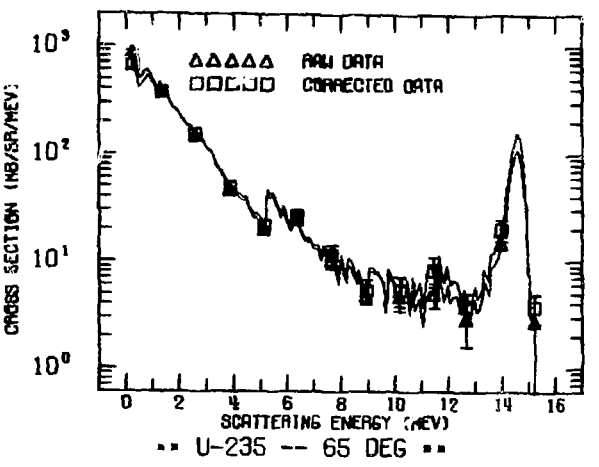
ΔΔΔΔΔ RAW DATA
□□□□□ CORRECTED DATA
CROSS SECTION (MB/SR/MEV)
SCATTERING ENERGY (MEV)
** U-235 -- 65 DEG **

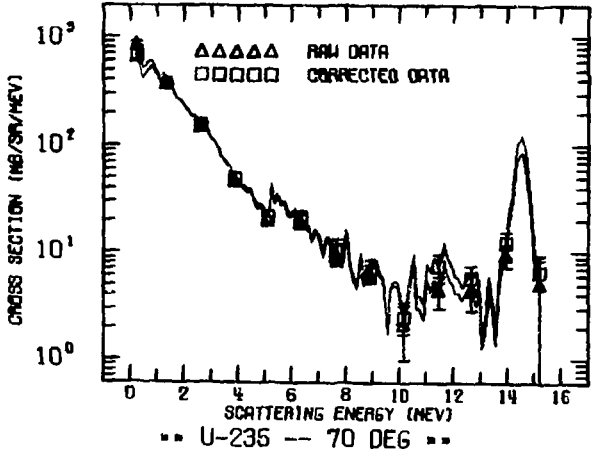
ΔΔΔΔΔ RAW DATA
□□□□□ CORRECTED DATA
CROSS SECTION (MB/SR/MEV)
SCATTERING ENERGY (MEV)
** U-235 -- 70 DEG **

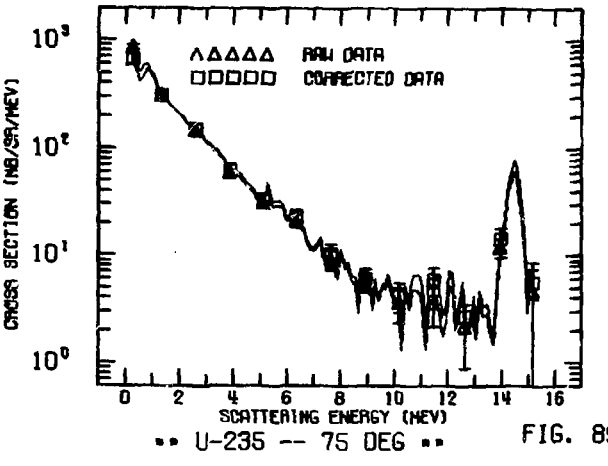
ΔΔΔΔΔ RAW DATA
□□□□□ CORRECTED DATA
CROSS SECTION (MB/SR/MEV)
SCATTERING ENERGY (MEV)
** U-235 -- 75 DEG **

FIG. 89

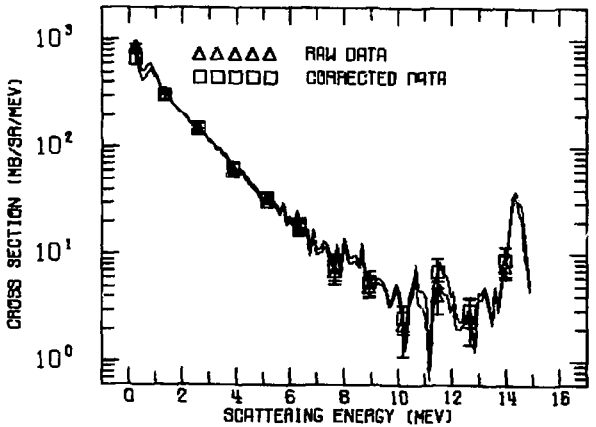
ΔΔΔΔΔ RAW DATA
□□□□□ CORRECTED DATA
CROSS SECTION (MB/SR/MEV)
SCATTERING ENERGY (MEV)
•• U-235 -- 80 DEG ••

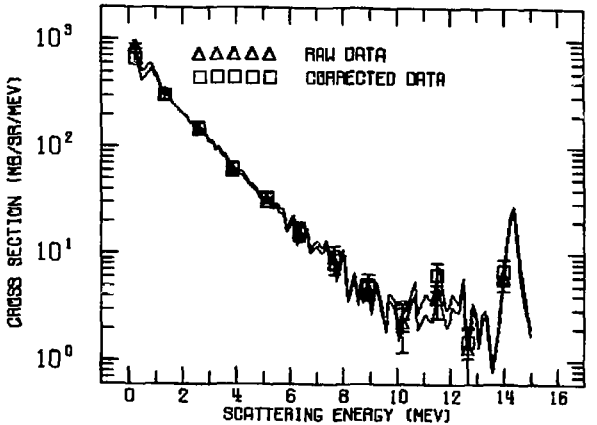
ΔΔΔΔΔ RAW DATA
□□□□□ CORRECTED DATA
CROSS SECTION (MB/SR/MEV)
SCATTERING ENERGY (MEV)
•• U-235 -- 85 DEG ••

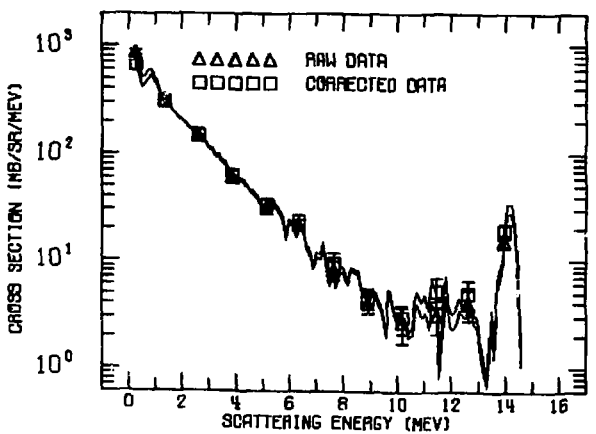
ΔΔΔΔΔ RAW DATA
□□□□□ CORRECTED DATA
CROSS SECTION (MB/SR/MEV)
SCATTERING ENERGY (MEV)
•• U-235 -- 95 DEG ••

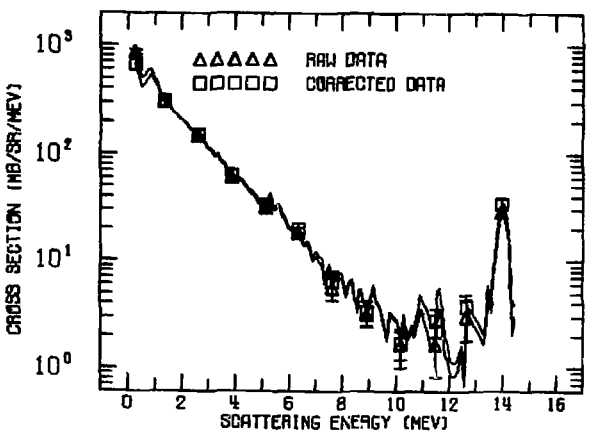
ΔΔΔΔΔ RAW DATA
□□□□□ CORRECTED DATA
CROSS SECTION (MB/SR/MEV)
SCATTERING ENERGY (MEV)
•• U-235 -- 100 DEG ••

FIG. 90

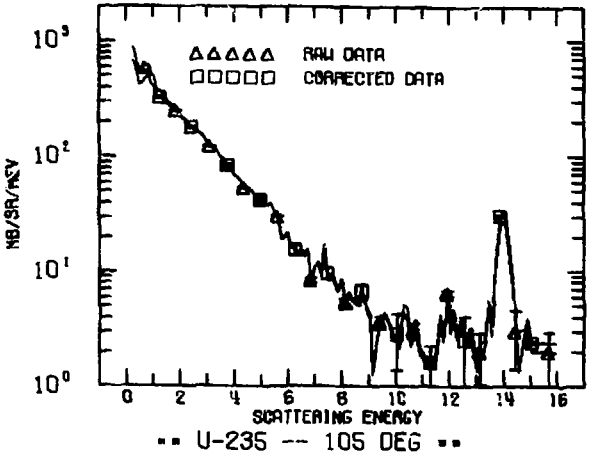
ΔΔΔΔΔ RAW DATA
□□□□□ CORRECTED DATA
MB/SR/MEV
SCATTERING ENERGY
** U-235 -- 105 DEG **

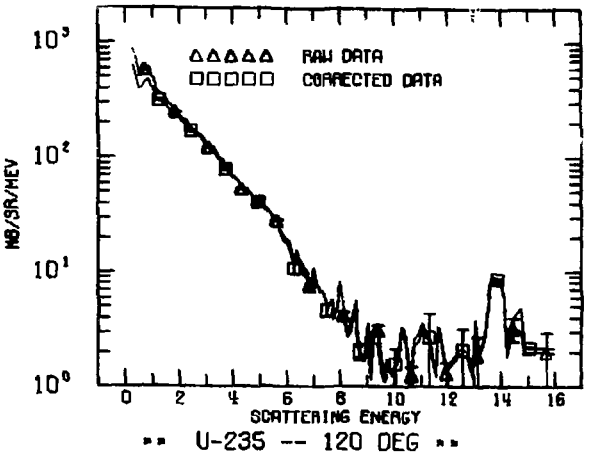
ΔΔΔΔΔ RAW DATA
□□□□□ CORRECTED DATA
MB/SR/MEV
SCATTERING ENERGY
** U-235 -- 120 DEG **

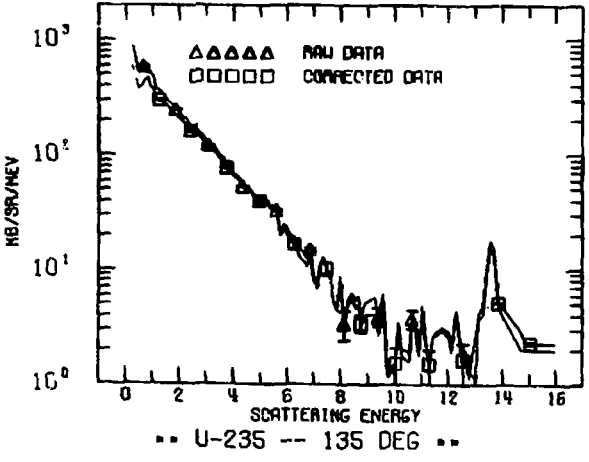
ΔΔΔΔΔ RAW DATA
□□□□□ CORRECTED DATA
MB/SR/MEV
SCATTERING ENERGY
** U-235 -- 135 DEG **

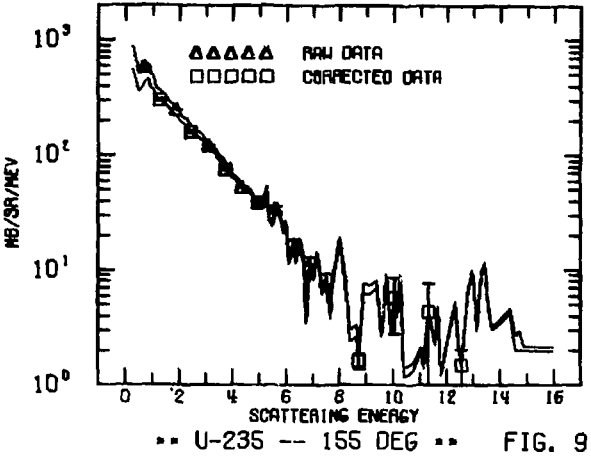
ΔΔΔΔΔ RAW DATA
□□□□□ CORRECTED DATA
MB/SR/MEV
SCATTERING ENERGY
** U-235 -- 155 DEG **

FIG. 91

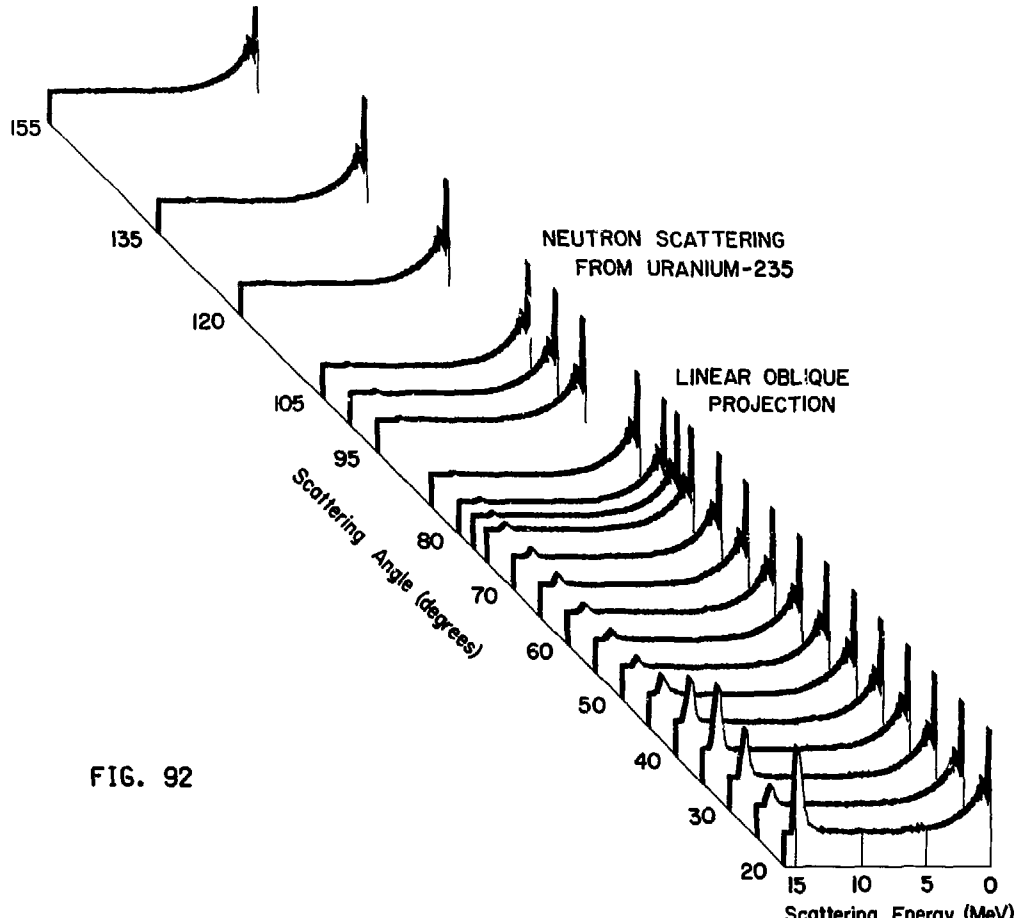
NEUTRON SCATTERING
FROM URANIUM-235
LINEAR OBLIQUE
PROJECTION
155
135
120
105
95
80
70
60
50
40
30
20
Scattering Angle (degrees)
15
10
5
0
Scattering Energy (MeV)

FIG. 92

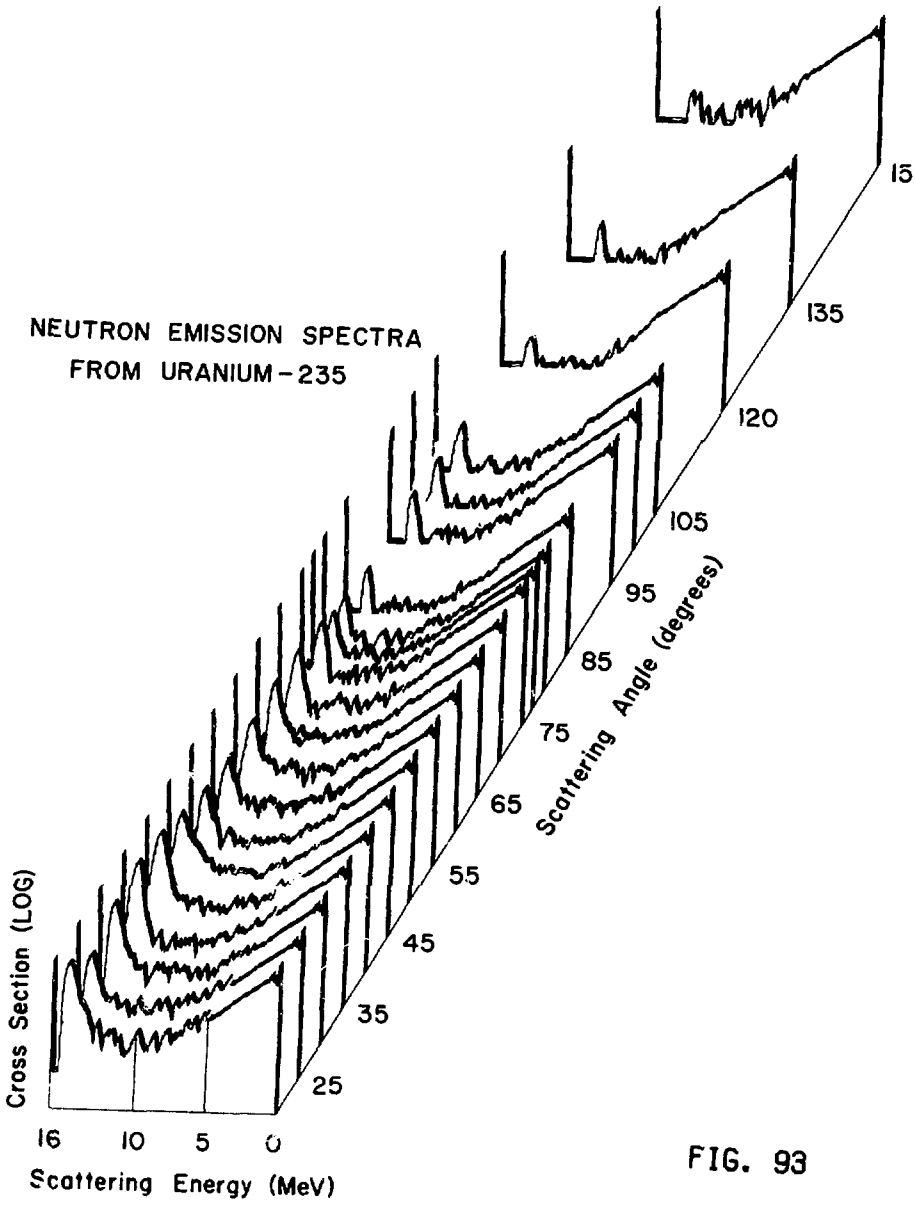
NEUTRON EMISSION SPECTRA
FROM URANIUM-235
Cross Section (LOG)
16
10
5
0
Scattering Energy (MeV)
25
35
45
55
65
75
85
95
105
120
135
155
Scattering Angle (degrees)

FIG. 93

EXPERIMENTAL ANGULAR DISTRIBUTION

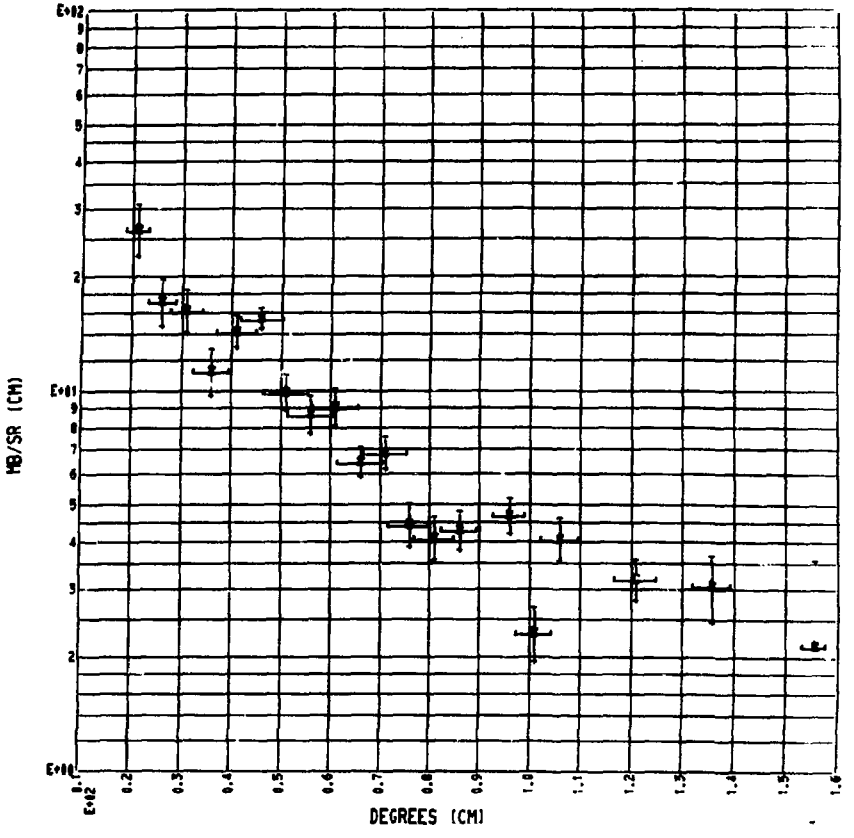

** U-235 **

Q-VALUE SUM BETWEEN -1.50 AND -3.00 MEV

FIG. 94

1e4

EXPERIMENTAL ANGULAR DISTRIBUTION

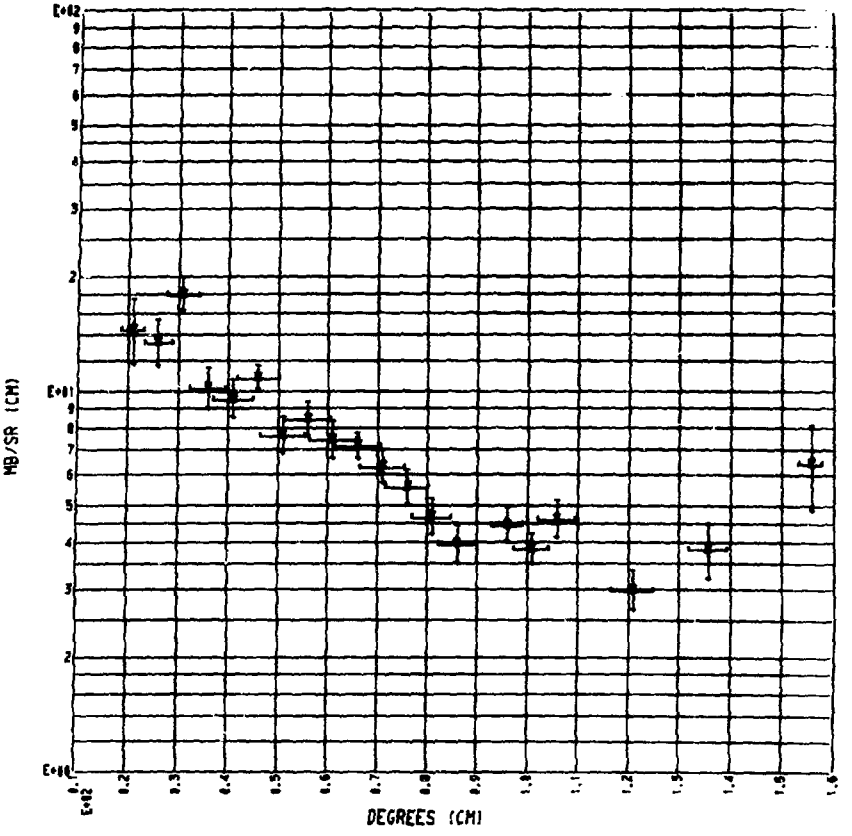

** U-235 ** Q-VALUE SUM BETWEEN -3.00 AND -4.50 MEV

FIG. 95

EXPERIMENTAL ANGULAR DISTRIBUTION

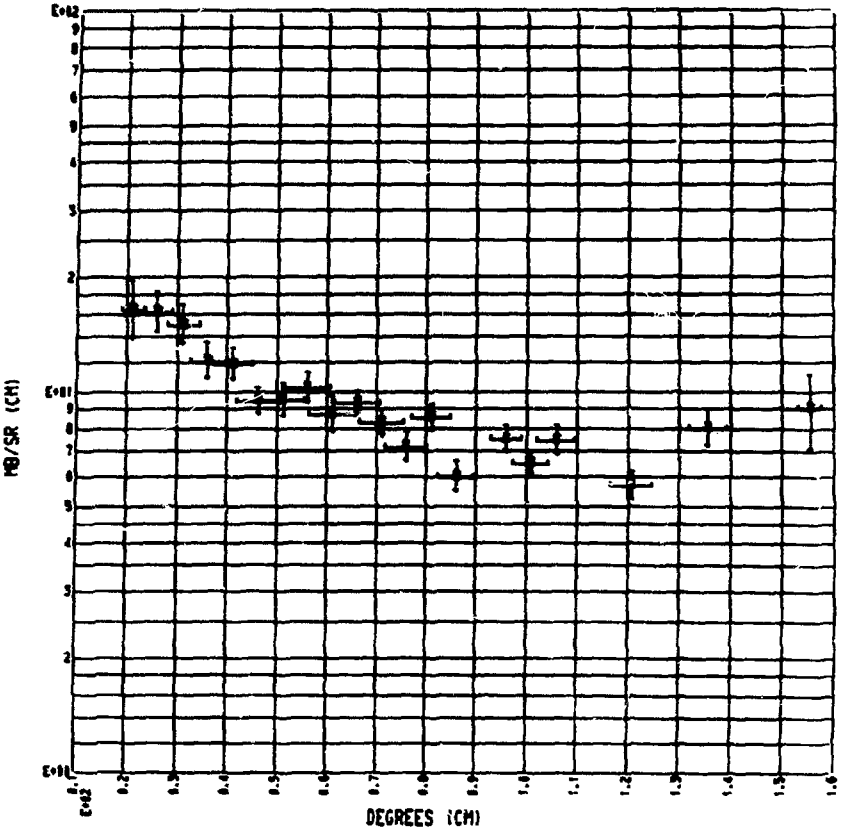

** U-235 ** Q-VALUE SUM BETWEEN -4.50 AND -6.00 MEV

FIG. 96

EXPERIMENTAL ANGULAR DISTRIBUTION

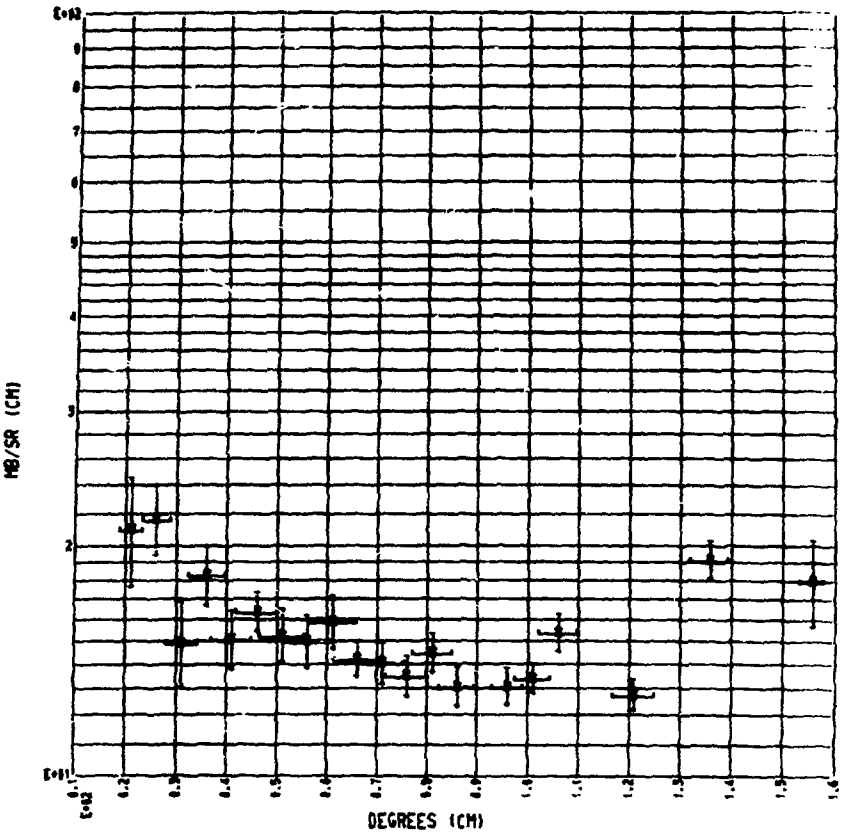

** U-235 ** Q-VALUE SUM BETWEEN -6.00 AND -7.50 MEV

FIG. 97

IV.H. Uranium-238

The emission spectra from a ^{238}U ring target with 14 MeV neutrons incident were observed at 19 angles. The elastic angular distribution is shown as Fig. 98. Figs. 99 through 103 contain the spectra observed at each angle. The data have been corrected for multiple scattering and flux attenuation.

The elastic angular distribution was compared to the measurement of Voignier.[42] Inelastic measurements have been made by Bertin et al.[43] and Boschung et al.[44]

Figs. 104 through 107 are plots of the angular distribution for group of levels at excitation energies up to 7.50 MeV.

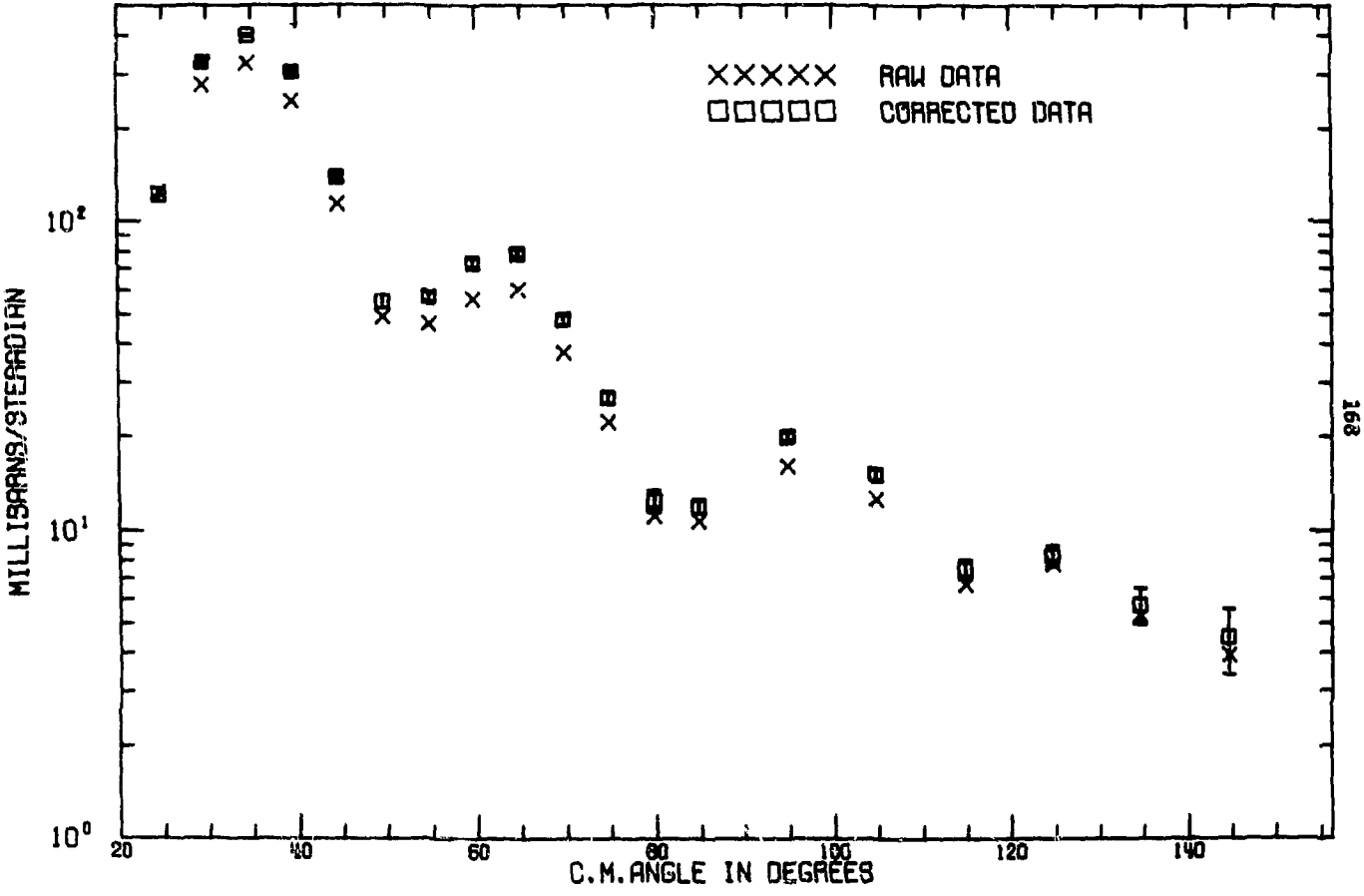

URANIUM-238 ELASTIC SCATTERING FIG. 98

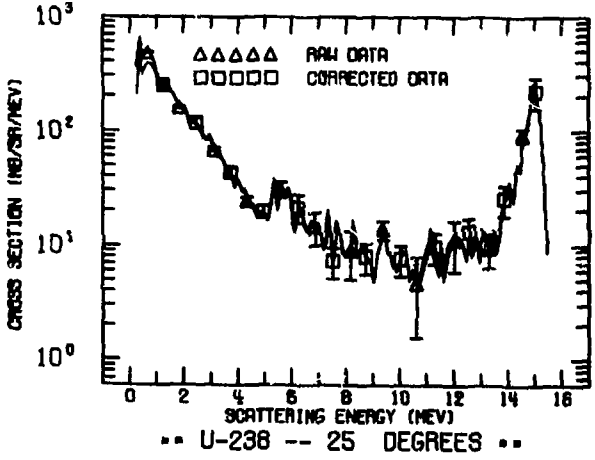

•• U-238 -- 25 DEGREES ••

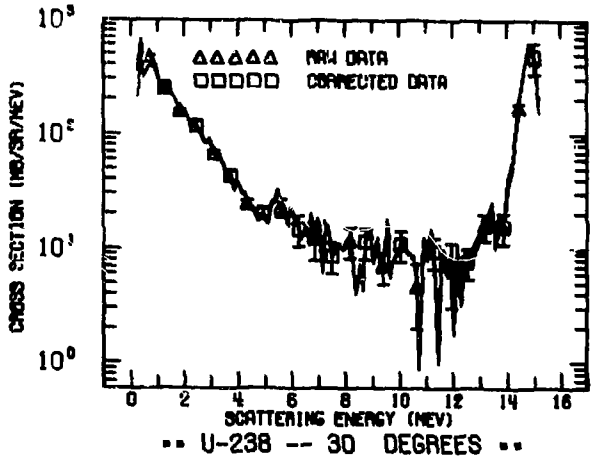

•• U-238 -- 30 DEGREES ••

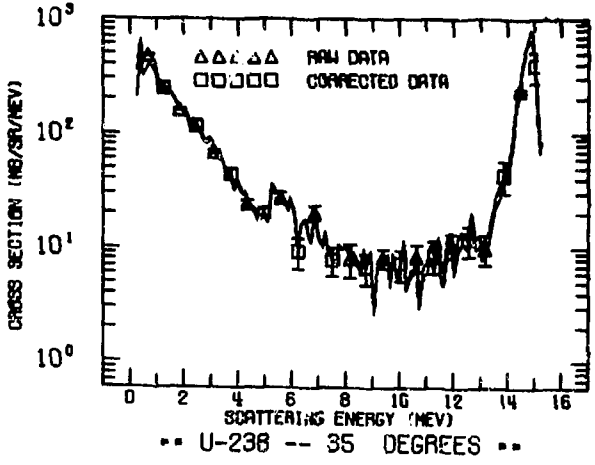

•• U-238 -- 35 DEGREES ••

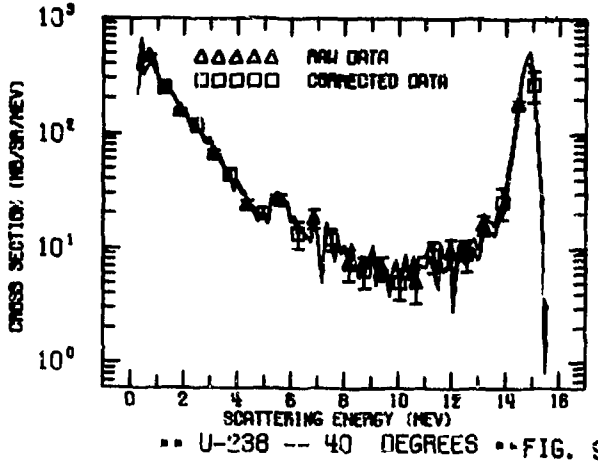

•• U-238 -- 40 DEGREES ••

169

FIG. 99

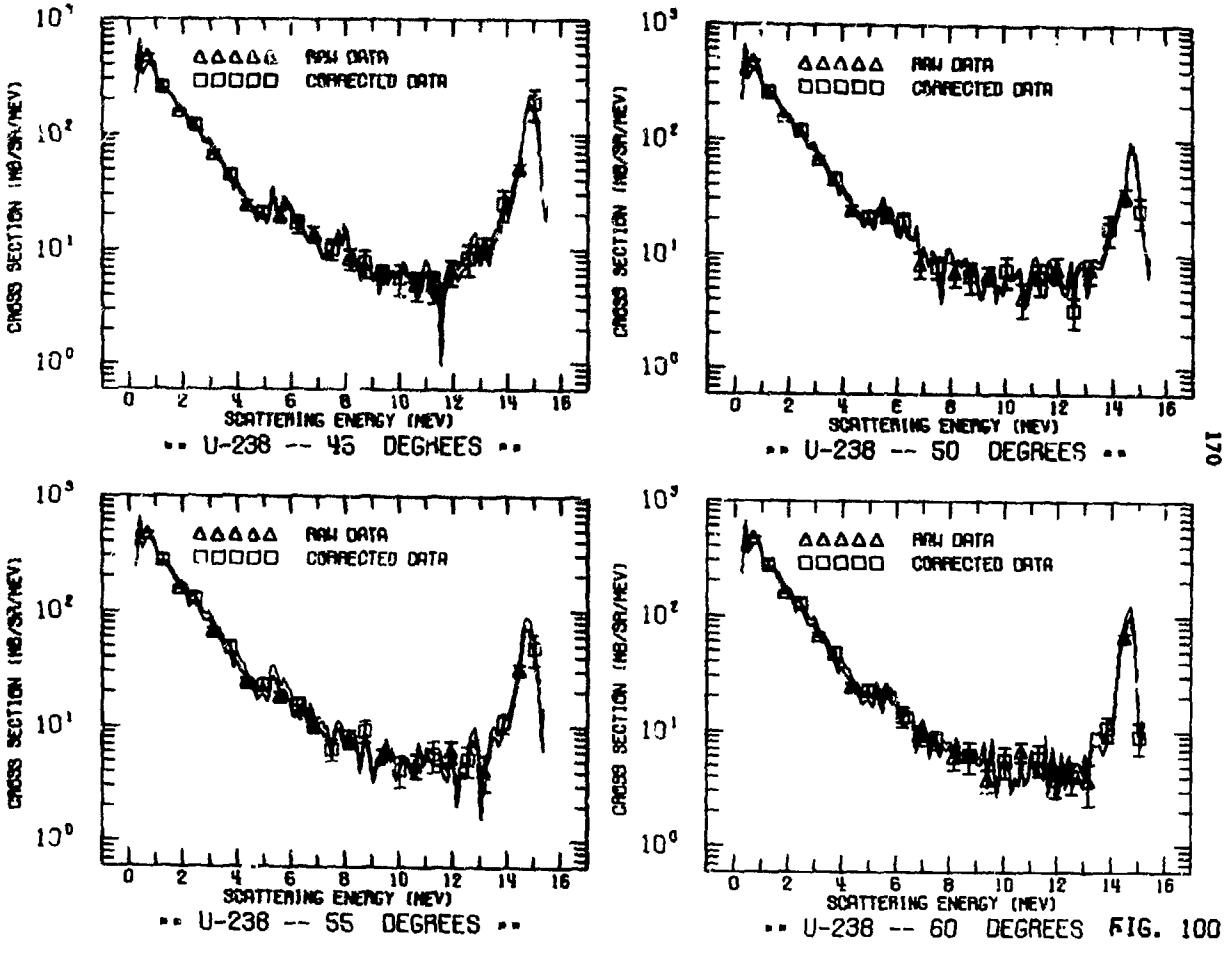
ΔΔΔΔΔ RAW DATA
□□□□□ CORRECTED DATA
CROSS SECTION (MB/SR/MEV)
SCATTERING ENERGY (MEV)
** U-238 -- 45 DEGREES **
** U-238 -- 50 DEGREES **
** U-238 -- 55 DEGREES **
** U-238 -- 60 DEGREES **

FIG. 100

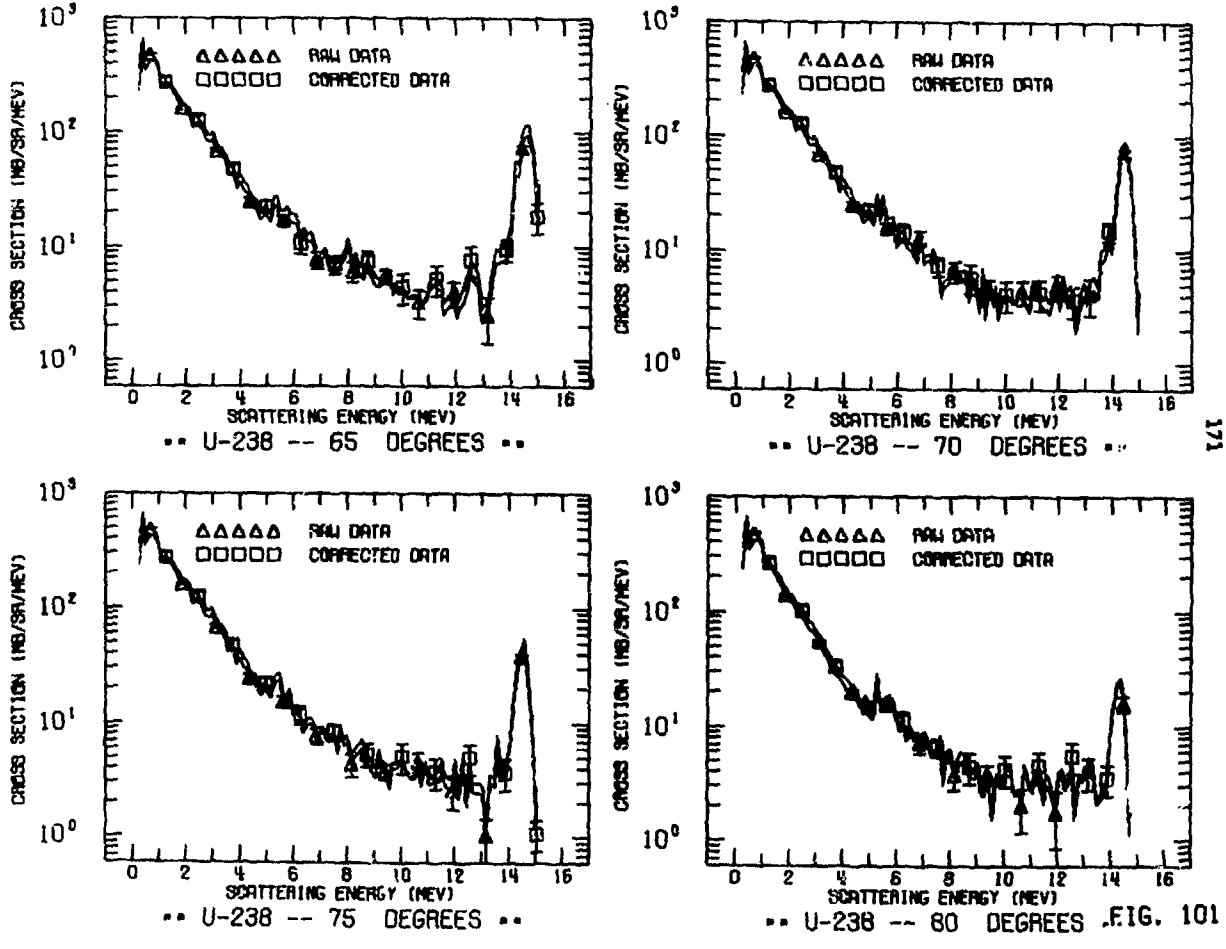
ΔΔΔΔΔ RAW DATA
□□□□□ CORRECTED DATA
CROSS SECTION (MB/SR/MEV)
SCATTERING ENERGY (MEV)
•• U-238 -- 65 DEGREES ••
•• U-238 -- 70 DEGREES ••
•• U-238 -- 75 DEGREES ••
•• U-238 -- 80 DEGREES ••

FIG. 101

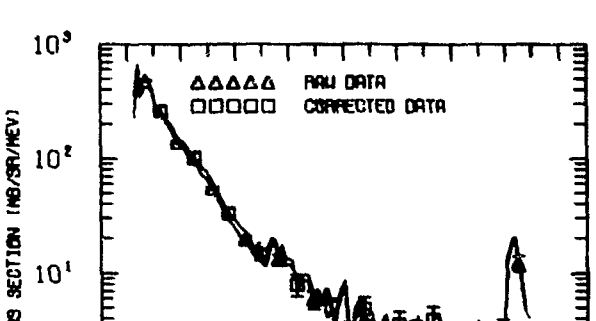

•• U-238 -- 85 DEGREES ••

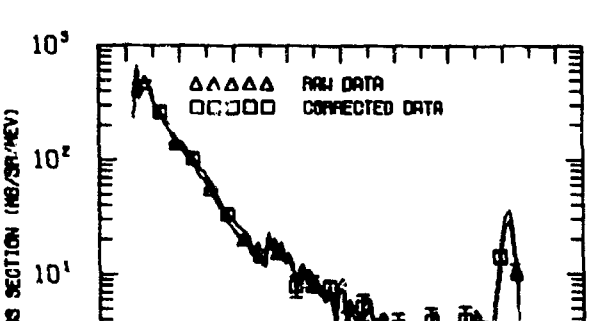

•• U-238 -- 95 DEGREES ••

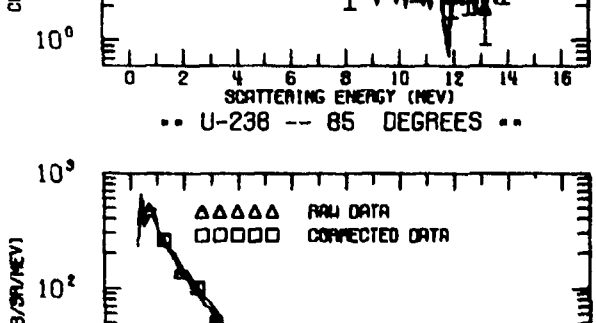

•• U-238 -- 105 DEGREES ••

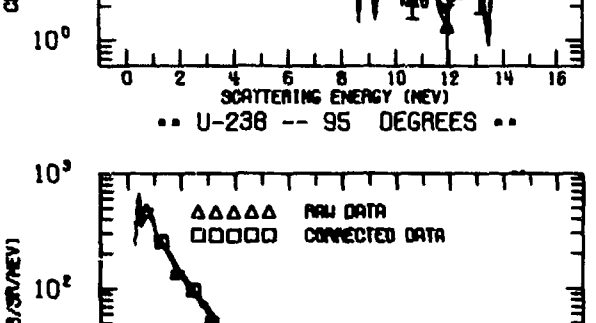

•• U-238 -- 115 DEGREES ••

FIG. 102

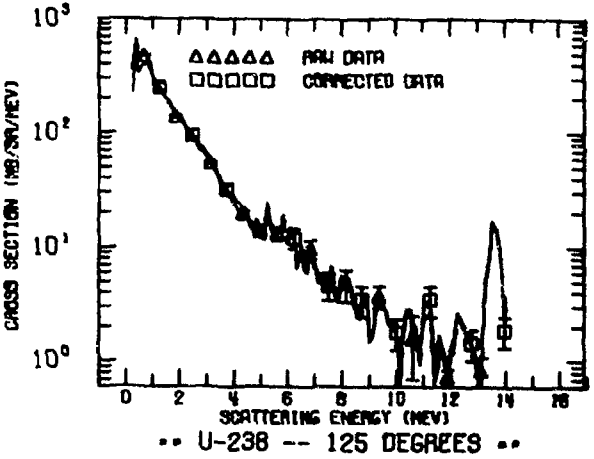
ΔΔΔΔΔ RAW DATA
□□□□□ CORRECTED DATA
CROSS SECTION (MB/SR/MEV)
SCATTERING ENERGY (MEV)
•• U-238 -- 125 DEGREES ••

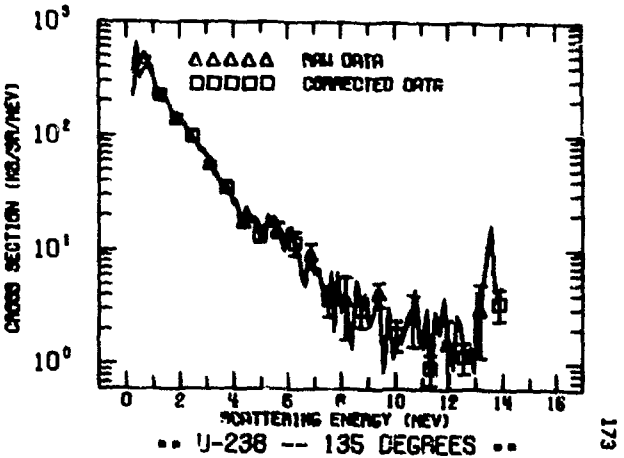
ΔΔΔΔΔ RAW DATA
□□□□□ CORRECTED DATA
CROSS SECTION (MB/SR/MEV)
SCATTERING ENERGY (MEV)
•• U-238 -- 135 DEGREES ••

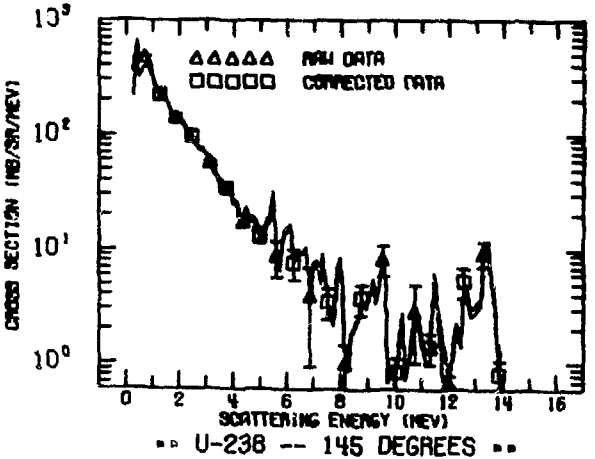
ΔΔΔΔΔ RAW DATA
□□□□□ CORRECTED DATA
CROSS SECTION (MB/SR/MEV)
SCATTERING ENERGY (MEV)
•• U-238 -- 145 DEGREES ••

FIG. 103

EXPERIMENTAL ANGULAR DISTRIBUTION

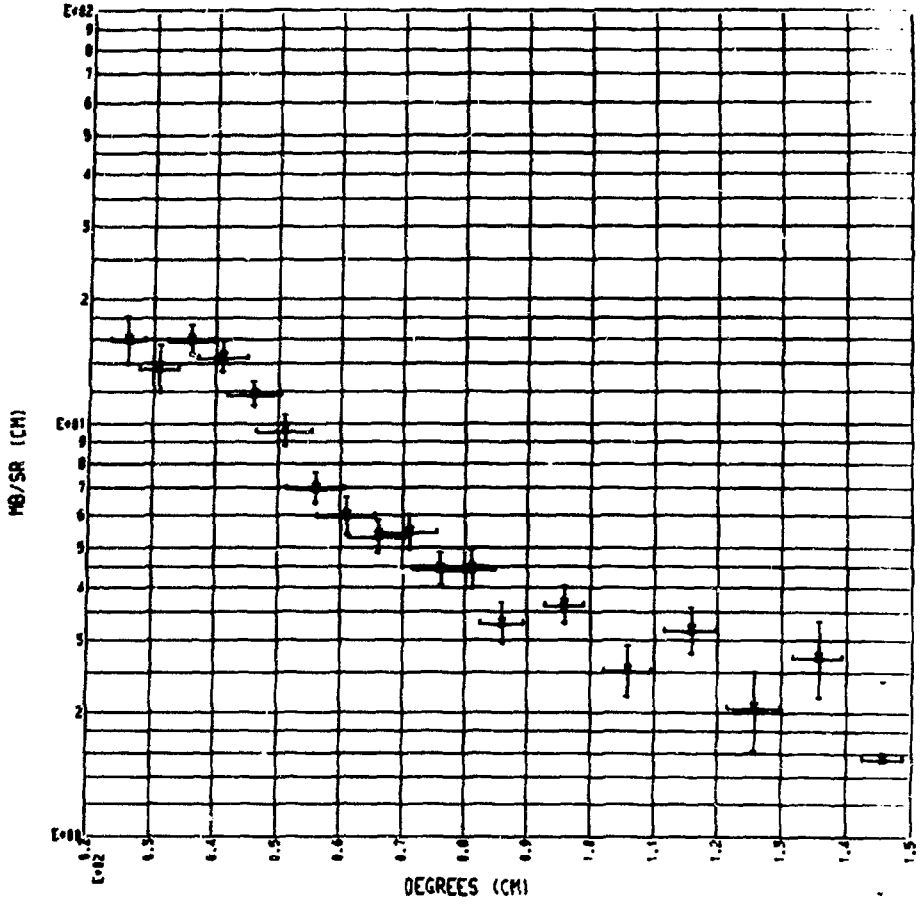

URANIUM-238 Q-VALUE SUM BETWEEN -1.50 AND -3.00 MEV

FIG. 104

EXPERIMENTAL ANGULAR DISTRIBUTION

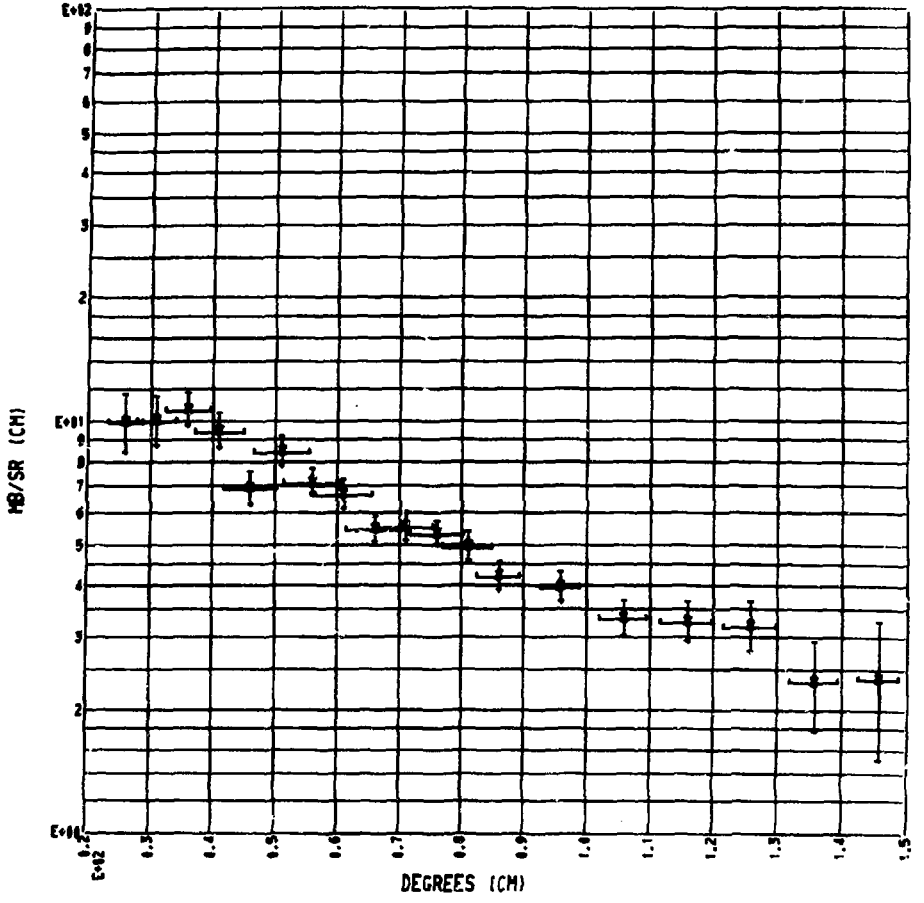

URANIUM-238 Q-VALUE SUM BETWEEN -3.00 AND -4.50 MEV

FIG. 105

EXPERIMENTAL ANGULAR DISTRIBUTION

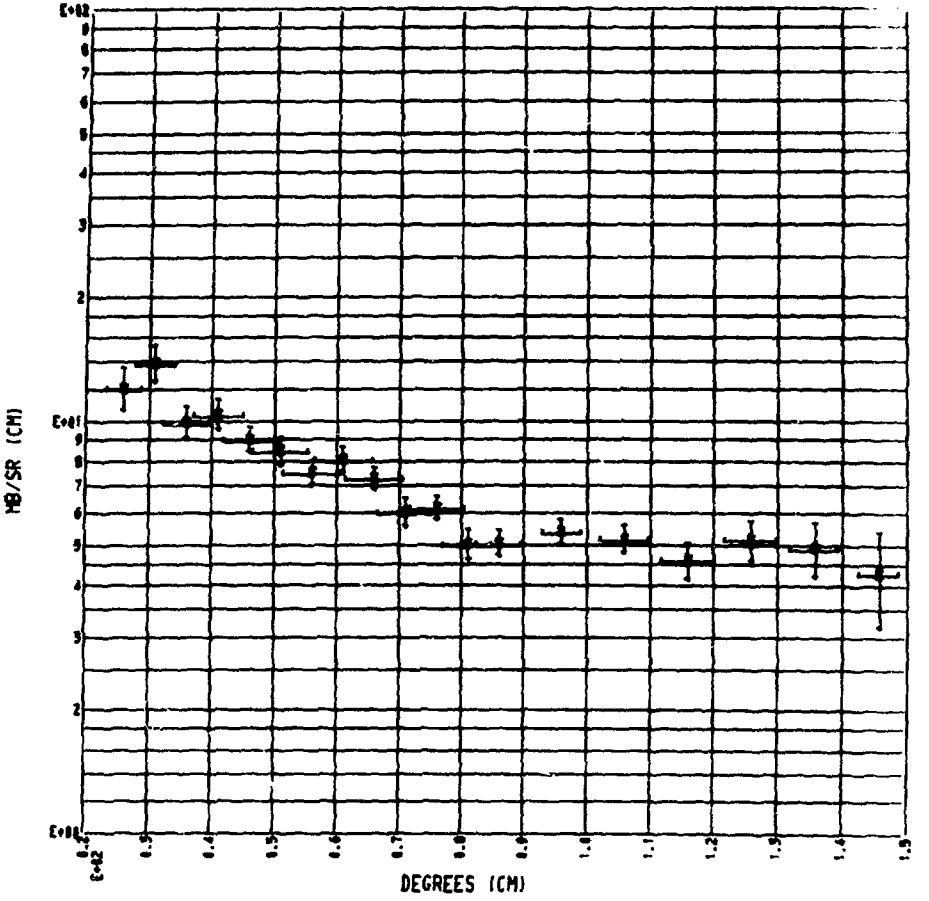

URANIUM-238 Q-VALUE SUM BETWEEN -4.50 AND -6.00 MEV

FIG. 106

EXPERIMENTAL ANGULAR DISTRIBUTION

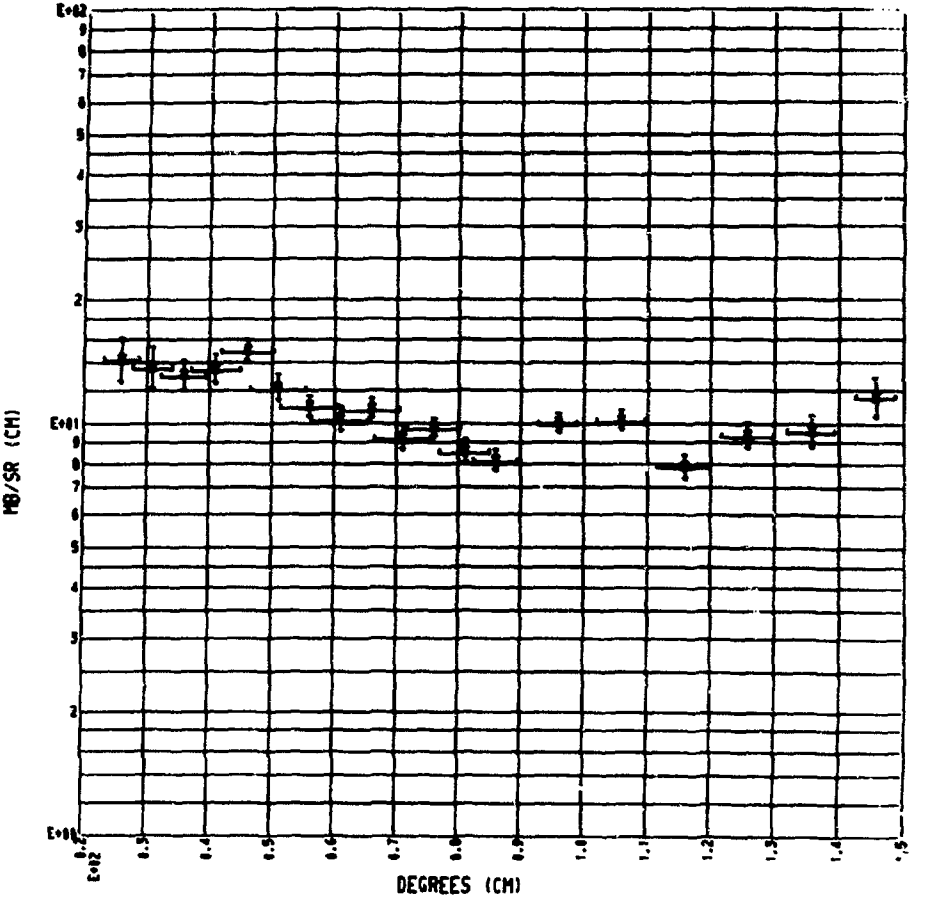

URANIUM-238 Q-VALUE SUM BETWEEN -6.00 AND -7.50 MEV

FIG. 107

IV.I. Plutonium-239

Safety consideration required the plutonium-239 ring to be encased in a stainless steel can (see Fig. 108). The data were thus complicated by the presence of a considerable mass of elements near atomic weight 56. The presence of the stainless steel was not unambiguously removed, so the data from the ^{239}Pu and stainless steel can are presented.

Fig. 109 shows the observed low energy spectrum. The solid line is generated by connecting points each 10 keV. Fig. 110 shows one of the three (45°, 95°, 135°) medium energy spectra measured. The elastic peak in Fig. 110 is abnormally broadened by the presence of the lighter mass stainless steel can. Points each 100 keV are connected.

Figs. 111-129 contain the observed high energy spectra. In each figure, the medium energy spectrum observed nearest the angle indicated is plotted between 1 and 5 MeV. The low energy spectrum observed at 95° is plotted between 0 and 1 MeV in each figure. The solid line connects points each 100 keV.

Fig. 130 shows the extracted elastic differential cross section. Figs. 131-135 contain the differential scattering cross section to other energy levels, relative to the elastic peak. Figs. 131 and 132 are forward peaked, indicating a direct scattering cross section. Figs. 133 and 134 are roughly isotropic. Figs. 135 shows a differential cross section increasing at backward angles. This effect is ascribed to the energy asymmetry of the source and kinematic shift in inelastic scattering toward backward angles. The spectrum of neutrons energies shown in Fig. 135 is dominated by the fission spectrum, which is isotropic in energy relative to zero, not energy relative to the elastic peak as indicated in each of the Figs. 131 through 134.

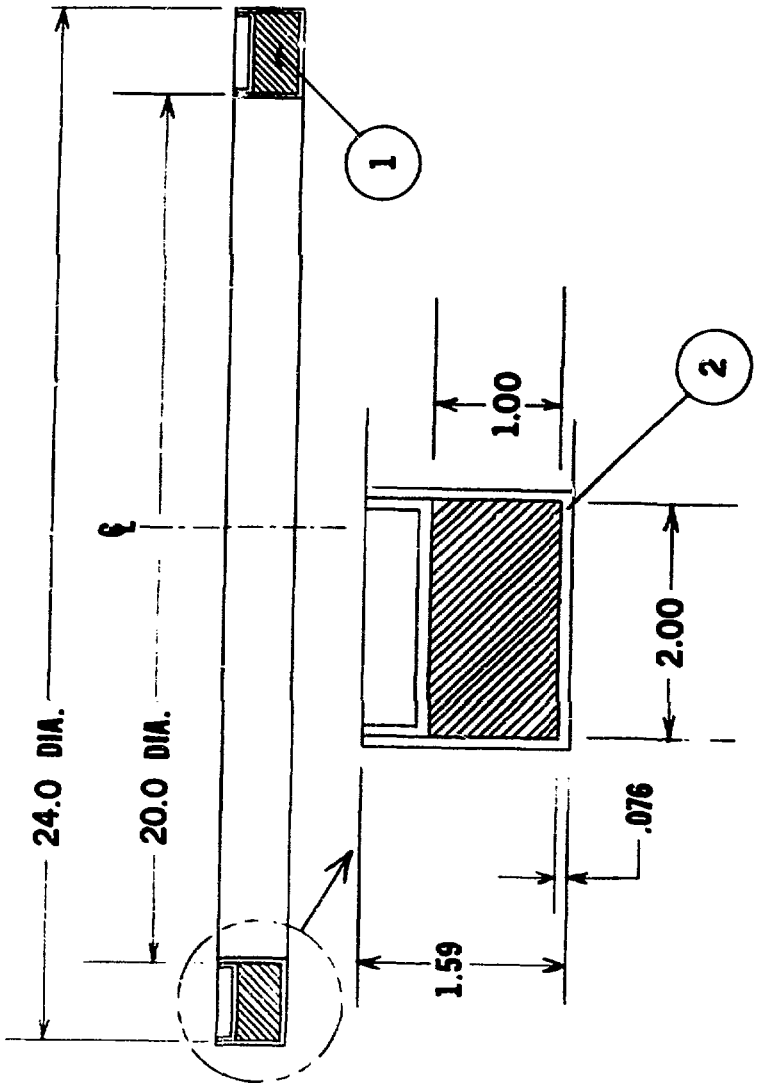

All Dimensions in Centimeters

1-DELTA PU W/1 % GA
2-SST 304

Fig. 108

DIFFERENTIAL ENERGY SPECTRUM

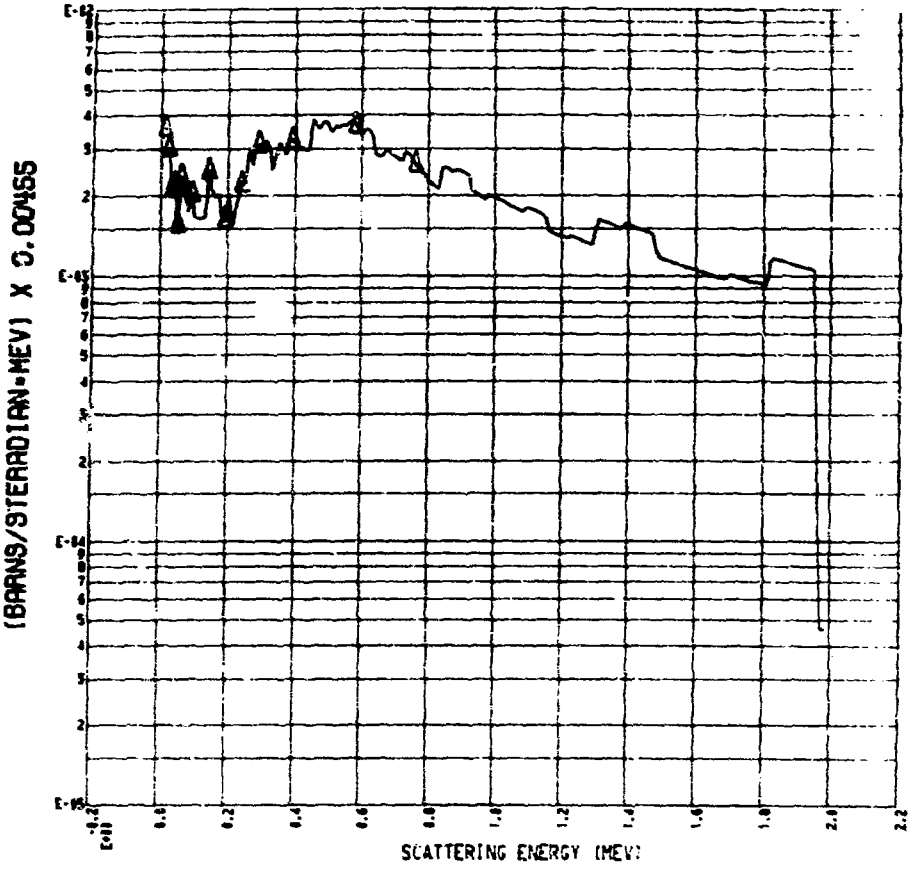

** PU-239 RING -- 040506 **

FIG. 109

DIFFERENTIAL ENERGY SPECTRUM

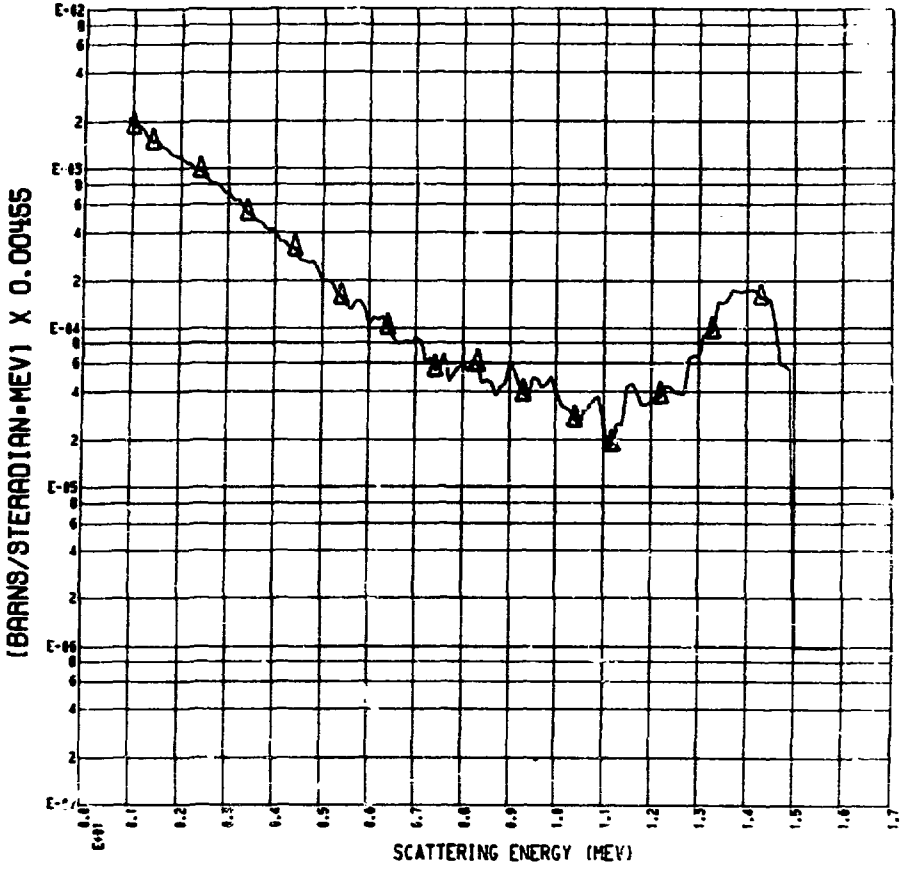

** PU-239 -- 95 DEGREES -- 40902 **

FIG. 110

DIFFERENTIAL ENERGY SPECTRUM

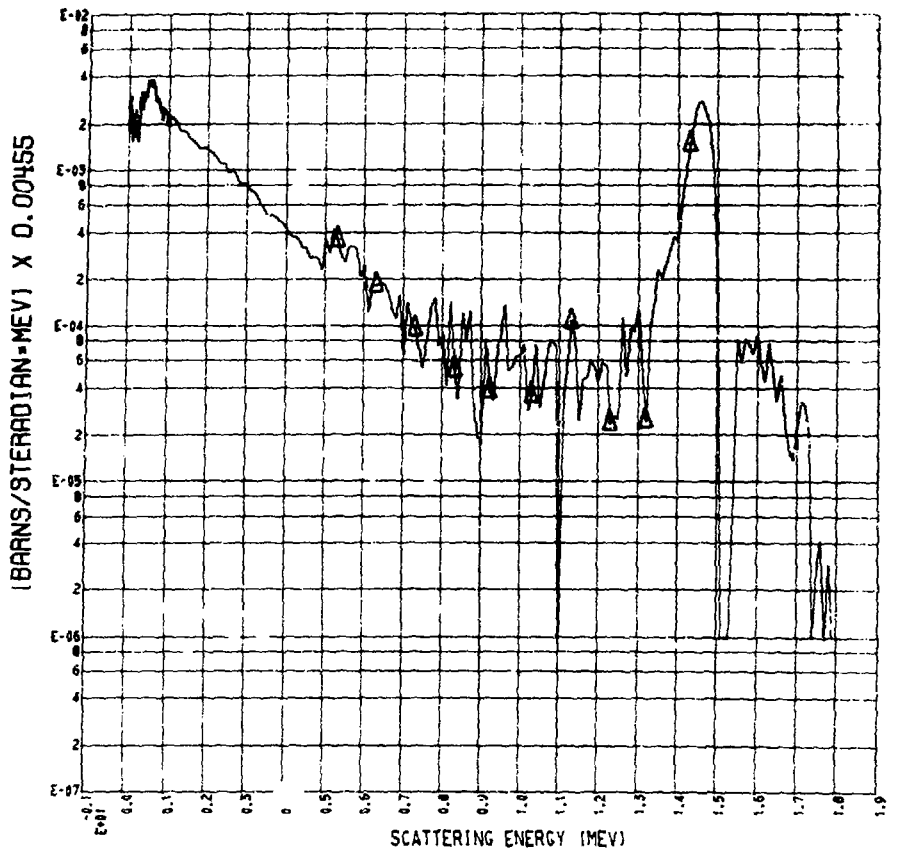

** PU-239 -- 25 DEG **

FIG. 111

DIFFERENTIAL ENERGY SPECTRUM

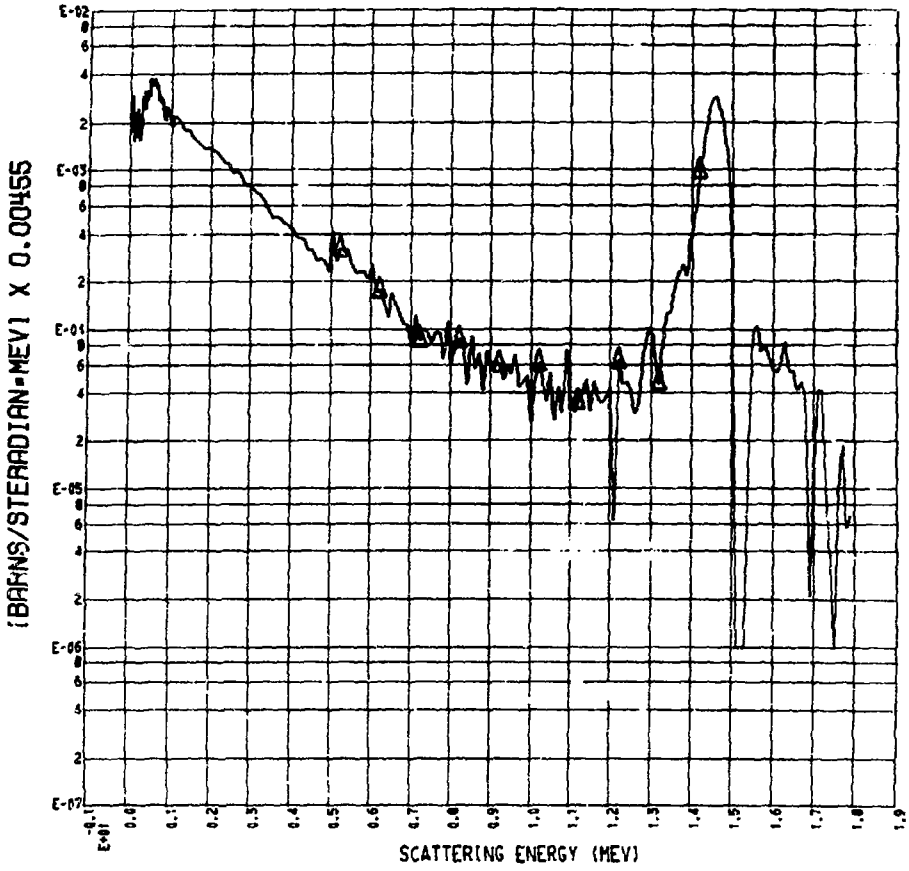

** PU-239 -- 30 DEG **

FIG. 112

DIFFERENTIAL ENERGY SPECTRUM

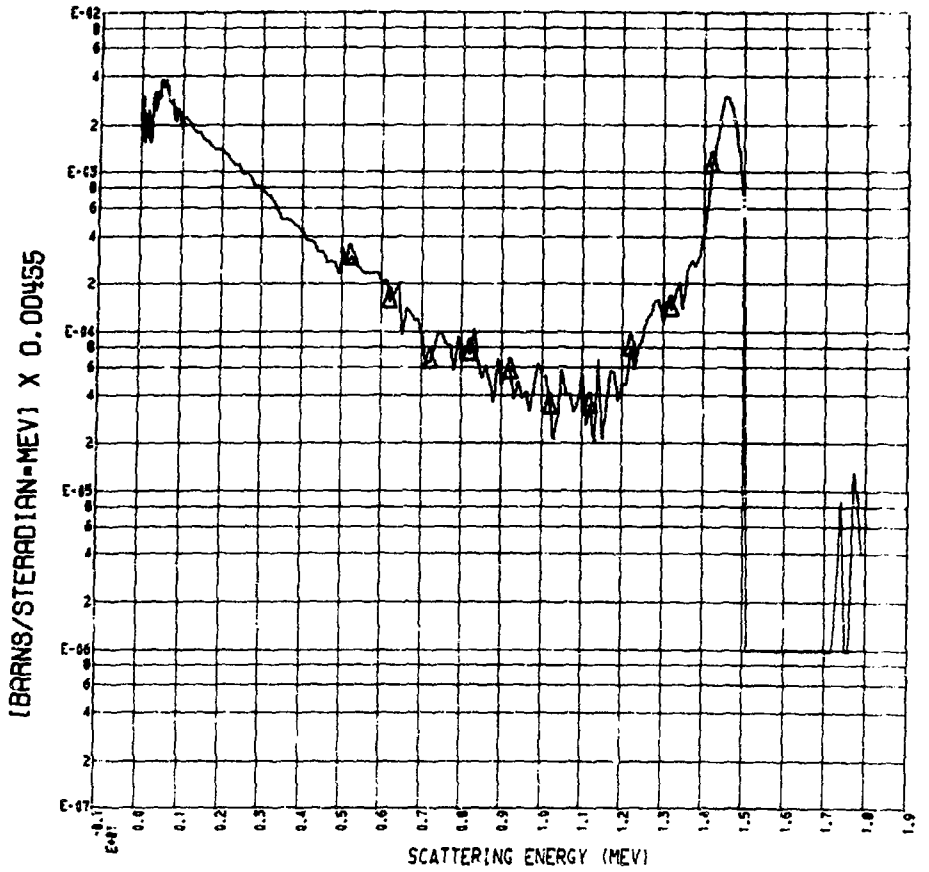

** PU-239 -- 35 DEG **

FIG. 113

DIFFERENTIAL ENERGY SPECTRUM

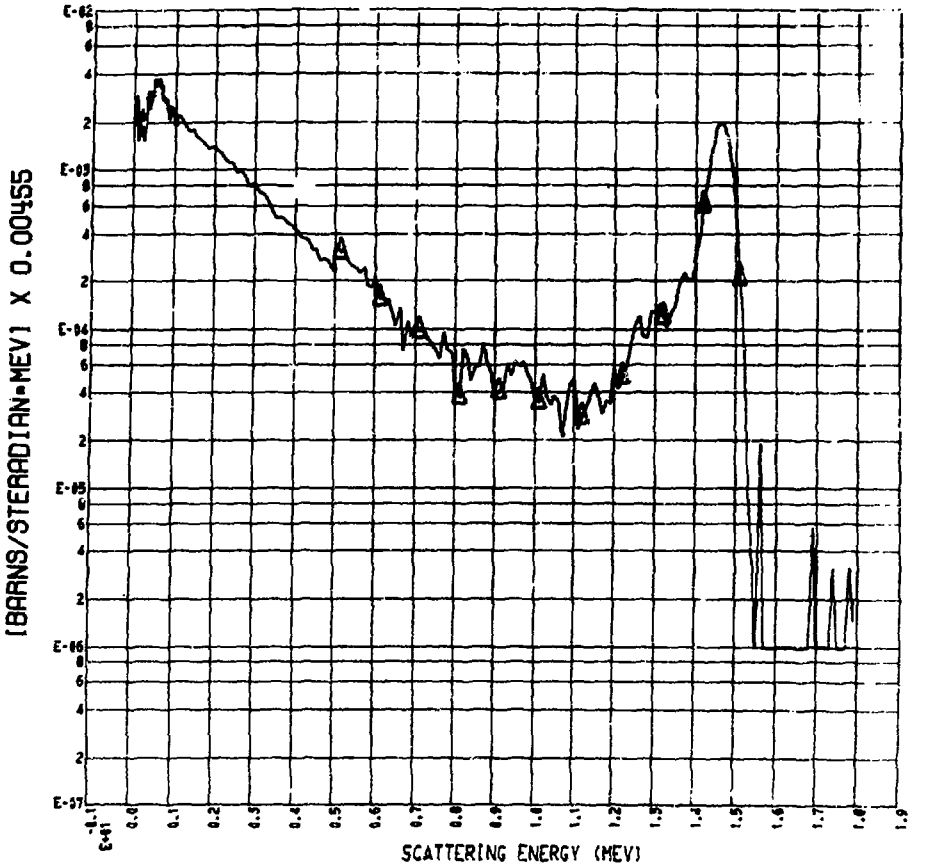

** PU-239 -- 40 DEG **

FIG. 114

DIFFERENTIAL ENERGY SPECTRUM

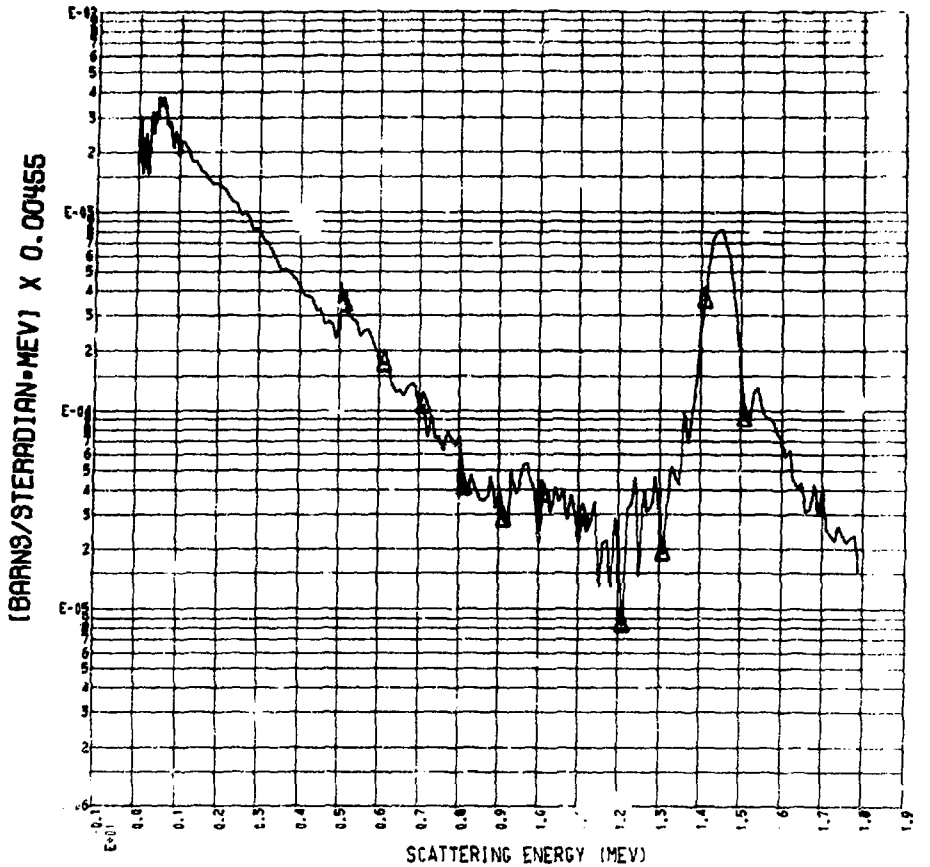

** 39 -- 45 DEG **

FIG. 115

DIFFERENTIAL ENERGY SPECTRUM

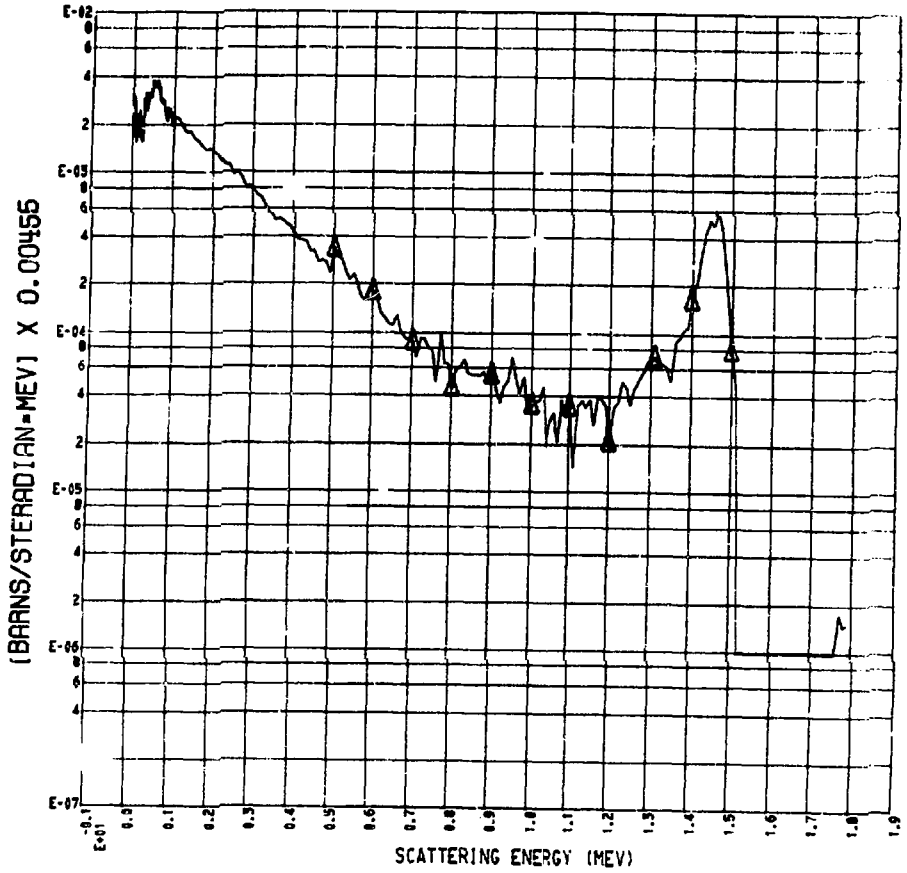

** PU-239 -- 50 DEG **

FIG. 116

DIFFERENTIAL ENERGY SPECTRUM

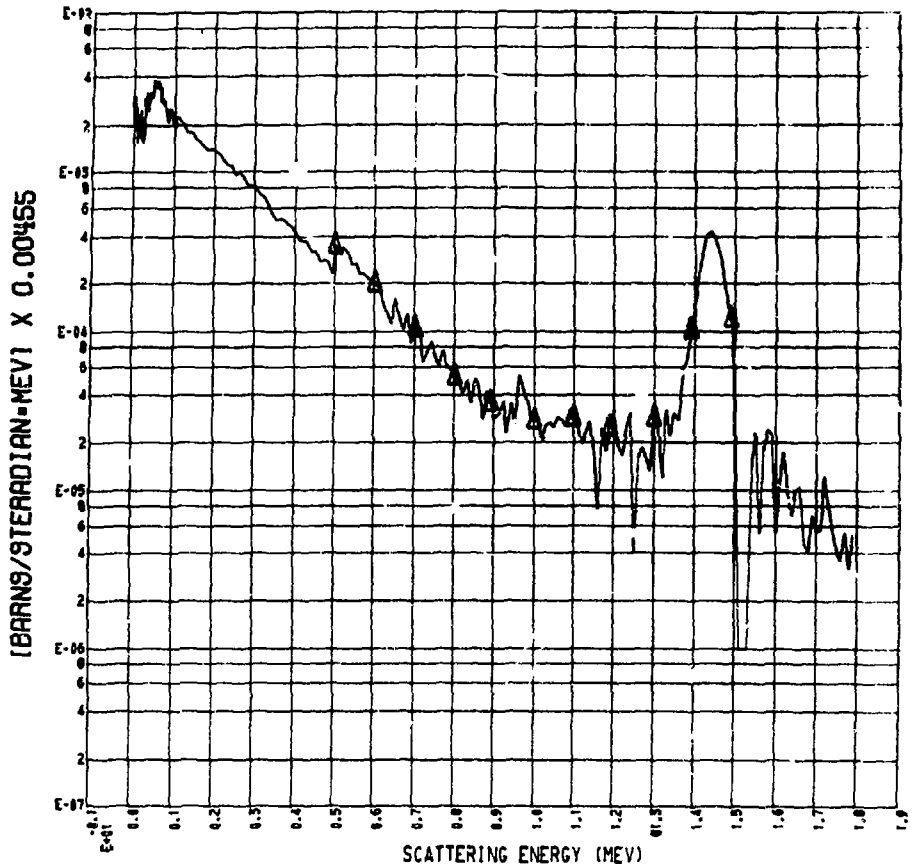

** PU-239 -- 55 DEG **

FIG. 117

DIFFERENTIAL ENERGY SPECTRUM

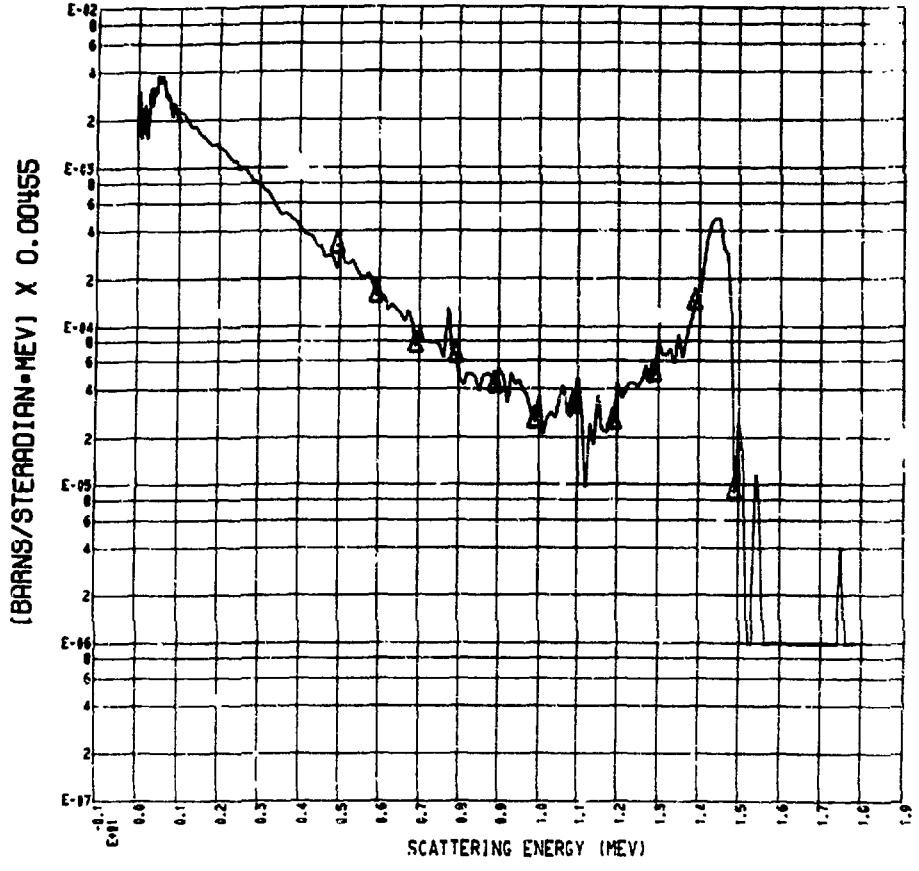

** PU-239 -- 60 DEG **

FIG. 118

DIFFERENTIAL ENERGY SPECTRUM

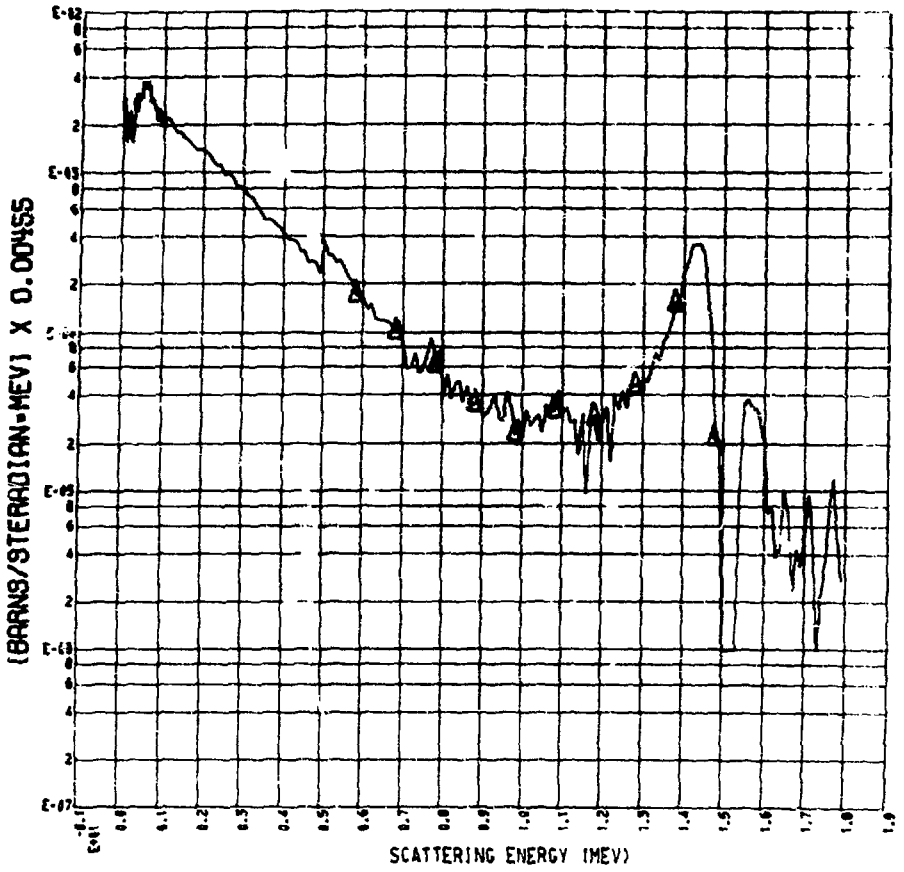

** PU-239 -- 65 DEG **

FIG. 119

DIFFERENTIAL ENERGY SPECTRUM

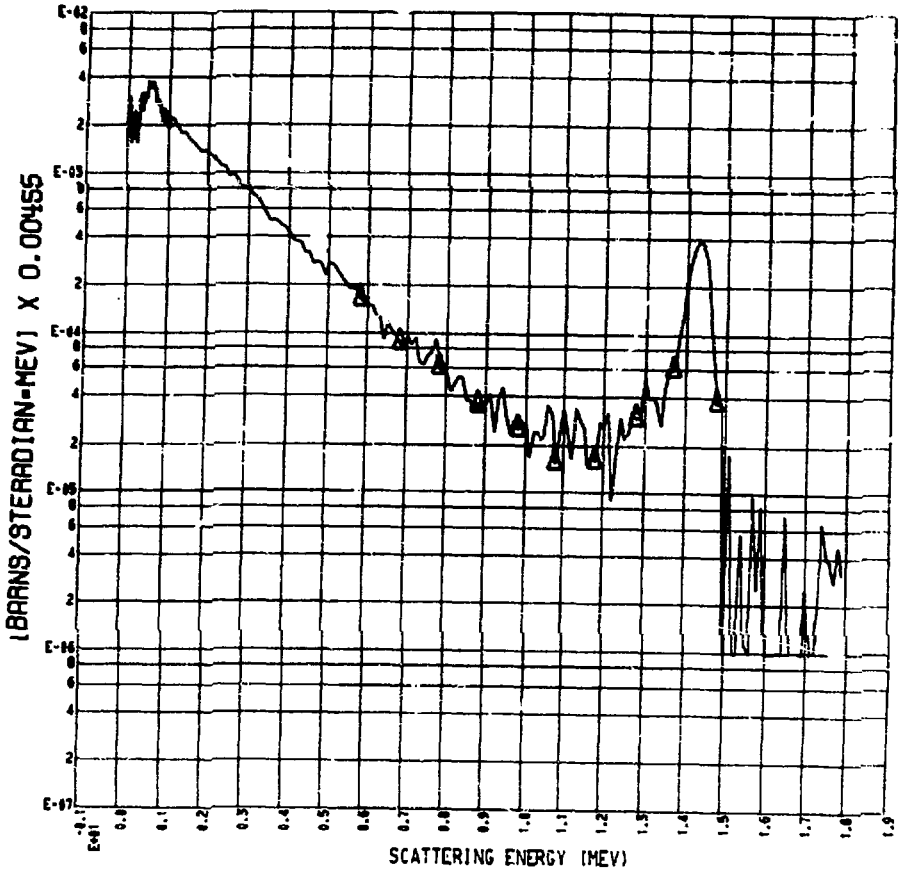

** PU-239 -- 70 DEG **

FIG. 120

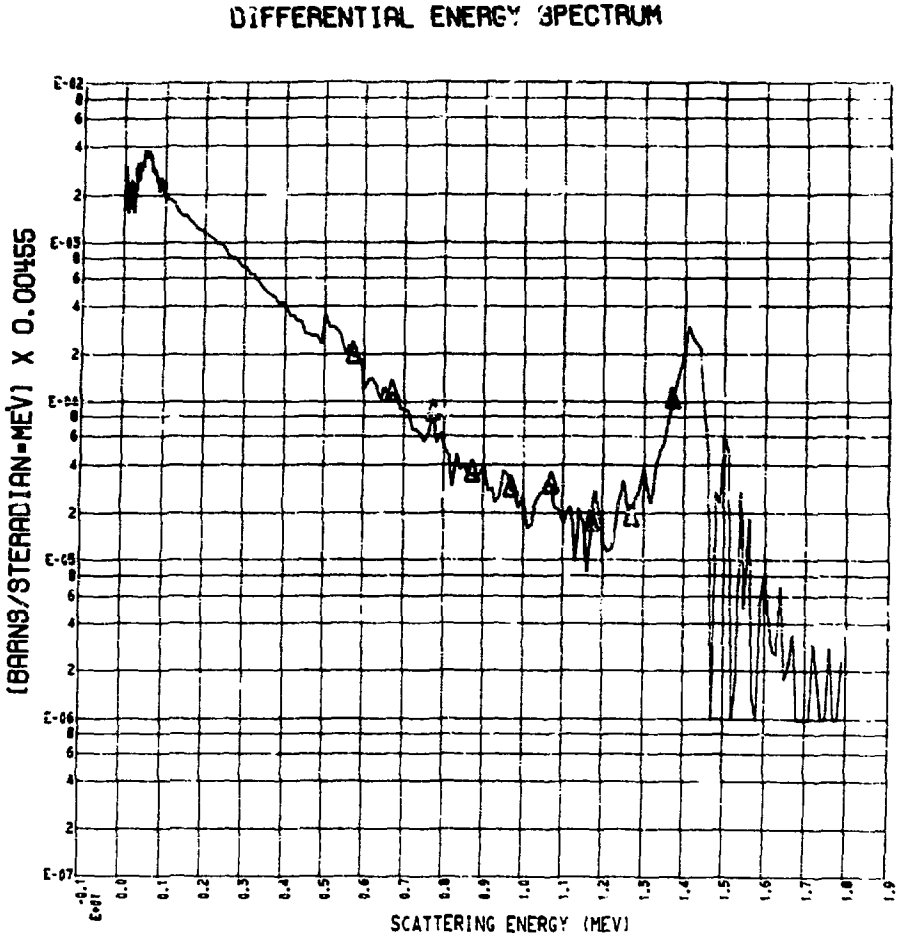
DIFFERENTIAL ENERGY SPECTRUM
(BARNS/STERADIAN-MEV) X 0.00455
SCATTERING ENERGY (MEV)
** PU-239 -- 75 DEG **

FIG. 121

DIFFERENTIAL ENERGY SPECTRUM

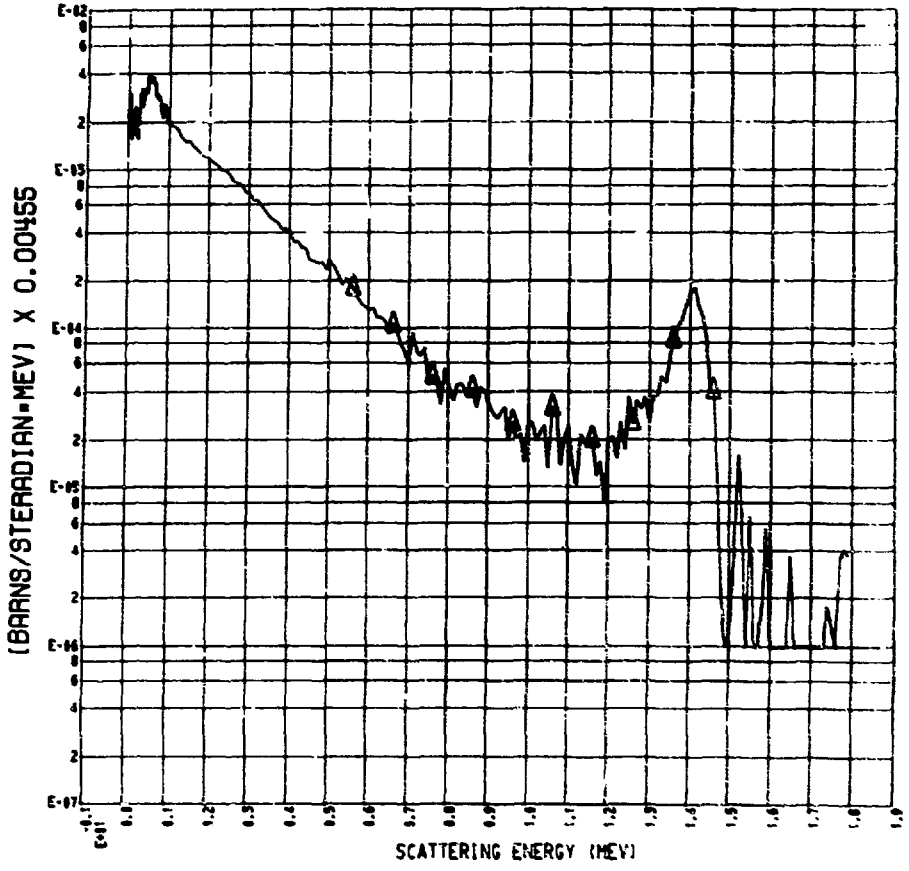

** PU-239 -- 80 DEG **

FIG. 122

DIFFERENTIAL ENERGY SPECTRUM

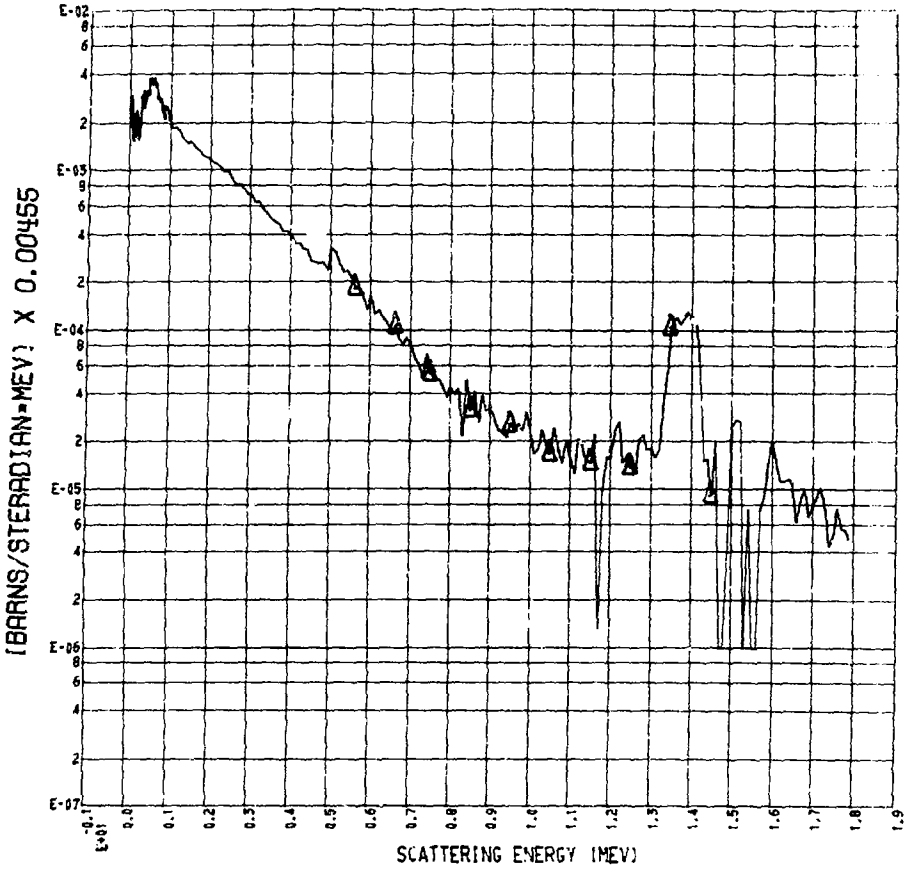

** PU-239 -- 85 DEG **

FIG. 123

DIFFERENTIAL ENERGY SPECTRUM

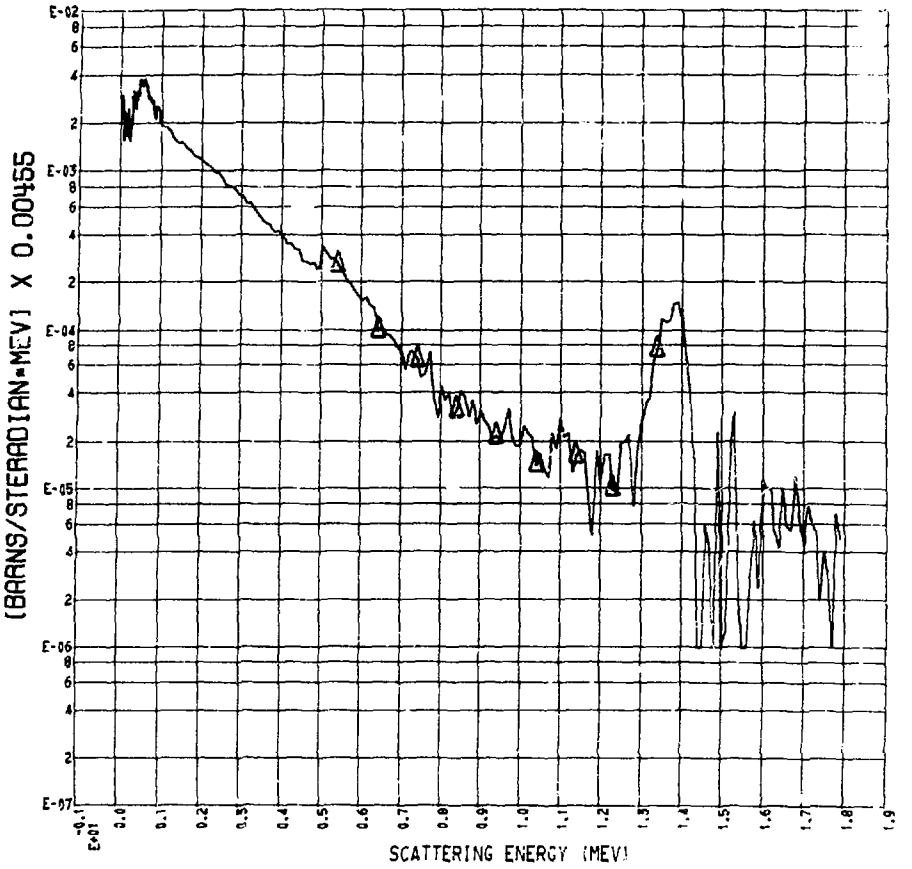

** PU-239 -- 95 DEG **

FIG. 124

DIFFERENTIAL ENERGY SPECTRUM

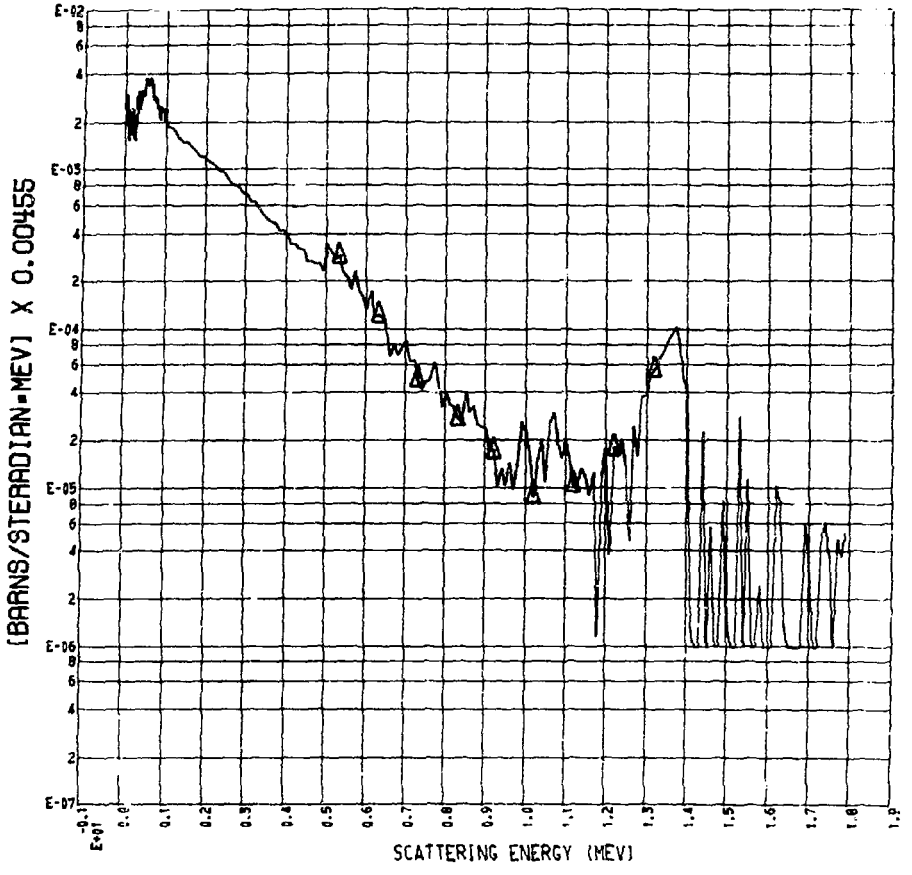

** PU-239 -- 105 DEG **

FIG. 125

DIFFERENTIAL ENERGY SPECTRUM

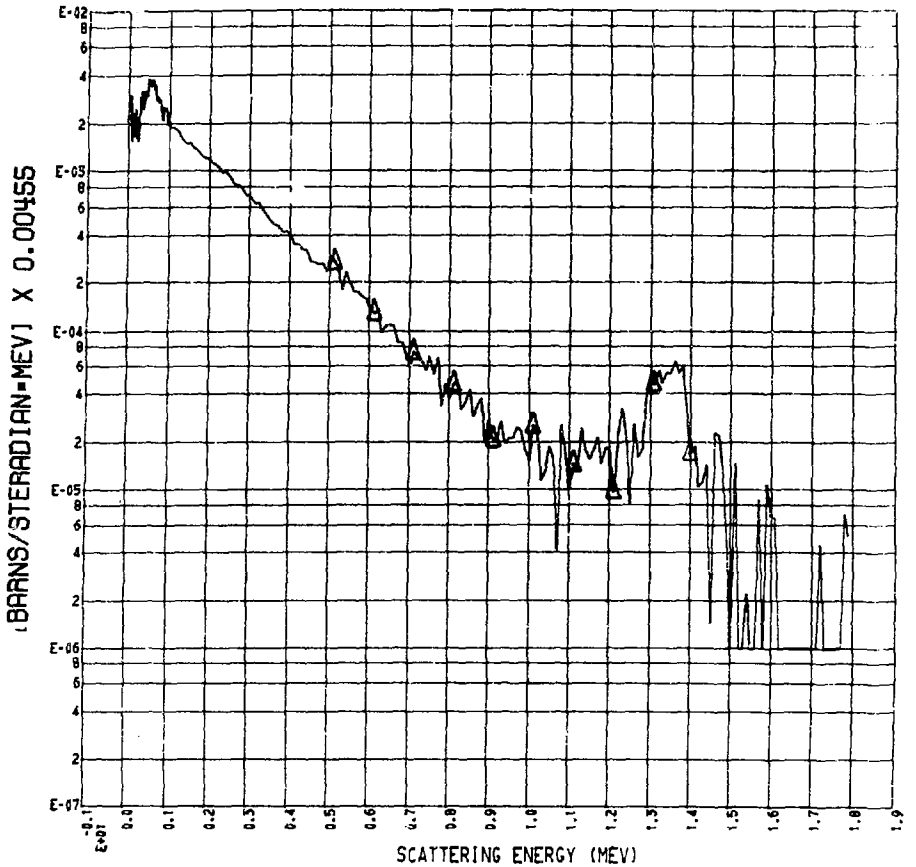

** PU-239 -- 115 DEG **

FIG. 126

DIFFERENTIAL ENERGY SPECTRUM

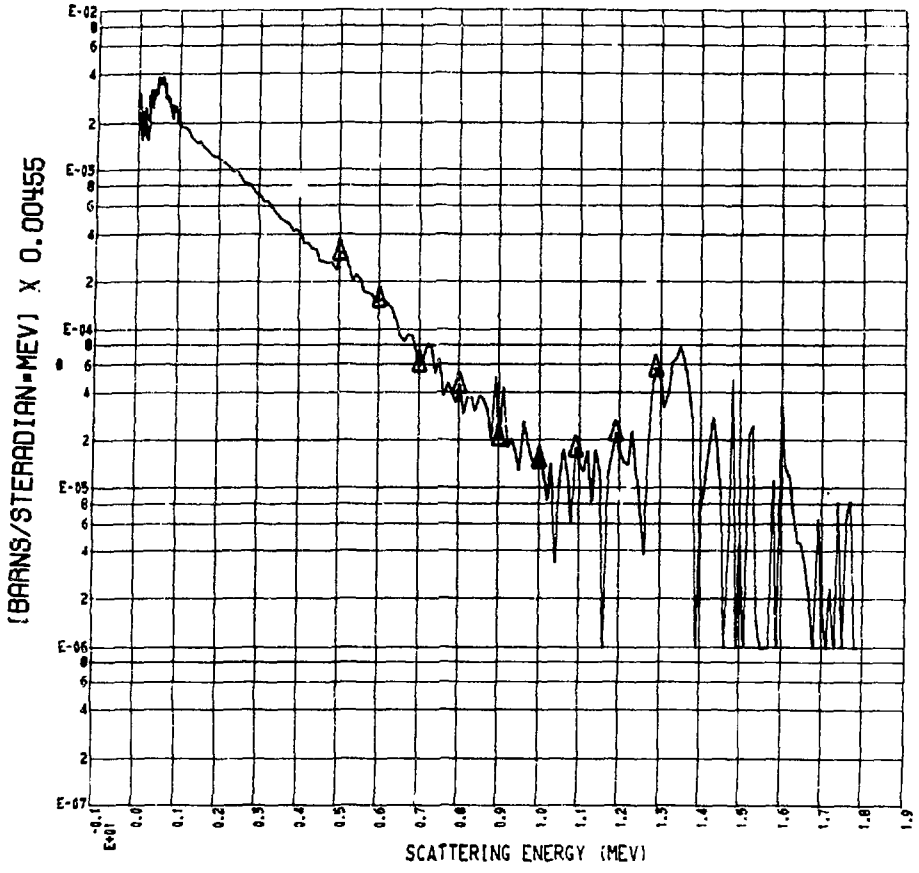

** PU-239 -- 125 DEG **

FIG. 127

DIFFERENTIAL ENERGY SPECTRUM

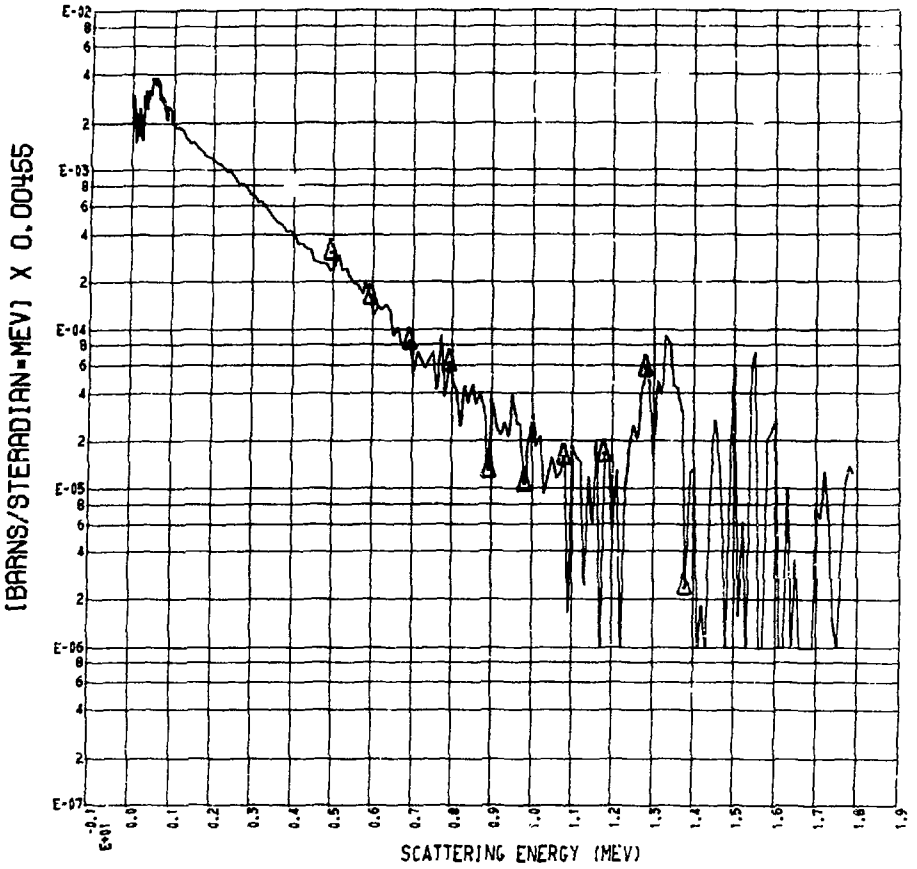

** PU-239 -- 135 DEG **

FIG. 128

DIFFERENTIAL ENERGY SPECTRUM

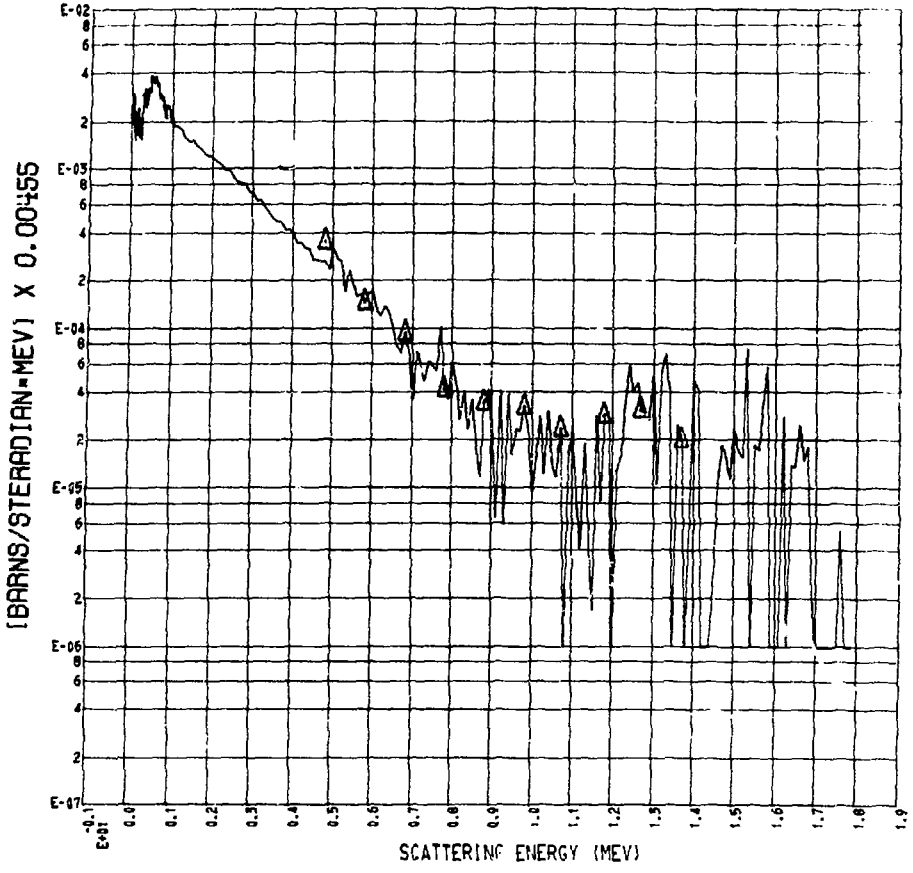

** PU-239 -- 145 DEG **

FIG. 129

ELASTIC ANGULAR DISTRIBUTION

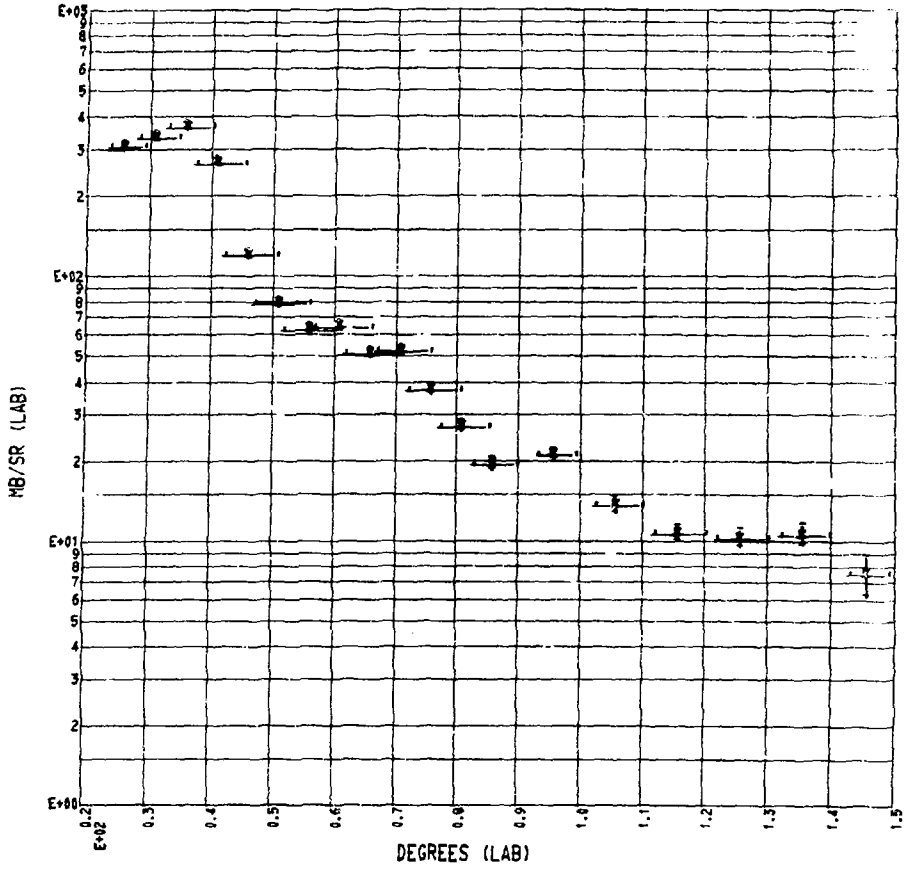

** PU-239 ** Q-VALUE SUM BETWEEN 0.50 AND -0.50 MEV

(ELASTIC)

FIG. 130

EXPERIMENTAL ANGULAR DISTRIBUTION

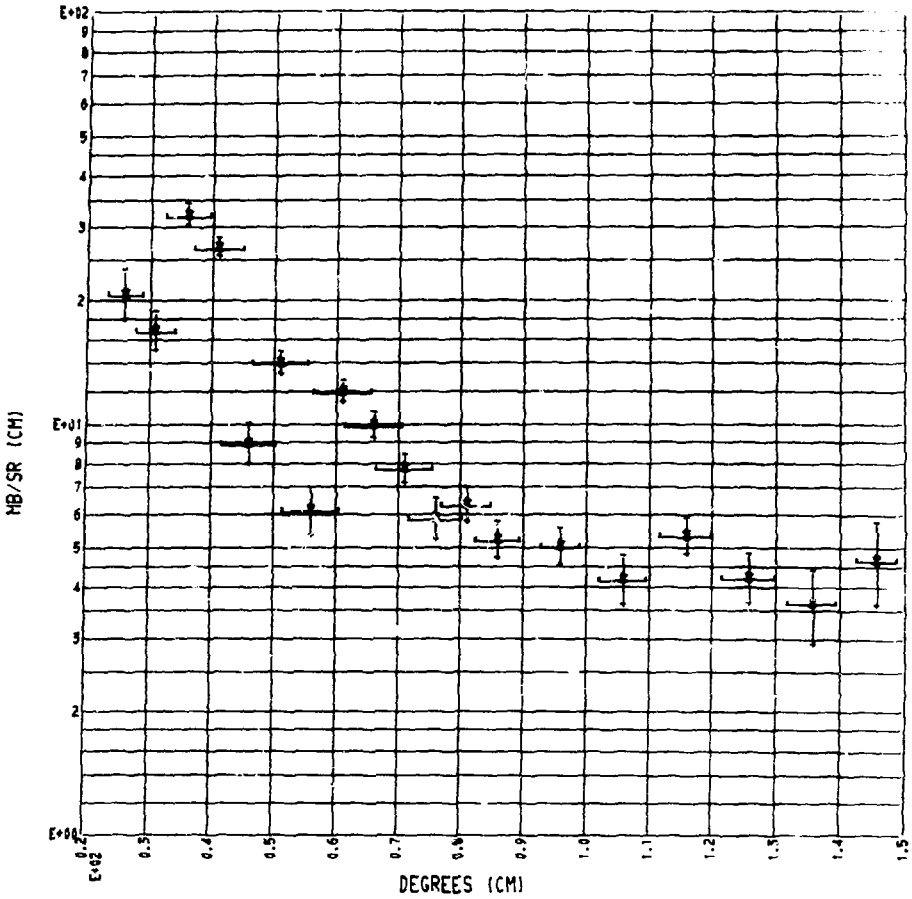

** PU-239 ** Q-VALUE SUM BETWEEN -1.50 AND -3.00 MEV

FIG. 131

EXPERIMENTAL ANGULAR DISTRIBUTION

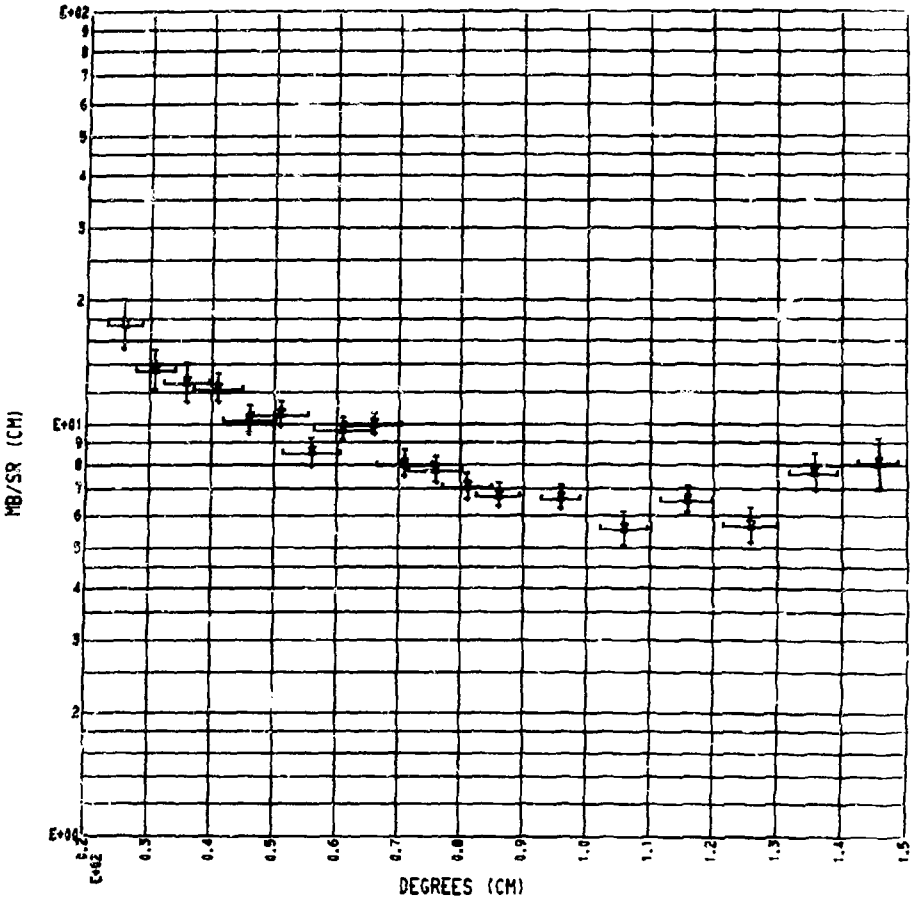

** PU-239 ** Q-VALUE SUM BETWEEN -3.00 AND -4.50 MEV

FIG. 132

EXPERIMENTAL ANGULAR DISTRIBUTION

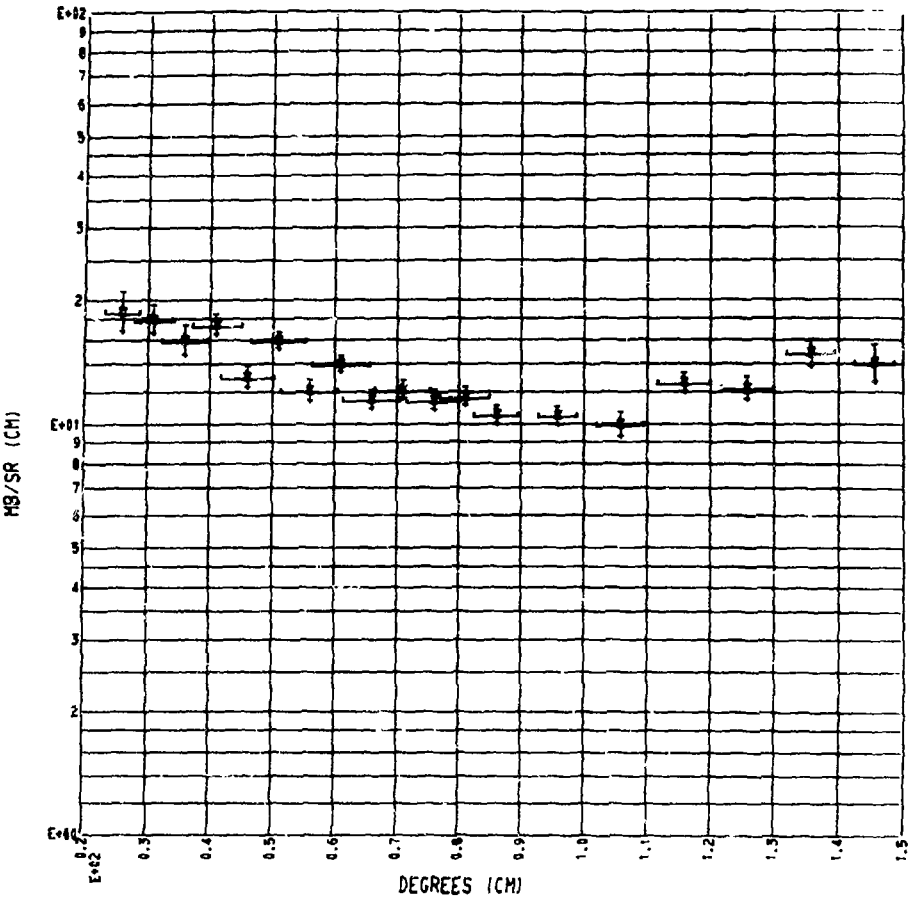

** PU-239 ** Q-VALUE SUM BETWEEN -4.50 AND -6.00 MEV

FIG. 133

EXPERIMENTAL ANGULAR DISTRIBUTION

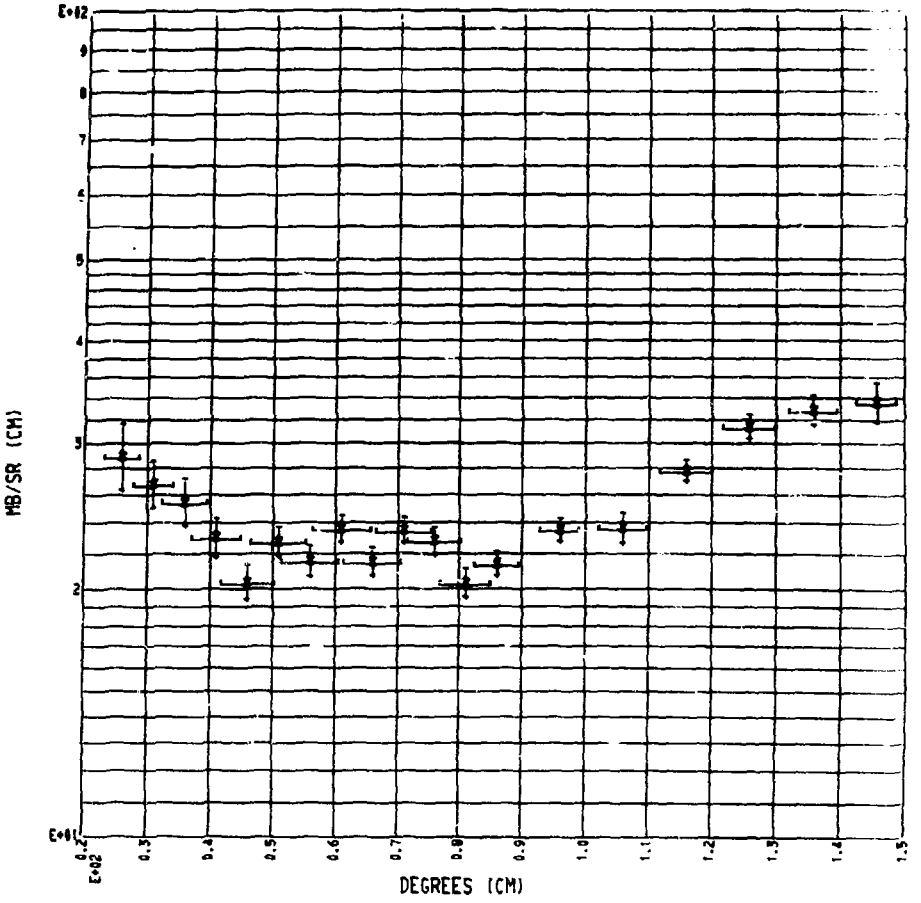

** PU-239 ** Q-VALUE SUM BETWEEN -6.00 AND -7.50 MEV

FIG. 134

EXPERIMENTAL ANGULAR DISTRIBUTION

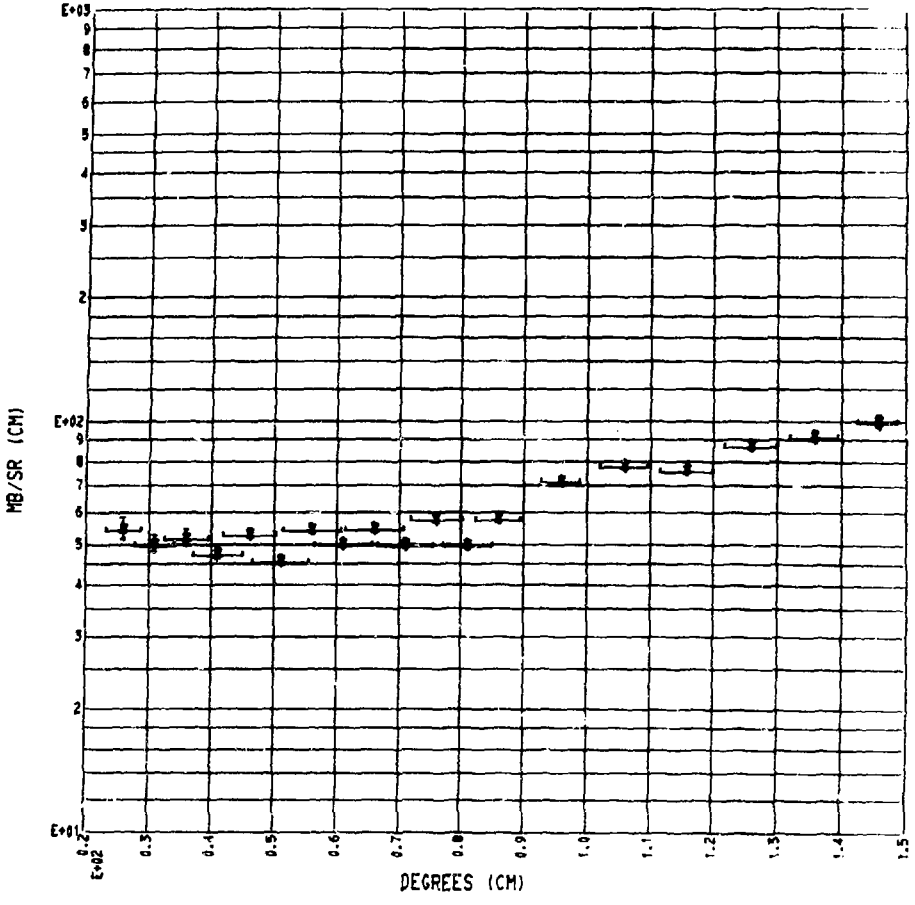

** PU-239 ** Q-VALUE SUM BETWEEN -7.50 AND -9.00 MEV

FIG. 135

V. Summary

The differential neutron emission spectra emitted by ^{239}Pu, ^{238}U, ^{235}U, Pb, Nb, Ni, Fe, Al, and C when bombarded by nominally 14 MeV neutrons from the $T(d,n)^4He$ reaction, were measured in ring geometry. The energy resolution ($E(MeV)^{3/2}/200$), the range of energies measured (10keV to 14 MeV), and the range of angles at which measurements were made (20-160 degrees), combine to make the measurements presented herein the most complete and precise of their type.

The data should be immediately useful to applied scientists and nuclear engineers for use in the study of 14 MeV neutron transport problems. The homogenity of the data over a wide range in Z values makes evaluation simple and the data easily utilizable. These data open channels of investigation for theoretical physics. Especially promising in this regard are the recently described[14,15] pre-equilibrium phenomena.

The sheer bulk of data taken dictated that there would be many interesting investigations of the data left undone. There remains a wealth of information which could be easily extracted from the data as presented herein. Cross sections could be integrated over angle, but optical model calculations[23] are needed for determination of the elastic cross section near zero degrees. This was done in the case of ^{235}U, and the total cross section compared favorably with published total cross sections.

The extracted angular distributions could be improved slightly by fitting the known line shape (see Sect. II.A.7 and Fig. 19) to the data. This process would allow separation of closely spaced levels of greatly

different magnitude. This would make possible the accurate determination of the angular distribution of the 2^+ level in iron, for example.

Much of the data is presented without the multiple scattering correction. This was done because the Monte Carlo code used to make the correction was especially inaccurate in the region where direct and pre-equilibrium scattering dominate (5 to 12 MeV). The correction should be calculated with a code which treats the phenomenon correctly. At any rate, the correction is believed to be less than 10% in this region.

I regret that I was unable to subtract the effects of the stainless steel container from the plutonium data. This could have been done experimentally by constructing an identical container and making a direct subtraction or by correcting the data by calculational methods. The code used for the multiple scattering correction made such a correction in principle. The error is large enough, however, to justify further investigation.

ACKNOWLEDGMENTS

I take great pleasure in thanking:

Dr. John D. Anderson for his able guidance in my research program, for numerous informative conversations and suggestions, for the hours of his time spent taking data in my absence, and for encouragement and assistance in many phases of my work as a graduate student.

Dr. Stewart D. Bloom for his able instruction and valuable administrative assistance, both in the classroom and in the laboratory, without which my efforts would have surely faltered.

Dr. Eugene Goldberg for insuring that I had the time, place, and resources necessary for completion of this work and for spurring my efforts to completion.

My colleagues Dr. Calvin Wong, Dr. Steven Grimes, Dr. Jay Davis, Mr. James McKenzie, Mr. Clinton Logan, Mr. William Bartolini, Mr. Bertram Pohl, Mr. John McClure and Dr. Mitchell Gregory for many interesting and informative conversations -- both technical and non-technical.

Dr. Luisa Hansen whose continued interest in my work and well-being is sincerely appreciated.

Mr. Lewis Mego and other members of the ICT crew for their excellent support in providing the necessary beams.

Barbara Pereira for timely and excellent support in preparing this manuscript.

Doris Hine for being Doris Hine.

Appendix A

Experimental Geometries for Measuring Neutron Scattering

1. General

The experimental geometry used for a particular experiment is at best a compromise. It is desired that a high neutron flux be obtainable in a geometry which requires few corrections to the data due to multiple scattering, background, and source polarization. Equipment costs, set up time, and running times must be reasonable.

Ring geometry was chosen for this work as the best geometry available. Other possible geometries will be discussed in this appendix in order that the reasons for this choice become obvious. There is an infinite number of possibilities regarding the shape and location of the scattering material, the shielding and collimation, the neutron source, and the detector. Only three possibilities in common usage are discussed here, but others are possible and have been used.

2. Cylindrical Geometry

Fig. 136 a is a schematic representation of cylindrical geometry in which the neutron source and a cylindrical scatterer remain stationary and the angular distribution is measured by varying the detector location. This geometry facilitates the accurate measurement of the scattered angular distribution since the target is symmetric to all scattering angles. Source polarization difficulties are avoided since the zero degree source neutrons are scattered from the cylindrical sample. Source neutron energy is easily varied by varying the energy of the charged particle beam and by using various neutron producing reactions.

Serious difficulties arise from cylindrical geometry due to the need for a large scatterer to detector distance in order that time-of-flight can be used to determine scattered neutron energy. If the scatterer is large enough to yield reasonable flux levels at a distant detector, multiple scattering becomes a large effect and seriously degrades the accuracy of the cross section determination. The cylinder diameter is thus limited to about 1/4 mean-free-paths. If the preferred shadow shield geometry shown in Fig. 136a is used, shields must be prepared for all angles.

3. Flat Plate Geometry

The flat plate geometry depicted in Fig. 136b has many of the advantages of cylindrical geometry but fewer disadvantages. Neutron flux at the detector is about a factor of five higher, thus reducing the running time at each angle, yet multiple scattering is approximately the same since it is primarily a function of plate thickness. It is possible to obviate the need for multiple shadow shields to cover the desired angular range by enclosing the detector in a collimator system which "sees" only neutrons scattered from the sample.

Flat plate geometry suffers from poor angular resolution, variation in the scattered neutron's flight path, and low count rate.

4. Ring Geometry

The principle advantages of ring geometry are high count rate and small multiple scattering corrections.

The count rate is about a factor of 30 higher than cylindrical geometry experiments of comparable angular resolution and multiple

scattering correction. Ring geometry in the present application features a stationary neutron source, detector, shadow shield and collimator. The ring position is changed to define the scattering angle. Since a neutron source energy of 14 MeV was desired, the $T(d,n)^4He$ reaction was used at low deuteron energy. A low energy accelerator capable of high deuteron fluxes was used to increase the detected flux to a factor of 100 more than observed in the typical cylindrical geometry experiment.[42] At low deuteron energy the source is not polarized,[45] thus eliminating one of the difficulties of ring geometry. Source neutron energy and flux aniostropy are only minor problems at the low deuteron energies used. Fig. 136 c is a ring geometry schematic.

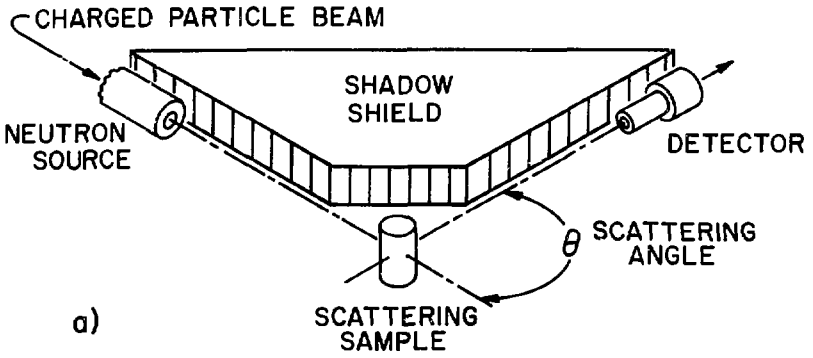
CHARGED PARTICLE BEAM
SHADOW SHIELD
NEUTRON SOURCE
DETECTOR
θ
SCATTERING ANGLE
SCATTERING SAMPLE
a)

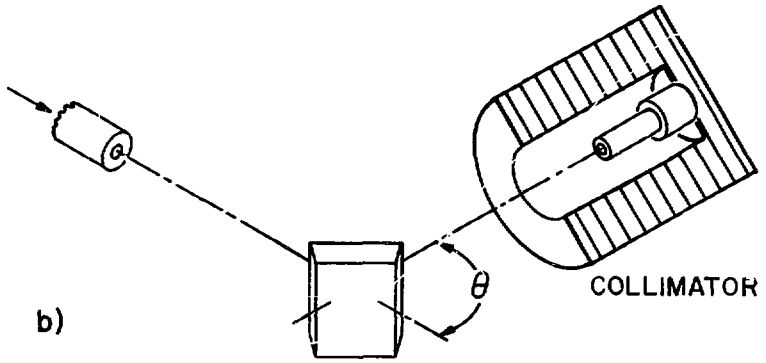
θ
COLLIMATOR
b)

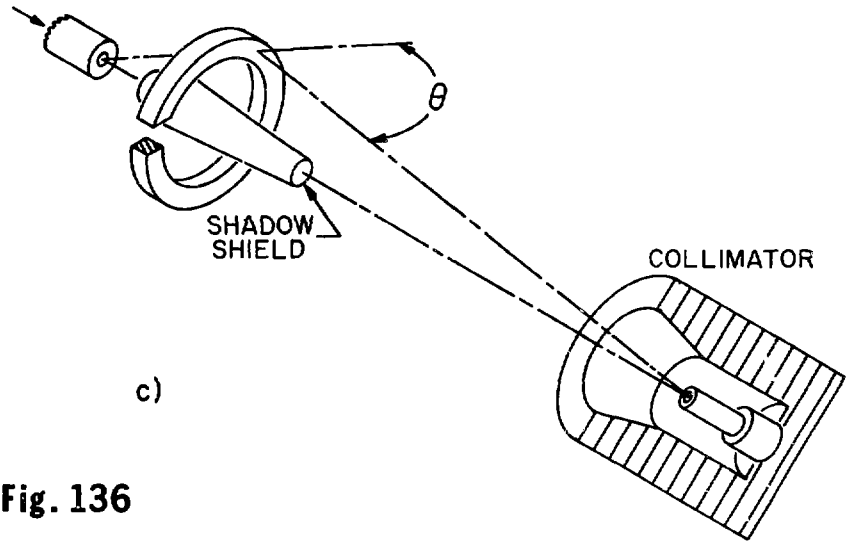
θ
SHADOW SHIELD
COLLIMATOR
c)

Fig. 136

References

1. C. Wong, J. D. Anderson, P. Brown, L. F. Hansen, J. L. Kammerdiener, C. Logan, B. Pohl, UCRL-51144 (Nov. 1971).
2. L. F. Hansen, J. D. Anderson, E. Goldberg, J. Kammerdiener, E. F. Plechaty, and C. Wong, Nucl. Sci. & Engr. 40, 262-282 (1970).
3. T. Wiedling, Symposium on Neutron Standards and Flux Normalization, Argonne, Ill. (21 Oct. 1970) pp. 437-451.
4. G. D. Sauter, P. A. Robinson, UCRL-50856 (1970)
5. L. F. Hansen, J. D. Anderson, E. Goldberg, E. F. Plechaty, M. L. Stelts, and C. Wong, Nucl. Sci. & Engr. 35, 227-239 (1969).
6. T. Ericson and V. Strutinski, Nucl. Phys. 8, 284 (1958).
7. J. L. Fowler and J. E. Brolley, Jr., Rev. of Mod. Phys., Vol. 28, No. 2, 103-134 (1956).
8. J. Benveniste and J. Zenger, UCRL-4266 (1954).
9. E. F. Plechaty and J. R. Kimlinger, UCIR-522 (Feb. 1971).
10. J. H. Coon, R. W. Davis, H. E. Felthauser, and D. B. Nicodemus, Phys. Rev. 111, 250 (1958).
11. A. Sal'nikov, N. I. Fetisov, G. N. Lovchikova, G. V. Kotel'nikova, V. B. Anufrienko and B. V. Devkin, Trans. of IZVESTIA AKAD NVAK SSSR 32, 653 (1968).
12. P. H. Stelson, R. L. Robinson, H. J. Kim, J. Rapapart, G. R. Satchler, Nucl. Phys. 68, 97 (1965).
13. R. W. Bauer, J. D. Anderson, L. J. Christensen, Nucl. Phys. 47 (1963) 241-250.

14. B. A. Pohl, J. D. Anderson, J. W. McClure, C. Wong, UCRL-50563.

15. T. G. Masterson, Nucl. Instr. and Meth. 88, 61 (1970)

16. Private communication with J. McClure, LLL, Livermore, whose detector efficiency calculation is based on the formalism of A. Elwyn, J. V. Kane, S. Ofer, and D. H. Wilkerson, Phys. Rev. 116, 1490 (1959).

17. E. F. Plechaty and Kimlinger, SORS Monte Carlo Neutron-Transport Code, UCRL-50532 (1968).

18. S. M. Grimes, J. D. Anderson, B. A. Pohl, J. W. McClure, C. Wong, UCRL-73138 (1971).

19. C. K. Cline and M. Blann, Univ. of Rochester Report, UR 3591-17 (1971)

20. D. Cummings, LLL, Livermore, Ca. Private Communication.

21. J. B. Parker, J. H. Towle, D. Sams, W. B. Gelboy, A. D. Purnell, and H. J. Stevens, Nucl. Instr. and Meth. 30, 77 (1964).

22. J. B. Parker, J. H. Towle, D. Sams, and P. G. Jones, Nucl. Instr. & Meth. 14, 1 (1961).

23. H. J. Amster, E. J. Teshan, M. Walt, "Computer Techniques," Ch. IV.I, Fast Neutron Physics, Part I, J. B. Marion and J. L. Fowler, editors, Intersciences Publishers, Inc., New York (1960).

24. J. B. Anufrienko, B.V. Devkin, G. V. Kotel'nikova, Yu.S.Kulabukhov, G. N. Lovchikova, O. A. Sol'nikov, L.A. Timokhin, V. R. Trubnikov, N. I. Fetisov, Sov. Jour. Nucl. Phys. 2, 589 (1966).

25. G. C. Bonazzola and E. Chiavassa, Phys. Rev. 140, B835 (1965).

26. F. P. Agee and L. Rosen, "Calculation of Neutron Cross Sections Using a Local Optical Potential with Average Parameters." Los Alamos Scientific Lab. LA-3538-MS Vol. II.

27. J. D. Anderson, C. C. Gardner, M. P. Nakada, C. Wong, Phys. Rev. 110, (1958).

28. Paul A. Robinson, LLL, Livermore, Calif., Private communication.

29. M. P. Nakada, J. D. Anderson, C. C. Gardner, and C. Wong, Phys. Rev. 110, 1439 (1958).

30. R. Bouchez, J. Duclos, and P. Perrin, Nucl. Phys. 43, 623 (1963).

31. J. D. Anderson, C. C. Gardner, J. W. McClure, M. P. Nakada, and C. Wong, Phys. Rev. 111, 572 (1958).

32. J. Voignier, G. Clayeux, F. Bertrand, report CEN. Limeil, [illegible]ance "Inelastic Neutron Scattering Cross Sections in Several Elements with 14.1 MeV Neutrons."

33. O. A. Sal'nikov, G. V. Lovchikova, G. V. Kotelnikova, V. S. Nesterenko, N. I. Fetisov and A. M. Trufanov, Sov. Jour. Nucl. Phys. 12, 620 (1971).

34. E. R. Graves and R. W. Davis, Phys. Rev. 97, 1205 (1955).

35. R. W. Bauer, J. D. Anderson, and L. J. Christensen, Nucl. Phys. 48, (1963) 152-158.

36. R. L. Clarke and W. G. Cross, Nucl. Phys. A95, 320 (1967).

37. D. Steiner, Nucl. Appl. & Tech. Vol. 9, p. 83-92 (July 1970).

38. C. M. Logan, UCRL-51224 (1972).

39. C. Y. Fu, F. G. Perey, ORNL-4705, 50 (Oct. 1971).

40. In.S.Zamiatnin, J. N. Safine, E. K. Gutnikova, and N. I. Ivanova, Sov. Jour. Atomic Energy 4, 443 (1958).

41. Yu. A. Vasil'ev, Yu. S. Zamyatnin, Yu. I. Il'in, E. I. Sirotinin, P. V. Toropov, and E. F. Fomushkin, Soviet Physics JETP, 11, 483 (1960).

42. J. Voignier, Report CEA-R-3503 (1968).

43. A. Bertin, G. Clayeus, "Study of Fission Neutron Spectra by Means of Fast Fission Chamber with an On-Line Computer" report CEA CE Linneil, France.

44. P. Boschung, St. Gagneux, B. Hoop, Jr., P. Huber, Z. Lewandowski, and R. Wagner, Helvetica Physica Acta, 42, 225 (1969).

45. W. Haeberli, "Polarization of Neutrons in Reactions and Scattering," Ch.V.G., Fast Neutron Physics, Part II, J. B. Marion and J. L. Fowler, editors, Intersciences Publishers, Inc. New York (1960).

NOTICE

"This report was prepared as an account of work sponsored by the United States Government. Neither the United States nor the United States Atomic Energy Commission, nor any of their employees, nor any of their contractors, subcontractors, or their employees, makes any warranty, express or implied, or assumes any legal liability or responsibility for the accuracy, completeness or usefulness of any information, apparatus, product or process disclosed, or represents that its use would not infringe privately-owned rights."

Printed in USA. Available from the National Technical Information Center, National Bureau of Standards, U. S. Department of Commerce, Springfield, Virginia 22151
Price: Printed Copy $3.00; Microfiche $0.65.